UNIVERSITY OF
LIVERPOOL

Department of Chemistry

The Synthesis and Separation Properties of Organic Cage Compounds

Thesis submitted in accordance with the requirements of the
University of Liverpool for the degree of Doctor of Philosophy

Adam Kewley

November 2014

Adam Kewley

The Synthesis and Separation Properties of Organic Cage Compounds

Abstract

Microporous materials play an important role in a variety of industrial and domestic applications. While a diverse range of microporous materials have been identified, this thesis focuses on porous organic cages (POCs) because they have received much attention as synthetically tunable, solution processable, microporous materials. After introducing the latest developments in POC synthesis and the general application of microporous materials as selective sorbents, this thesis presents three developments in organic cage chemistry: a high-throughput workflow for the discovery of POCs, which yielded a novel organic cage compound; the measurement of selective adsorption by POCs, wherein the first instance of chiral selectivity by a POC was recorded; and the first instance of applying POCs as stationary phases for gas chromatography, which produced columns that separate racemic mixtures, alkylaromatic isomers, and alkane isomers.

Chapter 2, *discovering novel organic cages*, presents attempts to use high-throughput and *in-silico* techniques to accelerate the discovery of novel organic cages. These methods were utilised to isolate a novel organic cage, **CCX**-*S*, which is characterised and discussed. Chapter 3, *organic cages as selective sorbents*, presents the development of approaches for measuring selective adsorption. These methods were used to identify the first reported instance of enantioselective adsorption by an organic cage. Further measurements to explain this separation behavior are also presented. Chapter 4, *chromatographic separations with organic cages*, presents one method of practically leveraging the presented separation behavior. In Chapter 4, the coating of capillary columns with **CC3** is presented. These columns were used to successfully perform gas chromatographic separations, the first recorded instance of using a POC to do so. The columns were further improved by modifying the coating method and using prefabricated **CC3** nanoparticles. This modification enabled difficult separations to be performed using the column; for example, the separation of hexane's five isomers.

Publications resulting from work Presented in This Thesis

From Chapter 3, my work on the enantioselective separation of compounds by **CC3** contributed directly to a Nature Materials publication.[66] At the time, the accurate measurement of chiral selectivity by **CC3** was a novel development that had not previously been reported. Evidence presented in this chapter was also used to substantiate a patent application (UK Patent Application No. 1411515.8 - "Separation using solid organic molecular cages").

From Chapter 4, the development of **CC3** columns and the analysis of their separation behavior contributed directly to a Chemistry of Materials publication.[140] The research demonstrated the first instance of applying an organic cage as a gas chromatographic stationary phase and, more importantly, that organic cages are capable of performing separations that are quite difficult to do with conventional stationary phases.

Nature Materials allows authors to submit front-cover designs. The editor's favorite is chosen for the official monthly issue of Nature Materials. My submission, which was accepted as the cover for the 10th issue of its 13th volume, is shown above. To create the design, the arrangement was 3d modelled in Blender followed by final touch-ups in Adobe Photoshop.

Abbreviations

1-PE	1-Phenylethanol
β-CD	Beta cyclodextrin
CC1, **CC2**, **CC3**	Covalent cages 1, 2, and 3
CCX-*S*	Covalent cage "X"
CD	Cyclodextrin
CSP	Chiral stationary phase
DCC	Dynamic covalent chemistry
ee	Enantiomeric excess
FTIR	Fourier transform infrared (spectroscopy)
GC	Gas chromatography
GC-FID	Gas chromatography (using a) flame ionization detector
HPLC	High-performance liquid chromatography
HT	High throughput
MOF	Metal-organic framework
NMR	Nuclear magnetic resonance (spectroscopy)
PXRD	Powder x-ray diffraction
scXRD	Single-crystal x-ray diffraction
SEM	Scanning electron microscope
TGA	Thermogravimetric analysis
XRD	X-ray diffraction

Contents

1 **Introduction**

Tasks such as the capture of carbon dioxide,[1] storage of hydrogen,[2] or separation of hydrocarbons[3] have received much attention due to their respective impacts on global warming, energy storage, or material production cost. A variety of techniques have emerged for performing these tasks; for example, trapping carbon dioxide in large brine reservoirs,[4] amine scrubbers,[5] or ionic liquids.[6] This thesis focuses on another popular approach: the use of microporous materials as solid adsorbents.

A porous material is defined as a substance that contains accessible voids. Based on the diameter (d) of these voids, the material can be classified into three (IUPAC defined)[7] subcategories: macro- ($d > 50$ nm), meso- (2 nm $< d <$ 50 nm); or micro-porous ($d < 2$ nm). All three are used in applications where high surface-area-to-volume ratios are needed, such as in catalysis[8] and sorbents.[9] However, because the voids of microporous materials are on the molecular scale, their interaction with guest molecules differs.

In macro- and meso-porous materials, guest molecule diffusion is governed primarily by guest to guest interactions while guest to pore-wall interactions are negligible. By contrast, in microporous materials, guest molecule diffusion is governed by guest to pore-wall interactions.[10] As a result, they have a strong influence on guests, in some cases, strong enough to adsorb and store gases such as hydrogen[11] or carbon dioxide.[12] Further, as slight differences in guests' structures can greatly affect their adsorption behaviour, microporous materials may be used in separation technologies, a major topic of this thesis.

Deciding which microporous material to use in a particular technology can be challenging. In this introduction, three subcategories of microporous materials—inorganic, hybrid, and organic—shall be discussed. However, because there are numerous materials in each category, too many to cover here, discussions are limited to a subset of these materials. For detailed explanations of materials not covered in this chapter, the reader is directed towards reviews referenced in Table 1-1.

Table 1-1 | Established classes of microporous materials. Citations refer to review articles for each material. Underlined materials receive particular attention throughout this introduction as they are more relevant to topics discussed throughout this thesis.

Inorganic	Hybrid	Organic
		Activated carbons[17]
		Calixarenes[18]
		Conjugated microporous polymers (CMPs)[19]
		Covalent organic frameworks (COFs)[20]
	Metal coordinated cages[14]	Covalent triazine frameworks
	Metal-organic frameworks (MOFs)[15]	
Zeolites[13]		Cucurbiturils[21]
	Zeolitic imidazolate frameworks (ZIFs)[16]	Hypercrosslinked polymers (HCPs)[22]
		Polymers of intrinsic microporosity (PIMs)[23]
		Porous aromatic frameworks[24]
		Porous organic cages[25]

1.1   Inorganic Microporous Materials

Inorganic microporous materials tend to have a rigid pore structure and high crystallinity. Zeolites, which are inorganic microporous materials, are composed of a repeating pore network of crystalline aluminosilicates (Figure 1-1). Usually, they are highly crystalline, chemically inert, and, as many occur naturally, they can be cheap.[13] They are widely applied, featuring in technologies such as industrial catalysts,[26] water purifiers,[27] and molecular sieves,[13] which demonstrates the general importance of microporous materials.

While zeolites have received widespread application, they do have limitations. First, their rigid aluminosilicate building blocks only arrange into limited topologies;[28]
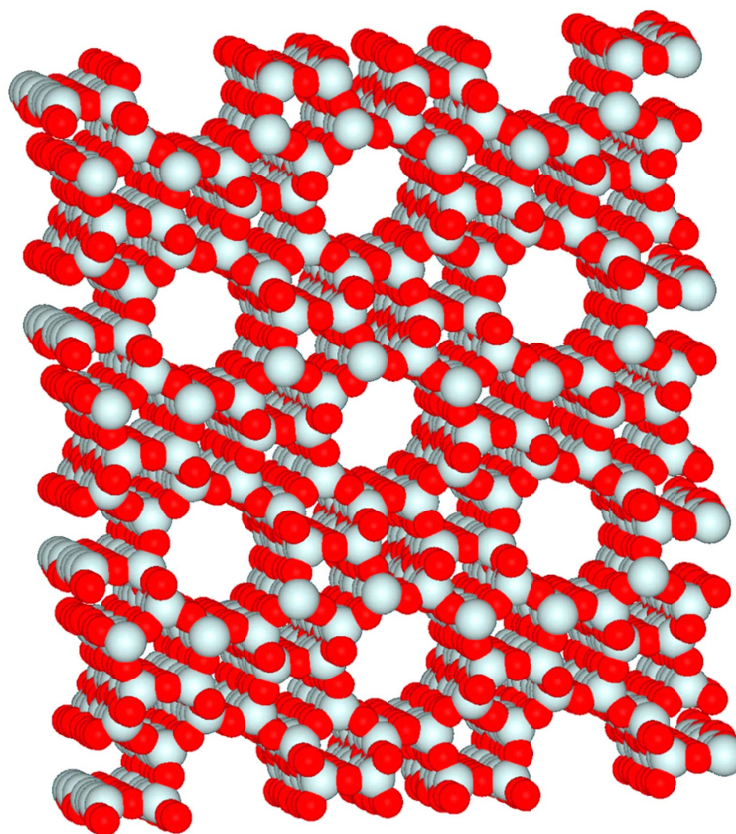
Figure 1-1 | Zeolite socony mobil-5 (ZSM-5). Darker red atoms indicate aluminium, lighter grey atoms indicate silicon. Patented by the Mobil Oil Company in 1972,[29] ZSM-5 is widely used in the petroleum industry as a catalyst for isomerization reactions.[30,31]

consequently, zeolites have difficulty performing separations that require alternative topologies.[32] Second, they are less chemically diverse than hybrid/organic microporous materials, so fewer strategies[33] are available to fine-tune them for specialist applications. Finally, their insolubility and high crystallinity can make them brittle[34] which complicates their use as membranes. This is less of an issue with organic materials, such as polymers. However, in applications where these limitations can be avoided, zeolites are extremely valuable. In particular, they have been applied as selective adsorbents and chromatographic stationary phases (see Section 1.5), applications which are particularly relevant to this thesis.

1.2   Hybrid Microporous Materials

Hybrid microporous materials contain both inorganic and organic components. Metal-organic frameworks (MOFs), which are hybrid microporous materials, contain repeat units of organic ligands coordinated to metal ions (or clusters) to create 1-, 2-, or 3-dimensional networks (Figure 1-2). The initial development of MOFs is
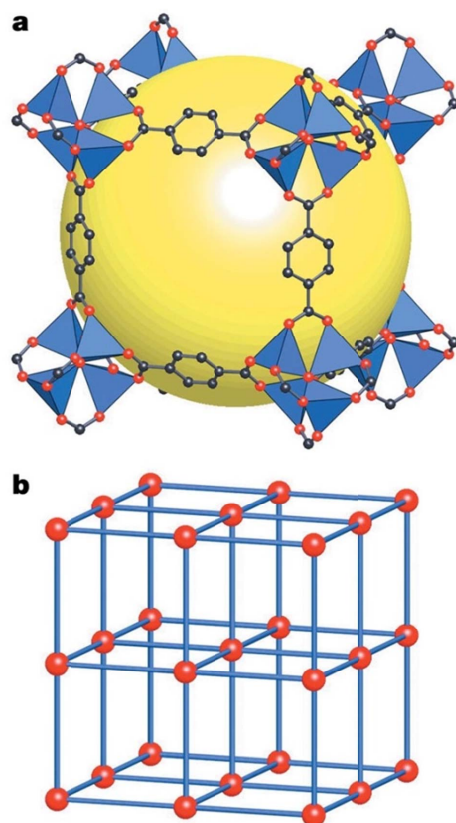
Figure 1-2 | MOF-5 structure and topology. a, ZnO_4 tetrahedra (blue, corners) joined by benzene dicarboxylate linkers (O, red and C, black) to give an extended 3D cubic framework with a 12 Å pore diameter. **b**, topology of MOF-5. Reprinted from reference source.[35]

attributed to Robson and Hoskins[36,37] while Yaghi and coworkers are attributed with initially demonstrating their permanent porosity in 1999.[38] Since then, MOFs have been investigated to such a great degree that the number being found is growing exponentially.[39] MOFs tend to be synthesised via one-pot self-assembly reactions between organic ligands and metal salts in solution.[40] Because a broad range of organic compounds are capable of coordinating to a variety of metals (and clusters), MOFs, like other hybrid microporous materials, tend to be highly tunable, especially when compared with purely inorganic materials.[41] This tuning of MOFs by "reticular synthesis", a phrase coined by Yaghi and coworkers,[35] has enabled MOFs to receive broad applicability in technologies such as hydrogen storage,[42] drug delivery,[43] separations,[40] and sensors.[44]

While hybrid materials, such as MOFs, inherit some of the benefits of their organic and inorganic components, they also inherit some of their disadvantages. First, most organic ligands are synthetic and tend to cost more than naturally occurring inorganic materials.[45] Secondly, MOFs tend to require more controlled and milder synthetic

conditions than inorganics.[40] Finally, unlike some organic microporous materials, hybrid materials are insoluble in organic solvents, which make them difficult to fine-tune for coating and membrane applications. Nevertheless, hybrid materials have been successfully applied as selective sorbents[40] and chromatographic stationary phases,[46] which makes them a significant source of inspiration for this thesis.

1.3   Organic Microporous Materials

Like hybrid microporous materials, organic microporous materials have been used in sensing,[47] gas storage,[48] and sorption[49] applications. However, unlike hybrid materials, some organics are solution processable. This solution processability is particularly interesting because it can be used in conjunction with molecular recognition[50,51] or recrystallisation[52] to tune the materials. Consequently, these kinds of unique properties make organic materials particularly effective in applications where inorganic and hybrid materials are less suitable, such as in separation membranes.[53-55]

Some organic microporous materials, such as covalent organic frameworks (COFs),[20] are well-ordered extended frameworks while others, such as organic cage compounds,[25] are discrete molecules. Because of this diversity, numerous organic microporous materials have been identified, too many to comprehensively cover here. Instead, this section focuses on porous organic cages because they feature throughout this thesis.

1.3.1   Porous Organic Cages

Organic cage compounds are discrete, macrocyclic, molecules containing an inner void. As summarised by Mastalerz and Zhang,[25] organic cages were reported as early as the 1960s.[56] However, many incremental developments occurred before their synthesis was sufficiently straightforward and their permanent porosity was measured. One of the earliest such measurements was reported by the Cooper group in 2009.[57] Since then, a variety of porous organic cages have been synthesised with behaviours including on-off porosity switching,[52] ternary co-crystal formation,[51] exceptional surface areas,[58] and molecular shape-sorting.[49]

Organic cages may be formed through reversible or irreversible bond formation. Those formed by the latter tend to be more robust than the former; however, irreversible syntheses tend to depend on the statistical chance of cage formation, which is

usually low.[25] Consequently, there are few high-yielding irreversible synthetic approaches. The highest yielding are summarised by Mastalerz and Zhang.[25] High yield and purity is especially important when synthesising cage compounds for analytical and preparative experiments, such as those featured later in this thesis. Consequently, this introduction only focuses on cage synthesis *via* reversible bond formation because these approaches allow a reaction mixture to equilibrate to the thermodynamically preferred cage compound and, hence, tend to be high yielding with simple syntheses.

General reviews of dynamic covalent chemistry—the study of supramolecular compound formation *via* reversible bond formation[59]—report that shape-persistent organic cage compounds can be produced from disulfide formation or phenol/aldehyde condensation; however, no significant progress has been made in using these moieties yet.[60,61] By contrast, several organic cage compounds have been produced *via* boronic ester formation and imine condensation.

The formation of organic cage compounds by boronic ester formation is particularly noteworthy because it is already used to produce COF compounds.[20,62] In 2009, Severin and coworkers reported the synthesis of a [6+3+2] cage compound through the co-condensation of 4-formylphenylboronic acid, pentaerythritol, and trisamine.[63] In 2014, Mastalerz and coworkers produced a larger permanently mesoporous organic cage by the reversible formation of 24 boronic ester units.[58] With a window width of 4 nm, this is one of the largest organic cages reported. However, while this demonstrates that boronic ester formation is capable of producing impressive cage structures, these compounds were only recently reported. Consequently, their application as selective sorbents or chromatographic stationary phases has not yet been studied— or is discussed further in this thesis—but could be interesting.

A more frequently used approach to the formation of organic cages is *via* the reversible formation of imine bonds.[25] The earliest report of this was by Cram and Quan in 1991, who synthesised a molecular container (hemicarcerand) from two tetraformylcavitand molecules and four 1,3-diaminobenzene molecules in a [2+4] condensation reaction.[64] Subsequently, a variety of cage compounds have been produced using this approach. In particular, the synthesis of cages *via* a one-pot imine condensation between an aromatic trialdehyde and an aliphatic diamine is relevant to Chapter 2 of this thesis, where this approach is used throughout.
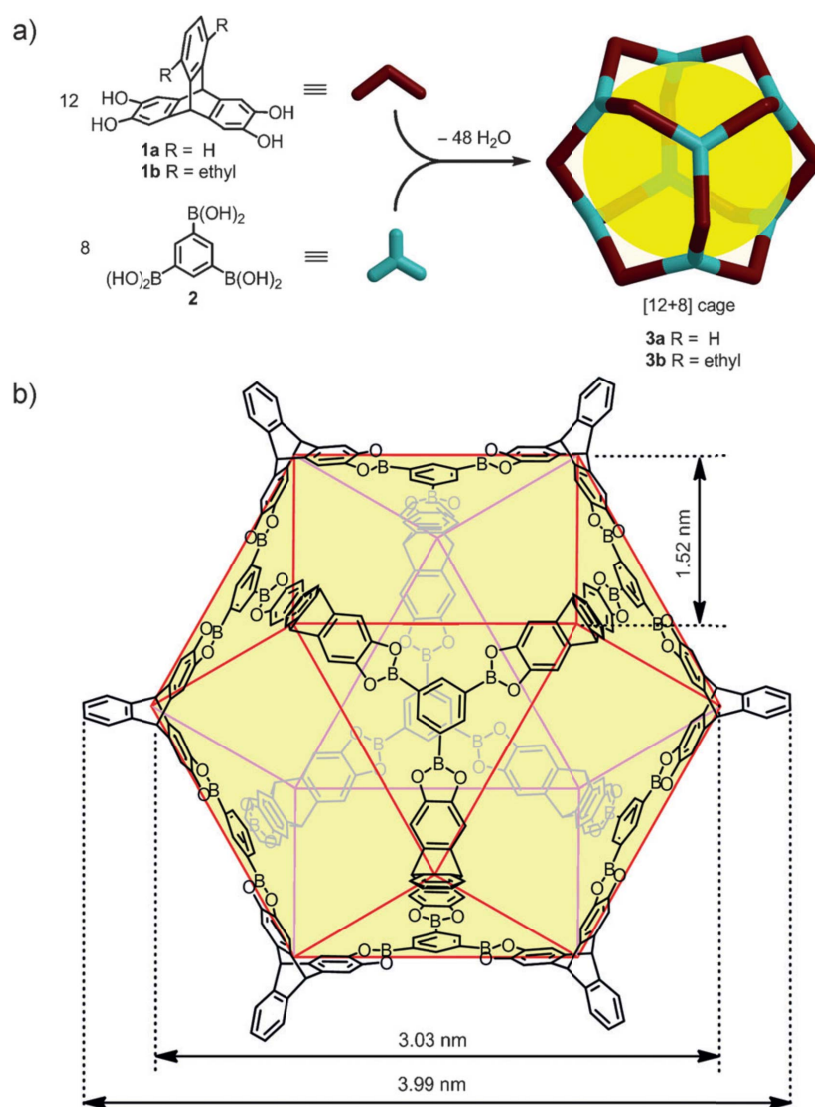
Figure 1-3 | Organic cage compound produced by boronic ester formation. a) one-step 48-fold condensation of twelve molecules of triptycene tetraol (**1a** / **1b**) with eight molecules of the triboronic acid (**2**) to form cuboctahedral [12+8] cages (**3a** / **3b**). Edges of the cuboctahedral geometry are highlighted in red. Figure reprinted from literature source.[58]

The Cooper group reported using imine condensations to produce three of the earliest reported porous organic cage compounds by reacting 1,3,5-triformylbenzene with ethylene diamine; 1,2-propylenediamine; or (*R,R*)-1,2-diaminocyclohexane to form **CC1**, **CC2**, or **CC3** respectively (Scheme 1-1 for **CC3**).[57] These early procedures had yields ranging from 18 to 37 % which have since been improved to over 90 % by tuning the reaction conditions.[50,65] Similar tuning approaches are presented in Chapter 2, with an aim to maximise the probability of isolating a novel organic cage compound; further, **CC3** features throughout this thesis, partly due to its pore structure and processability.
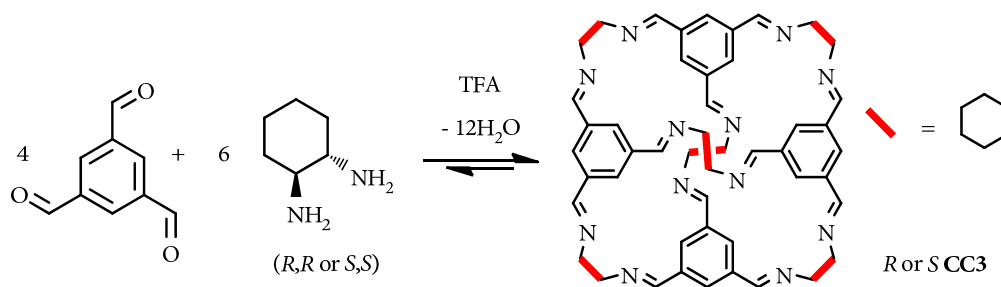
Scheme 1-1 | Synthesis of **CC3** by a one-pot [4+6] cycloimination reaction of *four* trialdehydes and *six* diamine molecules. The reaction is catalysed by trifluoroacetic acid (TFA). Scheme reprinted from literature source.[66]

Porosity in organic molecules is especially interesting because it is rarely observed: most molecules pack efficiently in the solid state to form structures with minimal void volume.[57] With respect to imine cages, porosity is a consequence of their internal molecular voids and their inefficient packing. Due to the interplay of these two contributions, slight differences in a cage's chemical structure can affect its overall pore structure (Figure 1-4). For example, due to the window-to window packing of **CC3**, chirality in its outer cyclohexane groups directly contribute to its overall diamondoid pore structure (Figure 1-4). Consequently, homochiral **CC3** packs to form a chiral solid,[57] which might enable it to chirally select guests. Investigations into using **CC3** to perform chiral separations are presented in Chapters 3 and 4.

CC3 also features in Chapters 3 and 4 for two additional reasons. First, gram quantities of high-purity homochiral **CC3** may be straightforwardly produced in high yields,[50] which reduces reproducibility issues in analytical experiments. Second, while homochiral **CC3** is soluble in chlorinated solvents, achiral *rac-***CC3** is poorly soluble in these solvents; consequently, these differences of solubility may be leveraged to produce monodisperse *rac-***CC3** nanosuspensions (Figure 1-5).[50]

As reported by Mastalerz and coworkers, imine cages can also be produced from the imine condensation of aromatic triamines with aromatic dialdehydes (e.g. Figure 1-6).[67–69] The use of aromatic amines enables long-range rigidity in the amines to be achieved, which could enable larger imine compounds to be synthesised. Indeed, the volume of this compound's internal cavity exceeds **CC1-CC3**, likely due to the additional rigidity offered by the adamantoid triamine used. Producing further imine cages from aromatic amines could yield interesting cage structures; accordingly, attempts to do so are presented in Chapter 2.
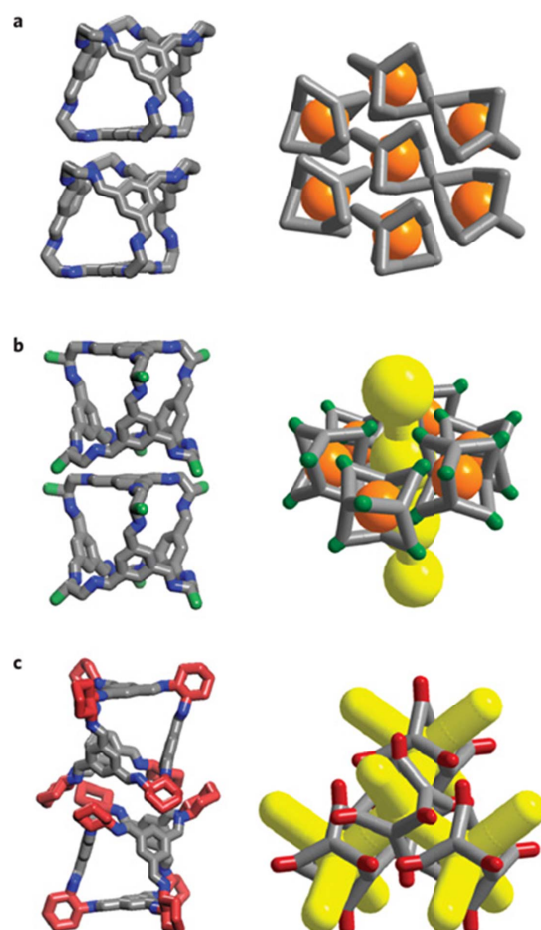
Figure 1-4 | Schematic of cage-cage packing in the crystal structures of imine cages CC1 (a), CC2 (b), and CC3-*R* (c). In **CC1**, adjacent cages pack in a window-to-arene fashion, which results in isolated voids (orange spheres). **CC2** forms similar window-to-arene stacks, which also forms isolated voids, but the outer methyl groups (green) frustrate efficient packing, which generates 1D pore channels (yellow). **CC3** packs window-to-window, which generates a chiral interconnected diamandoid-pore network (yellow). Figure reprinted from literature source.[57]
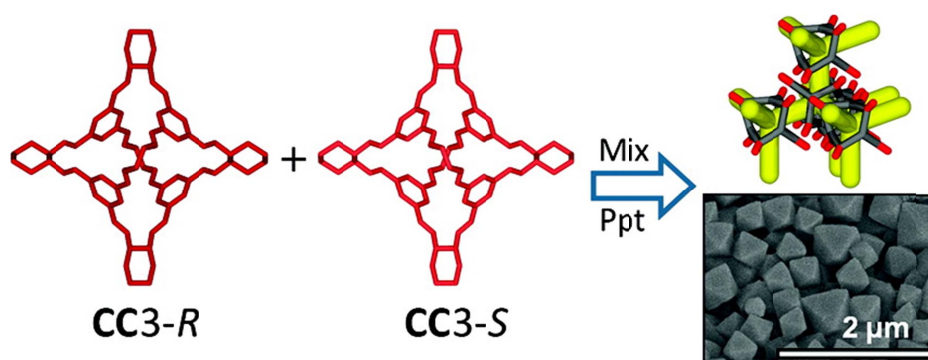

Figure 1-5 | Exploiting chiral molecular recognition in CC3. Homochiral **CC3**-*R* and **CC3**-*S* are soluble in chlorinated solvents but, because *rac*-**CC3** is insoluble in the same solvents, rapidly combining solutions of **CC3**-*R* with **CC3**-*S* forms *rac*-**CC3** nanosuspensions. Figure reprinted from literature source.[50]
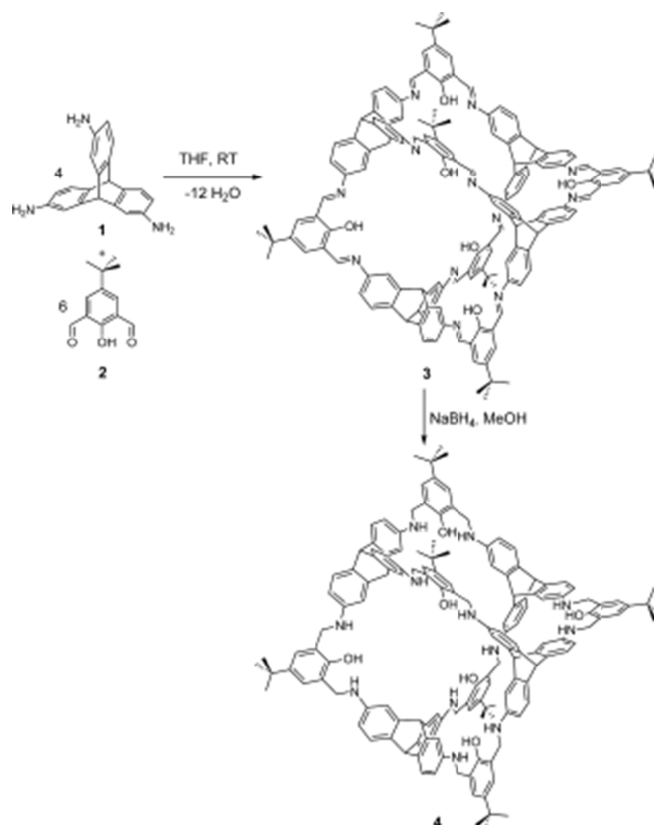
Figure 1-6 | Synthesis of organic cage compounds from the reaction of aromatic triamines with aromatic dialdehydes. Figure reprinted from literature source.[68]

Imine cages have been altered by strategies such as derivatization or recrystallisation to produce denrimer cores[70] or switchable sorbents,[52] demonstrating that they can have a wide variety of valuable properties. Rationalising these properties is desirable; however, organic cages tend to have complex structure-property relationships. For example, the Cooper group demonstrated that slight differences in precursor chain length can lead to odd-even effects in cage syntheses.[71] In similar studies, Mastalerz and coworkers demonstrated that altering the position of functional groups on a precursor can dramatically change measured surface areas.[67] These complex relationships are difficult to predict with conventional approaches, which necessitates developing new approaches for their discovery.

1.4   Materials Discovery

While complex structure-property relationships can make organic cages challenging to rationally design and synthesise,[67,71] these challenges are not unique to cages. Approaches such as *in-silico* screening,[72] High-Throughput (HT) experimental techniques,[73,74] or combinations thereof,[75] have been used to tackle similar issues in MOF,[72,74,76] catalyst,[77,78] and drug[79] discovery.

In computational chemistry, a particularly exciting development is the *in-silico* generation of novel compounds. Two popular approaches tend to be used: substituting parts of known structures, as demonstrated by Snurr and coworkers to generate hypothetical MOFs,[80] or generating a structures from their constituent atoms, as demonstrated by the Cooper group to generate hypothetical organic cages.[71] In the latter approach, models for each precursor were built in [2+3], [4+6], and [8+12] ratios with geometries similar to earlier cages discovered by the Cooper group. These models were then energy minimised to find the lowest energy conformation. This approach is reported to perform well at reproducing previously reported imine cage structures and energetics; accordingly, it was incorporated into the cage discovery screens presented in Chapter 2. However, *in-silico* approaches tend to generate hypothetical compounds faster than conventional experimental approaches can investigate them, which necessitates the development of complementary HT approaches.

Streamlining experimental procedures with HT techniques has received sustained interest across a variety of fields.[81] As summarised by Kohn and coworkers,[75] the earliest HT approaches tended to focus on producing complex mixtures of compounds in a single reaction vessel and particularly relied on sophisticated analysis procedures. An early example of this approach was demonstrated by Menger and coworkers in 1995,[82] who used it to discover phosphatase catalysts. The approach worked—it generated catalytically active mixtures—but it was difficult to identify the actual component responsible for the catalysis.

In 1998, Schultz and coworkers circumvented these issues when streamlining the discovery of photoluminescent mixtures by using a "spatially resolved" approach.[83] In their approach, different mixtures were printed at specific locations on a surface and an imaging system was used to identify mixtures of interest. These spatially resolved approaches have become increasingly popular over the last few decades.[84] At the time of writing, the use of spatially arranged multi-well reactor arrays is a popular approach for performing syntheses in parallel. Spatial approaches, combined with robotic platforms, can perform screening reactions at a rate fast enough to investigate targets generated by *in-silico* techniques.[85,86] The combination of HT approaches with *in-silico* techniques is presented throughout Chapter 2. However, accelerated approaches may be bottlenecked by subsequent analysis steps.

Identifying an accompanying analysis approach for HT syntheses can be challenging. Of particular relevance to this project is the measurement of permanent porosity in microporous samples. However, the measurement of gas adsorption isotherms using volumetric adsorption analyzers tends to be slow, only capable of analysing a few samples in parallel per day. Encouragingly, novel approaches to speed this process up are in development. Kaskel and coworkers reported a new tool, infrasorb-12, which is capable of analysing twelve samples in parallel in under 5 minutes.[74] These developments are relatively recent, so conventional HT analysis approaches are utilised in this thesis; however, developments like these could aid future HT methodologies.

Overall, there has been a range of developments made to circumvent the complexity of microporous materials discovery. Chapter 2 focuses on integrating *in-silico*, spatially resolved, and robotically assisted techniques with an aim to greatly accelerate microporous materials discovery. The resulting HT pipeline could be a valuable asset for finding novel materials to use in a range of applications.

1.5   Applications of Microporous Materials

Microporous materials are well-suited to applications which exploit their molecular-scale pores and high surface areas. They have received attention in hydrogen storage,[2] carbon dioxide capture,[87] sensing,[88] and catalysis[89] applications. Of particular relevance to this thesis is their use in separations, which play a significant role in daily life and industry. Specifically, discussions here are limited to two popular separation technologies: selective sorbents, for bulk separations, and chromatographic stationary phases, for analytical-scale separations.

1.5.1   Selective Sorbents

While distillation accounts for 90-95 % of separations in the chemical industry,[90] it is unfeasible in some scenarios. A popular alternative is 'adsorptive separation',[40] which is used in familiar technologies such as water purifiers[27] and gas filters.[91] In adsorptive separation, a mixture is separated by selectively adsorbing its components into a microporous material (Figure 1-7). Relevant to this thesis is the use of organic cages to perform adsorptive separations. Cages have already been used to separate hydrocarbon[49,92] or carbohydrate[93] mixtures; however, fewer investigations are available than for materials such as MOFs or zeolites. Consequently, the numerous reports of separations by these materials also provide a useful insight into the separation behaviour of microporous materials.
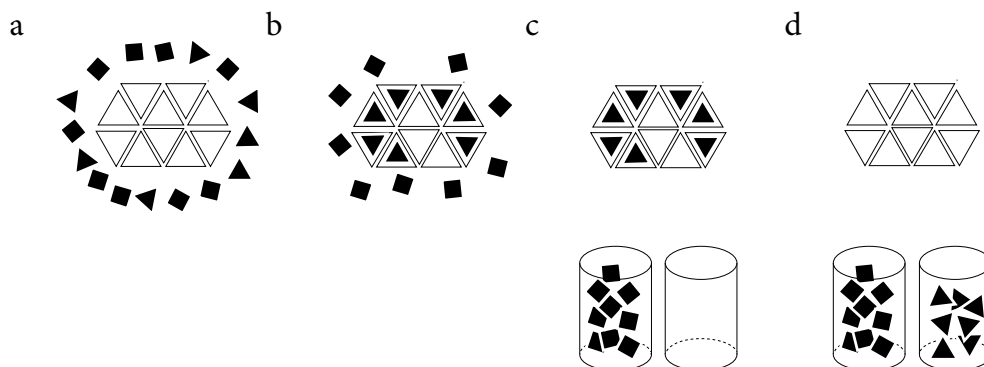
Figure 1-7 | Schematic of the adsorptive separation process. A mixture is exposed to a microporous material (a), which selectively adsorbs certain components of the mixture (b). Components which remain in the solution or gas phase can then be collected (c) and adsorbed components are subsequently desorbed for collection (d).

C8 alkylaromatic isomeric compounds containing *o*-xylene (oX), *m*-xylene (mX), *p*-xylene (pX), and ethylbenzene (EB) are important industrial feedstock chemicals which tend to be produced as a mixture of all four components.[40] These can be challenging to separate by distillation because of their similar boiling points, particularly in the case of separating pX from mX and EB, which have boiling points of 138, 139, and 136 °C respectively. Consequently, fractional crystallisation methods are used to separate these compounds in industry[94] but adsorptive separation methods have also received much attention because they could simplify the process. Accordingly, the use of a range of microporous materials,[95] including MOFs,[96] zeolites,[95] and organic cages[49] to separate C8 alkylaromatics has been reported.

Initial experimental investigations in using MOFs for C8 alkylaromatic separations were reported by Denayer and coworkers in 2008.[97] Breakthrough measurements of binary mixtures with MIL-47 indicated that two of the four isomers could be separated with pX/oX isolated as a mixture. It was also found that adsorption selectivity increased with an increasing degree of pore filling, indicating that selectivity is pressure dependent. Thus the efficient separation of these components is thought to be due their different packing modes within the pores of MIL-47. A follow-up study by the same group investigated MIL-53, a flexible MOF, and found no adsorption preference between oX and EB below the "pore-opening" pressure.[98] Above it, however, selectivity increased with increasing pressure (Figure 1-8). This is believed to be a result of different packing modes of the adsorbed molecules in its pores.

While some MOFs, such as MIL-47 and MIL-53, appear to separate alkylaromatics due to differences in packing, other MOFs have been shown to separate them based on differences in equilibrium position and diffusion speed. For example, Yan and coworkers investigated the adsorption and separation of C8 alkylaromatics with MOF-5 and $Zn_3(bdc)_3$ and found the former to be equilibrium dominated while the latter to be diffusion-dominated.[99] The pores of MOF-5 have an approximate cross section of 12 Å, which is larger than the C8 alkylaromatic isomers' kinetic diameters (5.85-6.85 Å), so the isomers are differentiated by their differing affinities with MOF-5. However, the exact source of this differentiation is not explored in the study. Instead, the lower polarity of MOF-5 when compared with $Zn_3(bdc)_3$ is hypothesised to enhance its separation capabilities. By contrast, the triangular pores of $Zn_3(bdc)_3$ have a short edge length of ~7 Å which allow it to separate isomers through diffusion effects. pX, which has the smallest kinetic diameter (5.85 Å), diffused quickest through $Zn_3(bdc)_3$, which resulted more being retained on a $Zn_3(bdc)_3$ column in breakthrough measurements.

In related studies, the Cooper group demonstrated that **CC3**, a porous organic cage, is capable of separating C8 and C9 alkylaromatics.[49] As with MIL-47,[97] the separation effect is hypothesised to be due to the different packing modes of the adsorbed
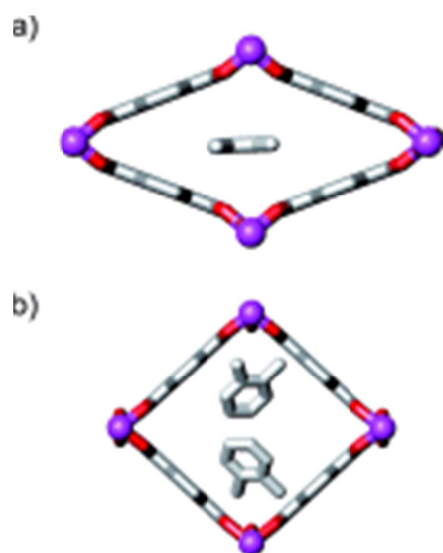

Figure 1-8 Structures of a) MIL-53*iX* and b) MIL-53*ht*, as reported by Denayer and coworkers. MIL -53*iX* and -53*ht* represent the structure of MIL-53 when exposed to low and high partial pressures of xylene vapour respectively. The pore diameter of MIL-53*iX* is significantly reduced when compared with MIL-53*ht*. Flexibility in the structure of MIL-53 enables it to transform between these two structures, which enables it to "breathe" additional xylene molecules at higher loading pressures. Figure reprinted from literature source.[98]

molecules within **CC3**. X-ray diffraction measurements indicated that *meta*-substituted components reside within the cage's cavity while *para*-substituted components reside in inter-cage cavities. As there are twice as many inter-cage cavities, the overall structure of **CC3** is able to accommodate more *para*-substituted compounds. Also, as with MIL-53,[98] flexibility within the structure of **CC3** appears to play a role. *para*-Substituted compounds are larger than the narrowest point in the channels (5.32 Å); however, flexibility within the structure allows the cage to accommodate larger components. The role of flexibility is particularly relevant to investigations of shape selectivity by **CC3**, which are presented in Chapters 3 and 4, as its flexibility might enable it to perform a variety of shape-selective separations.

The separation of racemic mixtures is also an important industrial and analytical process. Their separation has become increasingly important in the pharmaceutical field due to the appreciation that two enantiomers of a drug often have different activities in the human body. Indeed, in 2004 five of the top ten selling drugs—61 % of the global sales of pharmaceuticals—were single enantiomer products.[100] However, because enantiomers are chemically identical, the separation of racemates can be particularly challenging.

Usually, if asymmetric syntheses are unavailable, two main strategies have evolved for the separation of chiral compounds: an indirect method, which involves the formation of diastereomers by reacting compounds with a chiral derivatising agent (CDA); and the direct method, based on the reversible formation of diastereomers with an achiral compound.[101] Because a broad variety of CDAs are available, the former is commonly used in industry. However, indirect approaches introduce additional steps into the synthetic procedure, which can be costly. Further, CDAs are not available for all molecules.

In direct approaches, chiral hosts preferentially bind to an enantiomer of a racemate, a process referred to as enantioselective molecular recognition.[102] The forces involved are non-covalent intermolecular interactions such as dipole-dipole, induced dipole, hydrogen bonding, van der Waals, or π-stacking interactions. The earliest chiral hosts were natural materials such as wool, paper, or cellulose;[102] however, some racemates can be particularly difficult to separate with these materials, which necessitates stronger differentiators. As guest to pore-wall interactions are strong in microporous materials, they are capable of strongly differentiating guests. Consequently, mi-

croporous materials such as MOFs[103] and zeolites[104,105] have received particular attention as specialist enantioselective sorbents.

One of the earliest examples of enantioselective molecular recognition in **a** MOF was reported by Kim and coworkers in 2000.[106] In their approach, D-POST-1, a chiral MOF, was synthesised by reacting an enantiopure building block (Figure **1**-9, **1**) with Zn^{2+} ions and found to enantioselectively exchange $[Ru(2,2'-bipy)_3]^{2+}$ complexes into its structure with an 66 % enantiomeric excess (*ee*). Further, D-POST-1 was shown to be capable of performing enantioselective esterification, although the resulting product mixture had a modest *ee* of 8 %.

Subsequently, in 2001, two reports of enantioselectivity towards organic racemates were released in quick succession: Lin and coworkers reported the synthesis of a homochiral MOF composed of porous lamellar lanthanide bisphosphonates[107] which enriched *trans*-1,2-diaminocyclohexane to an *ee* of 13.6 %; Che and coworkers reported the separation of 2-butanol in a zeolite/MOF hybrid to an *ee* of 98 %.[108] Since these initial investigations, further homochiral MOFs have been utilised as enantioselective sorbents, which has been summarised by Cui and coworkers.[100]
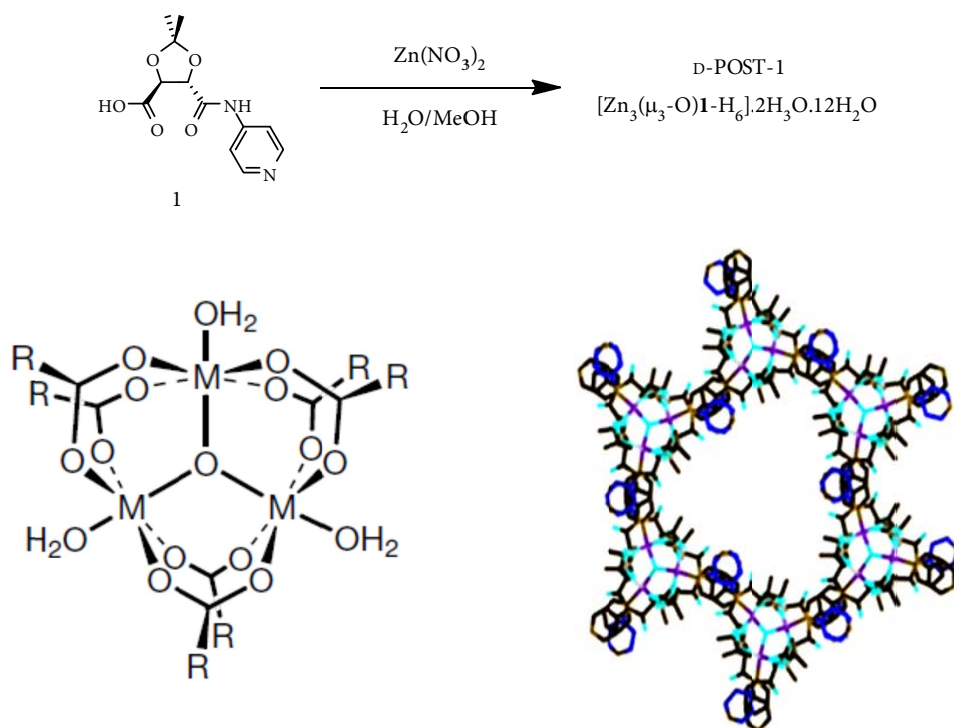

Figure 1-9 | Synthesis (top), trinuclear secondary building unit (bottom-left), and structure (bottom-right) of D-POST-1. Building units form a chiral hexagonal channel in D-POST-1. Figure reprinted and edited from literature source.[106]

In comparison to chiral MOFs, the synthesis of chiral aluminosilicate zeolites has historically met with limited success.[109] The chiral helical pore structure of zeolite beta, one of the most important zeolite catalysts in industry,[104] is a rare example of chirality in these materials; however, this polymorph is hypothetical and tends to intergrow with an achiral phase, preventing the isolation of single crystals.[104]

Recently, Zou and coworkers reported the synthesis of SU-15 and SU-32, zeolites composed of chiral layers,[104] but no enantioselective adsorption measurements have yet been carried out on these materials. Likewise, the same group also recently reported the synthesis of ITQ-37, a mesoporous chiral zeolite,[105] but, as with SU-15 and SU-32, no enantioselectivity measurements have yet been reported for this material.

Overall, microporous materials appear to perform well as selective adsorbents for a wide variety of mixtures. However, there are relatively few studies into the use of organic cages as selective adsorbents; specifically, their use as enantioselective sorbents has not been studied at all. Consequently, this topic is the focal point of Chapter 3, wherein the first instance of enantioselective molecular recognition by **CC3**-*R*, a homochiral organic cage, is presented.

1.5.2   As Chromatographic Stationary Phases

In chromatography, the separation of compounds depends on their differing affinities towards a stationary phase (simplified schematic in Section 6.1). In that respect, stationary phases share similarities with selective adsorbents. However, because components continually exchange on and off the stationary phase, particular emphasis is directed towards the reversibility and speed of adsorption.

Chromatography is a broad field which spans a variety of techniques. While techniques such as high-performance liquid chromatography (HPLC) are extremely popular, this thesis focuses on producing stationary phases for gas chromatography (GC). One reason is that GC is a highly efficient separation technique for separating volatile compounds which are more likely to have molecular sizes small enough to enter micropores. Another is that GC tends to use either hydrogen or helium as mobile phases, which are unlikely to solvate or recrystallise the stationary phase. Likely because of these considerations, studies of microporous stationary phases for other chromatographic techniques are reported to lag behind studies of their use in GC,[46] although some are available.[110,111]

Of particular relevance to this thesis are chiral stationary phases (CSPs) for GC, which separate enantiomers by favourable diastereomer-forming mechanisms such as hydrogen bonding, metal coordination, or inclusion.[112] These types of separation can be particularly valuable, yet challenging, to perform. Accordingly, the development of CSPs, such as cyclodextrins (CDs), has received much attention.[113,114]

CDs are inexpensive chiral cyclic sugar molecules produced from starch (Figure 1-10).[113] They contain three inequivalent –OH groups that may be selectively derivatised.[115] Methylated CDs are commonly applied as CSPs because they may be dissolved into liquid polymers and coated as liquid films in capillary columns.[116] Because of their relatively low cost and high efficiency, CD derivatives are the most common commercially-available CSPs.[117]

Because CDs contain an inner void, there is scope for them to separate compounds by their molecular size and shape. As discussed for selective sorbents, this can be a particularly useful method of differentiating chemically similar compounds, such as alkylaromatics. Indeed, early on in the adaption of CDs, Smolková-Keulemansová and coworkers identified CDs' ability to shape-separate xylene, diethylbenzene, and trimethylbenzene isomers by shape-selective inclusion compound formation (Figure 1-11).[118] The same researchers further investigated this effect for a wide variety of alkylaromatics and identified that, when compared with *para* and *meta* isomers, *ortho* isomers are sterically restricted from entering the CD's inner-ring, which results in weaker surface interactions and, consequently, lower retention times.[119]

While CDs are a popular stationary phase, their bowl-shaped inner-cavities might limit the scope of shapes they may differentiate. Consequently, researchers have investigated materials with alternative pore shapes, such as MOFs, as stationary phases for molecular shape[120] or chiral[121] separations. One of the earliest investigations into using MOFs as CSPs was reported by Fedin and coworkers in 2007.[122] In their approach, a chiral MOF was packed into a column to separate sulfoxide compounds by HPLC; however, the reported chromatograms contain quite broad peaks (Figure 1-12).
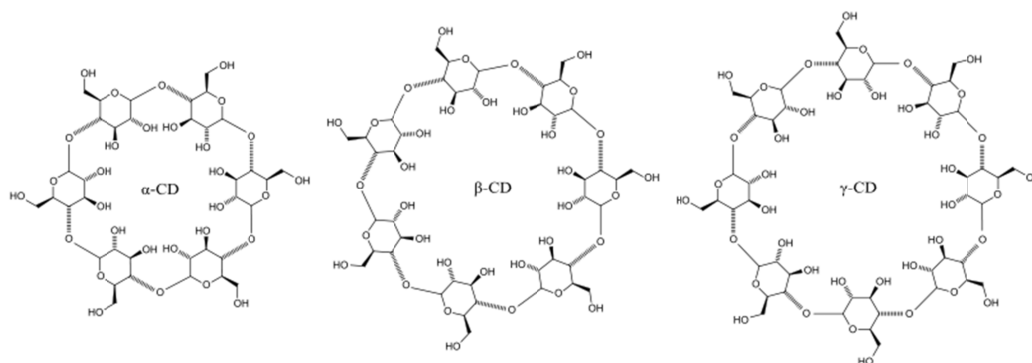
Figure 1-10 | Structure of α- (left), β- (middle), and γ-CD (right). As a result of their molecular complexation phenomena, CDs are widely used in many industrial products, technologies, and analytical methods.[113] The inner void of CDs are hydrophobic and bowl-shaped, with a smaller primary face and larger secondary face.
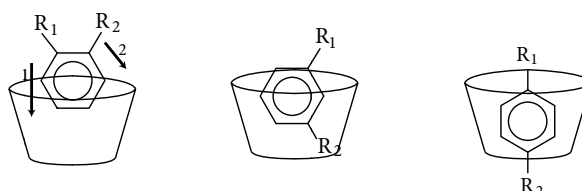

Figure 1-11 | Inclusion chemistry of CDs, as reported by Smolková-Keulemansová and coworkers. Figure remastered from literature original.[118]
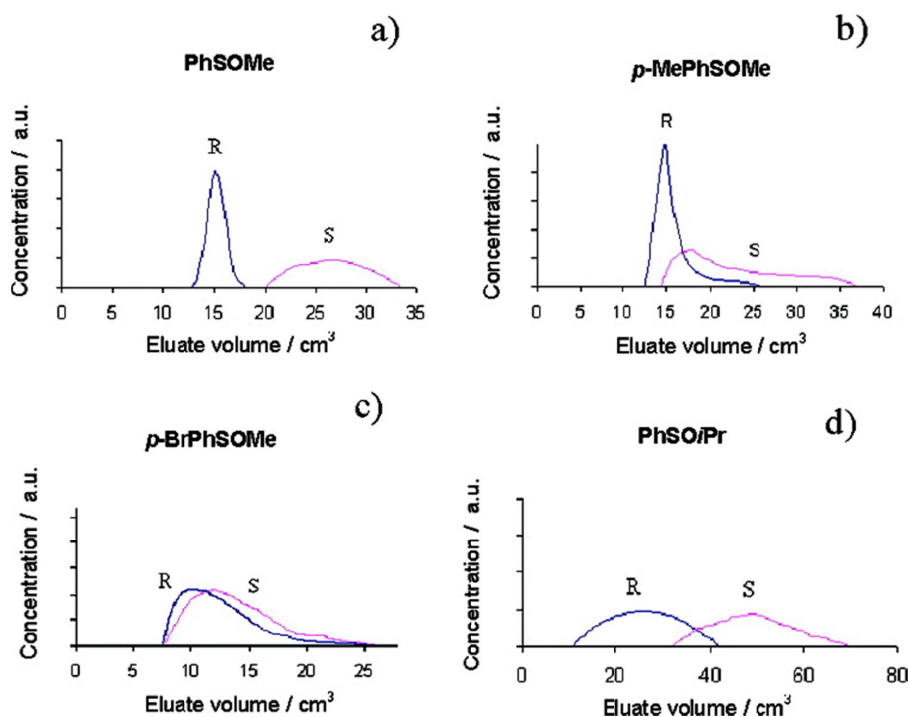

Figure 1-12 | HPLC chromatograms of alkyl aryl sulfoxides separated by a MOF, as reported by Fedin and coworkers. Peaks are noted to be quite broad; however, these chromatograms represent some of the earliest investigations into using MOFs as a CSP. Later developments (e.g. Figure 1-13) improved on these findings. Figure reprinted form literature source.[122]

Yuan and coworkers were the first to report the use of a chiral MOF, [{Cu(sala)}$_n$], as a CSP in a GC capillary column, which produced sharper peaks in the resulting chromatograms (Figure 1-13).[123] However, because MOFs are insoluble, the column was coated with the dynamic method where plugs of finely ground, suspended, MOF particles are pushed through the column. This approach is used in other reported coatings of MOFs;[124–126] however, it can is difficult to get an even coating with this approach,[117] which is discussed in more detail in Chapter 4.

Racemates separated by chiral MOFs tend to contain a hydrogen-bonding moiety which can act as a strong differentiator between enantiomers. By contrast, the separation of alkylaromatics, which contain no strong dipoles, can be difficult since comparatively weaker π-π and van der Waals surface interactions are the only handle for their differentiation.[102] Further, the separation of alkane isomers, where no π-π interactions are available, can be especially challenging. However, as explained in Section 1.5.1, the separation of alkylaromatics and alkane isomers are significant industrial processes. Accordingly, the separation of these compounds on MOF-coated GC capillary columns has received some attention.

Yan and coworkers were the earliest to report using a MOF, MIL-101, for the high resolution-separation of xylene isomers by GC.[124] In their approach, capillaries were coated with MIL-101 *via* the dynamic coating method and found to achieve baseline separation of *p*-xylene, *o*-xylene, *m*-xylene, and ethylbenzene. They noted that the separation efficiency of their coated capillary column exceeded efficiencies of packed columns. As the pore diameters of MIL-101 (1.4 and 1.6 nm) are much larger than the analytes (0.58-0.68 nm), the source of separation behaviour is not due to differences in diffusion speed. The explanation provided is that MIL-101's polarity and coordinatively unsaturated sites are responsible for the separation behaviour, which indicates that the separation of xylene isomers does not necessarily require a shape-restricting pore structure in the host.
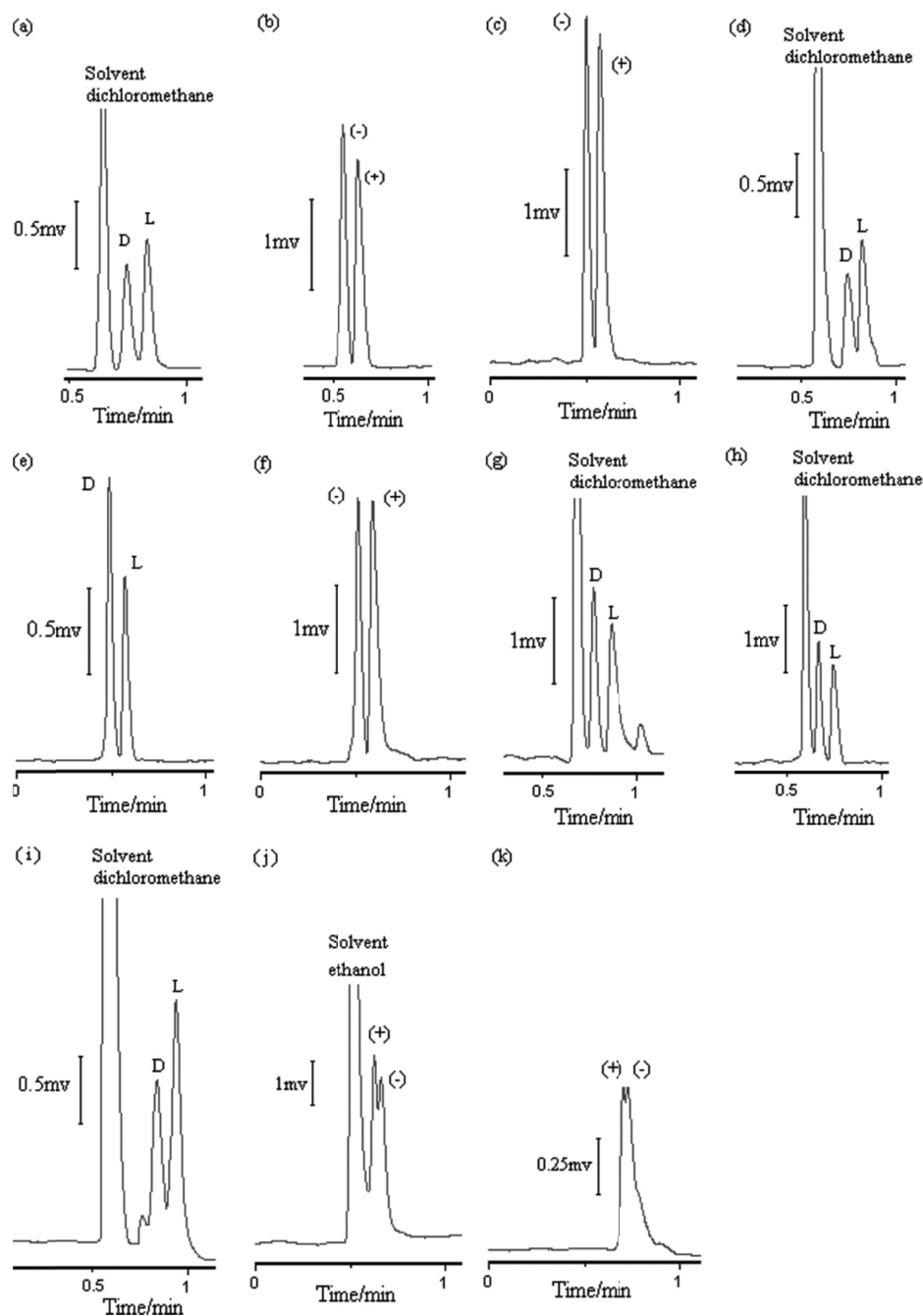
Figure 1-13 | GC chromatograms of chiral separations on a [{Cu(sala)}ₙ] coated open tubular capillary column, as reported by Yuan and coworkers. The separation of eleven mixtures is presented: isoleucine derivative (a); citronellal (b); 1-phenyl-1,2-ethanediol (c); leucine derivative (d); phenyl-succinic acid (e); 1-phenyl-ethanol (f); valine derivative (g); alanine derivative (h); proline derivative (i); caphor (j); and 2-methyl-1-butanol (k). Compared to earlier iterations of MOFs as CSPs, separation quality was much improved with further development and the use of GC to perform separations, which could, in part, be due to the inherently higher separation efficiency of GC when compared to LC techniques.[117] Figure reprinted from literature source.[123]

Dai and coworkers reported one of the first GC separations of branched from linear alkanes with MOF-508.[127] The MOF is doubly interpenetrated, which was reported to be a method of tuning the pores (Figure 1-14). In contrast to MIL-101, separations are reported to occur because of MOF-508's pore structure, which has pores slightly larger than a methane molecule. Consequently, MOF-508 was reported to be capable of separating alkane isomers, including isomers of hexane, which is particularly relevant to Chapter 4. However, MOF-508 was only capable of separating three of the five isomers of hexane, which necessitates further improvement (Figure 1-14).

Overall, microporous materials appear to be well-suited as GC stationary phases for performing separations other materials cannot. This shall be further investigated in Chapter 4, where organic cages are applied as a GC stationary phase, the first reported example of this.
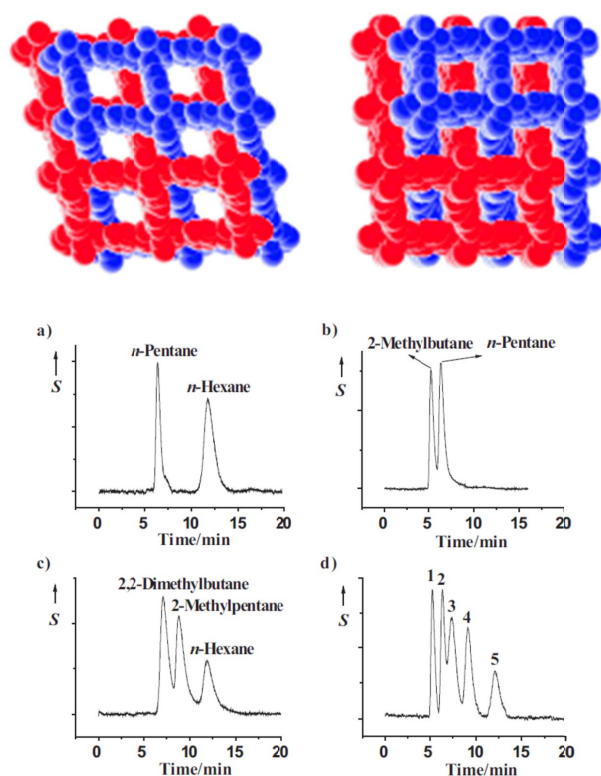

Figure 1-14 | Structure of doubly interpenetrated MOF-508 (top) and chromatograms of alkane mixtures separated on MOF-508 (bottom). d) Separation of an alkane mixture containing 2-methylbutane (**1**); *n*-pentane (**2**); 2,2-dimethylbutane (**3**); 2-methylpentane (**4**); and *n*-hexane (**5**). Figure reprinted (and edited) from literature source.[127]

1.6   Project Overview

This project aims to investigate the discovery, analysis, and practical application of organic cage compounds. Specifically, a pipeline for discovering further organic cage compounds is presented (Chapter 2), the host-guest behaviour of **CC3** is investigated (Chapter 3), and **CC3** is applied as a GC stationary phase (Chapter 4).

Chapter 2, *Discovering Novel Organic Cages*, presents a pipeline for discovering novel organic cage compounds. The acceleration of synthetic techniques is discussed and several screening experiments are performed with the intention of discovering novel materials. Additionally, computational techniques are augmented into the workflows to help select synthetic strategies. A novel organic cage compound was discovered in this manner.

Chapter 3, *Organic Cages as Selective Sorbents*, presents investigations into **CC3**'s behaviour as a host. Understanding host-guest behaviour of a material is a precursor to its application in technologies such as water purifiers, chemical sensors, and chromatographic columns. A series of quantitative measurements, models, and characterization techniques are used to build a comprehensive model of the behaviour of this system.

Chapter 4, *Chromatographic Separations with Organic Cages*, presents **CC3**-coated GC columns produced in a manner that could be commercially adapted. These columns are developed to improve separation efficiency and the separation of a variety of mixtures. Additionally, as in Chapter 3, the source of **CC3**'s separation behaviour is investigated with the aid of computational models.

2 Discovering Novel Organic Cages
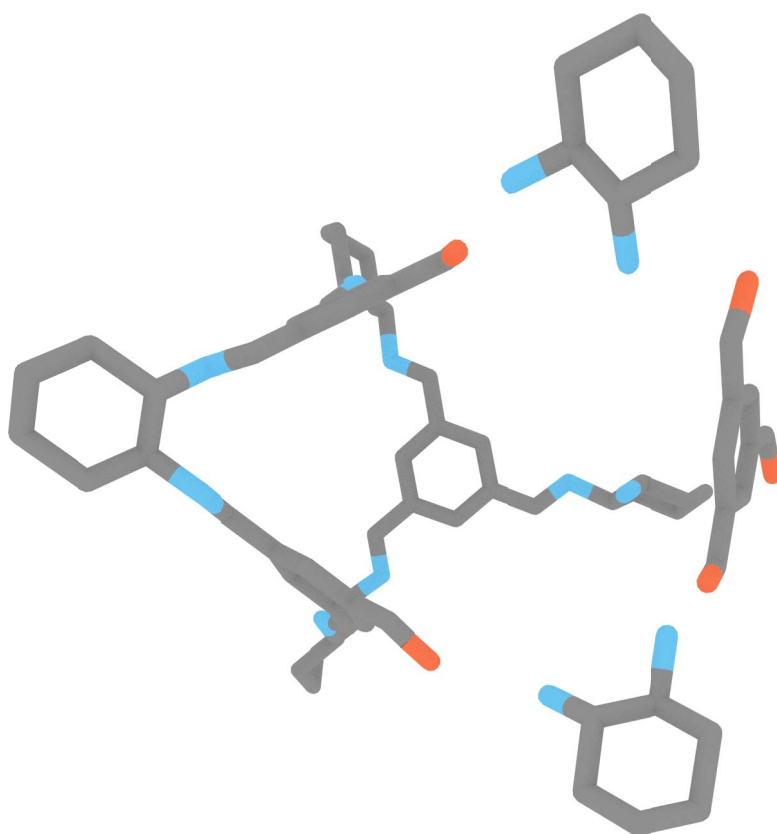
A material's behaviour typically emerges from a combination of factors. In some cases, these can be rationalised. Indeed, in Chapters 3 and 4, it is presented that the separation behaviour of a previously studied cage, **CC3**, may rationalised using computational models. Predicting the behaviour of an unknown, hypothetical, material is much more difficult and, in many cases, may only be achieved with the assistance of experimentation and analysis.

This chapter presents two changes to conventional synthetic workflows. First, *in-silico* approaches were used to produce synthetic targets. Second, automated robotic platforms were used to accelerate practical synthetic procedures. The resulting workflow was used to discover a novel organic cage compound.

2.1   Challenges of Organic Cage Discovery

Multiple routes for synthesising organic cages are available (Section 1.3.1). This Chapter focuses on the one-pot imine condensation of trialdehydes with diamines. Imine cages produced in this manner are well-studied, especially by the Cooper group, which has investigated their *in-silico* assembly,[71] derivatization,[70] crystallography,[52] and morphology.[50] However, establishing which precursors and reaction conditions will produce a shape-persistent imine cage can be especially challenging.

First, as discussed in Section 1.4, imine cages have a series of non-intuitive and complex structure-property relationships which makes predicting their properties challenging. The stoichiometry of imine condensations of trialdehydes with diamines can, in principle, produce n[2+3] (e.g. [2+3], [4+6], [8+12], …) organic cage compounds.[57,71] The Cooper group reported that *in-silico* design techniques can be used to help predict the thermodynamically preferred cage product from a complex mixture.[71] Following a similar procedure, many experimental screens presented in this Chapter were directed by analysing the structure of hypothetical products from computational methods, which is likely to be an improvement over qualitative guesses of the structure. However, while these approaches can be used to hypothesise the structure of a cage product, they are unable to account for the impact of synthetic conditions.

Second, a complex mixture of intermediates is produced by one-pot imine condensations. If the reaction conditions are not suitable, these components may react irreversibly to form imine polymer byproducts. Consequently, the concentrations,

addition-rates, and temperatures of cage syntheses need to be carefully controlled.[65] Carefully tuning these conditions is a time-consuming trial-and-error process that can be accelerated by approaches that increase practical throughput, such as HT automated platforms. However, these platforms perform procedures differently from conventional methods, necessitating some initial development.

2.2   Synthesising Organic Cages Using Automated Platforms

The Chemspeed Synthesizer SLT platform was used in synthetic screens. While the specifics of its use can be quite involved, it was simply used as an automated means of performing standard synthetic tasks – liquids may be transferred using an attached syringe pump, reaction vessels may be stirred using a base vortexer, and so on. However, some tasks, such as the transfer of liquids, were much easier to perform than others. Accordingly, synthetic methods were found to perform optimally when exploiting these strengths.

Imine cages have previously been synthesised by layering approaches.[50,57] These approaches involve placing solid trialdehyde within a reaction vessel followed by gently pipetting solvent, catalyst, and diamine solutions on top, which forms discrete layers. The vessel is left unstirred and the slow diffusion of precursors causes the reaction to proceed slowly. The layering approach tends to be the preferred because minimal solvent is used and, for some preparations, it directly produces high quality crystals. However, layering was found to be quite difficult to perform with robotic platforms for several reasons: solid-dispensing apparatus tended to produce uneven solid layers; slowly layering solutions required extremely low syringe-pump speeds, which tended to promote solvent evaporation within the liquid handling system; and the robotic arm on the platforms tended to move rapidly, disturbing the layers.

As an alternative to layering approaches, the Cooper group reported that the one-pot imine condensation of **CC1** may be performed entirely in solution using high-dilution slow-addition approaches.[65] This involves slowly adding dilute trialdehyde solutions to dilute stirred and cooled solutions of diamine, stirring the solution for 24 h to maximise product formation, and then isolating the final product by rotary evaporation. This approach should be much better suited to robotic platforms, more easily scaled up, and allow fine control over parameters such as reactant concentration, stirring rate, temperature and addition rate. Encouragingly, a trial experiment indicated that the approach translated well to automated platforms

(Figure 2-1). In that case, the synthesis of **CC1** with high-dilution slow-addition techniques had been investigated previously; however, the additional observation that **CC3** may also be synthesised in this manner reinforced the viability of the approach, which prompted its use with yet-untested precursors.

2.3   High-Throughput (HT) Imine Cage Discovery

Using parallel HT approaches, experimental parameters known to affect yield, such as reactant concentration,[65] could be varied in tandem. For example, a reaction could be performed at low concentration both with and without catalyst, rather than varying one parameter while fixing the rest. In principle, this is an optimal approach for elucidating ideal cage-forming conditions, especially for yet-untested chemistries.

While extended trialdehydes may be developed to enable the formation of larger cage compounds, diamine extension may also be used to increase the cage's size. In larger trialdehydes, extended aromatic linkages allow rigidity to be maintained.[128] By contrast, rigidity in the diamine is achieved through short—usually, two carbon—chains between the amine moieties. Extending this chain results in a loss of rigidity and, consequently, organic cages made from longer aliphatic diamines tend to collapse upon desolvation.[71]

One approach for introducing rigidity is to use an aromatic amine (aniline). The use of anilines to produce shape-persistent imine cages has been reported by Mastalerz and coworkers,[67,68,129,130] who have, for example, produced a cage from the reaction of a four tri-aniline molecules with six dialdehyde molecules (see introduction, Figure 1-6). In similar approaches, we used screening methods to investigate if organic cages could be produced by reacting benzene-1,3,5-tricarbaldehyde (Figure 2-2, **A**) with 4,4′-diaminodiphenylmethane (**B**).

Like aliphatic diamines, dianilines may undergo imine condensation with aldehydes. However, their nucleophilicity is likely to differ from aliphatic diamines due to conjugation effects. Indeed, the pKb of **B** is calculated to be 8.68, indicating that it is likely to be significantly less nucleophilic than, for example, ethylene diamine, which has a pKb of 4.11.* With that consideration, a broad screen in which a range of temperatures, concentrations, and catalysts were varied was conducted (Figure 2-2).

---

* pKb values calculated using ACD/Labs V11.02
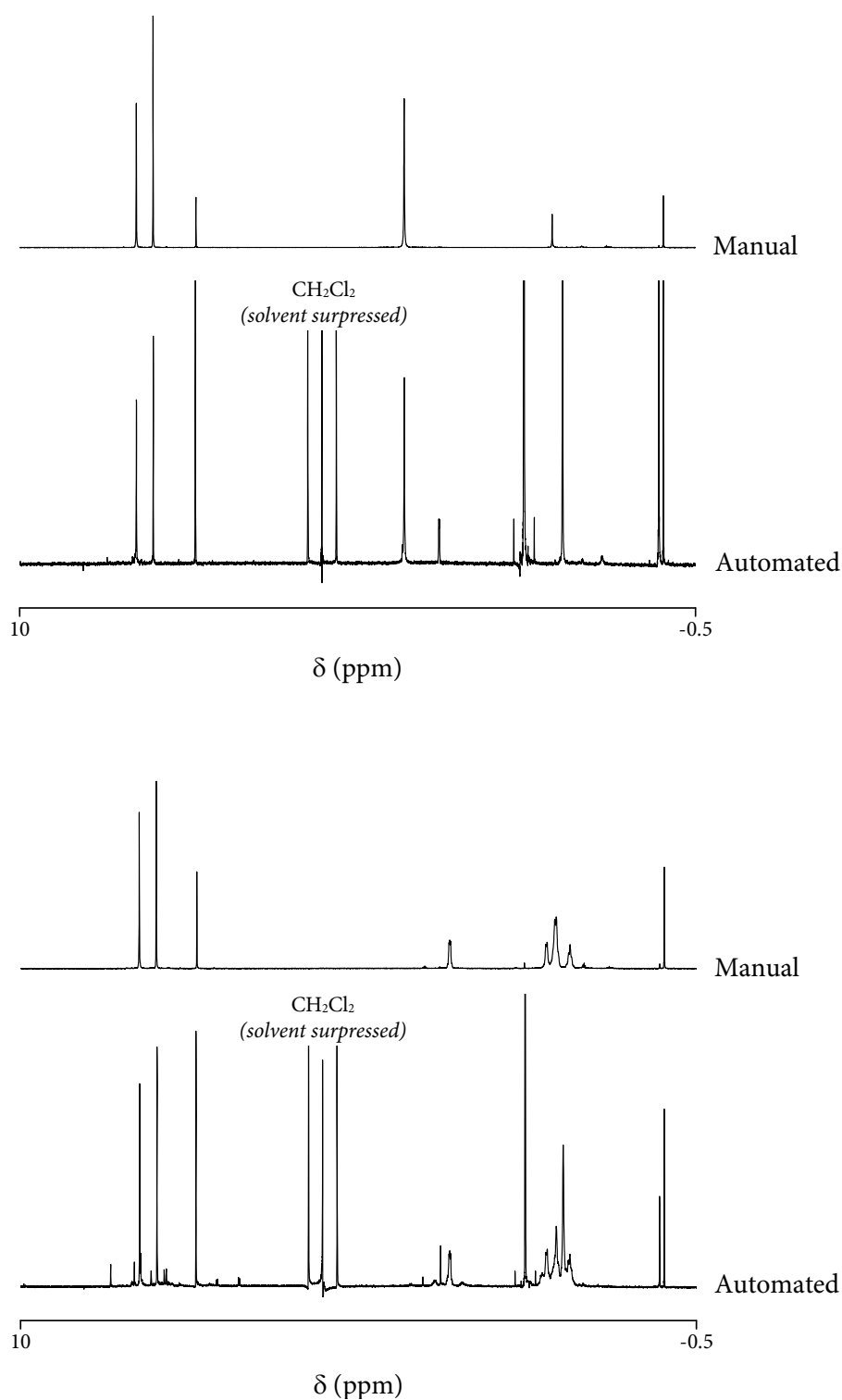
**Figure 2-1 | ¹H NMR (CDCl₃) spectra of CC1 (top) and CC3 (bottom) produced by manual and robotically-automated methods**. Analyses from automated methods were solvent (dichloromethane) suppressed. A layering approach was used in manual syntheses. In the automated approach, platforms slowly (0.1 mL min⁻¹) added dilute diamine solutions to dilute trialdehyde solutions.
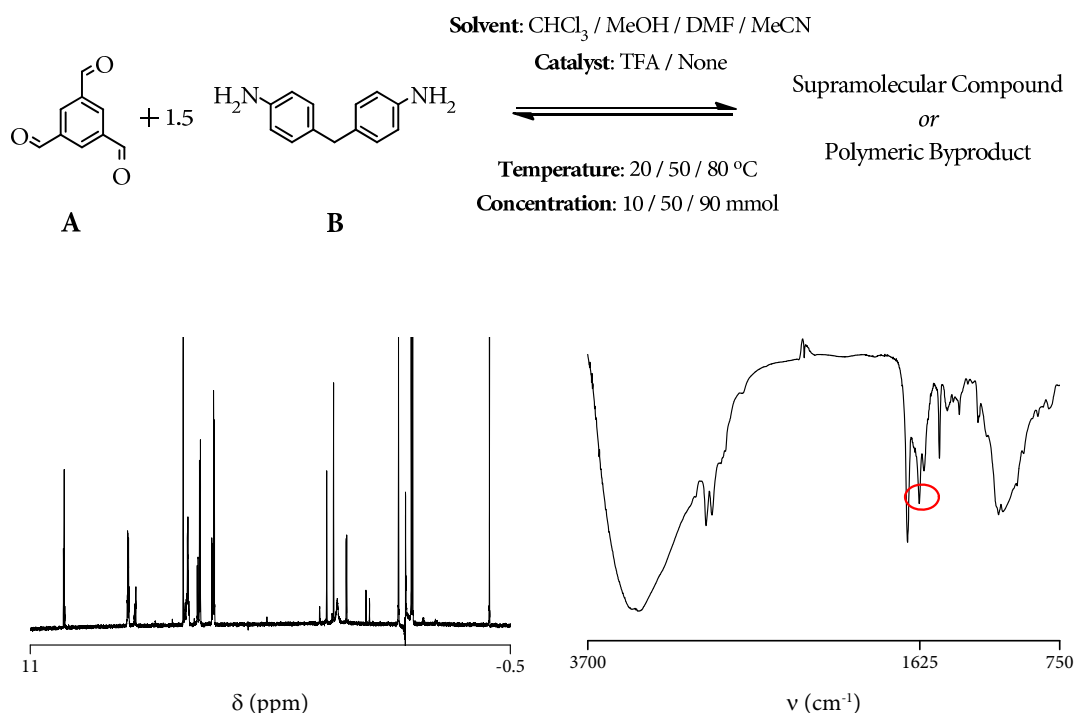
Figure 2-2 | Attempted synthesis of an organic cage from di-aniline precursors. The reaction of benzene-1,3,5-tricarbaldehyde (**A**) with 4,4'-methylenedianiline (**B**) was performed with different solvents, temperatures, and concentrations with and without trifluoroacetic acid (TFA) catalyst. However, imines formed from anilines have a lower degree of reversibility. As a result, syntheses tended to produce polymer suspensions.

For most products of the screen, FTIR measurements indicated the formation of an imine moiety around 1625 cm^{-1}. However, most samples were observed to contain insoluble precipitates. These were likely to be imine polymer byproducts. This is further reinforced by ^{1}H NMR analyses which only measured negligible concentrations of imine environments and starting materials remaining in the solution phase.

The formation of polymer in preference to a cage product is likely to be due to the differences in the reversibility of imine formation between anilines and aliphatic diamines. High-yielding organic cage syntheses rely on reversibility to equilibrate intermediates into the final product, a dynamic covalent chemistry[59] process that eventually results in the thermodynamically preferred product. Imine formation from anilines is likely to be less reversible;[131] consequently, because intermediates are less-able to reverse from (unfavourable) oligomer formation, precipitation occurred. If this is the case, cage formation from anilines is more likely to rely on statistical chance in the absence of any directing effects.

In order to maximise the efficacy of subsequent screens, *in-silico* methods were utilised. Using commercially available precursors as inputs, a collection of possible cages were built *in-silico* using a previously described method (Figure 2-3).[71] These models helped direct the design of HT screens, which focused on the effect of reaction optimization and ideal precursor combinations for cage formation.

a)   b)

c)   d)   e)
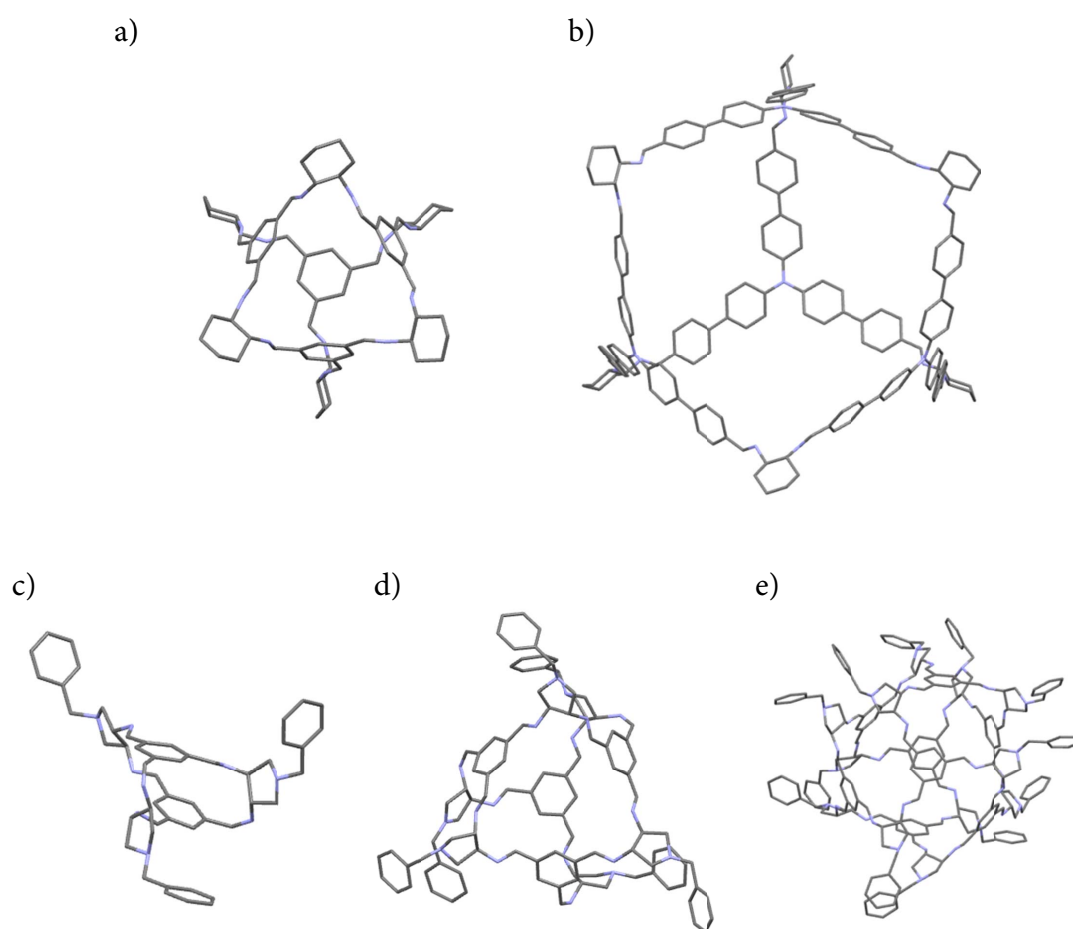
Figure 2-3 | Models of organic cage compounds built *in-silico*. Combinations of diamines and trialdehydes were built into [2+3], [4+6], and [8+12] arrangements followed by conformational energy minimisation. A more detailed explanation of the process can be found in the experimental Section (7.1.2, p98). Six models are presented: **CC3**, a known cage (a); the [4+6] combination of *tris*([1,1'-biphenyl]-4-carbaldehyde) with (1*R*, 2*R*)-1,2-diaminocyclohexane (b); the [2+3] (c), [4+6] (d), and [8+12] (e) combination of benzene-1,3,5-tricarbaldehyde with (3*S*, 4*S*)-3,4-diamino-1-benzylpyrollidine. *Calculations carried out by Dr. Kim Jelfs.*

Models were valuable endpoints which indicated if a product is geometrically reasonable. However, it was especially challenging to model the affect that synthetic conditions have on cage compound formation.[71] With that in mind, a small set of reactions were conducted to measure the effect of precursor concentration and acidic catalyst. Specifically, the reaction of an extended trialdehyde linker, *tris*([1,1'-biphenyl]-4-carbaldehyde) (Figure 2-4, **C**), with either ethylene diamine (**D**); (1*R*, 2*R*)-1,2-diaminocyclohexane (**E**); or 1,2-diaminopropane (**F**) was investigated. Models indicated that the resulting [4+6] cage compounds should not contain strained bonds or clashing moieties. Additionally, because of the rigidity of the trialdehyde, their central voids were predicted to be shape persistent (e.g. Figure 2-3c).

In the screen, the concentrations of both the diamine and trialdehyde stocks were varied between 2, 10, and 20 mmol L^{-1}. These concentrations are close to precursor concentrations used in **CC1** syntheses.[65] Additionally, the reaction was conducted with or without trifluoroacetic acid (TFA) catalyst, which is used in other imine cage syntheses.[50,57] Lower concentration samples were observed to be clear solutions which, according to ^{1}H NMR and FTIR measurements, contained imine environments. However, attempts to isolate a cage product from these solutions were unsuccessful.

GPC analyses indicated the presence of large cage-sized compounds in some mixtures (e.g. Figure 2-4, bottom). However, a variety of other components were also present in these solutions, which thwarted recrystallisation. This particular system probably produced mixtures because of the trialdehyde's long biphenyl struts. Because of them, the resulting cage's windows are likely to be large compared to the cage's overall size, which could promote interpenetration.[132] This phenomenon has been observed for previously reported imine cages.[133] Additionally, the biphenyl moiety is more flexible than the struts of other trialdehyde precursors, which may enable it to form a mixture of [2+3], [4+6], and [8+12] cages rather than being geometrically constricted to a single stoichiometry.
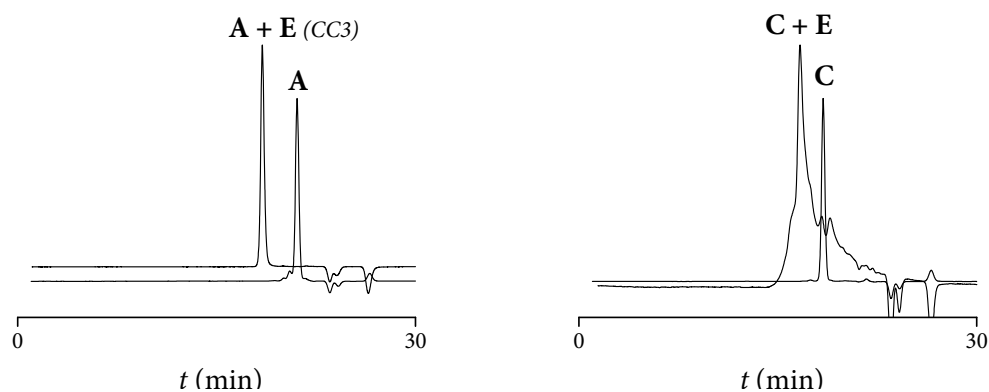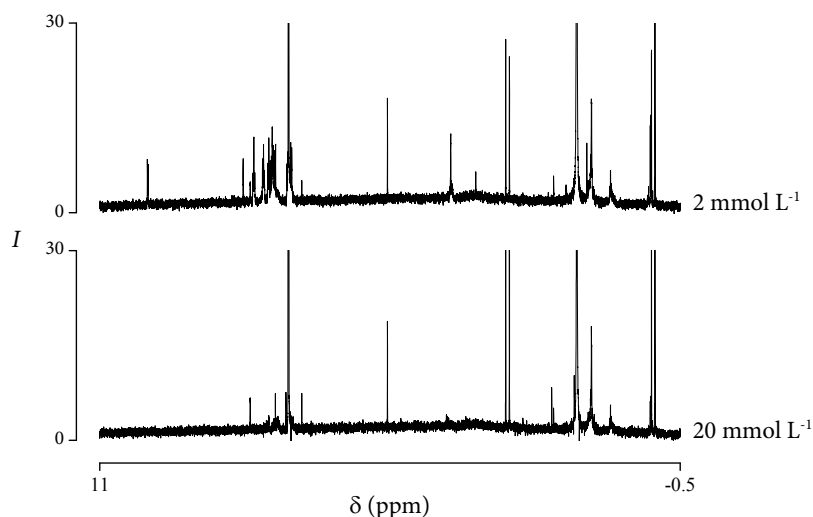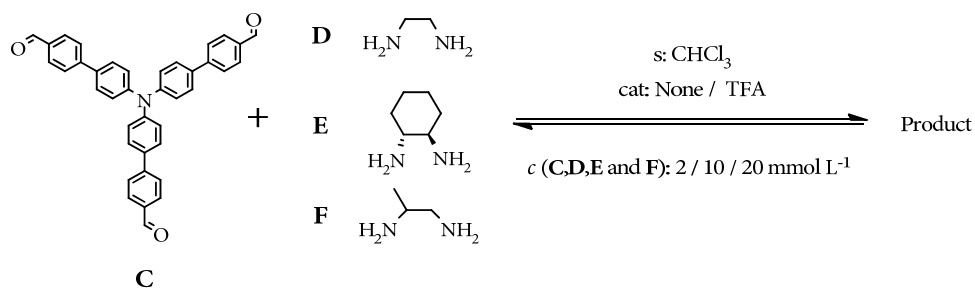
Figure 2-4 | Investigating the effect of reaction conditions on organic cage syntheses. Top: experimental screening conditions. **Middle:** Example ^{1}H NMR (CDCl$_3$) spectra of two reaction mixtures in which precursor stocks had concentrations of 2 and 20 mmol L^{-1}. Due to the formation of imine polymer byproducts, negligible aromatic- and imine-region NMR signals were measured for reactions conducted at higher concentrations. **Bottom**: GPC chromatograms of precursors when compared to their resulting reaction products. In GPC, larger components of a mixture elute at shorter retention times (*t*). The synthesis of **CC3** from its precursor; 1,3,5-triformylbenzene (**A**); is shown on the left side. A product from the screening procedure is shown on the right side. Comparing the two, it is apparent that screening products produced a broad range of compounds with a larger, possibly cage, compound eluting quickly. See experimental Section 7.1.3.4 (p100) for further details.

For known cage syntheses, a reduction in yield can be directly attributed to imine polymer formation. Varying precursor stock concentrations did appear to eliminate the formation of imine polymer; however, the reaction did not produce a single product. Based on these observations, it was hypothesised that only certain precursor combinations may produce single cage products and others, even after optimising synthetic conditions, form mixtures. To investigate this, a screening approach was developed to broadly screen a wider variety of precursor combinations in parallel.

In the screen, the factorial combination of four aldehydes with four diamines, both catalysed and uncatalysed by TFA, was attempted (Figure 2-5). This approach appeared to be effective at identifying systems which merit further investigation. In most samples, infrared absorption around 1680 cm^{-1} confirmed the formation of an imine bond. Most combinations produced insoluble imine products (e.g.

32 Combinations
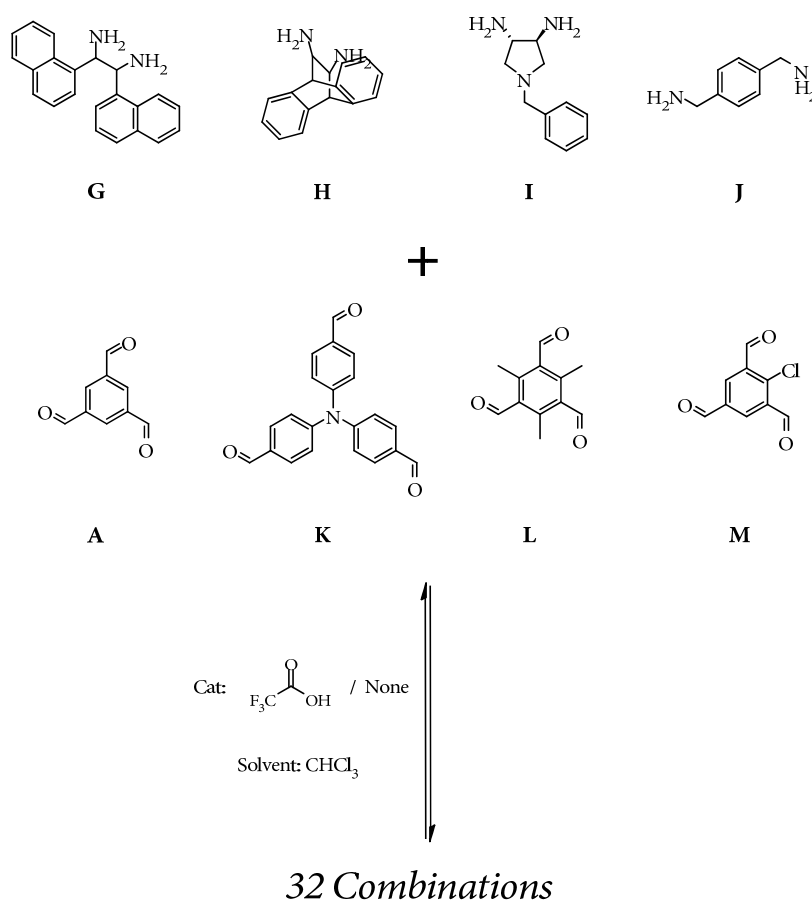
Figure 2-5 | Broadened screening approach. Dilute solutions of 1,2-di(1-napthyl)-1,2-ethanediamine (**G**); (11*R*, 12*R*)-9,10-ethanoanthracene-11,12-diamine (**H**); (3*S*, 4*S*)-3,4-diamino-1-benzopyrollidine (**I**); and *p*-xylylenediamine (**J**) were slowly added to solutions of benzene-1,3,5-tricarbaldehyde (**A**); *tris*(4-formylphenyl)amine (**K**); 2,4,6-trimethylbenzne-1,3,5-tricarbaldehyde (**L**); and 2-chlorobenzene-1,3,5-tricarbaldehyde (**M**) with and without TFA catalyst.

Figure 2-6, left) but some produced clear solutions containing soluble imines (right, further sample images in Appendix, p131). Unfortunately, the majority contained byproducts. In those cases, subsequent isolation attempts were unsuccessful. However, the reaction of benzene-1,3,5-tricarbaldehyde (**A**) with (3*S*, 4*S*)-3,4-diamino-1-benzopyrollidine (**I**) was found to produce soluble, symmetrical, imine environments as judged by ^{1}H NMR (Figure 2-6, right). Further, MALDI-TOF-MS analysis of this product gave a peak corresponding to 1582 g mol^{-1}, consistent with a [4+6] cage structure composed of four units of **A** and six units of **I** and a molecular formula $C_{102}H_{102}N_{18}$. This product is referred to as **CCX**-*S* for the remainder of this Chapter, where scale-up and characterization attempts are discussed.

2.4 Scale-Up and Characterization of a Novel Organic Cage Compound

The high-dilution slow-addition methods used in the screens were straightforwardly scaled up by increasing the stock volumes used.[65] The reaction was scaled up to 886 mg with a yield of 96 %; however, the isolated powder was determined by PXRD to be amorphous, necessitating further crystallisation steps.
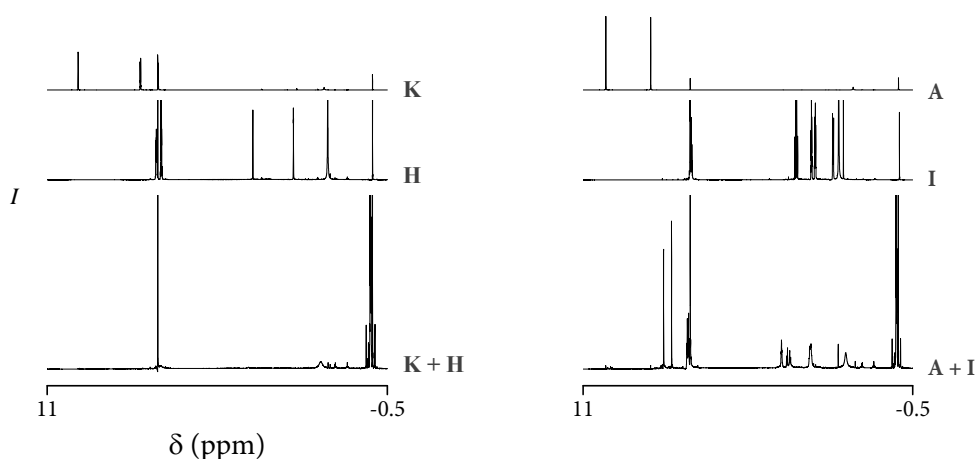
Figure 2-6 | Comparison of screening results. ^{1}H NMR analyses of reactants and their resulting product. **Left**: the reaction of *tris*(4-formylphenyl)amine (**K**) with (11*R*,12*R*)-9,10-dihydro-9,10-ethanoanthracene-11,12-diamine (**H**). **Right**: the reaction of benzene-1,3,5-trialdehyde (**A**) with (3*S*,4*S*)-3,4-diamino-1-benzylpyrrolidine (**I**). Both reactions were one-pot imine condensations of aromatic trialdehydes with aliphatic diamines, one produced soluble cage compounds with symmetrical imine environments (right) while the other produced an insoluble imine polymer (left).

Single crystals of **CCX**-*S* were difficult to obtain. Evaporation from a range of pure solvents and controlled thermal cycling techniques did not yield single crystals. However, using the vial-in-vial vapour diffusion technique, a screen of 42 solvent/antisolvent combinations identified two combinations that produced crystalline solids: 2,2,2-trifluoroethanol / methanol (TFE / MeOH); and dimethylacetamide / methanol (DMAC / MeOH). Unfortunately, TFE / MeOH crystals were observed to be twinned, making their resulting diffraction patterns difficult to refine. By contrast, DMAC / MeOH crystals did not have this issue. Single crystal XRD (scXRD) analysis of those crystals indicated that the solvated **CCX**-*S* molecules crystallised in the trigonal space group P3, a = 30.1537(9), c = 10.9405(3) Å, V = 8614.9(4) Å^3, Z = 3, ρ = 1.103 g·cm^{-3} (Figure 2-7).

Analysis of this crystal structure indicated that the internal void of **CCX**-*S* is similar to previously reported compounds. It has triangular window shape with a diameter of 5.7 Å (Figure 2-7). Similarly-shaped windows with diameters of 5.8, 6.1, and 5.8 Å have been measured for **CC1**, **CC2**, and **CC3** respectively.[57] However, the windows of **CCX**-*S* may be inflated by the presence of solvent guests. Indeed, variable-temperature scXRD measurements indicated a phase change in **CCX**-*S* to a hexagonal space group P (a = 30.57, c = 11.06 Å), which might be due to its collapse upon solvent evaporation. This hypothesis was reinforced by analysis of refined computational models, which indicated that **CCX**-*S*'s internal cavity is deflated in the absence of solvent molecules (Figure 2-8). Unfortunately, the lower quality of diffraction data at elevated temperatures prevented experimental refinement of this desolvated structure.

While flexible *exo*-functional benzyl moieties are unique to **CCX**-*S*, they appear to negatively impact its solid-state properties. scXRD measurements indicated greater disorder in the *exo* benzyls. This is likely to frustrate ordered packing of the cage molecules, which explains why **CCX**-*S* was difficult to crystallise. Additionally, the outer moieties are, in principle, small enough to interpenetrate nearby **CCX**-*S* molecules, which could explain the observation that amorphous **CCX**-*S* was nonporous to N$_2$. There is still a possibility that desolvated crystalline **CCX**-*S* *is* porous; however, bulk crystallisation experiments tended to produce low quality semi-crystalline solids.
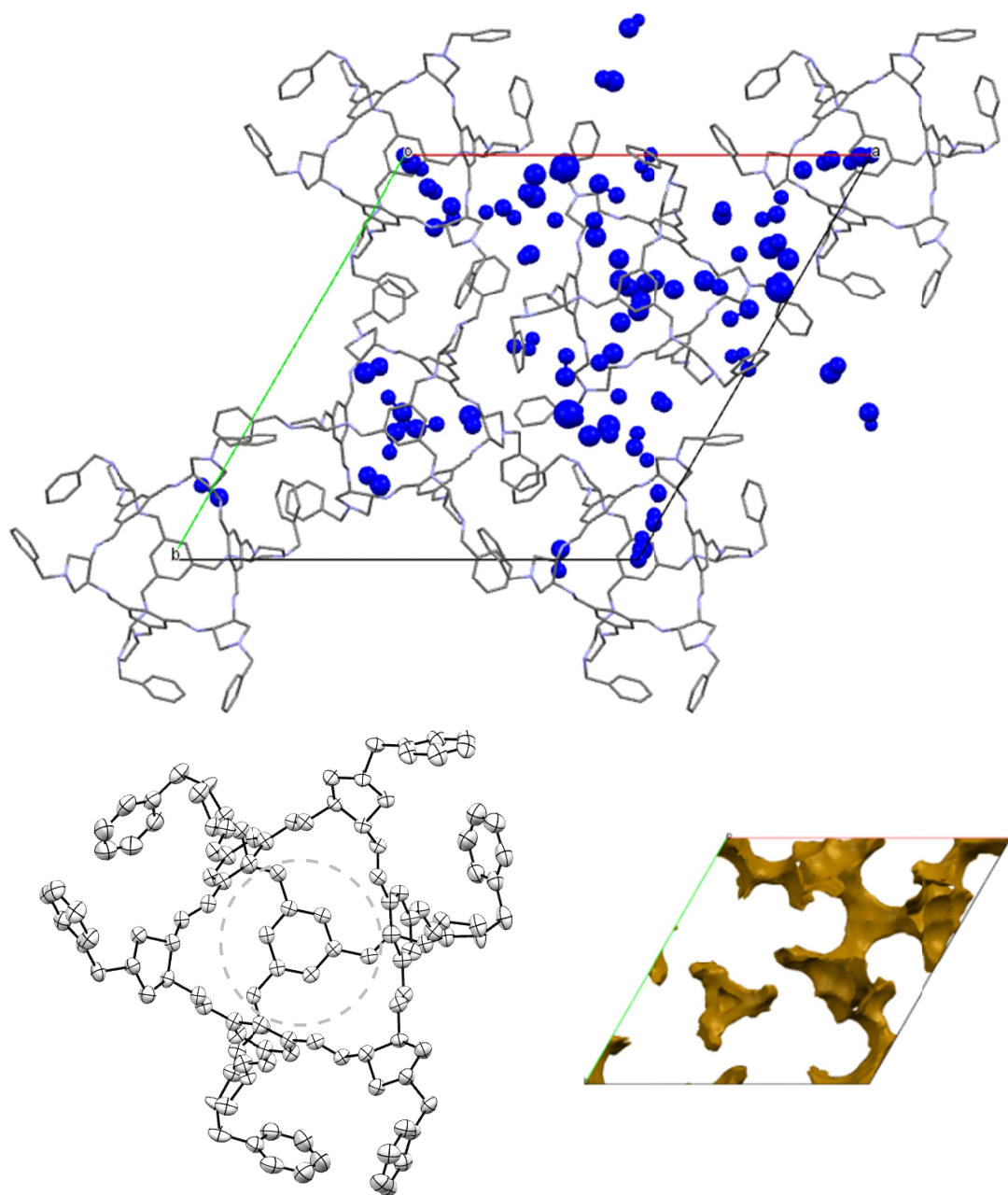
Figure 2-7 | scXRD structure of solvated CCX-*S*. Top: measured unit cell of **CCX**-*S*, viewed along the *c*-axis. Solvent molecules are coloured in dark blue for clarity. **Bottom-left:** an ellipsoid representation of a single **CCX**-*S* molecule, viewed along the *c*-axis. Solvent molecules are removed for clarity. The dashed circle indicates the shape used for window-diameter calculations. **Bottom-right:** the solvent accessible surface (120 pm probe size) of **CCX**-*S* upon *in-silico* desolvation, viewed along the *c*-axis.

scXRD structure (solvated)	Modelled (desolvated)

Top

Side
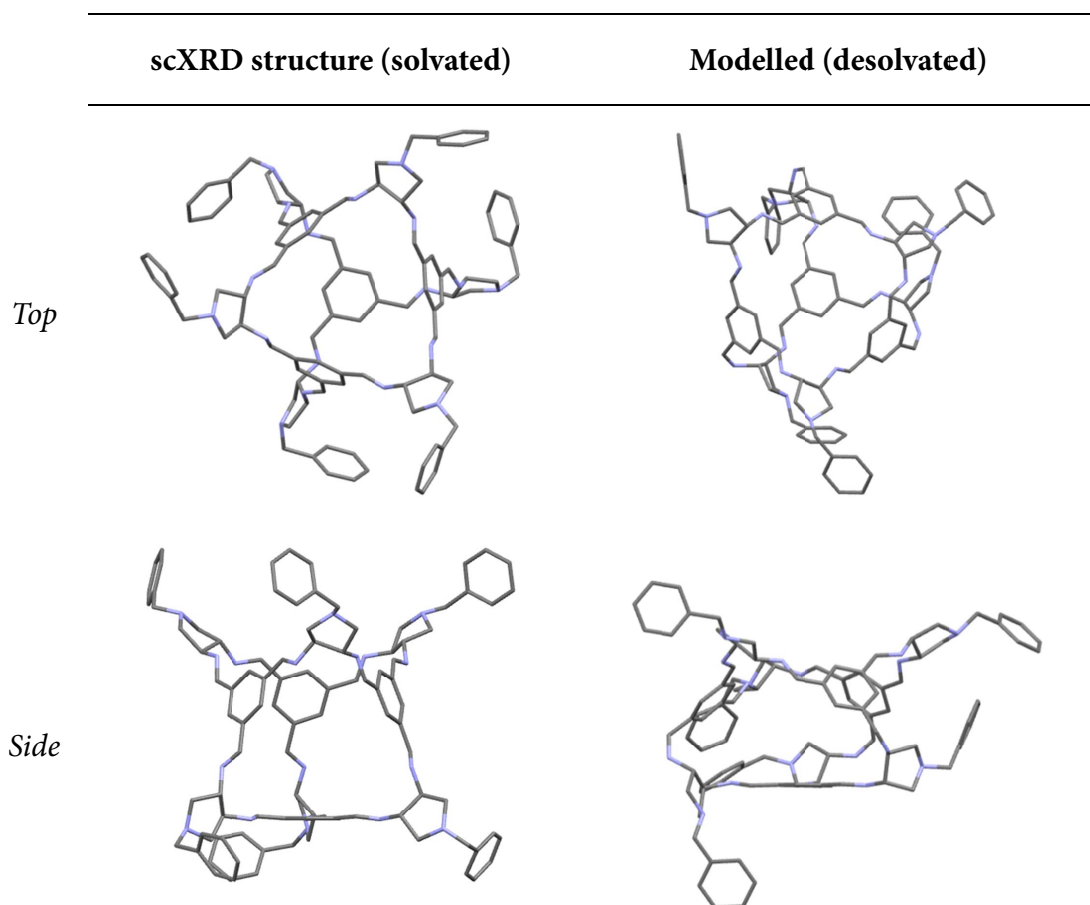
Figure 2-8 | Comparison of experimental and simulated structures of CCX-*S*. a) Space fill representation of **CCX**-*S* calculated from scXRD measurements, viewed along the *c*-axis. Solvent molecules are removed for clarity. b) *In-silico* modelled structure of **CCX**-*S*, showing a collapsed pore structure.

Despite these problems, the isolation of **CCX**-*S* may still prove useful. The preparation of its precursor, (3*S*,4*S*)-3,4-diamino-1-benzylpyrollidine (**I**), might in principle be modified to change the *exo N*-benzylpyrollidone moiety.[134] Exchanging it with a bulker, more rigid, moiety might discourage interpenetration, increasing the resulting cage's porosity. This altered cage may have a similar internal void to previously reported cages but may have a higher solubility and amorphicity. This will require further investigation; however, modifying a cage's extrinsic functionality is particularly attractive and could enable the porosity tuning, polymerization, or surface binding.

2.5   Conclusions & Outlook

Automated platforms were utilised to accelerate the process of finding cage-forming reactions. Initially, techniques such as slow layering were directly reproduced but found to be difficult to perform on automated platforms. Accordingly, processes were developed to use high dilution, slow addition, methods which were previously demonstrated for the synthesis of **CC1**.[65] Utilising this method, **CC1** and **CC3** were successfully synthesised on the automated platforms (Figure 2-1, p29), proving its viability for use in subsequent screening experiments.

The synthesis of an organic cage compound was attempted by reacting an aliphatic trialdehyde; benzene-1,3,5-tricarbaldehyde (**A**, Figure 2-2, p30); with an aromatic diamine, 4,4'-methylenedianiline (**B**). Using the platforms, a broad screen was conducted to investigate a range of synthetic conditions. However, only poly-imine products were isolated, which is likely due to the lower nucleophilicity of aromatic diamines when compared with aliphatic diamines.

In order to maximise the efficacy of subsequent screens, models of possible cage products were built *in-silico* using a reported method (Figure 2-3, p31).[135] These were valuable endpoints; however, it was particularly challenging to model the effect of reaction conditions *in-silico*. Accordingly, a subsequent screen was developed to explore the effect of reaction conditions. The reaction of *tris*([1,1'-biphenyl]-4-carbaldehyde) with either ethylene diamine (**D**); (1*R*, 2*R*)-1,2-diaminocyclohexane (**E**); or 1,2-diaminopropane (**F**) was investigated (Figure 2-4, p33). *In-silico* models calculated the structure of a possible cage product (Figure 2-3c). This structure appeared to contain no strained bonds or clashing moieties. Encouragingly, ^{1}H NMR and FTIR analyses indicated soluble imine environments in some of the products. In particular, products synthesised from (1*R*, 2*R*)-1,2-diaminocyclohexane were observed to produce a large, soluble, imine-containing, compound. However, GPC analyses indicated that complex mixtures tended to be produced from these reactions, which thwarted isolation attempts.

Based on these observations, it was hypothesised that certain reactant combinations were likely to produce complex mixtures regardless of synthetic conditions. With that in mind, a combinatorial screen of many different trialdehyde-diamine combinations was performed (Figure 2-5, p34). Sixteen synthetic pairs were investigated. Products from the majority of pairs were observed to be complex mixtures. However, the reac-

tion of benzene-1,3,5-tricarbaldehyde (**A**) with (3*S*, 4*S*)-3,4-diamino-1-benzopyrollidine (**I**) produced single-component solutions of a previously unreported organic cage compound, **CCX**-*S*. Subsequent experiments focused on the scale up and characterization of this product.

The reaction was scaled up to produce 886 mg of **CCX**-*S* with a yield of 96 %. Single crystals of the cage were obtained from the vial-in-vial vapour diffusion of methanol vapour into a solution of **CCX**-*S* dissolved in DMAC. scXRD of these crystals confirmed the organic cage structure of **CCX**-*S* (Figure 2-7). Structural analysis of **CCX**-*S* indicates it has a similar window shape and diameter to **CC1**, **CC2**, and **CC3**; however, unlike these cages, computational models and variable temperature scXRD indicate that the pore structure of **CCX**-*S* is likely to collapse upon desolvation. Further, it is likely that **CCX**-*S*'s extrinsic benzyl moieties will interpenetrate—or at least block—adjacent neighbours, reducing its overall solid-state porosity. This is likely why amorphous **CCX**-*S* was measured to be nonporous to N_2.

Overall, attempts have been made to speed up traditional synthetic procedures by using automated platforms and computational modelling. While a novel material was discovered in this manner, it is clear that both the practical and computational procedures require further development. Regardless, the work in this Chapter shows that the combination of HT procedures with computational models could be a viable strategy for discovering new organic cages.

3 Organic Cages as Selective Sorbents
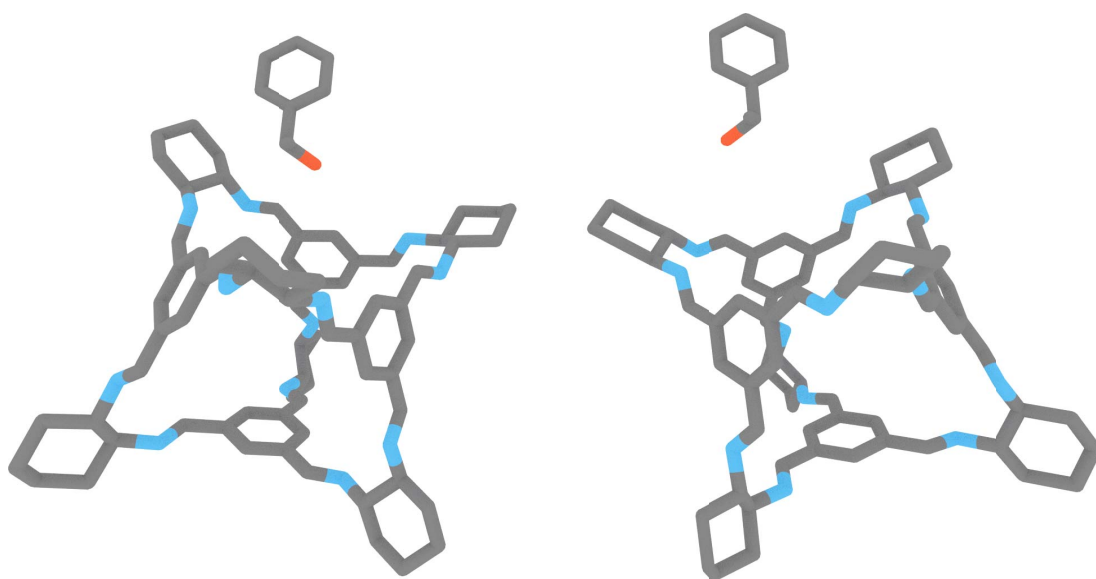
Technologies such as selective sorbents and chromatographic stationary phases rely on a porous material's ability to discriminate between compounds. This discrimination usually occurs due to a complex combination of interactions[40,102] which, if comprehensively understood, can help predict which mixtures the material can separate.[136] While organic cages have received attention for their ability to discriminate rare gases,[66] alkylaromatics,[25] alkali metal ions,[137] and carbohydrates,[93] there are still some systems, such as chiral compounds, which have not received attention. Their separation could be particularly valuable; however, measuring and understanding complex selectivity effects remains challenging.

This Chapter focuses on identifying and understanding the host-guest interactions responsible for selective adsorption in **CC3**. Three steps towards this goal are discussed: (i) the development of a straightforward measurement technique for identifying mixtures that **CC3** selectively adsorbs, (ii) further improving the technique's reproducibility, which enabled quantitative measurements of host-guest behaviour, and; (iii) using the fully developed technique to establish molecular and thermodynamic explanations of **CC3**'s host-guest behaviour.

Results presented in Section 0 of this Chapter contributed directly to a *Nature Materials* publication: "Separation of rare gases and chiral molecules by selective binding in porous organic cages".[66]

3.1   Screening for Selective Sorption Behaviour

A common method for measuring selectivity is 'adsorptive separation'.[40] In it, a host is soaked in a liquid guest mixture, the guest-adsorbed host is then isolated by filtration, washed to remove adsorbed guests, and the washings, which contain the desorbed guest, are analysed. One concern with this approach was that **CC3**-*R*, which is reported to be soluble in organic solvents such as dichloromethane,[57] may dissolve or recrystallise in concentrated guests. Recrystallisation is especially concerning because it is likely to frustrate analysis attempts; indeed, studies indicate that polymorphs of organic cages can have differing surface areas and pore topologies.[52]

To avoid recrystallisation, an alternative technique that minimised the amount of guest used was developed (Figure 3-1). Small volumes of guest mixtures were added to a vessel containing **CC3**-*R*, the vessel was sealed, agitated, and its headspace was analysed by gas chromatography (GC). The technique was used to screen a variety of
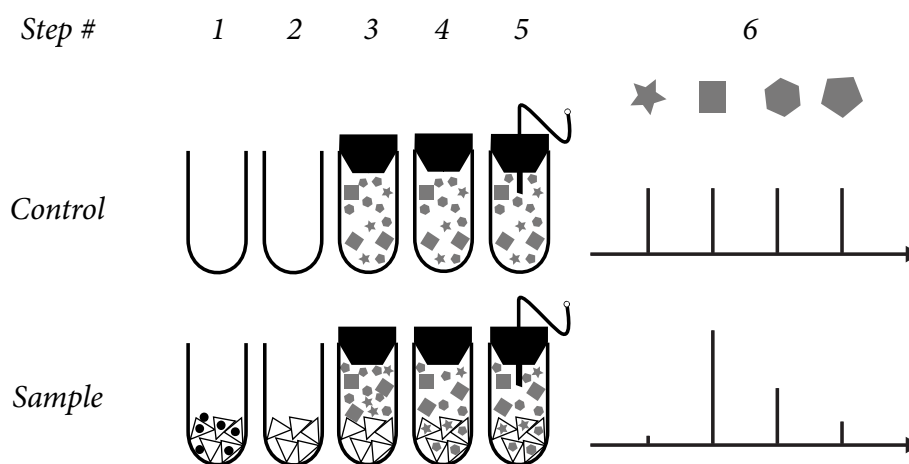
Figure 3-1 | Qualitatively measuring selective adsorption phenomena. Control and experimental samples were run in parallel. In experimental samples, hosts were added (1) and activated (2). A small quantity of guest mixture was added (3) and gently mixed (4) to allow it to exchange into the host; finally, the headspace concentration of the guest was measured (5). In control samples, the headspace concentration of a component is related to the amount added.[117,138] By contrast, in experimental samples, adsorbed components were unable to exchange with the headspace. Therefore, differences in measured headspace concentrations between control and experimental samples indicated selective adsorption by the host (6).

mixtures (see Appendix, p137). Most mixtures were binary but many-component mixtures were also analysed using this approach (see Appendix, p136).

As discussed in Section 1.5.1, the separation of xylene isomers is particularly important. The Cooper group investigated previously the separation of xylene isomers with **CC3**-*R*,[49] which demonstrated that the cage preferentially adsorbs C8 aromatics in the order *para*-, *meta*-, and then *ortho*-xylene due to shape sorting effects. Specifically, the narrower steric envelope of the *para* isomer promoted its adsorption into **CC3**-*R* when compared with the other isomers. Encouragingly, measurements performed using the newly developed technique corroborated that study: upon exposing a xylene isomer mixture to **CC3**-*R*, the resulting GC peak areas diminished following the same pattern: *para*- > *meta*- >> *ortho*-xylene (Figure 3-2).

This proved the viability of the technique and prompted measurements on unstudied guest mixtures. Of particular interest was the separation of racemates which, as discussed in Section 1.5.1, can be particularly valuable, especially in the pharmaceutical industry.[100] This class of separations rely on a combination of interactions between a homochiral host and guest.[102,112] **CC3**-*R* is reported to form a chiral pore network,[57] which should enable it to perform chiral separations. However, chiral selectivity may
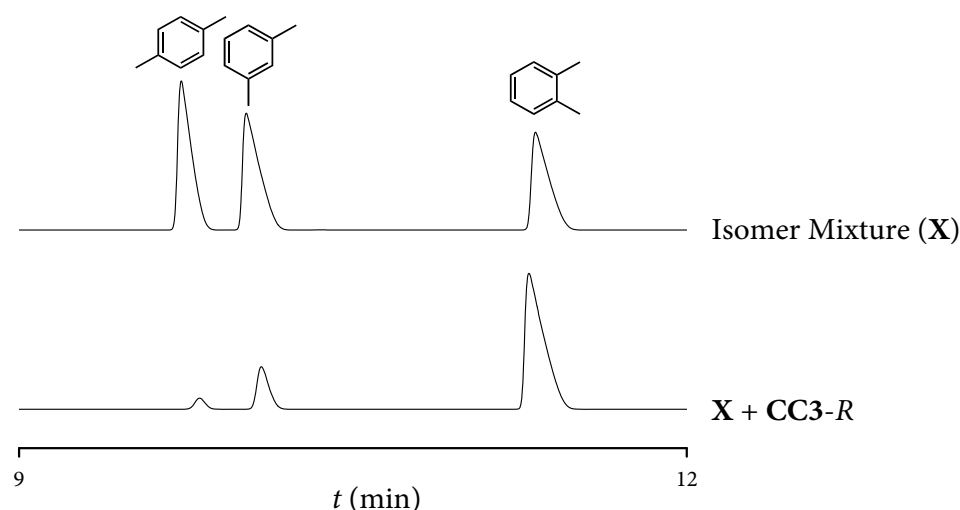
Figure 3-2 | Selective adsorption of xylene isomers into CC3-*R*. GC-FID chromatograms of a xylene isomer mixture before (top) and after (bottom) exposure to **CC3**-*R*. Due to a shape sorting effect by **CC3**-*R*,[49] the peaks for *p*-xylene and *m*-xylene were strongly diminished relative to the peak for *o*-xylene after exposure.

only occur for a small subset of racemates, which necessitated a straightforward measurement and screening approach.

Chiral selectivity was straightforward to measure with the developed technique primarily because enantiomers have equivalent boiling points. Boiling point equivalence means that, in racemic samples, their headspace concentration should be equal and, in non-racemic samples, unequal.[138] In practice, this means that after exposing a racemic mixture to **CC3**-*R*, the measurement of inequivalent enantiomer peak areas indicates chiral adsorption. To compliment this ease of measurement, a variety of racemic mixtures was sourced via a four step screening procedure which involved identification, shortlisting, method development, and analysis.

Racemic mixture identification involved using chemical databases. Mixtures that met three primary criteria were chosen. First, so that they are likely fit inside the pores of **CC3**, mixture components had a maximum molecular weight of 250 g mol^{-1}. Second, to prevent possible hydrolysis of **CC3**'s imine moieties, the mixtures' pKas were between 5 and 9. Finally, to make them suitable for GC analysis, mixtures' had a maximum boiling point of 200 °C. This procedure identified 182 eligible racemic mixtures.

Shortlisting of the mixtures reduced them down to a more manageable number. Mixtures were chosen to span a wide variety of different chemical systems but safety, shelf-life, and price were also taken into account. A total of 65 systems for GC method development were chosen at the end of this step (full list in Appendix, p137).

Because the shortlisted mixtures spanned a broad range of functionalities, GC method development was another part of the screening process. To accurately measure any deviations from *ee* = 0, a GC method that achieved near-baseline separation of the mixture was required. However, for most systems, bespoke GC methods were required to achieve this separation, which was quite challenging. The development of bespoke methods was achieved iteratively and, overall, 16 systems were separated *via* GC for adsorption analysis.

Adsorption analysis on these sixteen mixtures identified that six enantioselectively adsorb into **CC3**-*R* (Table 3-1). Selectivity was mirrored for **CC3**-*S*. For example, inequivalent enantiomer peak areas were measured after exposing *rac*-3-hydroxytetrahydrofuran to **CC3**-*R* (Figure 3-3, top) but no inequivalent was observed after exposure to *rac*-**CC3** (middle). Additionally, the inverse was seen in **CC3**-*S* (bottom). At the time, these findings were the first recorded example of chiral selectivity in **CC3**, which merited further investigation.
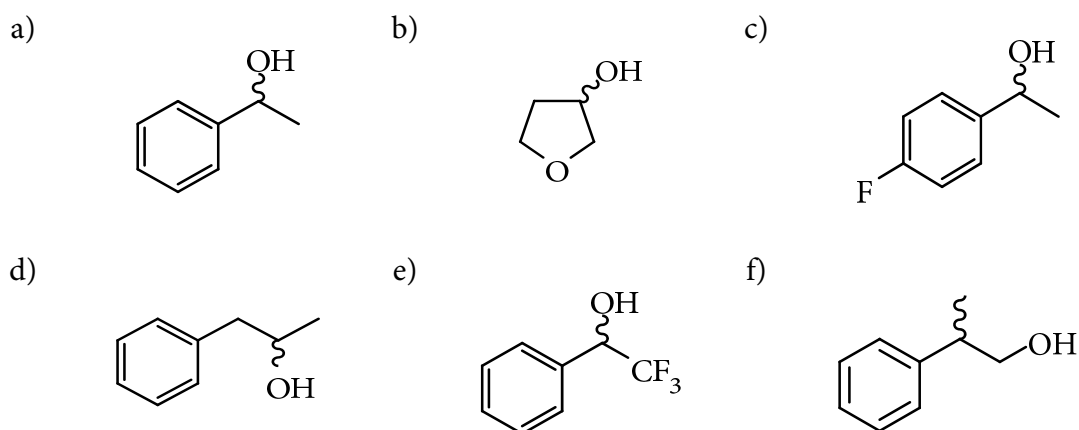
Table 3-1 | Racemic mixtures that selectively adsorb into CC3-R. Six mixtures were initially identified by the screening approach: *rac*-1-phenylethanol (*rac*-1-PE, a), *rac*-3-hydroxytetrahydrofuran (b), *rac*-4-fluoro-α-methylbenzyl alcohol (c), *rac*-1-phenyl-2-propanol (d), *rac*-α-(trifluoromethyl)benzyl alcohol (e), and *rac*-3-phenyl-1-propanol (f). In each case, a deviation from *ee* = 0 was measured when analysing the headspace of these mixtures after exposing them to **CC3**-*R*.
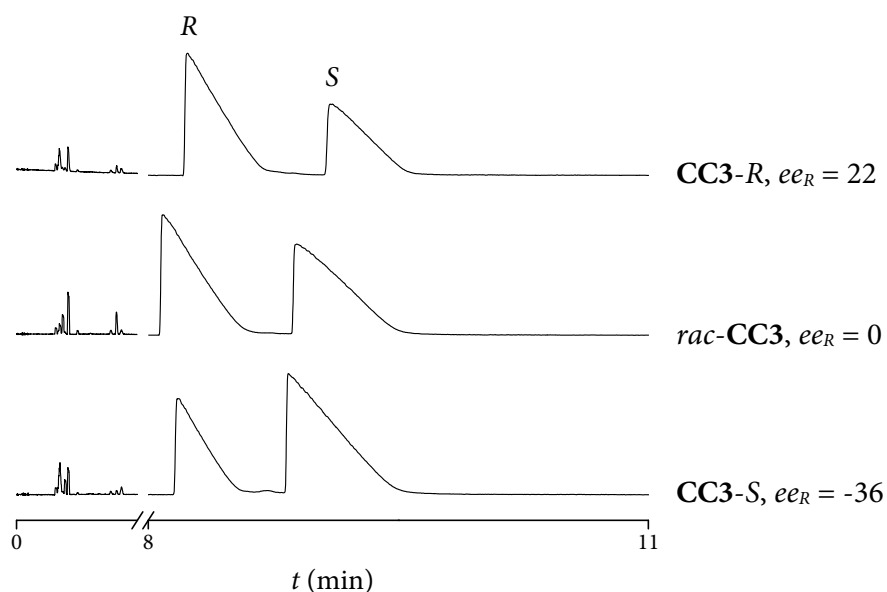
Figure 3-3 | Chirally selective adsorption by CC3-*R*. GC-FID chromatograms of samples after exposing *rac*-3-hydroxytetrahydrofuran to **CC3**-*R* (top), *rac*-**CC3** (middle), or **CC3**-*S* (bottom). Enantiomeric excesses calculated from relative peak areas are annotated. *rac*-3-Hydroxytetrahydrofuran was measured to have an enantiomeric excess (*ee*) of 0. No chiral selectivity was seen for *rac*-**CC3**. Opposite chiral adsorption was seen between **CC3**-*R* and **CC3**-*S*; however, due to inaccuracies in the technique, *ee* values were not precisely mirrored.

## 3.2 Developing a Quantitative Technique for Measuring Selective Sorption

While this technique was capable of screening through a variety of systems, identifying several guest mixtures that **CC3** can separate, it was not suitable for quantitative analysis because of its low reproducibility (Figure 3-4). This was an issue since, in order to rationalise the behaviour of **CC3**, selectivity values needed to be compared with other techniques—for example, selectivities yielded from computational models and from crystallographic measurements—with a high degree of accuracy.

The source of low reproducibility was deemed to be due to uneven host-guest mixing. Guest molecular weights were, on average, an order of magnitude lower than **CC3**. Consequently, in order to achieve an equimolar guest:**CC3** ratio, small volumes of guests were added. These volumes were too small to mobilise the **CC3** powder to slurry, which resulted in poor mixing of the guest and host. A solvent could have been used to circumvent this issue; however, two effects complicate this. First, **CC3**-*R* may have dissolved or recrystallised in the solvent, which might have affected its uptake and selectivity. Second, solvent molecules could have displaced the guest of
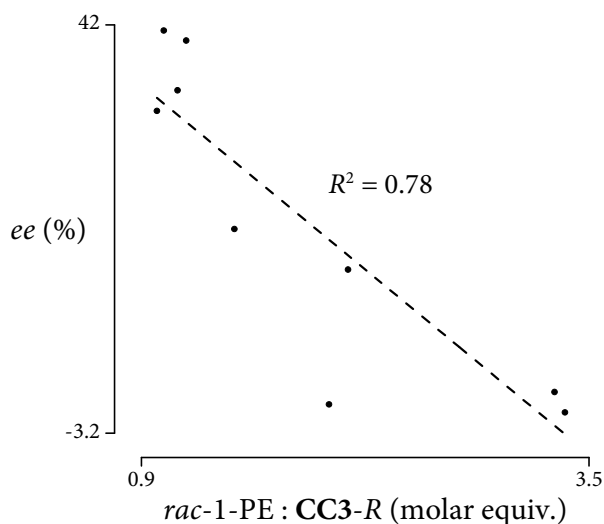
Figure 3-4 | Poor guest mixing reduces reproducibility. Measured *ee*s of *rac*-1-PE after exposure to different amounts of **CC3**-*R*. As **CC3**-*R* is not mobilised in any solvent, it is difficult to evenly distribute the guest. As a result, measurements with this technique tend to have a poor degree of correlation.

interest from **CC3**-*R*, or at least compete with the guest, which would reduce guest uptake. These concerns were confirmed by experimental measurements, which indicated that measured enantiomeric excesses were highly affected by solvent (Figure 3-5).

Interestingly, selectivity was less affected by sterically bulky solvents. Indeed, the highest excesses were recorded for the bulkiest: 3,5-di-*tert*-butyltoluene (45 %). This is probably because bulkier solvents have difficulty entering the pores of **CC3** and, as a consequence, are unable to displace or compete with the guest of interest. This is creates a 'voids in slurry' effect wherein guests exchange with **CC3** with minimal solvent interruption.[139] In the context of these studies, this observation was particularly useful because it identified solvents that evenly distribute guests among the host without affecting the host-guest interaction.

Further measurements were performed using 1-*tert*-butyl-3,5-dimethylbenzene as a solvent. This was chosen in preference to 3,5-di-*tert*-butyltoluene, which produced slightly higher excesses, because, at the time of experimentation, it was about 10x cheaper. The use of 1-*tert*-butyl-3,5-dimethylbenzene significantly improved reproducibility when compared with solvent-free measurements; however, calibration fits were still not to an acceptable standard ($R^2 > 0.99$). The GC instrumentation was the
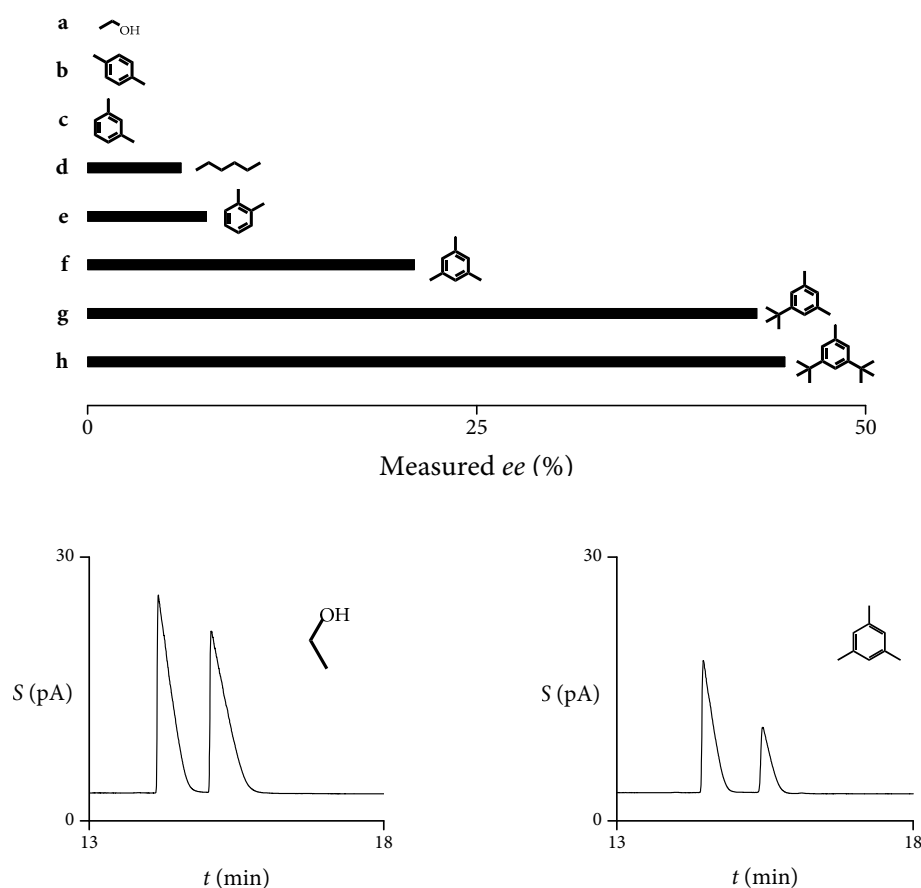
Figure 3-5 | Effect of solvent on measured *ee* values. Top: measured enantiomeric excesses of *rac*-1-PE from selective adsorption experiments conducted in 8 different solvents: ethanol (**a**), *p*-xylene (**b**), *m*-xylene (**c**), hexane (**d**), *o*-xylene (**e**), mesitylene (**f**), 1-*tert*-butyl-3,5-dimethylbenzene (**g**), 3,5-di-*tert*-butyltoluene (**h**). Bottom: example GC-FID headspace chromatograms after mixing **CC3**-*R* with *rac*-1-PE dissolved in either ethanol (bottom-left) or mesitylene (bottom-right).

suspected source of this error, which was corrected for with the addition of bromo-mesitylene as an internal standard.[117] Bromomesitylene was chosen because, like 1-*tert*-butyl-3,5-dimethylbenzene, it is likely to be too large to enter the pores of **CC3**. With this change, fitting quality greatly exceeded previous measurements. In most cases, $R^2 > 0.999$ was achieved in subsequent calibration fits.

These changes are implemented in subsequent analyses presented in this Chapter. In most cases, activated **CC3** samples were exposed to stocks of guests dissolved in 1-*tert*-butyl-3,5-dimethyl benzene containing small (<2 mg mL^{-1}) quantities of bromo-mesitylene. The resulting slurries were then stirred overnight and filtered. The filtrates were analysed by static-headspace GC-FID to determine the quantity of guest remaining (see Experimental Section 7.2.1, p103, for analysis method).

3.3   Explaining Selective Sorption Behaviour

With this improved technique, values such as the moles of **CC3** (n_{CC3}), the added stock concentration (c_a), the added stock volume (V) and the guest concentration after adsorption (c_m) were known to a high degree of accuracy and, using these, several additional metrics were calculated.

The percentage of guest adsorbed (Equation 3-1) showed the efficacy of adsorption and the remaining guest in solution after adsorption. Discussions of selectivity and thermodynamic competition shall primarily use this metric (e.g. Figure 3-6). In later discussions, sorption behavior is rationalised by using modelling and crystallography, two host-centric techniques that tend to generate molecular-scale values. Accordingly, two host-centric measures of adsorption behaviour were also calculated: equivalents adsorbed (Equation 3-3) and the enantiomeric excess of guests within the host (ee_{host}, Equation 3-4). The former described uptake relative to the moles of cage. The latter provided a host-centric perspective of selectivity.

These metrics were valuable when attempting to understand the host-guest behaviour of **CC3**. To simplify rationalizations, two assumptions were made. First, adsorption was likely to be an exothermic but entropically unfavourable process. Second, adsorption (Scheme 3-1a) and substitution (b) were assumed to describe most of the interactions occurring and other, more complicated, processes may be ignored.

Adsorption (Scheme 3-1, **a**) should dominate when the host contains empty sites and depletes the solution phase of guests that would otherwise exchange with adsorbed guests. While the adsorption enthalpy for one guest may be larger than another, the adsorption of both guests is strongly favoured. Because of this, adsorption-dominated processes are likely to observe weaker selectivity.

$$\text{Percent of Guest Adsorbed} = \frac{c_m}{c_a} \times 100 \qquad \text{Equation 3-1}$$

$$n_{ads} = (c_a - c_m)V \qquad \text{Equation 3-2}$$

$$\text{Equivalents Adsorbed} = \frac{n_{ads}}{n_{host}} \qquad \text{Equation 3-3}$$

$$ee_{host} = \frac{nR_{ads} - nS_{ads}}{nR_{ads} + nS_{ads}} \times 100 \qquad \text{Equation 3-4}$$

$$\textbf{b}\quad \Delta H_{\text{substitution}}$$

$$[\text{Host}][\text{A}] + \text{B} \xrightarrow{\hspace{3cm}} [\text{Host}][\text{B}] + \text{A}$$

$$\textbf{a}\quad \Delta H_{\text{des}}\,\text{A} \qquad\qquad \textbf{c}\quad \Delta H_{\text{ads}}\,\text{B}$$

$$\text{Host} + \text{A} + \text{B}$$
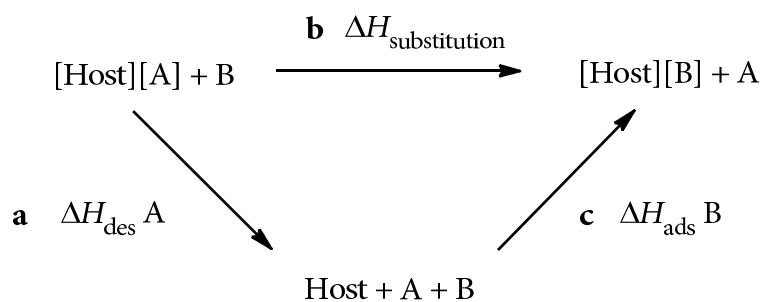
$$\Delta H_{\text{substitution}} = \Delta H_{\text{des}}\,\text{A} + \Delta H_{\text{ads}}\,\text{B}$$

$$\Delta H_{\text{des}} = -\Delta H_{\text{ads}}$$

$$\Delta H_{\text{substitution}} = \Delta H_{\text{ads}}\,\text{B} - \Delta H_{\text{ads}}\,\text{A}$$

Scheme 3-1 | Substitution may be calculated in terms of differences between adsorption enthalpies. In the case of the **CC3**-*R* acting as a host for 1-PE, adsorption is thermodynamically preferred both enantiomers, so both should be adsorbed non-selectively. However, when substitution becomes the dominant process, the greater adsorption enthalpy of (*R*)-1-PE when compared with (*S*)-1-PE leads to selectivity. This is because the enthalpy change of substitution is affected by the difference, rather than the absolute value of, adsorption enthalpies between two guest pairs.

Guest substitution (Scheme 3-1, **b**) should dominate when host sites are filled and sufficient guest remains in the solution phase. Unlike adsorption, substitution couples two host-guest systems. Because the enthalpy of substitution is the difference between the adsorption enthalpy of the incoming guest and the desorption enthalpy of the evacuated one (Scheme 3-1, bottom), the equilibrium position of substitution is acutely affected by the differences of adsorption/desorption enthalpies between two guests. Consequently, substitution-dominated processes should observe stronger selectivity than adsorption-dominated processes.

Measurements were performed to investigate these hypotheses (Figure 3-6). They measured the amount of 1-PE adsorbed (black lines), measured *ee* (red lines), and in-host *ee* (blue lines) at various mixing times (Figure 3-6, a), mixing temperatures (b) and ratios of *rac*-1-PE to **CC3**-*R* (c). These measurements underlined the usefulness of calculated metrics as directly measured excesses tended to give a misleading impression of selectivity. For example, the highest measured excesses were recorded at the longest mixing times; however, calculations indicated the opposite effect on selectivity within the host. Adsorbance measurements helped explain this observation: up to 82 % of the available 1-PE was adsorbed at lower ratios so, while directly measured

excesses were high, they only represented the 18 % of 1-PE that remained in solution after depletion.

In-host excesses trended downward with increasing mixing time (Figure 3-6a). This is likely to be a consequence of 1-PE diffusion into **CC3**-*R* particles. At short times, few 1-PE molecules had adsorbed into the **CC3**-*R* particles while the majority
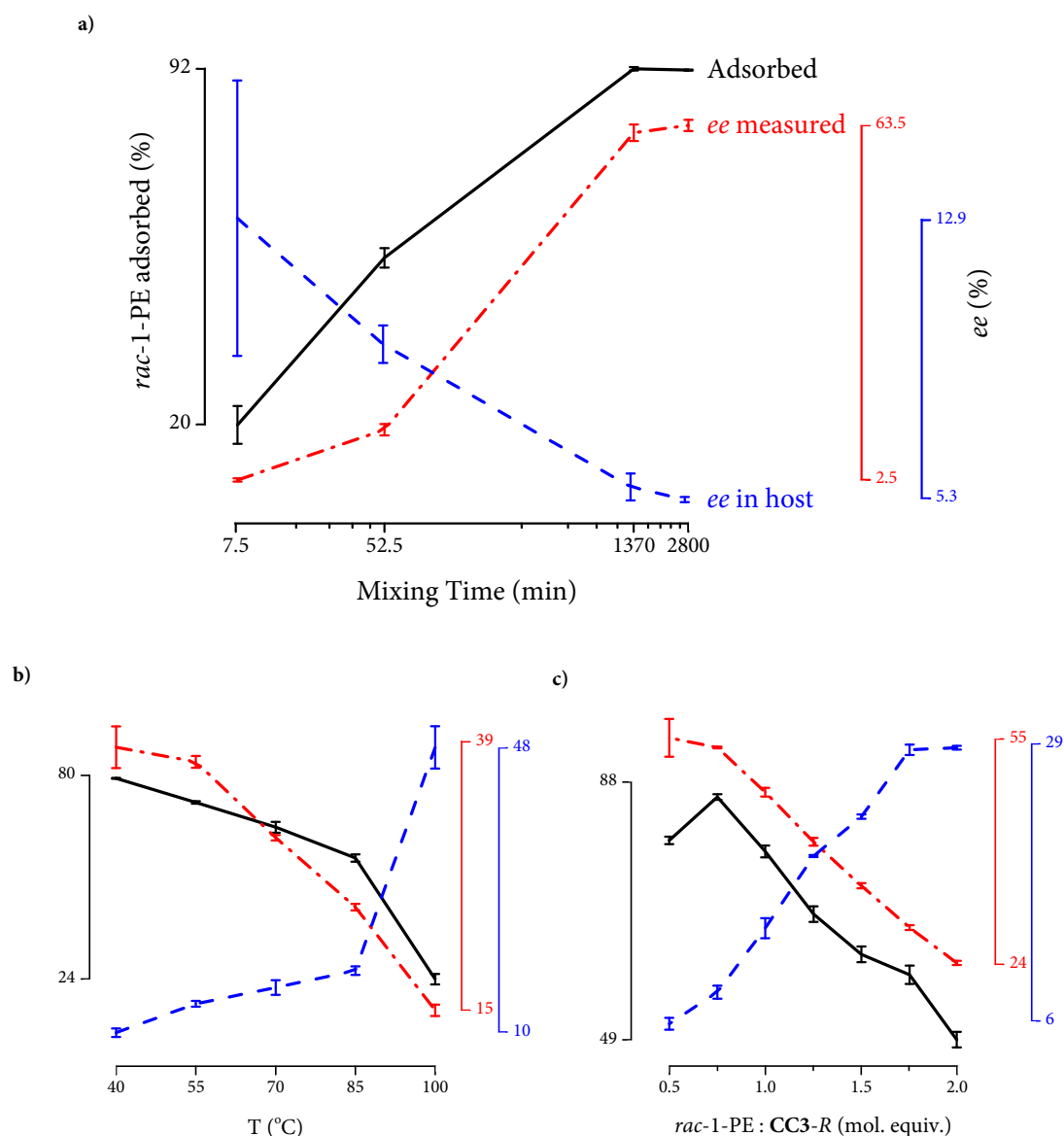
Figure 3-6 | Effect of experimental conditions on the adsorption of *rac*-1-PE into CC3-*R*. The effect of mixing time (**a**), mixing temperature (**b**), and equivalents of 1-PE (**c**) on the percentage of guest adsorbed (black lines), measured *ee* values (red lines), and calculated in-host ee values (blue lines) were investigated. Adsorbance and measured ee follow the same trend but in-host excesses are opposite. Explanation of each trend is provided in the main text.

remained in solution. In this scenario, the substitution of 1-PE molecules with the particles' surfaces dominated and, consequently, in-host excesses were high. After further mixing, adsorption dominated by indiscriminately depleting the solution of 1-PE which accordingly decreased in-host excesses. The trend of decreasing selectivity appeared to stop once particles were saturated and the system had reached equilibrium.

In-host excesses trended upwards with increasing temperature (Figure 3-6b). This was likely to be a consequence of increased 1-PE desorption at raised temperatures. Adsorption is an entropically unfavourable process, consequently, increasing temperature favoured desorption (black line trended downward). While this lowered the overall uptake of 1-PE, it increased the proportion of 1-PE molecules in solution to engage in substitution processes, which increased in-host excesses. The trend of increasing selectivity may continue up to a temperature where adsorption becomes a non-spontaneous process or, more likely, the host decomposes. However, the proportion of adsorbed 1-PE would have been negligible before that point.

In-host excesses trended upwards with increasing *rac*-1-PE:**CC3**-*R* ratios (Figure 3-6c). At lower ratios, adsorption dominated by indiscriminately depleting the solution of available 1-PE to fill vacant **CC3**-*R*, which led to low in-host excesses. At higher ratios, there was adequate 1-PE available to fill the **CC3**-*R* with enough remaining for subsequent substitution processes to dominate, which accordingly increased in-host excesses. This trend of increasing excesses appeared to taper off from a 1.75 *rac*-1-PE:**CC3**-*R* ratio which indicated that excesses would eventually converge to a value that is representative of the substitution mechanism's equilibrium point.

Across all three investigations, measured *ee* values (red lines) trended upwards with adsorption (black lines) while in-host *ee* values (blue lines) followed the opposite trend. This reinforced the hypothesis that, in order to optimise selectivity, guest substitution should be maximised. Overall, quantitative development enabled this phenomenon to be measured; however, these approaches were unable to elucidate the molecular source of selectivity. The inclusion of crystallographic and computational techniques was a further requirement to achieve that.

3.4   Modelling CC3's Enantioselective Sorption Behaviour

Computational modelling, performed by Dr Linjiang Chen, calculated the source of selectivity to be preferred intramolecular interactions, including the formation of a hydrogen-bond, between **CC3**-*R* and (*S*)-1-PE which do not exist for **CC3**-*R* and (*R*)-1-PE (Figure 3-7). This difference in host-guest interactions results in different association enthalpies for each enantiomer when interacting with homochiral **CC3** and explained the observed selectivity effect.

Models provided a valuable insight into the measured host-guest behaviour. However, further experimental measurements were necessary to reinforce the conclusions of these computational studies. In both models and in previous discussions, there were series of assumptions about how **CC3** behaves during adsorption that required further experimental validation (Table 3-2).
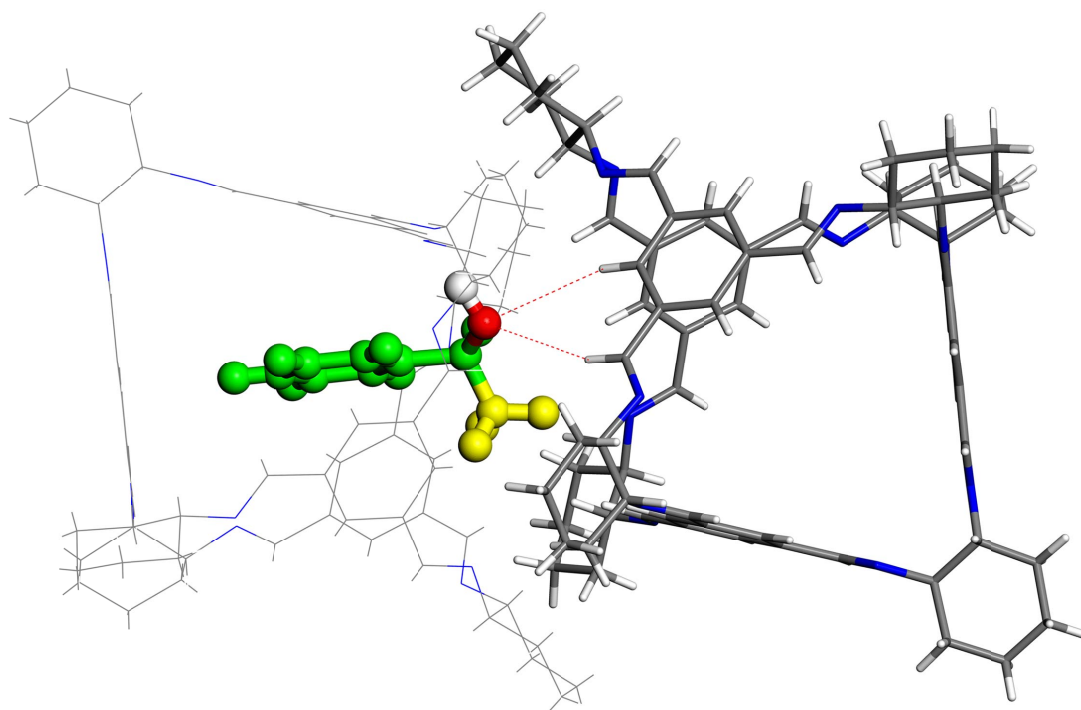
**Figure 3-7 | Computational models indicated the source of selectivity.** Structure of a (*S*)-1-PE molecule between two **CC3**-*R* molecules. Models indicated that the observed chiral separation effect was a consequence of favourable intermolecular interactions between (*S*)-1-PE and **CC3**-*R*, including the formation of a hydrogen bond (dotted red lines), that were not formed between (*R*)-1-PE and **CC3**-*R*.[66]

Table 3-2 | The available explanations of the host-guest behaviour of cages depended on a series of assumptions about how they behave. Experiments were devised to validate these assumptions.

CC3 Behaviour	Experimental Measurement of Behavior
Host-guest exchange does not involve the formation of any chemical bonds	Chemical analysis (NMR, FTIR) of the cage solid after adsorption
As a consequence of above, host-guest formation should be reversible	Attempt to remove guest occupants by exclusion with excess solvent or heating under vacuum
The crystal phase of **CC3** remains unchanged by adsorption	Crystallographic analysis of **CC3** after adsorption *and* desorption (above) of the guest
CC3-*R* has the exact opposite chiral selectivity of **CC3**-*S*	Perform technique on both **CC3**-*R* and **CC3**-*S* in parallel
rac-**CC3** does not observe any chiral selectivity and still adsorbs guests, although non selectively (as above)	Perform GC measurements on *rac*-**CC3**
Although *rac*-**CC3** should observe uptake (as above) its co-crystalline form may observe different uptake from enantiopure **CC3**	Perform measurements on **CC3**-*R+S*, an equal mixture of **CC3**-*R* and **CC3**-*S*. Compare these results with those for co-crystalline *rac*-**CC3**
CC3 remains in the solid phase	Find proportion of **CC3** in the solution phase by HPLC analysis
Calculated in-host excesses are representative of true in-host excesses and may be directly compared with models	Calculate in-host excesses from guest-depleted filtrates *and* analyze the excesses of filtrates used to desorb guests

A workflow was designed to experimentally validate these assumptions (Figure 3-8, p110 for detailed explanation). In the workflow, **CC3** samples were activated (Figure 3-8, step **1**) and a solution of *rac*-1-PE in 1-*tert*-butyl-3,5-dimethylbenzene added (**2**). Vials were sealed and stirred overnight (**3**) and subsequent filtration (**4**) yielded *guest-depleted* filtrates and *guest-adsorbed* solids. In some cases, guests were desorbed from guest-adsorbed solids by repeating the process (from step **2**) with excess acetonitrile to yield *extracted-guest* filtrates and *guest-desorbed* solids. Overall, this approach yielded both solid- and solution-phase samples after guest-adsorption and guest-extraction processes. Four forms of **CC3** were investigated: **CC3**-*R*, **CC3**-*S*, *rac*-**CC3**, and **CC3**-*R+S* (an equimolar mixture of **CC3**-*R* and **CC3**-*S*). Measurements were performed in triplicate across seven different *rac*-1-PE:**CC3** ratios.
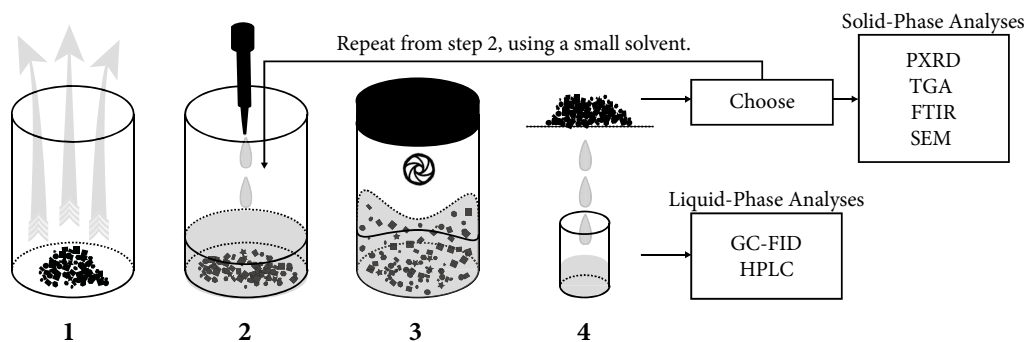
Figure 3-8 | Experimental workflow for performing and analysing host-guest exchange. Host compounds are degassed (**1**), guest solutions are added (**2**) followed by mixing overnight (**3**) and separating host-guest adducts by filtration (**4**) to yield guest-depleted filtrates and guest-desorbed solids. For some samples, the process was repeated from step **2** with acetonitrile to yield extracted-guest filtrates and guest-desorbed solids.

GC measurements on guest-depleted filtrates were similar to previous discussions; however, the four forms of **CC3** could be directly compared within a single experiment (Figure 3-9). As with previous measurements, there existed some impurity peaks in the baseline. These were straightforwardly removed by background subtraction. Encouragingly, **CC3**-*R* and **CC3**-*S* produced precisely mirrored enantiomeric excesses while *rac*-**CC3** produced no measurable excess. The equivalents adsorbed for each sample were calculated from these measurements (Equation 3-3, p49). The resulting trends are plotted in Figure 3-12.

Guest-excluded filtrates, which contained guests excluded from within the host after an acetonitrile washout, were also measured by GC-FID (Figure 3-10). Unlike measurements on guest-deprived solutions where in-host excesses must be subsequently calculated, guest-excluded filtrates directly represented in-host excesses. However, only enantiomeric excesses could be used from these measurements as the washout and filtration processes precluded accurate quantification. Specifically, the bromomesitylene peak, which is used to quantify uptake, was invalidated by the filtration and washout steps.

In guest-excluded washouts, bromomesitylene was observed to have a greatly reduced signal relative to 1-PE. The observed weak signal indicated that bromomesitylene had, as hypothesised, difficulty adsorbing into **CC3**, which reinforced the viability of using it as a non-interrupting internal standard. Its adsorption is likely to be even lower than measured because much of the recorded signal is from surface residue – bromomesitylene's high boiling point and viscosity prevented its removal by filtration.
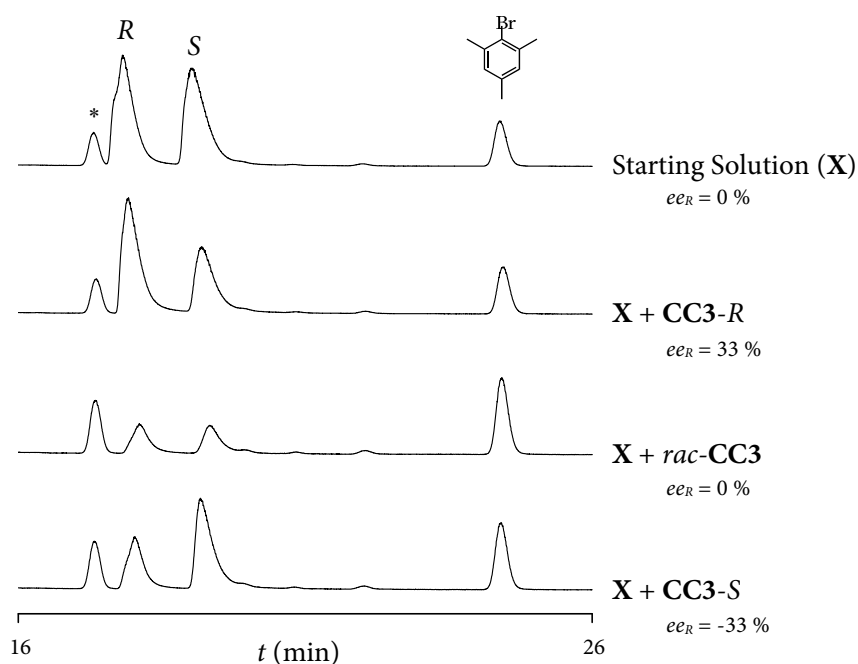
Figure 3-9 | GC-FID chromatograms of guest-deprived filtrates. The 1-PE (enantiomers labelled) in these plots is representative of what was left in the solution phase after adsorption into **CC3**. Equal and opposite enantiomeric excesses were observed for **CC3**-*R* and **CC3**-*S*. *rac*-**CC3** yielded no enantiomeric excess, but peaks were still diminished in intensity relative to the bromomesitylene internal standard. The effects of impurities, such as the impurity marked with an asterisk, were removed by subtraction. Full chromatogram in Appendix (p139).
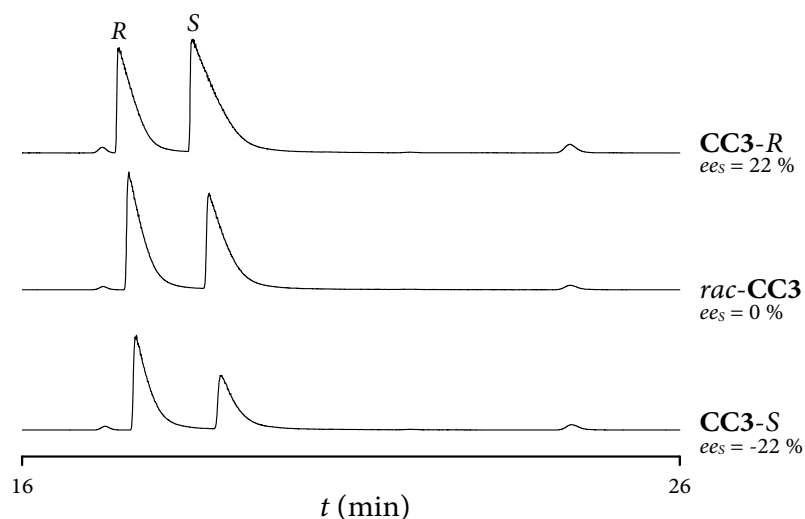
Figure 3-10 | GC-FID chromatograms of guest-extracted filtrates. As acetonitrile washed out the majority of adsorbed 1-PE within **CC3**, the 1-PE in these plots is representative of what was adsorbed in **CC3** after equilibration with a 1-PE solution. Equal and opposite enantiomeric excess were observed for **CC3**-*R* and **CC3**-*S*. Values measured in this manner are plotted as solid lines in Figure 3-12. Full chromatogram in Appendix (p140).

While quantifying adsorption from analysis of guest-excluded filtrates is difficult, measured *ee* values are more likely to be representative of in-host excesses than back-calculated values. However, on comparing indirectly-calculated to directly-measured values, both methods appeared to produce similar results (Figure 3-11). Differences are likely to be a consequence of the indirect nature of back-calculated values, which relied on several metrics which were difficult to calibrate.

As discussed previously, higher guest:host ratios produced higher selectivities. Likewise, the same observation was made in this study but direct comparisons between different forms of **CC3** could be made (Figure 3-12). The measured selectivities (solid lines) of **CC3**-*R* were opposite to **CC3**-*S* while *rac*-**CC3** and **CC3**-*R+S* showed no selectivity. Overall, excesses appeared to begin to taper off around 30 %, which is in agreement with computationally derived values (Figure 3-18, p64). For homochiral **CC3** samples, which are soluble in deuterated solvents, the amount adsorbed matched values from ¹H NMR measurements (Figure 3-14).
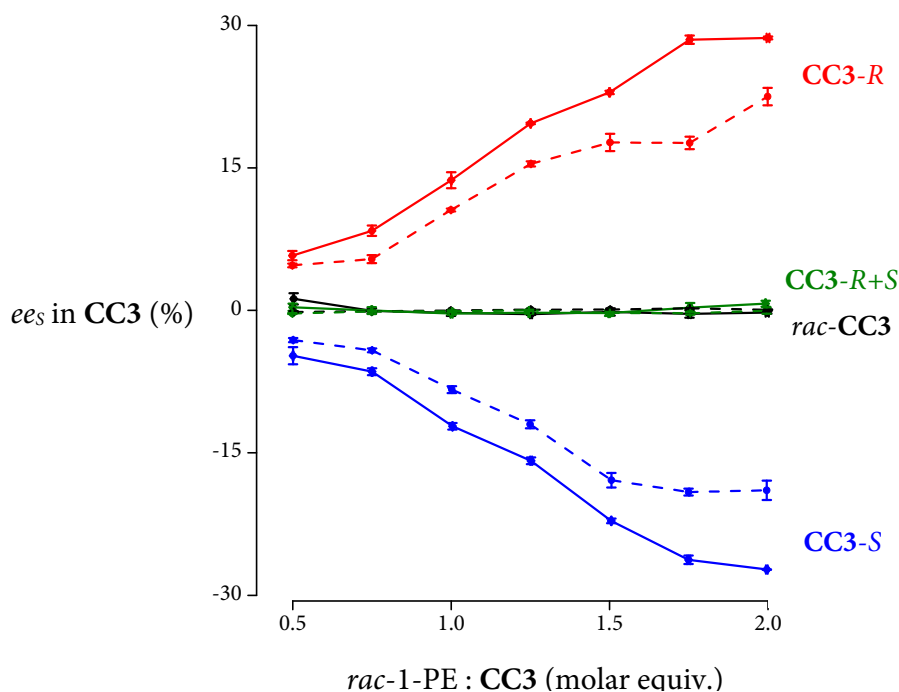

Figure 3-11 | Calculated vs measured concentration dependence. Solid lines: measured values of in-host excess from guest-excluded filtrates. **Dashed lines**: back-calculated in-host excesses from guest-deprived filtrates (using Equation 3-4, p49).
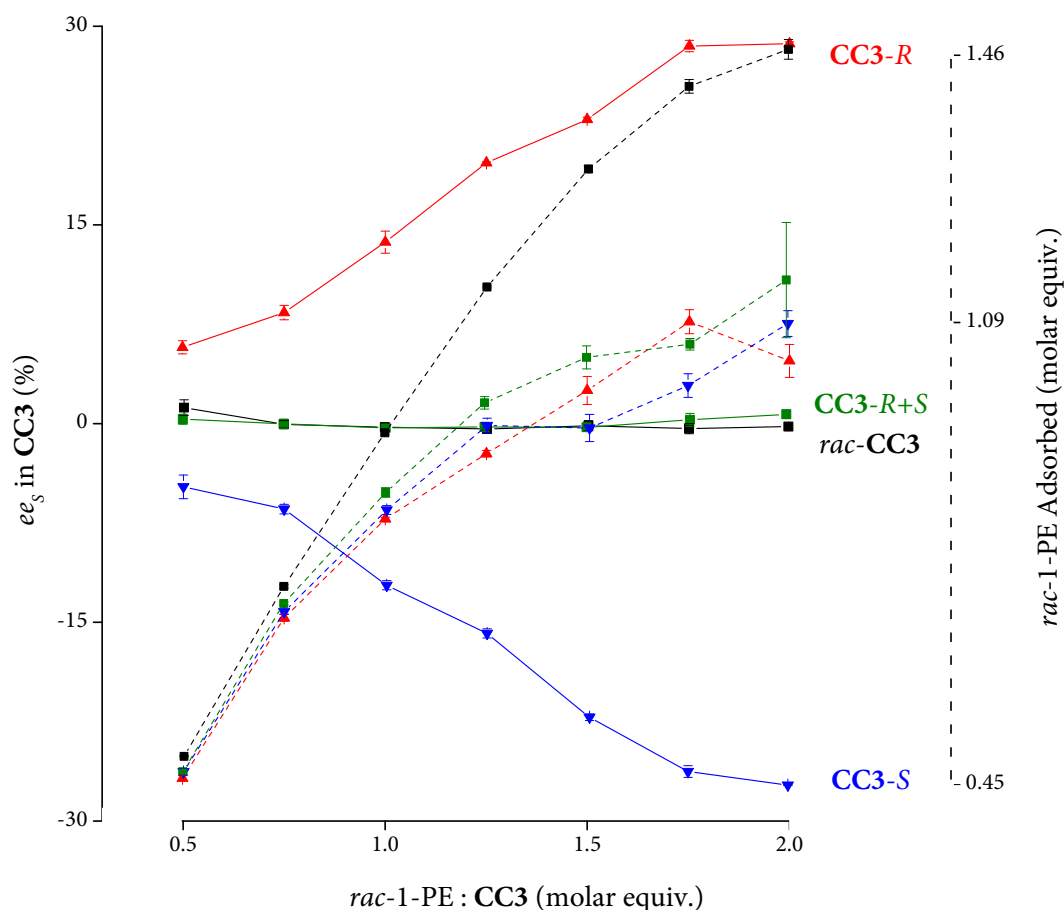
Figure 3-12 | The effect of *rac*-1-PE:CC3 ratio on in-host excesses (solid lines) and equivalents of *rac*-1-PE adsorbed (dotted lines). Four forms of **CC3** are presented: **CC3**-*R* (red lines), **CC3**-S (blue lines), *rac*-**CC3** (black lines), and **CC3**-*R+S* (green lines). Approximately equal and opposite excess values were measured for **CC3** enantiomers. Near-zero excesses were observed for *rac*-**CC3** and **CC3**-*R+S*. A similar level of guest adsorption, with an average maximum of 1.09 equivalents, was measured for all but *rac*-**CC3**. The higher maximum adsorbance measured for *rac*-**CC3** (1.46 equivalents) is likely due to its more rapid crystallisation process, which produced smaller particles and an increased level of voids/defects in the solid, as described previously.[50]

Differing uptake values (Figure 3-12, dotted lines) were observed for *rac*-**CC3**, which reached 1.46 equivalents of 1-PE per cage. The other forms of **CC3** reached an average of 1.09 equivalents. A more rapid crystallisation process is used to synthesise *rac*-**CC3** which results in increased voids/defects in its solid-phase structure and a smaller particle size.[50] This could explain why *rac*-**CC3** was capable of adsorbing a greater amount of 1-PE; however, greater adsorption could also have been due to *rac*-**CC3**'s lower solubility in the guest mixtures.

HPLC was therefore used to measure the amount of **CC3** dissolved in guest-deprived solutions (Figure 3-13). While *rac*-**CC3** was not detectably soluble (black line), the
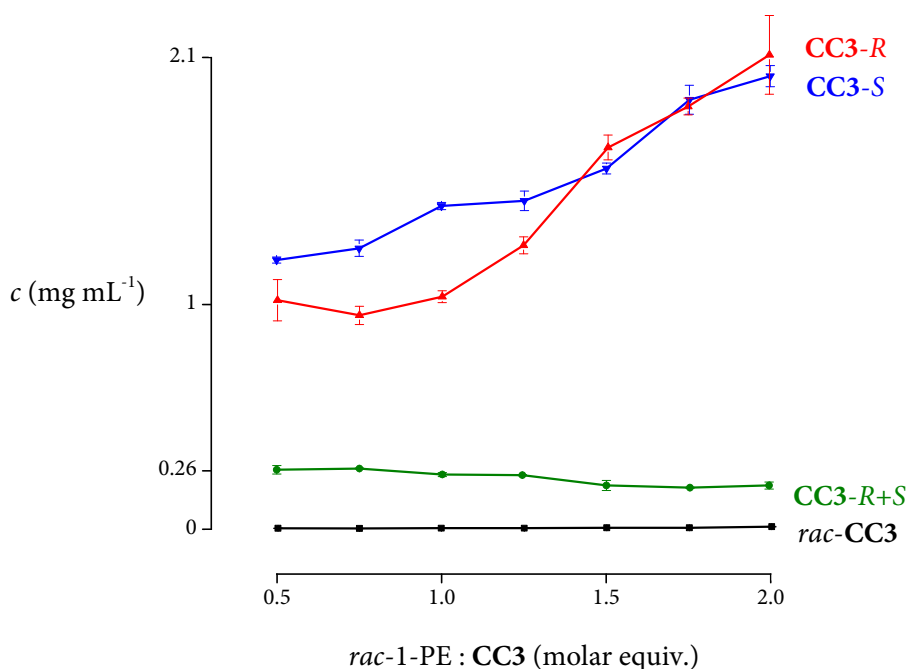
Figure 3-13 | CC3's solubility in 1-PE solutions at different *rac*-1-PE:CC3 ratios. The solubility of **CC3**-*R* in pure 1-*tert*-butyl-3,5-dimethylbenzene solvent is 0.67 mg mL^{-1}. **CC3** is normally poorly soluble because the solvent has difficulty entering **CC3**'s pores; however, because it can fit, 1-PE appears to affect the solubility of homochiral **CC3** species. *rac*-**CC3** is in an insoluble form of **CC3**; accordingly, the presence of 1-PE appears to have no effect. The chiral conglomerate, **CC3**-*R+S*, does dissolve slightly but, upon dissolution, it begins to form insoluble *rac*-**CC3**, preventing it from reaching equivalent concentrations to the homochiral forms.

dissolution of homochiral **CC3** appeared to be dependent on the equivalents of 1-PE (red and blue lines). Experiments indicated that the solubility of **CC3**-*R* in pure 1-*tert*-butyl-3,5-dimethylbenzne solvent is only 0.7 mg mL^{-1} (experiment 7.2.3.10, p111), which is likely because it is too large to maximise its surface interaction with the internal void of **CC3**. However, because it does fit in the cage, 1-PE was capable of aiding dissolution. Non-racemic forms of **CC3** dissolved to a maximum concentration of 2.1 mg mL^{-1}, around 7 % of the available solid. This effect is insufficient to account for the difference in adsorption between homochiral and racemic species by itself, so it is likely that the difference is a combination of this effect and the aforementioned difference of surface area between the species.

A further observation is that the solubility of **CC3**-*R+S* appeared to be invariant to the amount of 1-PE, dissolving to a mean concentration of 0.26 mg mL^{-1} (Figure 3-13, green line). However, this is slightly misleading since the chiral conglomerate is likely to spontaneously form insoluble *rac*-**CC3** precipitates upon dissolution. Indeed, experimental observations noted a slight cloudiness in higher-equivalent samples,

which was likely to the *rac*-**CC3** precipitate. However, because a small quantity of precipitate was produced, it was not possible to confirm that the solid was entirely *rac*-**CC3**. However, this explanation would account for the marginally higher adsorption of **CC3**-*R+S* compared to homochiral samples (Figure 3-12, green dotted line).

While the partial dissolution of **CC3** is concerning, it did not significantly affect the general observations presented. The subsequent application of this separation effect could avoid dissolution entirely by chemically bonding to a support, crosslinking, or, as reported in Chapter 4, performing solvent-free gas-phase separations.

Another point of interest is whether host-guest exchange involved any irreversible chemical changes in the host. ^{1}H NMR measurements indicated no such changes (Figure 3-14). The *rac*-1- PE guest appears to introduce additional chemical environments into the spectrum without affecting **CC3**'s. An absence of chemical changes in **CC3** was further supported by FTIR and TGA measurements (appendix, p141-142).
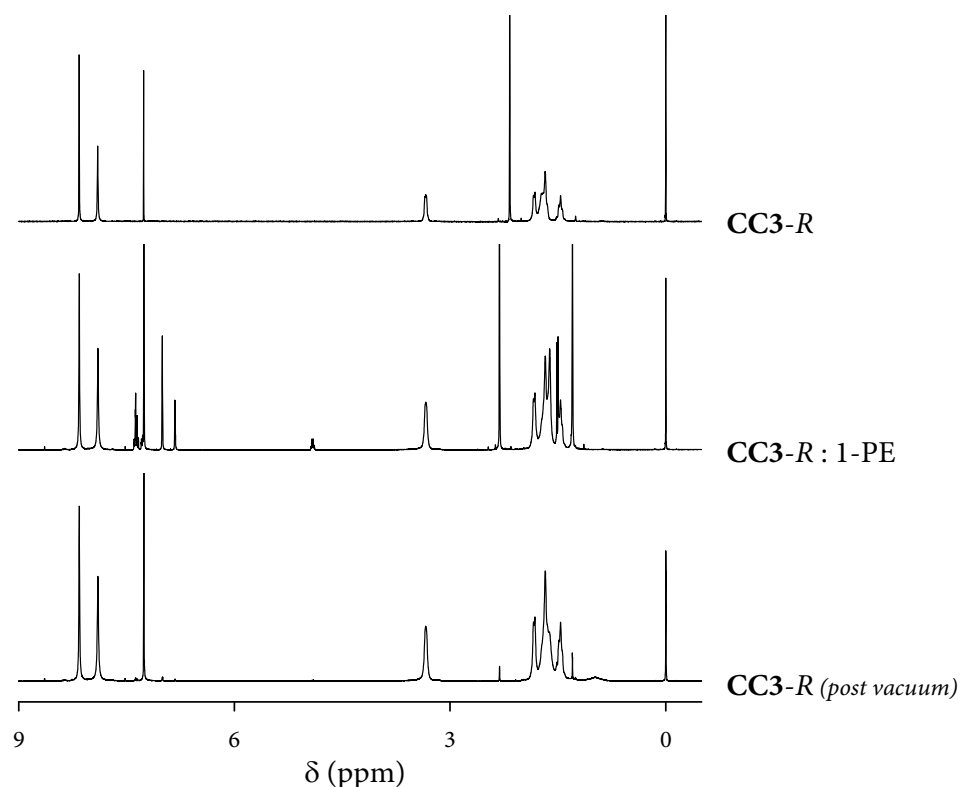
Figure 3-14 | ^{1}H NMR (CDCl₃) spectra of CC3-*R* at different stages of host-guest exchange. 1.5 1-PE:**CC3**-*R* equivalents were present for the exchange process of these representative samples. **CC3**-*R*, 1-PE, and residual 1-*tert*-butyl-3,5-dimethylbenzene solvent were observed after mixing (middle). Vacuum oven treatment removed 1-PE and the solvent with no observable chemical changes in **CC3**-*R* (bottom). Integration of the –CH_2 peak of 1-PE (4.9 ppm) against the CH=N peak of **CC3**-*R* (8.2 ppm) showed a ratio of 0.98:1 guest:host. This compares well with the ratio of 1.00:1.00 guest:host obtained from GC measurements (Figure 3-12).

There is also a possibility that the observed selectivity was a consequence of a enantioselective diastereomer recrystallisation. Encouragingly, PXRD measurements indicated that the crystal phase of **CC3** remained the same throughout the process (Figure 3-15). SEM analysis of the samples further reinforced this observation and indicated that, while the exchange process appeared to wash away small debris, it did not significantly alter the overall crystal morphology of **CC3** (Figure 3-16).

scXRD techniques were also utilised to measure the crystallographic properties of **CC3** during guest exchange. In these measurements, single crystals of **CC3** were soaked in homochiral 1-PE and analysed. As found with PXRD measurements, the crystal phase of **CC3** did not measurably change when 1-PE is present. Additionally, while 1-PE molecules were disordered within the structure of **CC3**, preventing their refinement, electron count calculations indicated that approximately 1.15 equiv. of 1-PE molecules were present per **CC3** molecule, which is close to saturation values found by the GC-FID measurements (*c.a.* 1.05 equiv.).
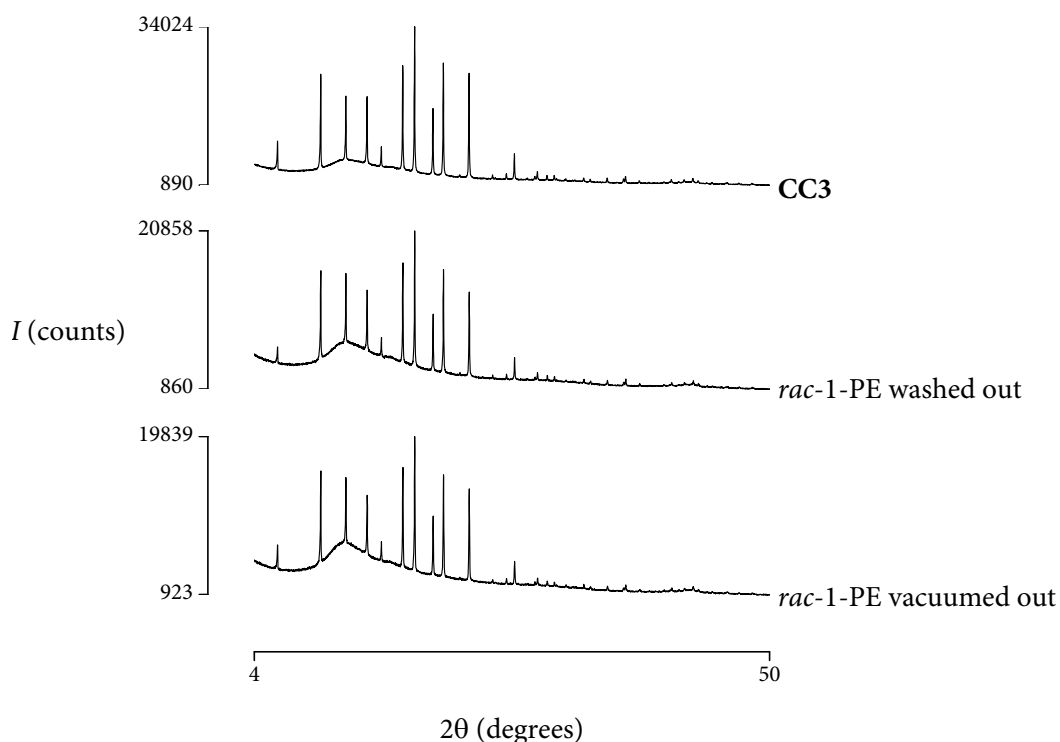

Figure 3-15 | Phase stability of CC3 during host-guest exchange. PXRD patterns of **CC3**-*R* before separation experiments (top); after 1-PE removal washout and drying (middle); and after 1-PE removal by exposure to vacuum (bottom). Patterns remained largely unchanged throughout the process, indicating that no phase change was induced by the adsorption and subsequent desorption of 1-PE.

CC3-*R*   *rac*-**CC3**   **CC3**-*S*

Before Host-Guest Exchange

After Removing 1-PE Guest with Acetonitrile
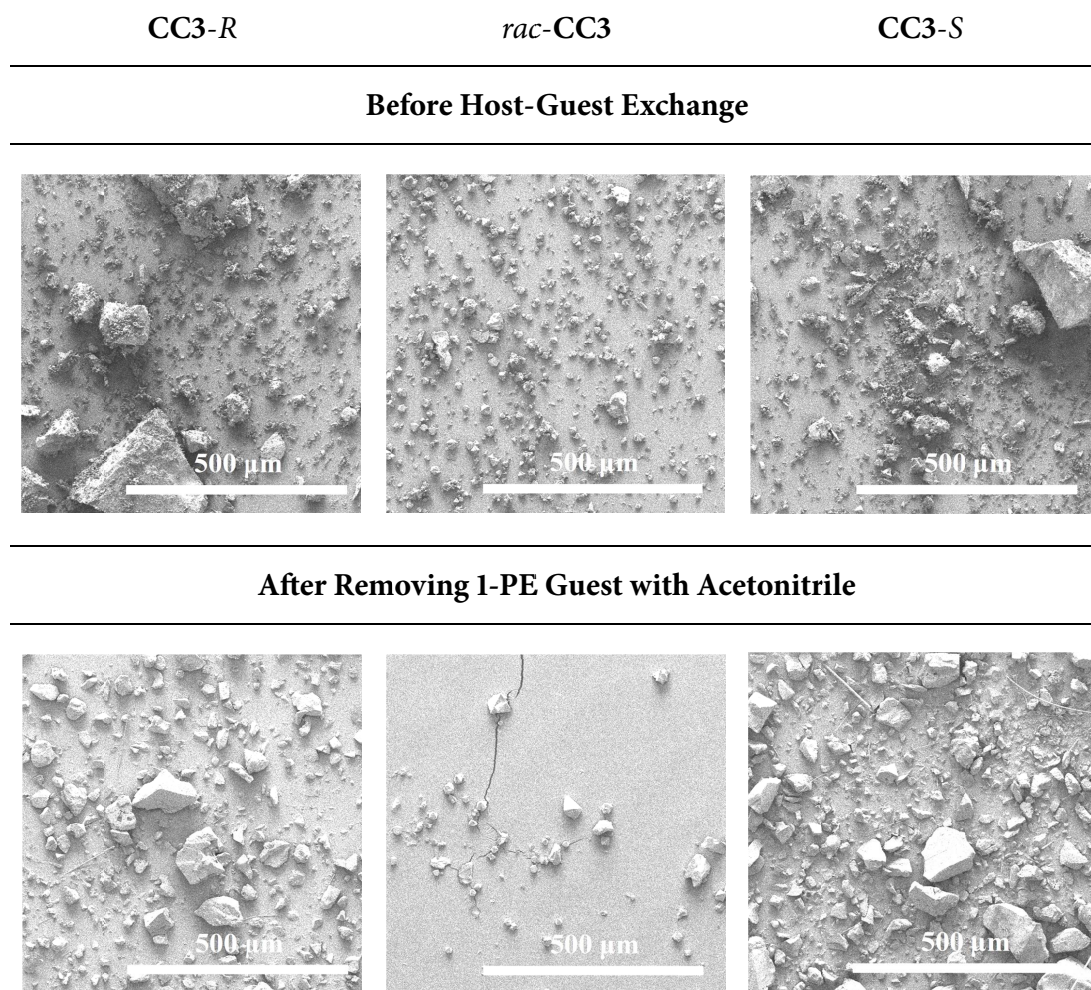
Figure 3-16 | SEM images of CC3 samples before host-guest exchange and after guest washout. SEM images of **CC3**-*R* (left), *rac*-**CC3** (middle) and **CC3**-*S* (right) before mixing with 1-PE solutions (top) and after washing the resulting guest-adsorbed solid samples with acetonitrile (bottom). Overall, the morphology and particle size of **CC3** was not substantially affected by host-guest exchange. It is likely that the lower amount of small debris was due to their removal during the filtration process wherein they became trapped in or (smaller particles) passed through the filter.

Overall, analyses reinforced the assumption that the host-guest process occurred because of enantioselective hydrogen bond formation that did not chemically, crystallographically, or morphologically alter the **CC3** host. Consequently, computational models which used these assumptions aligned well with experimental measurements. For example, in-host enantiomeric excesses, which had similar values across multiple experimental measurement techniques (Figure 4-11), were close to computationally calculated values (Figure 3-18). Alignment with computationally derived values is particularly exciting as the computational methods could be further utilised to discover other guest mixtures that **CC3** can separate.
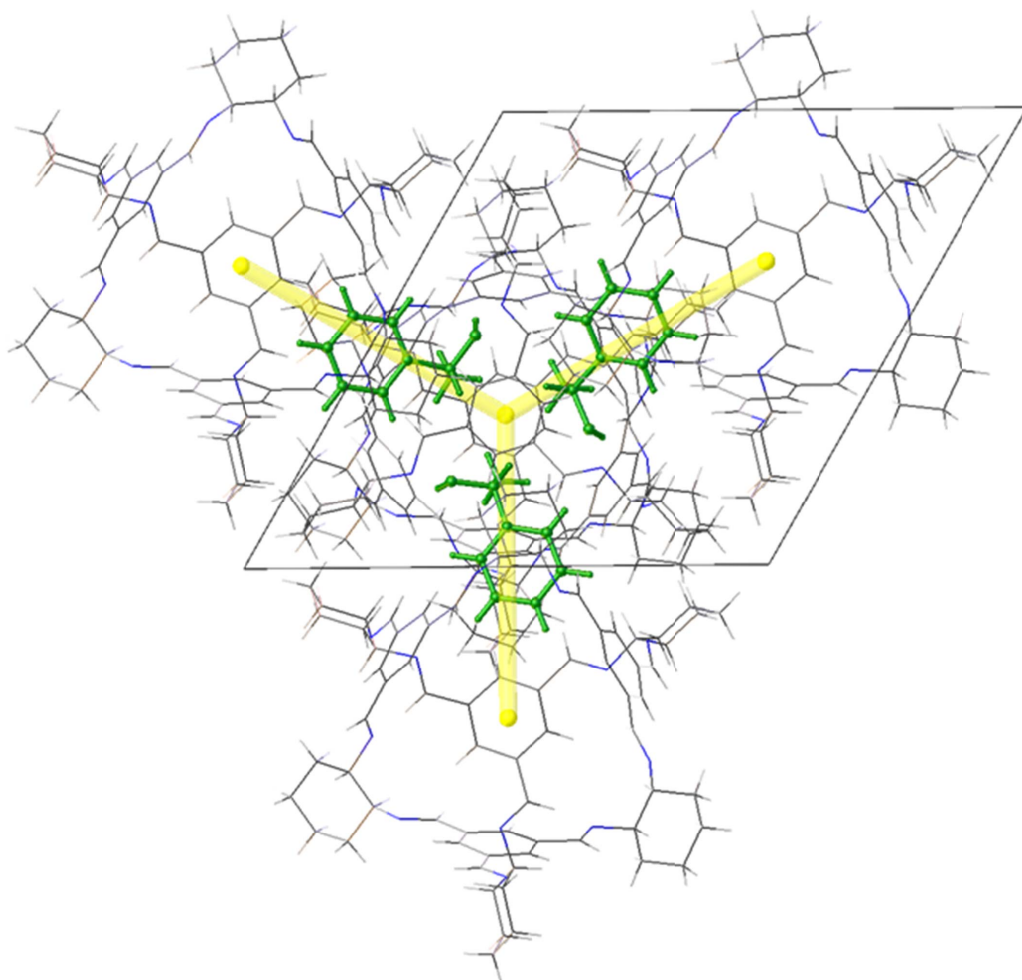
Figure 3-17 | Structural analysis of 1-PE adsorbed into CC3. Structures elucidated from single-crystal XRD analysis of a guest-adsorbed phase. The carbon atoms of 1-PE have been highlighted in green; however, these positions are representative since the precise arrangement of disordered 1-PE within the structure could not accurately be refined. The diamondoid network of **CC3** is shown in yellow. Electron count calculations indicated that approximately 1.15 1-PE molecules are present per **CC3** molecule, which is close to the 1:1 ratio that was measured experimentally. *Structure obtained by Dr Marc Little.*
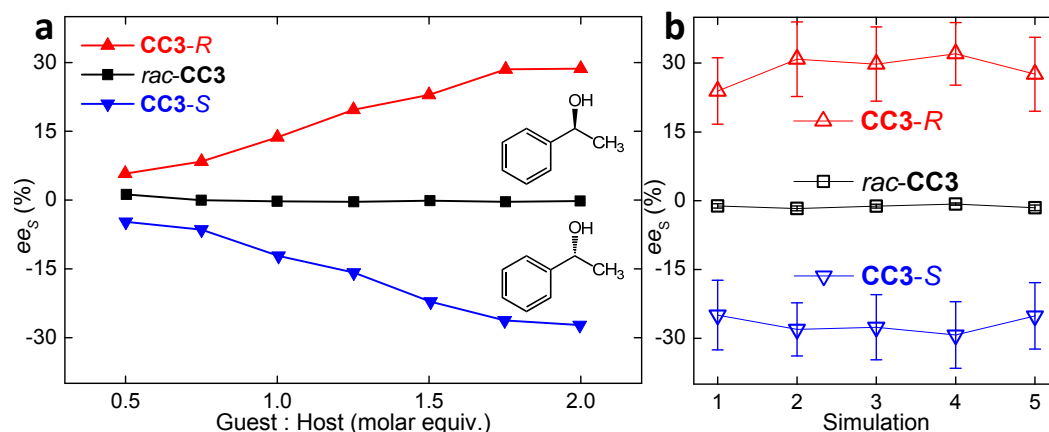
Figure 3-18 | Experimental and simulated enantiomeric excesses of 1-PE adsorption into CC3. a (left plot), Measured ee_S of 1-PE washed out of **CC3** over a range of guest:host ratios. **b** (right plot), Simulated ee_S obtained from advanced configurational-bias Monte Carlo simulations for 1-PE in the **CC3** host. All simulations were carried out at ambient temperature and pressure. Simulated maximum guest loadings and ee_S for 1-PE in **CC3** correspond closely with experimental observations at a guest:host ratio of 2. Five independent simulations were performed in each case. Figure reprinted from a resulting publication.[66]

3.5   Conclusions & Outlook

A screening method was developed and used to find several mixtures that selectively adsorb into **CC3**. It identified that **CC3** is shape selective towards the isomers of xylene (Figure 3-2, p44) which corroborates previous studies by the Cooper group.[49] Additionally, **CC3**-*R* was measured to selectively adsorb the enantiomers of several racemates, which had not previously been observed (Figure 3-3, p46).

A quantitative procedure to measure selectivity was subsequently developed. It used 1-*tert*-butyl-3,5-dimethylbenzene as a solvent because it had a minimal effect on host-guest interactions, likely due to its size exclusion (Figure 3-5, p48). This procedure was found to be reproducible across repeat experiments (see Appendix, p138), and was used to investigate the *rac*-1-PE:**CC3** host-guest system in greater detail. Specifically, mixing time, temperature, and guest amount were all found to affect observed uptake (Figure 3-6, p51).

Molecular simulations indicated that the source of chiral selectivity was favourable intermolecular interactions, including the formation of a hydrogen bond, between **CC3**-*R* and (*S*)-1-PE that does not exist between **CC3**-*R* and (*R*)-1-PE (Figure 3-7, p53). In order to substantiate these models, a procedure was developed to analyze the host-guest process (Figure 3-8, p55). **CC3**-*R*, **CC3**-*S*, *rac*-**CC3**, and **CC3**-*R+S* were exposed to *rac*-1-PE solutions and analysed with a variety of techniques. No chemical (Figure 3-14, p59) or morphological (Figure 3-15, p61) changes in **CC3** were measured during host-guest exchange, indicating that it is a reversible intermolecular host-guest interaction that could be further applied in other separation technologies. Chiral selectivity was only observed for homochiral **CC3** and measured *ee* values aligned well with computational simulations (Figure 3-18, p64).

As outlined, exploiting the behaviour of a porous material requires a robust understanding of its function. The experiments in this Chapter identified the source of chiral selectivity in **CC3**, its behaviour under a range of experimental conditions, and showed its stability throughout. All of these are important considerations when establishing which technologies **CC3** could be applied to. Further, more organic cages have possible additional advantages over extended frameworks. An example of exploiting the unique properties of solubility to create usable separation technologies is presented in the next Chapter.

4 Chromatographic Separations with Organic Cages
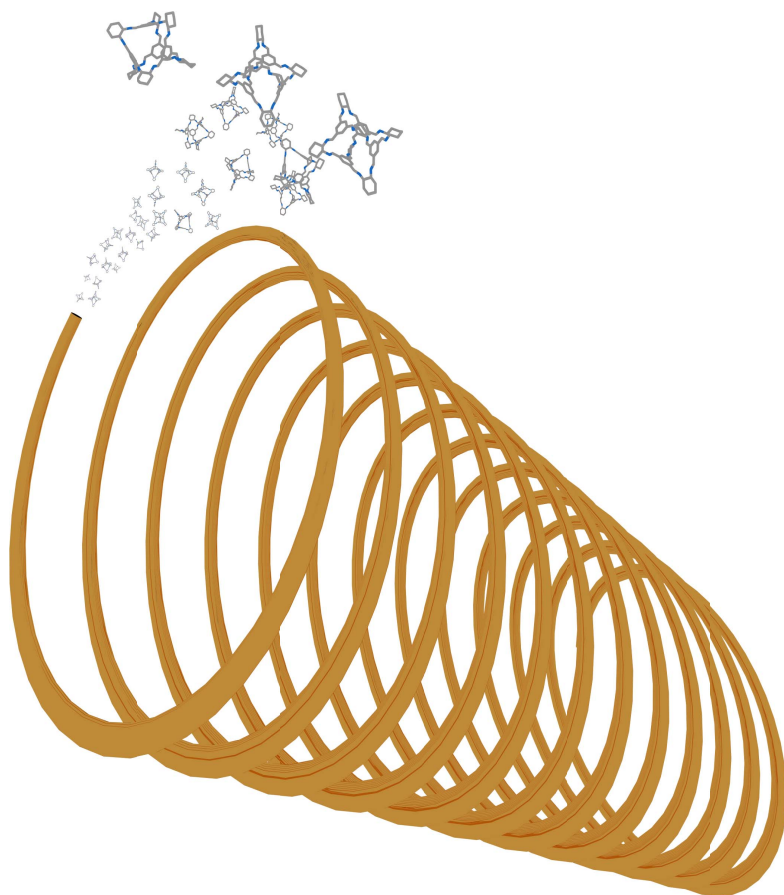
This Chapter presents the development of **CC3** as gas chromatography (GC) stationary phase (see Section 6.1, p89, for chromatography explanation). Several investigations are presented: the production of **CC3**-coated capillary columns; measurement of the separation behaviour of the resulting columns, which aligned well with investigations presented in Chapter 3, and; continuing from the investigations of Chapter 3, rationalization of the thermodynamics and kinetics of **CC3**'s separation behaviour.

The research presented in this chapter contributed directly to a *Chemistry of Materials* publication "Porous Organic Cages for Gas Chromatography Separations".[140]

4.1   Producing a GC Column

This Chapter focuses on the production of GC columns, rather than HPLC columns, for reasons discussed in the introduction (p17). GC columns are generally in packed or open-tubular capillary format. While packed columns have been demonstrated to perform interesting separations,[141] wall-coated open-tubular capillary columns are much more widely used because they are highly efficient, robust, and have generally high inertness.[99,117] However, due to their narrow diameters, high-quality coatings of insoluble materials can be difficult to produce inside capillaries.

The dynamic coating method is used in studies that utilise insoluble microporous materials. In dynamic coatings, a plug of slurried/concentrated stationary phase is pushed through the column under pressure. It is usually employed in conjunction with a dispersion method such as extended sonication.[125] Alternative approaches, such as layer-by-layer synthesis[142] or polymerization[143] have also been reported but are less widely used and are complex. By contrast, the static coating method, where capillaries are filled with coating solutions and the solvent is removed by evaporation, is commonly used in commercial processes because it is straightforward and produces a uniform coating inside the capillary.[117] However, in static coatings, the stationary phase must either be soluble or a stable nanosuspension.[144]

GC with a solid sorbent as the stationary phase, or gas-solid chromatography (GSC), is generally less attractive than gas-liquid chromatography (GLC). This because of the nonlinear adsorption isotherm of many solid sorbents, which makes the peaks obtained in GSC more asymmetric than GLC.[117] Further, solid sorbents commonly used in GSC have a much stronger interaction with guests than liquid stationary phases, which makes it difficult to separate polar or high-boiling-point compounds.

Accordingly, many high-performance stationary phases are liquid films. In those cases, a stationary phase, such as a per-methylated β-cyclodextrin,[116] is dissolved in a simpler phase, such as a polydimethylsiloxane (PDMS) and coated with the static method. Generally speaking, analyte exchange is faster in liquid films, which tends to produce sharper peaks in the resulting chromatogram.

Initial column production attempts tried to mimic the liquid films of commercial columns. **CCX**-*S*, the soluble novel cage presented in Chapter 2, was used because it did not precipitate from PDMS liquids. However, after coating, the resulting column retained some compounds but produced very broad peaks and no particularly interesting separation behaviour (see Appendix, p143). Broad peaks are likely due to the presence of tertiary amines within the structure of the cage: basicity can cause stationary phases to over-retain analytes, resulting in peak tailing. Separation behaviour was difficult to rationalise because little is known about the host-guest behaviour of **CCX**-*S*. Accordingly, column production attempts were refocused on producing a solid porous layer open tubular (PLOT)[110,117,143] column using a better-understood organic cage, **CC3**.

Findings from the previous Chapter and other studies[49] indicated that **CC3** should be capable of chiral and molecular shape separations. The value of separating each system is discussed in the introduction. Additionally, **CC3**'s solubility makes it suitable for the static-coating technique. However, while **CC3** may perform these separations as a selective sorbent, column development is required to adapt it to perform well as a chromatographic stationary phase.

4.2   Chiral Separations with a CC3-*R* Stationary Phase

In initial attempts, a 6 mg mL^{-1} solution of **CC3**-*R* in dichloromethane was used which, according to calculations (Equation 4-1),[117] resulted in a 0.375 μm thick film. This was thicker than most commercial columns, which usually have a film thickness of 0.12 μm, to ensure that a separation effect would be observed. However, because the film was too thick, mixtures separated on the column produced broad signals (Figure 4-1b). This was rectified by reducing the concentration of the coating solution to 3 mg mL^{-1}, which yielded a calculated film thickness of 0.19 μm and much more defined separation effect (Figure 4-1c).

$$d_\text{f} \ = \ 2.5 \times d_\text{c} \ \times \ (\% \text{ conc. of coating sol}^\text{n}) \qquad \text{Equation 4-1}$$

Separations, as in Figure 4-1, were noted to be broader than separations performed on commercial columns. The reason for this is hypothesised to be the morphology of the coating, which was likely to consist of many sizes of **CC3**-*R* particles. During elution, analytes may become temporarily adsorbed into larger particles and take time to desorb back into the mobile phase which, overall, manifests itself as a broadening effect. Attempts to improve this issue are discussed later, where prefabricated *rac*-**CC3** nanoparticles are used. However, while broadening is a concern, **CC3**-*R* was measured to have strong enough selectivity to overcome broadening effects.
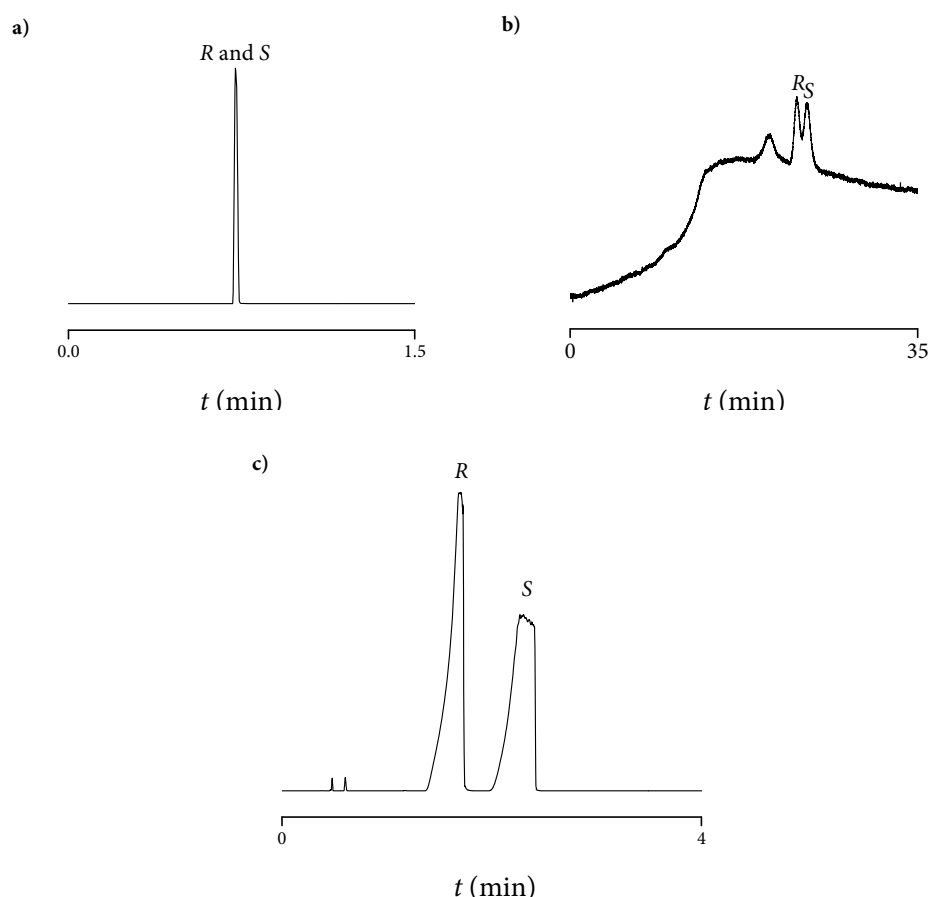

Figure 4-1 | Tuning column performance. GC-FID chromatograms obtained after eluting *rac*-2-butanol through a blank column (a), a thick (0.375 μm) coated **CC3**-*R*- column (b), and a thinner (0.19 μm) coated **CC3**-*R* column.

The **CC3**-*R* column separated multi-component mixtures, such as the separation of C6-C12 linear alkanes (Figure 4-2). Headspace analysis also indicated that pentane could also be separated by the column but it coelutes with the solvent in liquid injections (see Appendix, Figure 10-23, p145). The separation of alkanes is a well-established GC process and is a consequence of the large differences in boiling points.[117] Indeed, control experiments showed that heavier alkanes (C10+) will separate on a blank column due to this effect (see Appendix, p144).

In contrast to the separation of compounds by boiling point, chiral separations occur by favourable diastereomer-forming mechanisms such as hydrogen bonding, metal coordination, or inclusion.[112] As a result, it can be quite difficult to separate a racemate unless the stationary phase has a high selectivity for it. Chapter 3 presented the source of homochiral **CC3**'s chiral selectivity towards 1-phenylethanol (1-PE) to be favourable intermolecular interactions, which promoted the adsorption of (*S*)-1-PE into **CC3**-*R* more than (*R*)-1-PE. Encouragingly, separations performed on the **CC3**-*R* column corroborated that study. The column separated *rac*-1-PE, retaining (*S*)-1-PE more than (*R*)-1-PE (Figure 4-3).
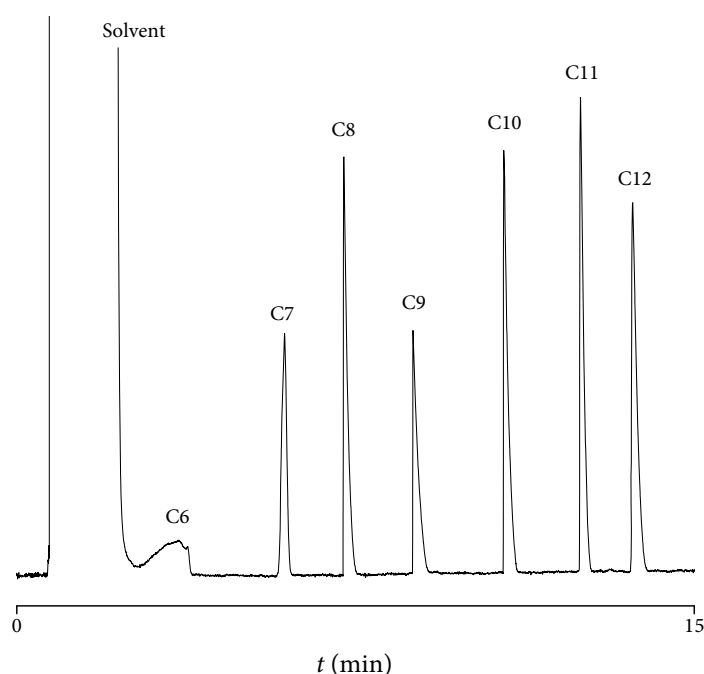

Figure 4-2 | Separation of linear alkanes using a CC3-*R* column. Separation of a mixture containing linear alkanes with chain lengths ranging from 6 carbons (*n*-hexane, C6) to 12 carbons (*n*-dodecane, C12). Control experiments available in the Appendix (p144).
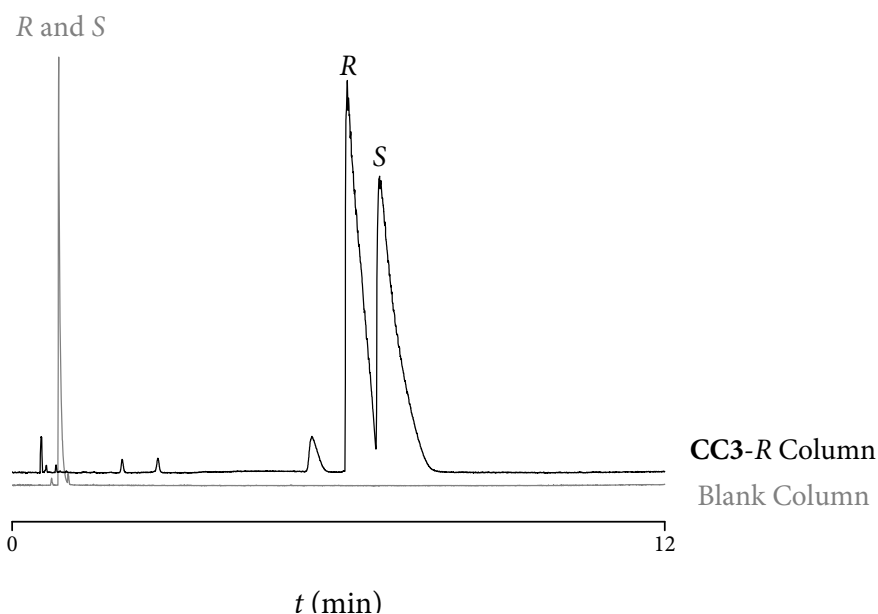
Figure 4-3 | GC-FID chromatograms of *rac*-1-phenylethanol (1-PE) eluted through a blank (grey line) and CC3-*R* coated (black line) column. Enantiomer labels (*R*/*S*) were found by measurement of homochiral 1-PE samples. (*S*)-1-PE was more strongly retained than (*R*)-1-PE by the column, which corroborates previous observations presented in Chapter 3.

Further chiral separations on the **CC3**-*R* column indicated that it was highly selective towards particular systems. Specifically, a high selectivity for 2-substituted alcohols was observed (Figure 4-4). The column separated a seven-component mixture of 2-substituted racemic alcohols. Further, headspace measurements indicated that the column strongly separates alcohols from methanol onwards (see Appendix, p147).

Establishing the source of such strong selectivity merited further investigation. As discussed in Chapter 3, selectivity is likely to be due to similar selective hydrogen-bond formation that occurs when separating *rac*-1-PE mixtures. This explanation is further reinforced when studying isostructural amines, which also separated on the column (Figure 4-5). Indeed, when comparing *rac*-1-PE to isostructural *rac*-α-methylbenzylamine, the same order of elution—*R* followed by *S*—was observed.

The column was unable to separate racemates without hydrogen-bond-forming moieties, such as chiral alkanes or alkylaromatics. These systems can be particularly difficult to separate because weaker induced dipole, van der Waals, or π-stacking interactions[102] are the only handle for their differentiation. This indicated that analytes hydrogen-bonding moieties are the primary differentiator used by **CC3**-*R* to separate enantiomers.
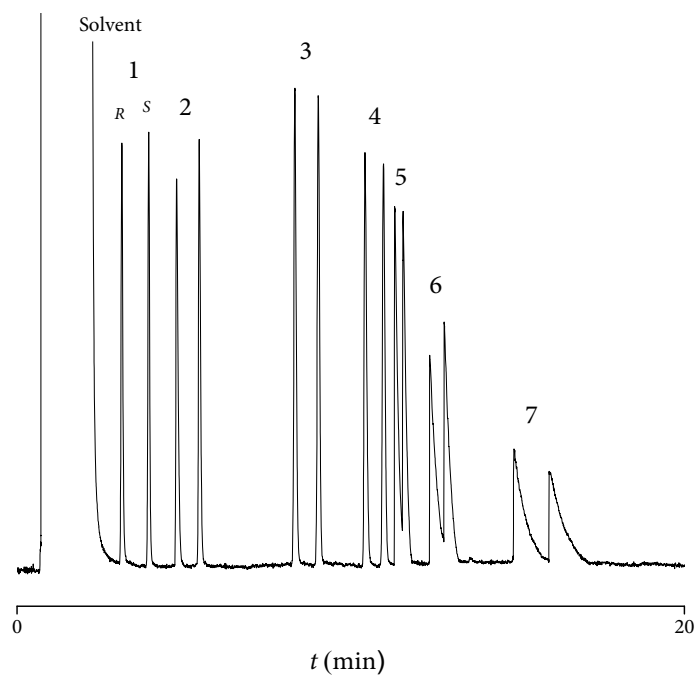
Figure 4-4 | Separation of 2-substituted chiral alcohol mixture. The mixture contained *rac*-2-butanol (**1**), *rac*-2-pentanol (**2**), *rac*-2-hexanol (**3**), *rac*-2-heptanol (**4**), *rac*-2-octanol (**5**), *rac*-2-nonanol (**6**), and *rac*-2-decanol (**7**) in diethyl ether. The absolute configuration (*R/S*) of the 2-butanol peaks has is labelled. Control experiments can be found in the Appendix (p146).
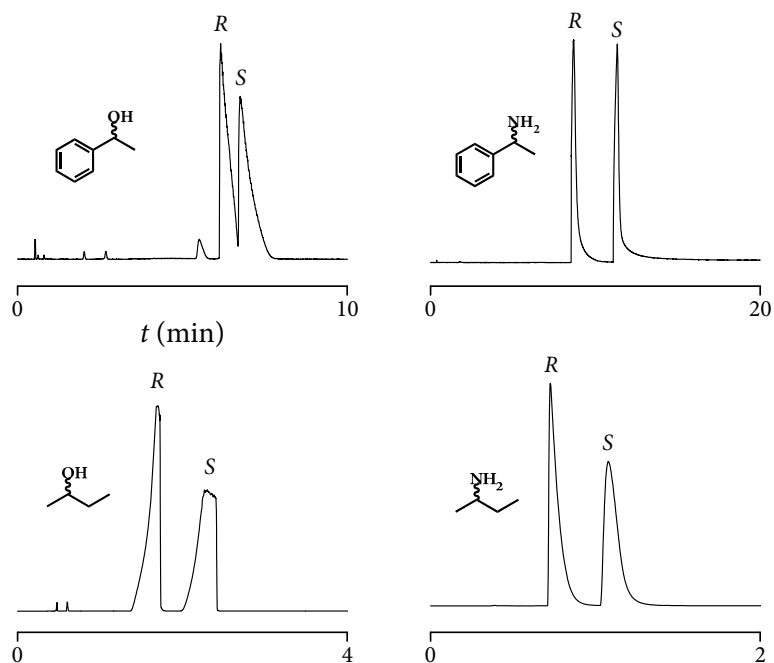
Figure 4-5 | GC-FID chromatograms of chiral alcohols (left) and isostructural amines (right) separated on the CC3-*R* column. Based on previous discussions, one source of chiral selectivity is likely to be geometrically-restricted hydrogen-bond formation. Isostructural amines should be capable of forming such bonds with similar geometries to the alcohols and, accordingly, similar separation behavior was seen in these systems.

Side chains that may interrupt hydrogen-bonding also appeared to have an effect on selectivity. For example, while chiral separation was measured for *rac*-2-heptanol, none was seen for *rac*-3-heptanol (see Appendix, p148). This was likely due to the additional steric bulk of a C_2H_5 group when compared with $-CH_3$. The conformational motion of the latter is unlikely to interrupt hydrogen-bond formation while the former could. This explanation is corroborated when analysing a range of other racemic mixtures (Figure 4-6). For example, while no selectivity was seen in saturated 3-substituted compounds, it was seen in unsaturated equivalents, such as *rac*-1-pentyn-3-ol (c). The same was true for cyclic compounds, such as *rac*-3-hydroxytetrahydrofuran (i).

This trend continued for other mixtures listed. Chiral diol compounds also separated on the column (g, h). However, the separation effect appeared to be weak, which is likely a consequence of non-stereospecific hydrogen-bonding from the achiral moiety. Other measurements gave the impression that separation was stronger when the chiral moiety is at the 3 position (h); however, this was misleading because *rac*-2-ethyl-1,3-hexanediol contains two chiral centers and, as a consequence, the observed separation was likely the separation of diastereomers.

In an attempt to understand the energetics of separation, the enthalpy and entropy of association with **CC3**-*R* was calculated from Van't Hoff relationships (method in experimental Section, 7.3.3, p113). Calculated values are presented in Table 4-1. In general, a 5-8 kJ mol^{-1} enthalpy and 10 J mol^{-1} K^{-1} entropy difference was measured between enantiomers. Simulated values[66] yielded larger energy differences (28.5 kJ mol^{-1}); however, these were calculated at 0 K from the most favourable configuration of a single 1-PE molecule per unit cell of **CC3**-*R*. By contrast, experimental calculations yielded values under standard conditions with an indeterminate ratio of 1-PE : **CC3**-*R*. Further, these experimental values are affected by imperfections in the coating, surface binding, and by diffusion within the crystallite. Hence, differences between experimental and computational values are to be expected.
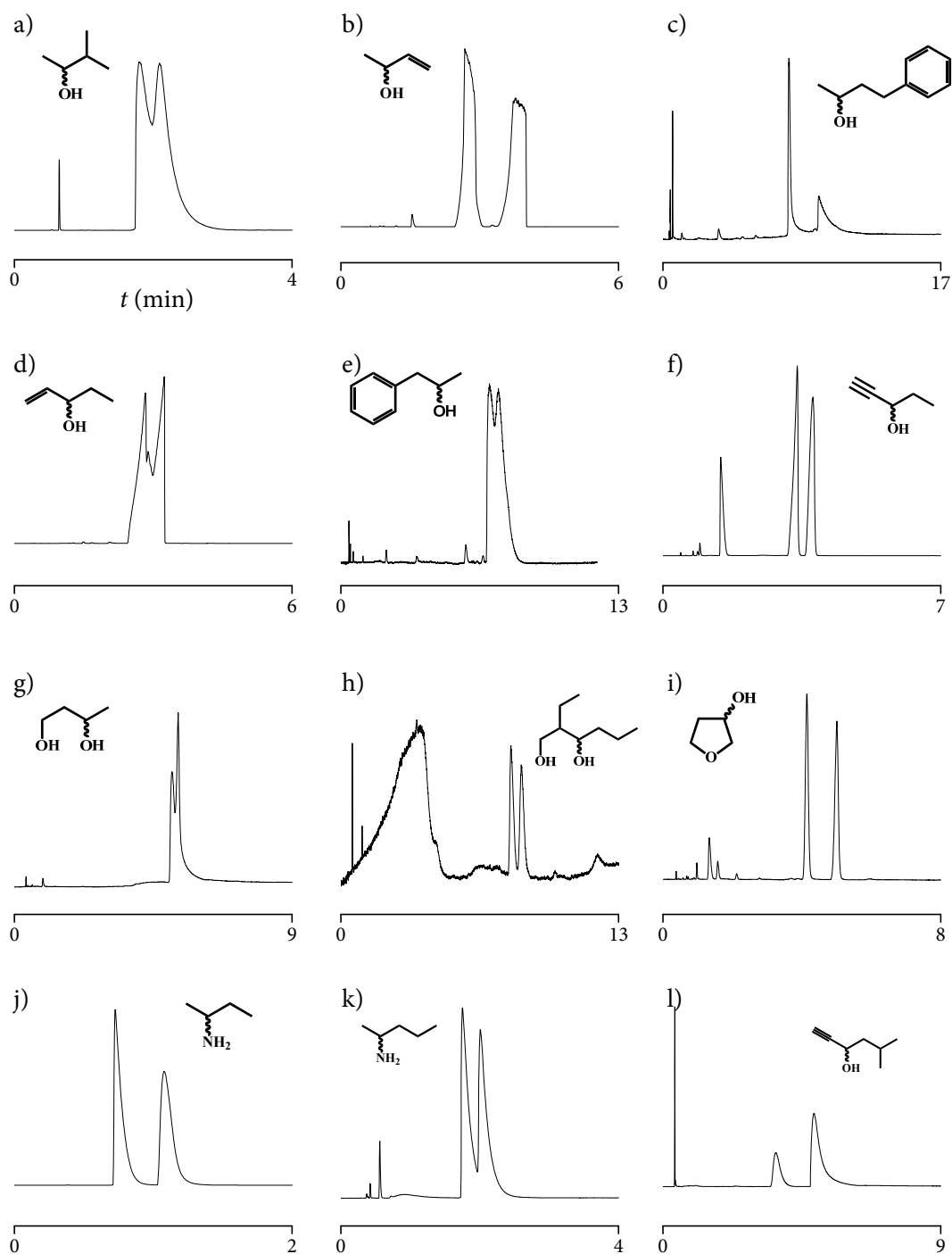
Figure 4-6 | Other chiral separations on the CC3-*R* column. The separation of twelve racemic mixtures containing either hydroxyl or amine moieties are presented: *rac*-3-methyl-2-butanol (a), *rac*-3-buten-2-ol (b), *rac*-4-phenyl-2-butanol (c), *rac*-1-penten-3-ol (d), *rac*-1-phenyl-2-propanol (e), *rac*-1-pentyn-3-ol (f), *rac*-butane-1,3-diol (g), *rac*-2-ethyl-1,3-hexanediol (h), *rac*-3-hydroxytetrahydrofuran (i), *rac*-2-aminobutane (j), *rac*-2-aminopentane (k), and *rac*-5-methyl-1-hexyn-3-ol (l). GC methods used to perform these separations are presented the Appendix (p126).

Table 4-1 | Thermodynamic values calculated from Van't Hoff linear fits for separations performed on the CC3-*R* column. Calculation method available in experimental Section (7.3.3, p113). A *c.a.* 5-8 kJ mol^{-1} enthalpic and 10 J mol^{-1} K^{-1} entropic gap between enantiomers was measured. Van't Hoff plots in Appendix, p149.

Compound	-ΔH_{ads} / kJ mol^{-1}	ΔS_{ads} / J mol^{-1}K^{-1}	R^2
(*R*)-1-Phenylethanol	79.3	-134	1.000
(*S*)-1-Phenylethanol	84.3	-143	0.999
(*R*)-α-Methylbenzylamine	73.7	-126	0.999
(*S*)-α-Methylbenzylamine	81.9	-136	1.000
(*R*)-2-butanol	77.0	-153	1.000
(*S*)-2-butanol	81.3	-160	1.000
(*R*)-*sec*-Butylamine	76.3	-151	1.000
(*S*)-*sec*-Butylamine	81.1	-159	1.000

Overall, the column performed a variety of chiral separations including those presented in Chapter 3. However, while some of these separations may be difficult to perform, many can be performed on commercially available columns. By contrast, fewer columns are capable of separating mixtures by molecular shape. The Cooper group previously reported that **CC3**-*R* may perform shape separations.[49] Accordingly, these kinds of separations were investigated with the column but, due to the broadening effect observed in the presented chromatograms, the separations were not quite baseline (e.g. Figure 4-8). To rectify this, further changes were made to the design of the stationary phase.

4.3   Molecular Shape Separations with a *rac*-CC3 Stationary Phase

Ideally, exchange with the stationary phase should be rapid, retaining components for a narrowly-distributed duration of time which, as a consequence, should produce sharp peaks in the chromatogram.[117] Unfortunately, this was not the case for some separations on the **CC3**-*R* column. In that case, it is likely that broadening was a consequence of non-linear adsorption into **CC3**-*R* crystallites within the column.

Peak broadening issues are not unique to **CC3**. Similar issues were encountered in the initial development of β-Cyclodextrin (β-CD), the core of many commercial stationary phases.[118,145] One major improvement to the efficiency of β-CD phases was their per-methylation to make them suitably soluble to dissolve in polysiloxanes to form

liquid films.[116] With respect to **CC3**, a similar approach would be ideal but no synthetic preparation is available at the time of writing. Instead, attempts were made to improve the performance of **CC3** columns through solid morphology control.

The Cooper group previously reported a method for producing stable, monodisperse, *rac*-**CC3** nanoparticle suspensions.[50] This approach was used to produce 5 mg mL^{-1} suspensions of *rac*-**CC3** nanoparticles in dichloromethane which were subsequently diluted to 1 mg mL^{-1} and directly coated within the column. The resulting coating thickness was calculated to be 0.0625 μm, which was thinner than the previous column (0.19 μm) but, as discussed, thinner films should result in higher separation efficiencies.[117] Unfortunately, the coating of prefabricated solids onto a surface behaves quite differently from direct precipitation. The resulting coating was poorly adhered to the columns surface. As a result, when the column was fitted and the mobile phase of the gas chromatograph enabled, a stream of dislodged particles entered, and coated, the detector to produce an intense signal. Consequently, it was clear that further changes would need to be made to improve particle adherence.

The adherence of solids to open tubular columns has been previously studied.[146] The use of an adhesive to stabilise particles was straightforwardly adopted into the *rac*-**CC3** coating solution. As before, a 1 mg mL^{-1} nanosuspension coating solution was produced but SP-2100, a commercially available PDMS GC stationary phase, was also added up to a concentration of 2.5 mg mL^{-1}. This solution was coated using the static method and, encouragingly, no intense detector signal due to particle dislodgement was observed when using the resulting column (see expt. 7.3.4.3, p115).

SEM images of the resulting column indicated the presence of particles within (Figure 4-7). The average particle diameter measured from these images is *c.a.* 100 nm, which is close to values measured in previous studies.[50] Improved column performance, in the form of sharper peaks and better-defined separation, was measured for the *rac*-**CC3** particle-coated column when compared with the **CC3**-*R* column (Figure 4-8) which enabled the analysis of difficult-to-separate mixtures, such as mixtures of compounds that may only be differentiated by their molecular shape.

The separation of xylene isomers is particularly well-studied because the isomers have defined molecular shapes that change negligibly with conformational motion. Accordingly, previous studies showed the selective adsorption of xylene isomers into

Empty Capillary	Polymer	Polymer and CC3
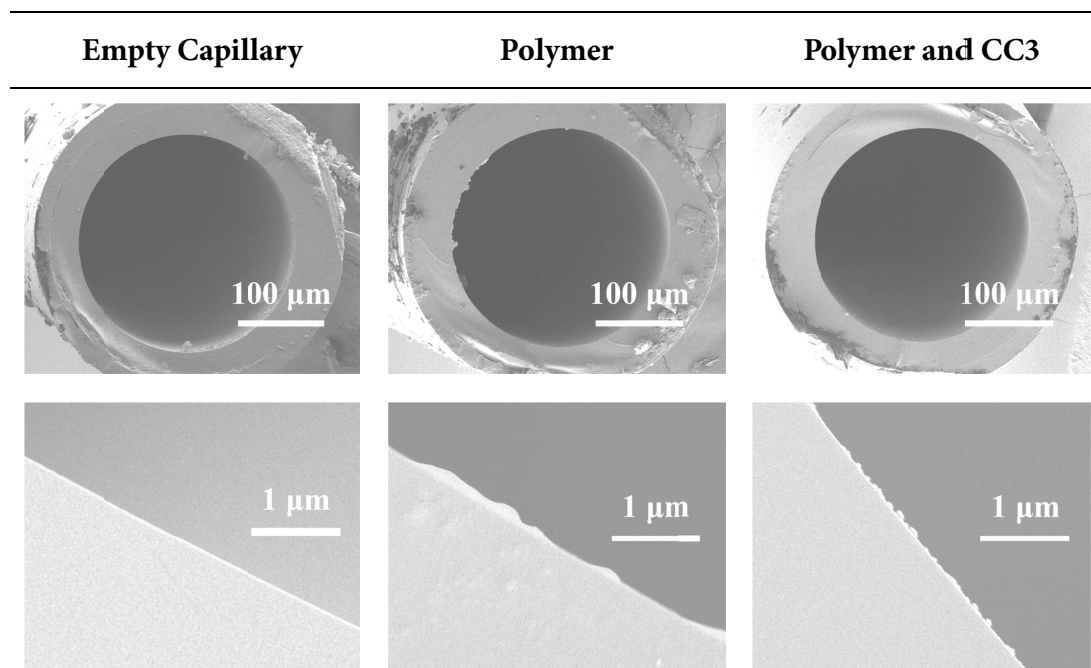
Figure 4-7 | SEM images of columns. SEM images of the *rac*-**CC3** nanoparticle-coated GC capillary columns. Left: blank, as purchased, fused-silica capillary columns. Middle: a control column coated with SP-2100. Right: the experimental *rac*-**CC3** nanoparticle column. In all cases, there were traces of debris from column cutting (see top row). However, surface coatings were only observed for the SP-2100 and *rac*-**CC3** columns. In the experimental column, small (d ≈ 100 nm) particles of *rac*-**CC3** were observed to be coated on the inner edge of the column.
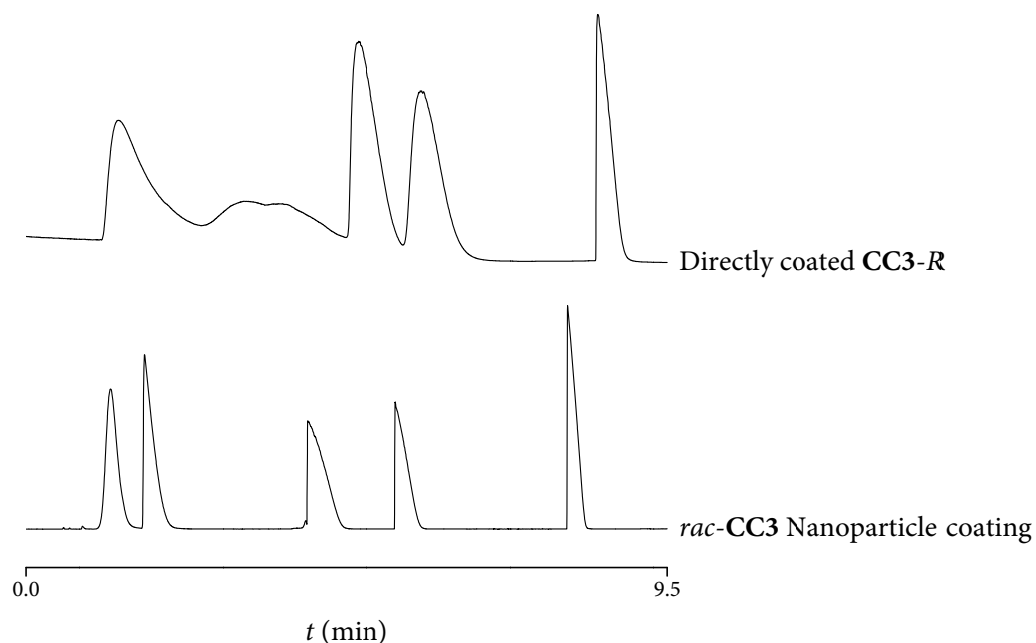
Figure 4-8 | Comparison of directly coated CC3-*R* and SP-2100 stabilised *rac*-CC3 nanoparticles. GC-FID chromatograms of a mixture of the five isomers of hexane eluted though the **CC3**-*R* column (top) and *rac*-**CC3** nanoparticle column (bottom).

CC3 with breakthrough measurements which found increasing association prefer-ence in the order *ortho- < meta- < para*-xylene.[49] This particular shape-sorting effect is a consequence of **CC3**'s rigid pore structure which, because it has a narrower geo-metric envelope, *para*-xylene diffuses through more easily. The same association order has been reported for other materials and the reverse may be achieved with reverse shape selectivity, a phenomenon measured in a MOF, UiO-66.[126,147]

Columns that separate compounds by molecular shape are particularly desirable since many difficult-to-separate mixtures are only differentiated by this property. Encouragingly, the *rac*-**CC3** column appeared to perform this class of separations. It separated xylene isomers with the expected elution order (Figure 4-9, left). The shape-sorting effect was particularly strong when separating mesitylene from ben-zene (Figure 4-9, right). The Cooper group previously reported that mesitylene has difficulty entering **CC3**.[49] Consequently, despite the boiling point of mesitylene be-ing 85 °C higher than benzene, it elutes through the *rac*-**CC3** column quickest. In general, the order of elution in conventional GC separations should conform to the boiling point of components;[117] however, the reverse is observed for these separa-tions.

t (min)
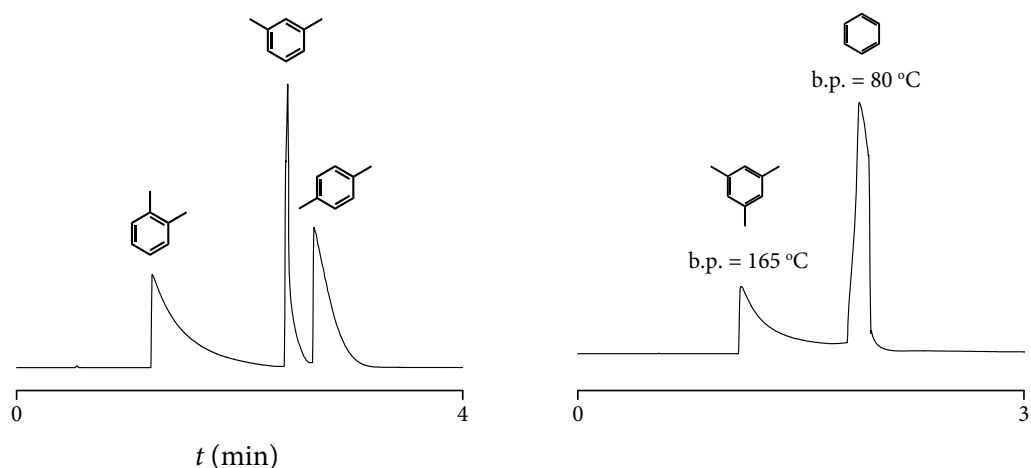
Figure 4-9 | Molecular-shape separations on the *rac*-CC3 nanoparticle column. GC-FID chro-matograms of a xylene isomer mixture (left) and mixture of benzene and mesitylene (right) eluted through the *rac*-**CC3** nanoparticle column. In both cases, the order of elution was the reverse of the components' relative boiling points. Molecular shape sorting by **CC3** has been previously re-ported.[49] The effect was particularly strong when comparing the retention time of mesitylene, which cannot easily enter the pores of **CC3**, to benzene. Control experiments in Appendix (p148-150).

While the separation of xylene isomers was interesting, these separations may be performed on conventional β-CD-based stationary phases because the central ring of CDs enables shape-selective inclusion mechanisms.[118] Indeed, the separation of xylenes on a conventional β-CD column is presented in Chapter 3 (Figure 3-2, p44). By contrast, because π-π interactions are not available, fewer stationary phases are capable of differentiating similar alkane isomers.

Recently, the use of MOFs to separate hydrocarbons has received much attention.[3] One specifically noteworthy challenge is the separation of the five structural isomers of hexane. In 2013, Long and coworkers reported the separation of hexane isomers using a MOF, Fe_2BDP_3, with triangular pores.[32] The triangular geometry, which is difficult to achieve in conventional zeolites, was reported to be optimal when separating the mixture. In addition to MOFs, this window shape can be achieved in organic cage compounds. **CC3** is known to have a similar window shape and, coincidently, all five structural isomers of hexane were separated by both the **CC3**-*R* stationary phase (Figure 4-8, top) and, with improved separation efficiency, the *rac*-**CC3** nanoparticle phase (Figure 4-10). This phenomenon was likely to be a consequence of the three-dimensional diamondoid structure of **CC3** which provided a rigid framework for molecular shape sorting.[148]

Control experiments indicated that *rac*-**CC3** is responsible for the separation effect (see Appendix, p150). The order of elution corresponded to the degree of branching
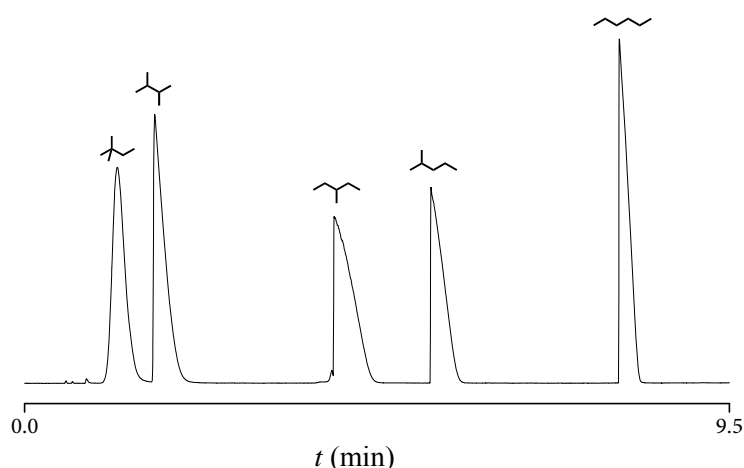

Figure 4-10 | The separation of the five isomers of hexane on the *rac*-CC3 stationary phase. GC-FID chromatogram of a hexane isomer mixture eluted through the *rac*-**CC3** column. The order of elution corresponded to the degree of branching in the isomer. Control experiments on blank and SP-2100 columns can be found in the Appendix (p150).

in the isomer, with more branched isomers eluting first. This is likely a consequence of van der Waals surface interactions between the isomer and *rac*-**CC3**. For example, computational models indicated that, as a guest, *n*-hexane achieves a high degree of surface interaction by contorting to **CC3**'s diamondoid arrangement (Figure 4-11). The rearrangement of guests into **CC3**'s diamondoid structure has been reported for polyiodides.[148] By contrast, the branched nature of other isomers diminishes these interactions, reducing the thermodynamic favourability of association. Accordingly, experimental thermodynamic values calculated from Van't Hoff relationships (Table 4-2) indicated an average enthalpic gap of 7 kJ mol^{-1} between each isomer associating with *rac*-**CC3**. However, differences between experimentally and computationally determined values also indicated that the effect may not be entirely thermodynamically driven.

Compared to experimental measurements, the computationally derived order of thermodynamic preference switches 2,2-dimethylbutane with 2,3-dimethylbutane. Experimentally, that would mean that the latter should elute first; however, this was
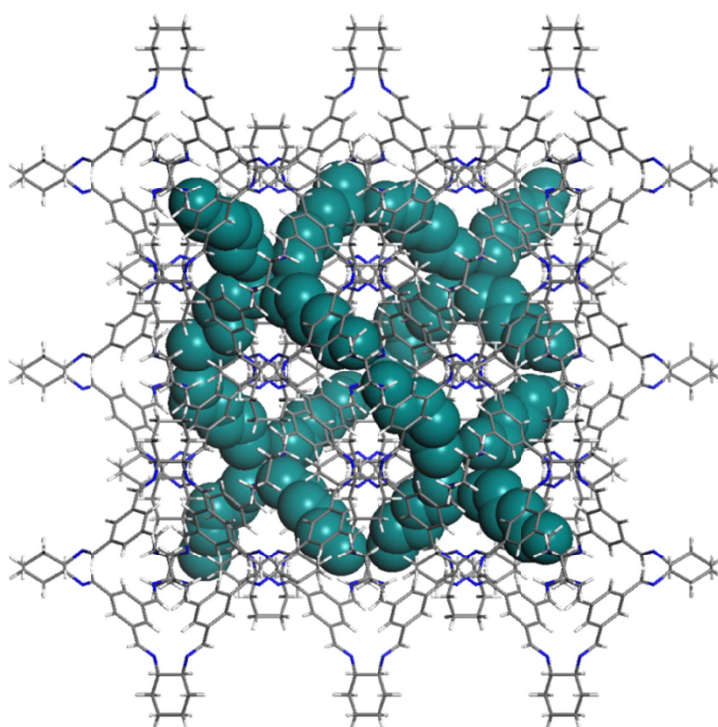
Figure 4-11 | The conformation of n-hexane within *rac*-CC3. *n*-Hexane molecules are highlighted in green. *n*-Hexane molecules appear to maximise van der Waals surface interactions with *rac*-**CC3** by conforming to the cage's diamondoid pore structure. Branched hexane isomers are less-able to maximise their surface interactions in this manner and, accordingly have comparatively weaker surface interactions, resulting in the presented elution order.

Table 4-2 | Thermodynamic values calculated from Van't Hoff linear fits. The method used to calculate these values is shown in the experimental Section (7.3.3, p113). Van't Hoff plot is available in Appendix (p149).

Hexane Isomer	$-\Delta H_{ads}$ / kJ mol^{-1}	ΔS_{ads} / J mol^{-1}K^{-1}	R^2
2,2-Dimethylbutane	44.5	-71	0.997
2,3-Dimethylbutane	50.7	-87	0.997
3-Methylpentane	61.3	-111	0.999
2-Methylpentane	65.8	-120	1.000
n-Hexane	72.8	-127	1.000

not measured to be the case. This was likely due to a combination of kinetic and surface effects. With respect to kinetic effects, time-resolved computational models indicated that the speed at which hexane isomers diffuse through **CC3** follows the same pattern as experiments (Figure 4-12). *n*-Hexane diffuses quickest through *rac*-**CC3** while branched isomers diffuse more slowly. With respect to surface effects, models assumed that most separation interactions occurred within the bulk structure, not the surface, of **CC3**. However, the use of high surface-area-to-volume ratio nanoparticles means that a significant proportion of interactions likely occurred at the surface. Further studies are required to fully quantify these effects.

A further point of interest was the robustness of the columns. In commercial environments, GC is a routine analysis technique in a wide variety of industries. There, high-throughput and automated analysis are much more common and, accordingly, a major point of interest is the stability of stationary phases. A long lifetime is desirable for any column coating. While short (<50 injections) lifetimes are acceptable for prototypes; identifying long-term durability is an important step in the development of a column.

The **CC3**-*R* column was tested by repeatedly injecting *rac*-3-hydroxytetrahydrofuran and measuring changes in the retention time of the eluted analytes (Figure 4-13). Differences in intensity could be attributed to the gradual depletion of sample headspace. No change in retention properties observed in these measurements. This is likely to be consequence of **CC3**'s stability. The Cooper group previously reported that **CC3** may be boiled in water or heated to *c.a.* 250 °C with no observable chemical change.[149] Additionally, it was qualitatively noted that the retention behaviour of the column did not change over its entire use (>300 injections).
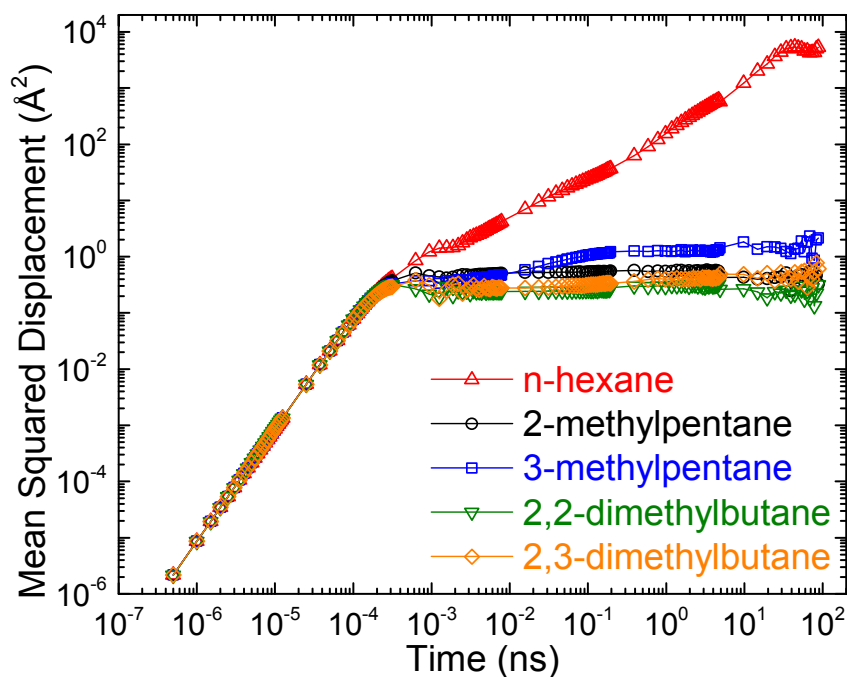
Figure 4-12 | Diffusion of hexane's five structural isomers through *rac*-CC3. After an initial period, *n*-hexane diffuses through the structure of *rac*-**CC3** fastest, followed by 3-methylpentane, 2-methylpentane, 2,3-dimethylbutane, and 2,2-dimethylbutane. The order of diffusion is the same as measured the order of elution from the *rac*-**CC3** column (Figure 4-10) but differs from thermodynamic calculations (Figure 4-11).
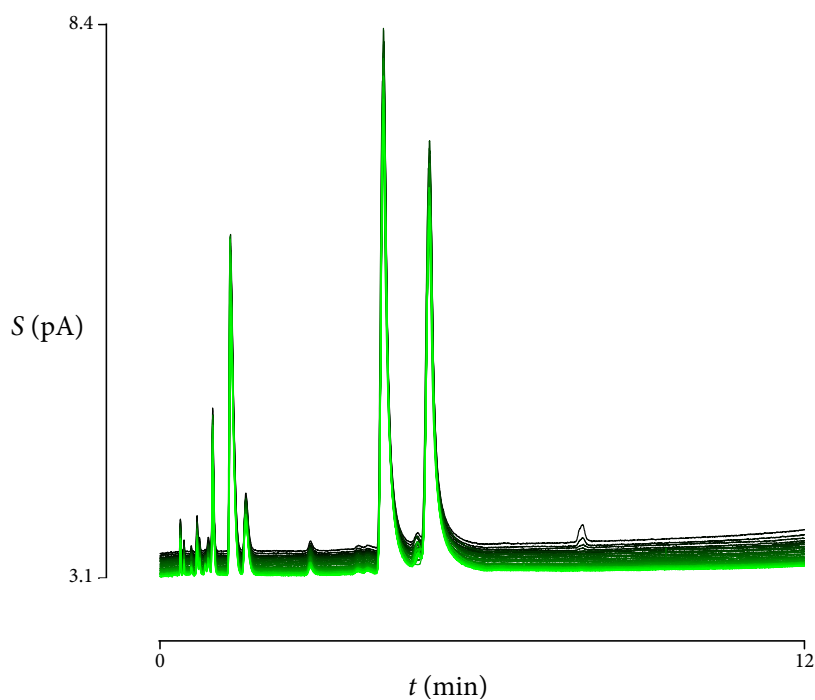
Figure 4-13 | Robustness of the CC3-*R* column. Overlaid GC-FID chromatograms of 36 repeat injections of *rac*-3-hydroxytetrahydrofuran eluted through the **CC3**-*R* column. The two major peaks indicate each enantiomer of the racemic mixture.

The presence of an adhesive raised an additional concern for the *rac*-**CC3** column. There was a possibility that, at higher temperatures, the adhesive would slowly morph and release *rac*-**CC3** particles into the detector. Film morphing may be measured as a change in column performance while particle dislodgement would produce intensity spikes in the chromatogram. To investigate this, a hexane mixture was repeatedly injected 50 times (Figure 4-14) onto the *rac*-**CC3** column. Encouragingly, no measurable performance changes or spikes were observed for these, or any other (>200), chromatograms obtained when using the column.

Both column formats appeared to be stable over at least 200 injections in both cases. Further testing would be required to asses if they have the necessary robustness for routine industrial analyses (>5000 injections) but the results are impressive for a prototypical stationary phase. The most popular commercial stationary phases consist of esterified β-cyclodextrins which can be vulnerable to hydrolysis. By contrast, organic cages may be derivatised by reduction followed by amide formation from acyl halides and acid anhydrides,[70] which is likely to result in a less-labile bond. This opens up the opportunity to use organic cage compounds as a core for a range of tailor-made stationary phases.
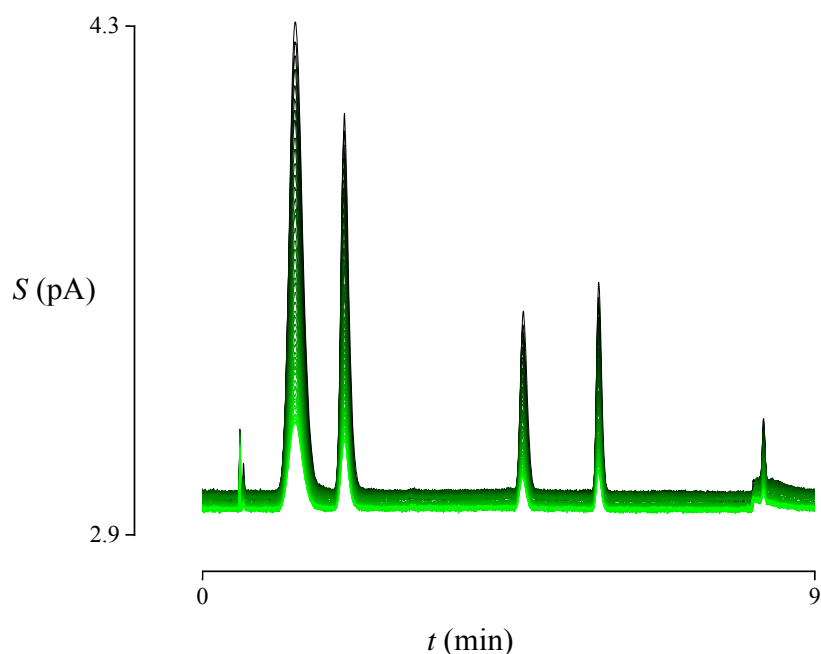

Figure 4-14 | Robustness of the *rac*-CC3 nanoparticle column. Overlaid GC-FID chromatograms of 50 repeat injections of a hexane isomer mixture onto the *rac*-**CC3** nanoparticle column. No change in retention time was measured between injections. A reduction in peak height can be directly attributed to the depletion of hexane vapour in the sample.

4.4 Conclusions & Outlook

A **CC3**-*R* GC capillary column was produced using the static coating method and observed to be capable of separating C5-C12 linear alkanes (Figure 4-2, p71), 2-substituted racemic alcohols (Figure 4-4, p73), and a range of other racemic alcohol mixtures (Figure 4-6, p75). (*S*)-1-PE was more strongly retained than (*R*)-1-PE by the column, which corroborates findings from the previous Chapter (Figure 4-3, p72). Likewise, the separation of isostructural amine compounds on the **CC3**-*R* column also reinforces those findings (Figure 4-5, p73) and underlines the importance of understanding host-guest interactions for establishing patterns of behaviour in a separation technology.

To improve separation performance, the **CC3** stationary phase was further developed. *rac*-**CC3** nanoparticles were produced as in a literature method.[50] A GC column containing these particles glued on its inner surface was produced (Figure 4-7, p78). This development improved peak shape (Figure 4-10, p80) and enabled more-difficult separations, such as the shape-selective separation of all three xylene isomers or benzene from mesitylene (Figure 4-9, p79), to be performed. The column also baseline separates all five isomers of hexane (Figure 4-10, p80), a particularly difficult mixture to separate.[32] Computational modelling indicated that the elution order of hexane isomers likely depends on a combination of thermodynamically favourable van der Waals interactions of an isomer with *rac*-**CC3** (Figure 4-11, p81) and an isomers speed of diffusion through **CC3**'s extended structure (Figure 4-12, p83).

There is also scope for the commercial adaption of **CC3** as a GC stationary phase. Both the **CC3**-*R* and *rac*-**CC3** columns displayed no change in retention ability over robustness-testing experiments (p83) or their use (>300 injections). Further, the amount of **CC3** used in either column costs less than £1, a negligible proportion of the overall retail price of a GC column.

Overall, **CC3** has been utilised as a stationary phase in GC columns. It is capable of performing specialist, in demand separations that are otherwise quite difficult. The source of these separation effects is molecular shape, molecular size, hydrogen bonding, or a mixture of all three. Further work includes expanding the number of compounds analysed on the columns to reveal which systems **CC3** optimally sepa-

rates. Additionally, there is a variety of other organic cage compounds[57,150,151] and cage derivatives[70] available. Similar studies on these opens up the opportunity for fine-tuned, designed, stationary phases based on organic cage chemistry.

5 Overall Conclusions and Outlook

Chapter 2 presented attempts to accelerate the discovery rate of novel organic cages. Specifically, the use of *in-silico* and HT techniques to help with discovery was investigated. Several screening experiments were conducted with a variety of precursors. While most screening experiments did not yield the desired target, the HT approaches were developed throughout. Rather than using HT techniques to carefully tune a synthetic approach, later screening experiments fully embraced the benefits of being able to broadly screen multiple precursor combinations, which identified a novel organic cage compound: **CCX**-*S*. This cage was measured to have a flexible extrinsic structure that made it highly soluble in chlorinated solvents. However, this structure also made it difficult to crystallise. Further, the amorphous form of **CCX**-*S* was measured to be nonporous to N_2, likely due to the interpenetration of the outer benzyl moieties. Overall, the HT and *in-silico* techniques presented throughout Chapter 2 could be applied to solve a broad range of synthetic problems. In that sense, the findings of Chapter 2 are not only relevant to cage compounds.

Chapter 3 initially presented the development of a straightforward, but qualitative approach for measuring selective adsorption. This approach identified that homochiral **CC3** is capable of separating racemic mixtures, which had not previously been reported. The quality of data from the technique was improved by using a bulky solvent, 1-*tert*-butyl-3,5-dimethylbenzene, to evenly distribute guest mixtures. The solvent was found to have a minimal effect on the host-guest process of interest, likely because it is too large to enter the pores of **CC3**. Of the mixtures investigated, the chiral separation of *rac*-1-phenylethanol (*rac*-1-PE) by homochiral **CC3** was focused on. Computational models hypothesised the source of selectivity to be favourable host-guest interactions between (*S*)-1-PE and **CC3**-*R* which do not occur between (*R*)-1-PE and **CC3**-*R*. Experiments align well with this hypothesis. Additionally, no chemical or crystal phase changes in **CC3** were measured during 1-PE adsorption and desorption, which indicated that **CC3** could be applied in practical separation technologies.

Following on from Chapter 3, Chapter 4 presented the first instance of applying **CC3** as a GC stationary phase. The static coating method, which is widely used in commercial column production processes, was used to coat a capillary column with **CC3**-*R*. This is in direct contrast to insoluble microporous materials, which require alternative coating methods. The column was observed to be capable of separating racemic alcohols and amines but the resulting chromatograms contained relatively broad signals when separating compounds with weaker differentiating moieties, such as hexane isomers. To rectify this, an improved column was produced by coating with prefabricated *rac*-**CC3** nanoparticles. This column was capable of separating compounds by molecular shape and capably separated all five isomers of a hexane mixture. The separation of hexane isomers has received much attention recently due to its high value in industry. Both columns were observed to have excellent lifetimes, which is important consideration for commercial interests. These developments have opened up the possibility of using other organic cages, and their derivatives, in GC columns to perform other difficult, high value, separations.

Overall, the research presented in this thesis highlights developments in the synthesis and separation properties of organic cages. It has shown how modern advances, such as *in-silico* and HT techniques, could potentially be incorporated augmented into conventional synthetic preparations. The overarching objectives of the work were therefore successful, and as a result of this project, we have developed new HT methods, new molecules, and new practical separation techniques.

6 **Characterization Techniques**

Characterization methods are arranged based on their relative usage throughout this thesis. Generally speaking, Chapters 3 and 4 are primarily focused on chromatography; specifically, gas chromatography (GC). Chapter 2 is a synthetic Chapter and primarily uses proton nuclear magnetic resonance (^{1}H NMR) and Fourier transform infrared (FTIR) analyses.

6.1   Analytical Chromatography

Chromatography is a collective term for a set of laboratory techniques for the separation of mixtures. The explanation provided here is focused on a branch of chromatography – analytical chromatography.

In chromatography, mixtures are dissolved into a fluid *mobile phase* and carried through a *column* containing a *stationary phase* (Figure 6-1, **a**). Components of the mixture may have differing affinities for the stationary phase which cause them to move through the column at different speeds. Provided the difference in speed is great enough, other diffusion effects do not interfere too much, and the column is sufficiently long, the components will separate within the column (Figure 6-1, **b**). A detector records components as they leave the column and plotting the recorded signal against time yields a *chromatogram* (Figure 6-1, **c**). Generally, time is recorded relative to the point of mixture introduction and is referred to as *retention time.*

Differences in retention times between components are a consequence of their affinity towards the stationary phase. Chromatographic literature[117] would refer to this as a *partitioning* effect wherein components within the mobile phase partition, and become temporarily immobilised on, the stationary phase. At its core, partitioning is usually a consequence of non-covalent intermolecular interactions such as dipole-dipole, induced dipole, hydrogen bonding, van der Waals, or π-stacking interactions,[102] greater partitioning results in a greater degree of component immobilization which results in a greater retention time. Chapter 4 focuses on exploiting **CC3**'s different affinities towards chiral enantiomers and chemical isomers to create a working column capable of separating a variety of compounds.

Peaks on the chromatogram may indicate separate components of the original mixture. Depending on the detector, the recorded signal may be used to calculate a
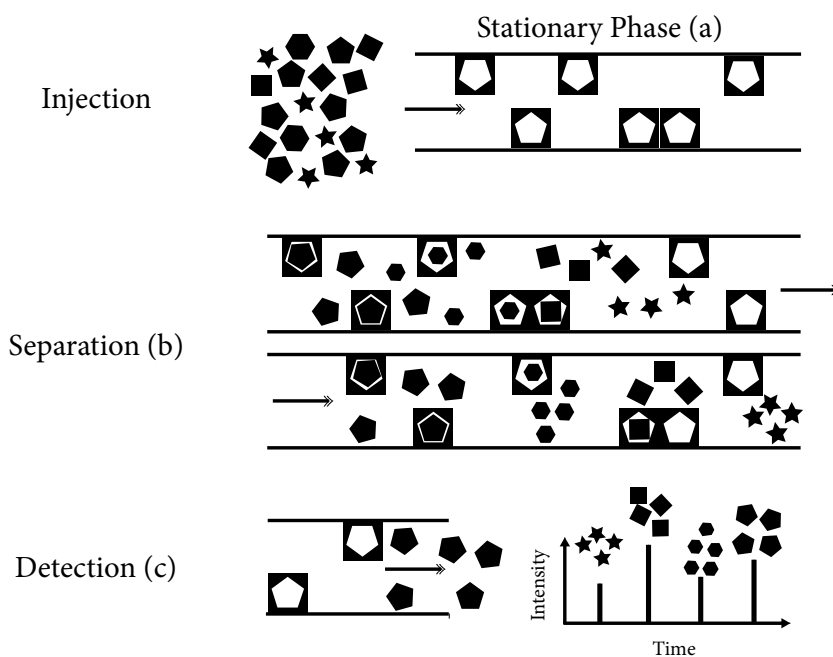
Figure 6-1 | Simplified schematic of the chromatographic process. A multi-component mixture is introduced onto a column containing a stationary phase. Due to differences in affinity between components and the stationary phase, they travel through the column at different speeds which, provided affinity differences are sufficient, results in the separation of components.

variety of metrics including a component's concentration in the mixture or its chemical and physical properties. In general, there is a positive correlation between the quantity of a component put onto a column and resultant signal. Consequently, component amounts in unknown mixtures may be calculated if the instrument has been calibrated. Calibration involves analysing standards of known concentration to calculate a relationship between recorded signal and concentration. In Chapter 3, this approach is used extensively to calculate the concentration of experimental mixtures (see experiment 7.2.1.1, p103).

6.1.1   Analytical Gas Chromatography (GC)

In GC, both the analyte mixture and mobile phase are gaseous. Generally speaking, GC instrumentation will have a heated injector to vaporise any introduced samples. The resulting gas is carried through the column with a gaseous mobile phase, usually helium or nitrogen, and gaseous components exchange onto a stationary phase as in any chromatographic technique. Both packed-bed and capillary columns are standard formats for GC. Capillary columns have, generally speaking, the highest separation efficacy, which is one reason why they are the focus of Chapter 4. This, combined with rapid component diffusion in the gas phase, results in GC usually

having a comparatively higher separation efficacy than HPLC and GPC.[152] However, a major drawback of GC is that analytes must be in the gas phase during separation; therefore, GC is unable to analyze compounds with high boiling points (> 300 °C approx.).

A variety of detectors may be coupled to a GC system. A flame-ionization detector (FID) is exclusively used in the GC analyses presented in this thesis.[153] As a brief overview, FID detectors work by ionising components leaving the column in a flame, the ions register as a change in current across two electrodes. In organic compounds, carbon ions are the primary source of a signal. Two chemically equivalent compounds, such as chiral enantiomers, will register identical signal strengths per unit amount present. FID detectors are extremely sensitive (2 pg C s^{-1})[117] yet have a wide signal range. Generally speaking, signals have linear relationships with the amount of a component in the detector. However, the response may become non-linear if component amounts vary by orders of magnitude. A quadratic signal to component concentration relationship was used in calibrations for experiments presented in Chapter 3 for this reason (see experiment 7.2.1.1, p104, and fitting comparison in Appendix, p138).

GC analyses presented in this thesis are performed as follows: All GC measurements were carried out using a Thermo Scientific TRACE 1310 instrument configured with an FID detector and the appropriate column (see specific experimental Chapter). Numeric integration and chromatographic calculations of the resulting peaks was performed using the supplied Chromeleon 7.1.2.1478 (Thermo Scientific Corporation) software package. GC methods for all chromatograms presented in this thesis are available in the Appendix (p126).

6.1.2 Analytical High-Performance Liquid Chromatography (HPLC)

In HPLC, both the analyte and the mobile phase are liquids or solutions. Samples are injected onto the column and pushed through, at high pressures, with a liquid mobile phase. HPLC columns generally contain densely packed solid particles of stationary phase.

While HPLC may not have the raw separating efficiency of GC techniques, there is a wider selection of specialist HPLC stationary phases which have strong selectivity towards certain chemical mixtures. More importantly, HPLC is capable of analysing

compounds with high boiling points, such as **CC3**. In Chapter 3, HPLC is used to measure the amount of **CC3** dissolved in experimental mixtures during a host-guest exchange process.

HPLC analyses presented in this thesis are performed as follows: All HPLC measurements were carried out using a UltiMate 3000 system (Dionex) attached with a UV/Vis diode array detector and equipped with a Syncronis C8 column (150 x 4.6 mm, 3 um, Thermo Scientific, SN 10136940, Lot 12459). The mobile phase was methanol at a flow rate of 0.5 mL min^{-1}. The injection volume was 5 μL and samples were prepared as described in respective carryouts. The column oven temperature was set to 30 °C. The resulting chromatogram was collected from UV absorbances at 254 nm. Peak areas were computed using the supplied Chromeleon 6.80 SR11 Build 3163 (Dionex) HPLC software.

6.1.3   Analytical Gel-Permeation Chromatography (GPC)

Like HPLC, solutions are injected onto the column and pushed through, at high pressure, with a liquid mobile phase in GPC. Unlike HPLC, GPC columns contain gels which separate components by size rather than chemical affinity. GPC was identified to be capable of separating cage compounds by their relative size and is used in Chapter 2 to analyze complex reaction mixtures containing a range of cage-sized products.

GPC analyses presented in this thesis are performed as follows: All GPC measurements were carried on a TDA Model 302 (Viscotek) attached with a refractive index detector and equipped with a ViscoGEL HHR-H guard column and two ViscoGEL GMHHR-H columns fitted in series. The mobile phase was chloroform at a flow rate of 1 mL min^{-1}. The injection volume was 100 μL and samples were prepared by dissolving into chloroform to a concentration of *c.a.* 1 mg mL^{-1} followed by filtration through a 0.2 μm PTFE syringe filter. The column oven temperature was set to 30 °C. Detector calibration was performed using a low molecular weight narrow polystyrene standard (99 kDa). Signals were recorded using the OmniSEC 4.6 software suite.

6.2   Crystallography

Crystallography is a science that examines the arrangement of atoms in solids. Provided molecules pack into a regular motif with long-range order, the resulting solid will diffract x-rays. Diffraction patterns may be analysed by a variety of methods to elucidate packing geometry and molecular structure.

6.2.1   Single-Crystal X-Ray Diffraction (scXRD)

scXRD is used to calculate the atomic structure of molecules within crystallised solids. Here, a two-dimensional x-ray detector measures diffracted x-rays from a single crystal at a series of three-dimensional emitter-detector angles. The resulting diffraction patterns (e.g. Figure 6-2) can be used to calculate the structure of packed molecules within the crystal. Fundamentally, these calculations are based on principles of symmetry, reciprocal space, and Bragg's law; however, modern-day crystallography will also involve a range of computational algorithms to refine scXRD datasets (e.g. SHELXD in preparation below).

A greater degree of crystal structure information is elucidated from scXRD than PXRD measurements but the former is representative of a single crystal, not a bulk quantity of sample. Consequently, it is common to use both techniques together. scXRD datasets can be computed into PXRD patterns for comparison with experimental measurements of bulk crystallinity.

scXRD is used in two Chapters of this thesis: in Chapter 3, where it is used to measure guest occupation in **CC3**'s structure after exposure to a variety of mixtures; and in Chapter 2, where it is used to elucidate the structure of **CCX**-*S*.
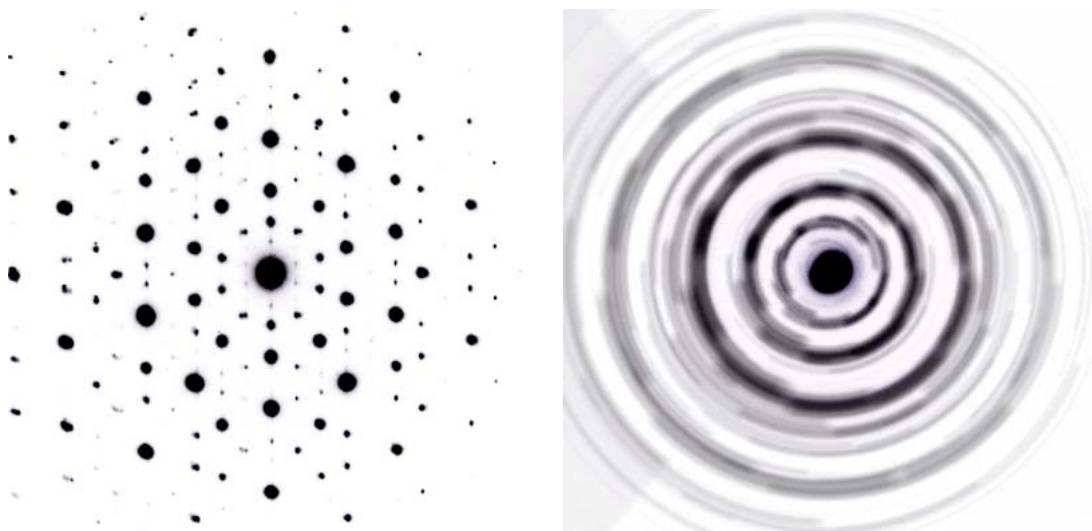
Figure 6-2 | scXRD (left) and PXRD (right) diffraction patterns. In scXRD, three-dimensional datasets are taken at each angle in order to calculate the three-dimensional arrangement of atoms in a crysal structure. By contrast, because crystallites are randomly organised in a powder, less information about the crystal structure can be calculated from PXRD measurements. However, powders are more easily attainable and PXRD measurements are generally easier to perform.

sxXRD analyses presented in this thesis are performed as follows: scXRD data was measured on a Rigaku MicroMax-007 HF rotating anode diffractometer (Mo-Kα radiation, λ = 0.71073 Å, Kappa 4-circle goniometer, Rigaku Saturn 724+ detector) or, if stated, at beamline I19, Diamond Light Source, Didcot, UK, using silicon double crystal monochromated synchrotron radiation (λ = 0.6889 Å). Empirical absorption corrections using equivalent reflections were performed with the program SADABS. Structure were solved with SHELXD,[154] or by direct methods using SHELXS,[154] and reined by full-matrix least squares on F^2 by SHELXL,[154] interfaced through the program OLEX2. Unless stated, all non-H atoms were refined anisotropically and H atoms were fixed in geometrically estimated positions using the riding model. In the absence of heavy scatters Friedel pairs were merged.

6.2.2   Powder X-Ray Diffraction (PXRD)

In PXRD, a detector measures the intensity of diffracted x-rays from a powder irradiated at a series of emitter-detector angles. In contrast to scXRD, PXRD yields a one-dimensional dataset – random orientation of particles within a powder prevents two-dimensional detectors (as in scXRD) from yielding the same amount of information for each angle of rotation (Figure 6-2). Consequently, while molecular structures may be calculated from PXRD patterns,[155] it is significantly more difficult to do so.

It is usually easier to produce powders from experiments than single crystals. PXRD measurements are usually faster to perform than equivalent scXRD preparations. Because of this, it is routinely used to measure sample phase during experimental preparations. In Chapter 3, PXRD is used to measure the phase of **CC3** during host-guest exchange processes. In Chapter 2, it is used to measure the crystallinity of synthetic products.

PXRD analyses presented in this thesis are performed as follows: High-quality PXRD data were collected in transmission geometry on a Bruker D8 Advance diffractometer with Ge-monochromated Cu $K\alpha_1$ radiation and a LynxEye PSD on samples held between Mylar films. Data were collected in the range 4° ≤ 2θ ≤ 50° with a step size of 0.013° over 2 hours. Lower quality HT PXRD data were collected in transmission geometry on a PANalytical X'Pert PRO multi-purpose diffractometer with Cu $K\alpha_1$ radiation. Samples were ground and mounted as loose powder onto the transparent film of a 96-well aluminium plate. Data were collected in the range 4° ≤ 2θ ≤ 50° with a step size of 0.01° over one hour.

6.3   Nuclear Magnetic Resonance (NMR) Spectroscopy

In NMR, a sample in a deuterated solvent is placed in a magnetic field, irradiated to a higher energy state with a radio-frequency pulse, and allowed to relax back to the ground state while detectors record sample emissions. With further calculations, the measurements are used to calculate chemical environments in the sample.

NMR is used in this thesis to measure distinct chemical environments within a sample. In Chapter 3, it is used to measure any chemical changes in **CC3** during host-guest exchange processes. In Chapter 2, it is used to measure chemical differences between the products and reactants of HT synthetic procedures.

NMR analyses presented in this thesis are performed as follows: Deuterated chloroform was pre-treated with either silver foil or 3 Å molecular sieves to remove traces of acid. Deuterated dichloromethane was purchased in sealed ampules and used immediately. Trimethylsilane is used as an internal standard. ^{1}H NMR spectra were recorded at 400.13 MHz using a Bruker Avance 400 NMR spectrometer. ^{13}C NMR spectra were recorded at 100.6 MHz.

6.4   Scanning Electron Microscopy (SEM)

In SEM, detectors measure electrons emitted from a solid surface as an electron beam scans over it. The position of the beam is controlled throughout the process so recorded emissions represent surface properties at specific positions. These measurements are commonly used to elucidate the topography of a sample. Modern SEM instruments control the emitted beams position to a great degree of accuracy which directly corresponds to topographical accuracy. Measurements with resolutions of up to 50 nm are presented here.

SEM was used to accurately measure the topography of samples. In Chapter 3, SEM is used to measure morphological changes in **CC3** during various stages of host-guest exchange. In Chapter 4, it is used to measure the structure of GC columns containing *rac*-**CC3** nanoparticles.

SEM analyses presented in this thesis are performed as follows: Imaging was performed using a Hitachi S-4800 cold field emission scanning electron microscope (FE-SEM). Samples were prepared on 15 mm Hitachi M4 aluminium stubs using an adhesive high purity carbon tab. The samples were then coated with a 2 nm layer of gold using an Emitech K550X automated sputter coater. The FE-SEM measurement scale

bar was calibrated using certified SIRA calibration standards. Imaging was conducted at a working distance of 8 mm and a working voltage of 3 kV using a mix of upper and lower secondary electron detectors.

6.5 Mass Spectrometry

In mass spectrometry, samples are ionised and deflected through a strong magnetic field into a detector. The degree to which ions deflect in the field directly corresponds to their mass to charge ratio (m/z) - heavier, less charged, ions deflect less than lighter, highly charged, ones. Mass spectrometers accurately control the magnetic field to scan through a range of m/z's and record a full mass spectrum.

Mass spectrometry is used in Chapter 2 to identify a novel organic cage compound.

Mass spectra presented in this thesis are acquired as follows: Matrix-Assisted Laser Desorption/Ionization Time of Flight Mass Spectrometry (MALDI-TOF-MS) was carried out using a Shimadzu Biotech Axima Confidence in linear positive ion mode with dithranol as a matrix.

6.6 Fourier-Transform Infra-Red (FTIR) Spectroscopy

In FTIR, infra-red radiation at a range of wavelengths is passed through an experimental sample into a detector. In addition, a blank control sample undergoes the same routine. The difference in recorded intensity between these samples is calculated to yield a spectrum. Within particular wavelength ranges, absorptions are associated with chemical bonding modes. For example, absorptions between 1600 and 1700 cm^{-1} may indicate an imine (C=N) bond.

FTIR is used in this thesis to measure the bonding structure of a sample. In Chapter 3, FTIR is used to measure chemical changes in **CC3** during host-guest exchange processes. In Chapter 2, it is used to measure the presence of any new bonding modes from synthetic screens and to characterise a novel organic cage compound.

FTIR analyses presented in this thesis are performed as follows: All IR spectra were collected on a Bruker Tensor 27 spectrometer. Samples were analysed for 32 scans at a resolution of 4 cm^{-1} using an Attenuated Total Reflection (ATR) cell (Quest ATR GS10800, Specac corporation) or using a IR-transparent 96-well silicon plate analyzer (using a Bruker HTS-XT extension). The recorded wavenumber range was 4000-400 cm^{-1}.

6.7   Thermogravimetric Analysis (TGA)

In TGA, the weight of a sample is recorded as it is exposed to increasing temperatures. It was used to measure the solvent desorption temperature, guest desorption temperature, and thermal decomposition temperatures of samples. It is used in Chapter 3 to measure desorption of guest and solvent from **CC3** during host-guest exchange processes.

TGA analyses presented in this thesis are performed as follows: Analyses were carried out using a Q5000IR analyzer (TA instruments) with an automated vertical overhead balance. The samples were heated in air from room temperature to 300 °C at a rate of 10 °C min^{-1}.

6.8   Volumetric Adsorption Analysis

This analysis measures the amount of a gas (nitrogen, in this thesis) adsorbed by a sample. As a simplification, the technique presented measures the difference in pressure between experimental samples and expected values for the apparatus. It is used in Chapter 2 to measure the (negligible) porosity of a novel organic cage compound.

Volumetric adsorption analyses presented in this thesis are performed as follows: The sample surface area was tested using B.O.C. high purity nitrogen grade N5 (99.999 %). Surface area was measured by nitrogen adsorption and desorption at 77.3 K using a Quantachrome NOVA 4200e volumetric adsorption analyser. Samples were degassed offline at 120 °C for 12 h under vacuum (10-5 bar) before analysis.

6.9   Elemental Analysis

Elemental analysis measures the amount of carbon, hydrogen, and nitrogen in a sample. It is used in Chapter 2 (experiment 7.1.3.6) as part of characterising a novel organic cage compound.

Elemental analyses presented in this thesis are performed as follows: Analysis was carried out using a Thermo Flash EA1112 Elemental Analyser. Samples were analysed as dry powders and the resulting data was processed using Eager 300 dedicated elemental analysis software.

7 **Experimental Methods**

7.1   **Discovering Novel Organic Cages**

Diamines, dianilines, *tris*(4-formylphenyl)amine, and trifluoroacetic acid were purchased from Sigma Aldrich. 2,2,2-trifluoroethanol was purchased from Alfa Aesar. Benzene-1,3,5-tricarbaldehyde was purchased from Manchester Organics UK. Methanol, *N,N*-dimethylformamide, acetonitrile, chloroform, and dichloromethane were purchased from Fisher Scientific. All chemicals were used as received.

Additional trialdehyde compounds were synthesised for experiment 7.1.3.5. Using literature methods,[156,157] Paul Reiss synthesised both 2,4,6-trimethylbenzene-1,3,5-tricarbaldehyde (**L** in Figure 2-5, p33) and 2-chlorobenzene-1,3,5-tricarbaldehyde (**M**) for use in experiment 7.1.3.5. *tris*([1,1'-Biphenyl]-4-carbaldehyde) (**C**) for use in experiment 7.1.3.4 was synthesised by Michael Briggs using a literature method.[128]

7.1.1   **Characterization Methods**

No specialised parameters were used for any characterization methods. Information about equipment and methodology can be found in the characterization techniques Section. GPC was used to size-separate possible cage products from reactants (example chromatogram in main text, Figure 2-4, p33). NMR and FTIR were used across many experiments to analyze chemical changes pre- and post-screening. Gas Sorption and scXRD measurements were performed on the novel organic cage product of experiment 7.1.3.6.

7.1.2   **Computational Methods**

Throughout Chapter 2, modelling techniques and outputs are discussed. Modelling was performed by Kim Jelfs and a similar approach has been applied to other cage compounds.[135]

As a simplified explanation, a range of precursors were screened. Any precursors that appeared to be obtainable and, more importantly, plausible for cage-synthesis were shortlisted and combined *in-silico* with the assumption that they predictably form [2+3], [4+6], or [8+12] organic cage compounds via imine condensation. The resulting cage products were then energy minimised into a preferable geometry to produce the final result. Example results in main text, Figure 2-3 (p31).

7.1.3   Experimental Methods

The overall project aimed to augment computational modelling with HT techniques. HT screening experiments were performed on the Chemspeed Synthesizer SLT platform. Stock solutions stated in this Section were prepared to within 1 % error range using accurate mass balances, graduated pipettes, and microsryringes.

7.1.3.1   The experimental platform was prepared in the following manner

In all automated experiments, vial racks and the appropriate solvent bottles were fitted. Experiments 7.1.3.2, 7.1.3.4, and 7.1.3.5 use HT reactor arrays – double jacketed reactors which allow for temperature and (below ambient) pressure control. Reactor arrays are purged by heating to 200 °C under vacuum and back filling with nitrogen. This process is repeated three to five times. Reactors are cooled to the experimental temperature. Once all the apparatus is fitted the platforms chassis is filled with nitrogen for the duration of the experiment.

7.1.3.2   The Automated Synthesis of CC1 and CC3-*R*

Solutions of benzene-1,3,5-tricarbaldehyde, ethylene diamine, and (1*R*,2*R*)-cyclohexane-1,2-diamine in chloroform were each made to a concentration of 20 mmol L^{-1}. These solutions were loaded into the robotic platform. Reactors were then cooled to 0 °C for the duration of the experiment.

The robotic procedure was as follows. The diamine solutions were transferred into their respective reaction vessels (*V* = 18.9 mL). With stirring, the benzene-1,3,5-tricarbaldehyde solution was slowly (12.6 mL at a rate of 0.1 mL min^{-1}) added to each reaction vessel. After addition, the vessels were left stirring and cooled for 18 h followed by warming to room-temperature. Finally, the reaction mixtures were transferred into septa-sealed sample vials. 50 μL aliquots were taken for solvent-suppressed ^{1}H NMR. For comparison, **CC1** and **CC3**-*R* were also synthesised manually using previously described methods.[50,65]

7.1.3.3   Investigating Optimal Conditions for a Cage-Forming Reaction Between 4,4'-methylenedianiline and Benzene-1,3,5-tricarbaldehyde

A schematic of this experiment is available in main text (Figure 2-2, p30). The experiment focused on the reaction between benzene-1,3,5-tricarbaldehyde (**A**) and 4,4'-methylenedianiline (**B**).

For each solvent of interest, stock solutions of **A** (c = 90 mmol L^{-1}); trifluoroacetic acid (c = 1 µL mL^{-1}); and **B** (at three concentrations: 90, 50, or 10 mmol L^{-1}) were made. These stocks were filled into sample vials and placed into the robotic platform. Reactions were either performed in 40 mL sample vials or 10 mL microwave vials for room-temperature and raised-temperature experiments respectively.

The robotic procedure was as follows. Varying volumes of the **A** solutions were added to each reactor and diluted with their respective solvent to concentrations of 10, 50, or 90 mmol L^{-1}. After dilution, the total solution volume was 2.8 mL in all reactors. Half of the reactors received 0.1 mL of the trifluoroacetic acid solution while the other half received 0.1 mL of their respective solvent. Finally, the 4.2 mL of the applicable **B** solution was added to each reactor. The total reaction volume for all samples is 5.1 mL. Room temperature reactors were stirred using a vortex mixer and raised-temperature reactors were rapidly transferred onto the microwave apparatus after addition. Room-temperature reactions proceeded overnight (*c.a.* 18 h) while heated reactions proceeded for 3 h. 50 µL aliquots of each sample were taken for solvent-suppressed ^{1}H NMR analysis (example in main text, Figure 2-2, p30). 40 µL aliquots of each sample were spotted onto a 96-well aluminium plate for FTIR (reflectance) analysis (representative example in main text, Figure 2-2, p30).

7.1.3.4   Investigating Optimal Conditions for a Cage-Forming Reaction between Several Diamines and *tris*([1,1′-biphenyl]-4-carbaldehyde)

This experiment focused on the reaction of *tris*([1,1′-biphenyl]-4-carbaldehyde) (**C** in Figure 2-4, p33) with either ethylene diamine (**D**); (1*R*,2*R*)-cyclohexane-1,2-diamine (**E**); or 2,3-diaminopropane (**F**). Additionally, the reactant concentration and presence of catalyst (trifluoroacetic acid) was also varied.

Stocks containing the reactants were produced at a concentration of 20 mmol L^{-1} in chloroform. Additionally, a trifluoroacetic acid stock was made at a concentration of 1 µL mL^{-1} in chloroform. HT reactor arrays were prepared as outlined in 7.1.3.1. The reactors were cooled to 0 °C for the duration of the experiment and warmed to room temperature before product transfer into a sample vial.

The screening procedure was as follows. Varying volumes of the **C** stock were added to each reactor and diluted to concentrations of 2, 10, or 20 mmol L^{-1} with total volumes of 6.5, 5.9, or 2.8 mL respectively. Half of the reactors received 0.1 mL the

trifluoroacetic acid solution while the other half received 0.1 mL of solvent. Depending on concentration, 0.4, 1.0, or 4.1 mL of the appropriate diamine stock was added at a rate of 0.2 mL min^{-1} to each reactor with stirring. The final volume of all reaction mixtures was 7 mL. After addition, the reaction vessels were left cooled and stirring for 60 h. Samples were transferred from the reaction vessel into sample vials. Images of the resulting products can be found in the Appendix (Figure 10-1, p129). Samples were dried in a HT rotary evaporator and analysed by ^{1}H NMR, GPC, and FTIR (silicon transmission plate). Example results from this experiment can be found in the main text (Figure 2-4, p33); further examples are in the Appendix (p130).

7.1.3.5   Combinatorial Screen between Four Trialdehyde Compounds and Four Diamine Compounds with Varying Catalyst Presence

This experiment focused on sixteen combinations of 1,2-di(1-napthyl)-1,2-ethanediamine (**G** in Figure 2-5, p34), (11*R*, 12*R*)-9,10-ethanoanthracene-11,12-diamine (**H**), (3*S*, 4*S*)-3,4-diamino-1-benzopyrollidine (**I**), or *p*-xylylenediamine (**J**) with benzene-1,3,5-tricarbaldehyde (**A**), *tris*(4-formylphenyl)amine (**K**), 2,4,6-trimethylbenzne-1,3,5-tricarbaldehyde (**L**), or 2-chlorobenzene-1,3,5-tricarbaldehyde (**M**). Each combination is attempted both uncatalysed and catalysed by trifluoroacetic acid.

Stock solutions containing the reactants were prepared at a concentration of 15 mmol L^{-1} in chloroform. Additionally, a trifluoroacetic acid stock was made at a concentration of 1 μL mL^{-1} in chloroform. HT reactor arrays were prepared as outlined in 7.1.3.1. The reactors were cooled to 0 °C for the duration of the experiment and warmed to room temperature before being transferred into a sample vials.

The screening procedure is as follows. For each reactor, 2 mL of the appropriate trialdehyde solution was added. Half of the reactors received 0.1 mL of the trifluoroacetic acid solution while the other half received 0.1 mL of solvent. With stirring, 3 mL of the appropriate diamine solution was slowly added to the appropriate reactor at a rate of 0.1 mL min^{-1}. After addition, the reaction mixtures were left cooled and stirring for *c.a.* 60 h. Samples were transferred into sample vials. Images of the resulting products can be found in the Appendix (p131). Vials were dried in parallel on a HT rotary evaporator and the resulting solids were analysed by ^{1}H NMR (CDCl$_3$) and PXRD. Example results from this experiment can be found in the main text (Figure 2-6, p35); further examples are found in the Appendix (p132).

7.1.3.6   Synthesis, Isolation, and Characterization of a Novel [4+6] Cage Compound, CCX-*S*, Produced by Imine Condensation of (3*S*,4*S*)-3,4-Diamino-1-benzylpyrrolidine with Benzene-1,3,5-Tricarbaldehdye

This experiment focused on the scale-up and isolation of a novel cage compound produced by the one-pot imine condensation of benzene-1,3,5-tricarbaldehyde (**A** in Figure 2-5, p34) with (3*S*, 4*S*)-3,4-diamino-1-benzylpyrollidine (**I**). The reaction was initially performed in experiment 7.1.3.5 and, in order to accurately mimic the conditions used on a HT platform, the addition was performed using the Atlas scale-up platform (Syrris Corporation).

With stirring, a solution of **I** (670 mg) in chloroform (233 mL) was added at a rate of 0.1 mL min^{-1} to a solution of **A** (373 mg) in chloroform (153 mL) at room temperature. After addition, the reaction mixture was left stirring for 72 h. ^{1}H NMR of the mixture indicated no remaining **A**. The reaction mixture was observed to be a clear amber solution. This was concentrated on a rotary evaporator (90 mbar, 20 °C) to an approximate volume of 15 mL. With stirring, the resulting clear deep-amber concentrate was slowly (*c.a.* 1 mL min^{-1}) added to approximately 400 mL of stirred, ice-cooled, methanol to yield an off-yellow coloured precipitate. The mixture was mobilised into slurry and filtered through a glass frit. Analysis indicated that the filtrate primarily contained unreacted **I**. The filtered precipitate was dissolved in chloroform, filtered into a clean vessel, and dried by rotary evaporation (130 mBar, 20 °C) to yield a dry granular yellow solid. Further drying was performed (20 mBar, 20 °C) overnight. Yield: 886 mgs, 96 %; ^{1}H NMR (CD$_2$Cl$_2$, 400 MHz) δ 8.18 (s, 12H, -C*H*=N), 7.91 (s, 12H, -ArH), 7.44-7.18 (m, 30H, -ArH), 4.17-4.00 (m, 12H, -CH$_2$), 3.85 (d, *J*=13.1 Hz, 6H, -CH), 3.73 (d, *J*=13.1 Hz, 6H –CH), 3.11-2.91 (m, 24H, -CH$_2$) ppm; ^{13}C NMR (CD$_2$Cl$_2$, 100 MHz) δ 161.57, 139.87, 136.85, 130.25, 129.03, 128.62, 127.29, 76.96, 61.11, 58.82 ppm; FTIR (KBr pellet, ν) 3405 (br), 3271 (w), 3083 (w), 3059 (w), 3025 (w), 3059 (w), 3026 (w), 2953 (w), 2882 (s), 2792 (m), 1643 (v.s.), 1598 (m), 1494 (m), 1476 (w), 1450 (m), 1378 (m), 1322 (m), 1288 (w), 1257 (w), 1213 (m), 1151 (m), 1105 (m), 1071 (m), 1050 (m), 1027 (m), 969 (w), 969 (m), 911 (w), 890 (w), 866 (w), 811 (w), 754 (s), 698 (s), 529 (w), 481 (w), 460 (w) cm^{-1}; MALDI-TOF (dithranol) *m/z* 1582 Da for C$_{102}$H$_{102}$N$_{18}$ [M+H]$^+$, 3160 Da for C$_{204}$H$_{204}$N$_{36}$ [M]$^+$; Elemental analysis: C, 70.61; H, 6.01; N, 14.55 (Expected: C, 77.54; H, 6.51; N, 15.96); Surface area (7 point BET): 4 m^{2}g^{-1}.

7.1.3.7   Crystal Growth Attempts (CCX-*S*)

To identify an ideal solvent/antisolvent combination to crystallise **CCX**-*S*, a set of vial in vial vapour diffusion experiments were performed. **CCX**-*S* was dissolved in six different solvents: chloroform; dichloromethane; *N*,*N*-dimethylformamide; *N*-methylformamide; 2,2,2-trifluoroethanol; or *N*-methylacetamide at an average concentration of 3 mg mL⁻¹. 1.5 mL aliquots of these solutions were filled into 3 mL vials which were subsequently capped and pierced. The vials were lowered into larger vials containing 3 mL of an antisolvent. Seven antisolvents were attempted: pentane, hexane, diethyl ether, isopropyl ether, acetonitrile, acetone, or methanol which resulted in 42 (6 × 7) solvent/antisolvent combinations. The combination of 2,2,2-trifluoroethanol with methanol appeared to produce crystalline solids. Combinations involving methanol did appear to 'pip' which prompted further solvents to be investigated. One further combination, *N*,*N*-dimethylacetamide with methanol produced single crystals which were of high enough quality for scXRD refinement.

7.2   Organic Cages as Selective Sorbents

Xylene isomers, mesitylene, bromomesitylene, and racemic guest were purchased from Sigma-Aldrich and used as received. 1-*tert*-Butyl-3,5-dimethylbenzene was purchased from Sigma-Aldrich, purified by vacuum distillation (55 °C, 1.7 mbar), and stored over 4 Å molecular sieves. Acetonitrile, methanol, ethanol, hexane, and chloroform were purchased from Fisher Scientific and used as received.

Finely ground **CC3**-*R*, **CC3**-*S*, and *rac*-**CC3** were prepared according to methods described previously.[50] A chiral conglomerate of **CC3**, **CC3**-*R+S*, was prepared by accurately weighing equal amounts of solid **CC3**-*R* and **CC3**-*S* into a vial (average particle size approx. 0.5–200 μm) followed by gentle shaking to mix the particles. In contrast to the homochiral and chiral conglomerate cages the average particle size of *rac*-**CC3** was smaller, approximately 0.5–50 μm.

7.2.1   Characterization Methods

7.2.1.1   Gas Chromatography (GC)

GC is the primary technique used in Chapter 3. All GC measurements were carried out on the equipment as described in the characterization Section (6.1.1, p90). GC methods for any chromatograms shown in the main text can be found in the Appendix (p126).

7.2.1.1.1   Selective Adsorption Screening Measurements

Non-quantitative screening experiments were used to rapidly identify guest-host systems for further study. A schematic of this technique is available in the main text (Figure 3-1, p43). In most cases, **CC3** was prepared in a headspace vial using the technique described in Section 7.2.3.1. A small (< 1 equiv.) amount of guest was added using a microsyringe and the sample were re-weighed to calculate the number of moles of guest added. The sample was analysed by GC against a control containing only guest. The relative peak areas of each component in the guest was analysed and compared with the control sample. As discussed in the main text, this approach enabled identification of selective adsorption but could not be used to calculate the molar uptake, percentage adsorbed, etc.

7.2.1.1.2   Quantitative Selective Adsorption Measurements

This technique was used in several experiments: 7.2.3.5, 7.2.3.6, 7.2.3.7, 7.2.3.8 and 7.2.3.9. It involved using 1-*tert*-butyl-3,5-dimethylbenzene as a solvent which is too big to participate in host-guest exchange mechanisms. Discussion of the development of this technique is found in the main text. Examples of quantitative GC measurements can be found in the main text (e.g. Figure 3-9, p56) and the Appendix (e.g. Figure 10-14, p139). The technique measures the concentration of guest left in the solution phase after mixing with **CC3**. In the project, the technique was developed with a *rac*-1-PE guest and **CC3** host system. Bromomesitylene was used as an internal standard. Its concentration does not need to be accurately controlled; however, it does need to be consistent within an experiment. Usually, base stock solutions of bromomesitylene ($c \approx 2$ mg mL^{-1}) are made and all stocks, calibrations, etc. are made from it to maintain consistency.

In each experiment, calibration standards were accurately prepared and analysed by GC. The peak areas for the 1-PE enantiomers ($A_{R/S}$) and bromomesitylene (A_{BrMes}) were recorded for each calibration standard. The response factor of each enantiomer (f_i) was independently calculated (Equation 7-1, from ref. [117]) and plotted against half the stock concentration ($\frac{c_{rac}}{2} = c_{R/S}$). Quadratic fits of these plots yielded a relationship between chromatographically measured f_i values and sample (R/S)-1-PE concentrations. Y-intercepts of the fits were set to f_i values measured for blank ($c = 0$) samples to accommodate for trace impurities present in some solvents. Quadratic fits were used in preference to linear fits due to the large 1-PE concentration range between

stock solutions and post-adsorption solutions (fitting technique comparison in Appendix, p138).

$$f_{i(R/S)} = \frac{A_{R/S}}{A_{BrMes}}.$$

The resulting quadratic equation can be used to calculate the concentration of (*R/S*)-1-PE in samples from their measured peak areas. The difference between the moles of *rac*-1-PE added and moles remaining were assumed to be equal to the moles adsorbed into **CC3**. Values calculated in this manner compared well with values calculated from ^{1}H NMR analyses (GC: 1.00, ^{1}H NMR: 0.98 equivalents of 1-PE for a representative sample).

7.2.1.2   Other Characterization Methods

HPLC measurements were carried out as described in Section 6.1.2 (p91). HPLC was used in two experiments. Firstly, in 7.2.3.10 it is used to measure the solubility of **CC3**-*R* in four bulky solvents. Second, in 7.2.3.9 it was used to measure the amount of **CC3** dissolved into solution during host-guest exchange.

NMR measurements were carried out as described in Section 6.3 (p95). ^{1}H NMR measurements were performed in experiment 7.2.3.9 to analyze the chemical state of **CC3** during the host-guest exchange process at varying concentrations. It was also used to verify the guest-adsorbed amounts calculated by GC methods.

TGA measurements were carried out as described in Section 6.7 (p97). Measurements were performed in experiment 7.2.3.9 to analyze any changes in the thermal stability of **CC3** at several stages of host-guest exchange.

FTIR measurements were carried out as described in Section 6.6 (p96). An ATR cell was used for measurements. Measurements were performed in experiment 7.2.3.9 to analyze any chemical changes in **CC3** at several stages of host-guest exchange.

SEM imaging was carried out using the equipment described in Section 6.4 (p95). Images were recorded in experiment 7.2.3.9 to view the change in morphology of **CC3** (if any) during different stages of host-guest exchange.

scXRD was carried out using the equipment described in Section 6.2.1 (p93). Crystallisations of **CC3**-*R* in the presence of 1-PE were performed to yield a guest-adsorbed crystal structure that was compared with models. Both the measurements and subsequent crystallographic calculations were performed by Marc A. Little. The implementation can be found in the ESI of the related publication.[66]

PXRD measurements were carried out using the equipment described in Section 6.2.2 (p94). Diffraction patterns were recorded for a variety of **CC3** powders obtained from experiment 7.2.3.9 including the starting, guest-adsorbed, and guest-desorbed states of **CC3**-*R*, **CC3**-*S*, *rac*-**CC3**, and **CC3**-*R+S*.

7.2.2   Computational Methods

Computational modelling was utilised in experiment 7.2.3.9 to elucidate the source of selective adsorption between **CC3**-*R* and *rac*-1-PE. Modelling was performed by Linjiang Chen. This Chapter focuses on measuring selectivity with experimental techniques and, as such, does not go into depth about the implementation details of the modelling. However, a full explanation of how the modelling implementation can be found in the publication related to the experiment.[66]

7.2.3   Experimental Methods

For all experiments, accurate liquid additions were performed with the appropriate microsyringe, graduated pipette, or measuring cylinder to achieve addition errors below 1 %. Stock solutions were made using volumetric flasks with the same error constraints. Spot checks on the accuracy of the glassware were performed intermittently. All weight measurements were performed on an accurate mass (± 0.05 mg) balance. This same balance was used in all experiments and is calibrated/re-centered before each set of measurements.

Many of these experiments contained a large number of samples and duplicates. Because of this, mean values with standard deviations (σ) are presented to save space but give an idea of the magnitude of the numbers quoted.

7.2.3.1   Activated CC3 samples for use in the following experiments were prepared as followed.

Unless specified otherwise, **CC3** was used in a finely ground, dried, form. **CC3** is hygroscopic and, consequently, was re-activated in a vacuum oven before use in an experiment.

Pre-weighed vials were filled with a known amount of **CC3**. Samples were placed in a vacuum oven at 60 °C for 4 h followed by raising the temperature to 90 °C overnight (*c.a.* 18 h). Once cooled, the filled vials were weighed in order to accurately calculate the moles of **CC3** in each vial.

7.2.3.2   The selective adsorption of xylene isomers into CC3-*R* was investigated in the following manner.

An isomer mixture of *ortho-* (34 % *w/w*), *meta-* (31 %), and *para*-xylene (35 %) was made. Approximately 50 mg of **CC3**-*R* was placed into a headspace vial and prepared as in 7.2.3.1. A small droplet of the mixture was added from a glass pipette and the vial was sealed. The sample and the mixture were both analysed by GC and compared. Measured chromatograms are presented in main text, Figure 3-2 (p44).

7.2.3.3   Screening for chirally selective adsorption was achieved in the following manner.

Batches (> 20) of samples containing **CC3**-*R* were prepared as in 7.2.3.1. Small droplets of racemic mixtures were spotted onto the samples and mixed. Samples were left for several hours before analysis. Each sample was analysed by static headspace GC for deviations from *ee* = 0. Because the number of different mixtures is large (>50), GC methods were developed iteratively against control samples before use in screening experiments. Only racemic (*ee* = 0 ± 1 %) mixtures with baseline separation were used to measure chiral adsorption.

7.2.3.4   The selective adsorption of *rac*-3-hydroxytetrahydrofuran enantiomers into CC3 was investigated in the following manner.

CC3-*R*, **CC3**-*S*, and *rac*-**CC3** were placed in headspace vials and prepared as in 7.2.3.1. For each sample, a small (< 10 μL) droplet of *rac*-3-hydroxytetrahydrofuran was added from a glass pipette and the vial was sealed. Samples and a *rac*-3-hydroxytetrahydrofuran control were analysed by GC and compared to measure selective adsorption. Resulting chromatograms are presented in main text, Figure 3-3 (p46).

7.2.3.5   The effect of solvent on the exchange between *rac*-1-phenylethnaol and CC3-*R* was measured in the following manner.

The effect of solvent was tested for seven solvents: ethanol; hexane; *o*-xylene; *m*-xylene; mesitylene; 3,5-di-*tert*-butyltoluene; and 1-*tert*-butyl-3,5-dimethylbenzene. In each case, **CC3**-*R* was prepared as in 7.2.3.1 ($\bar{w}$ = 38.6 σ 0.5 mg).

Stock solutions for addition to the **CC3**-*R* samples were prepared. Stocks of *rac*-1-PE ($\bar{c}$ = 36.5 σ 0.9 µmol mL^{-1}) and bromomesitylene in the solvent of interest were prepared. These solutions were added to the samples to give an equimolar ratio of *rac*-1-PE to **CC3**-*R* ($\bar{V}$ = 0.93 σ 0.04 mL). The resulting slurries were stirred for 18 h at room temperature and filtered through a 0.2 µm PTFE syringe filter. The filtrates were analysed by GC as in 7.2.1.1.2 to measure the *ee* and amount of *rac*-1-PE adsorbed.

In most cases, the samples (and calibrations) were sampled as liquid injections. However, due to its high boiling point, 3,5-di-*tert*-butyl-toluene had a broad solvent peak. To rectify this, samples with this solvent were sampled as headspace injections. As the calibrations are ran in the same manner, this should have no overall effect on the results. Results are presented in the main text, Figure 3-5 (p48).

7.2.3.6   The effect of equilibration temperature between *rac*-1-PE and CC3-*R* was investigated in the following manner.

Five equilibration temperatures were investigated in duplicate: 40, 55, 60, 75, 90, 105 °C. Ten **CC3**-*R* samples were prepared as in 7.2.3.1 ($\bar{w}$ = 28.7 σ 0.6 mg). To each sample, a stock solution of *rac*-1-PE (36.08 µmol mL^{-1}) and bromomesitylene in 1-*tert*-butyl-3,5-dimethylbenzene was added ($\bar{V}$ = 0.71 σ 0.01 mL) to achieve an equimolar ratio of *rac*-1-PE to **CC3**-*R*. The resulting slurry was placed in an incubator at the temperature of interest for two hours. Static headspace samples were taken directly from the incubator for GC analysis.

Calibrations were prepared in triplicate. Calibration standards were prepared at *rac*-1-PE concentrations of 0, 18.04, and 36.08 µmol mL^{-1} and used to produce a calibration curve to calculate the amount of (*R/S*)-1-PE adsorbed into **CC3**-*R*. Because headspace concentration is heavily affected by incubation temperature,[138] independent calibrations were taken for each temperature of interest (R^2 > 0.98 in all cases). Samples were analysed as in 7.2.1.1.2 to measure the *ee* and amount of 1-PE adsorbed. Results are presented in main text, Figure 3-6 (p51).

7.2.3.7   The effect of host-guest equilibration time between *rac*-1-PE and CC3-*R* was investigated in the following manner.

Four equilibration times were investigated in triplicate: 8, 52, 1400, and 2800 minutes. The stock and calibration solutions from 7.2.3.6 were used in this experiment. Twelve **CC3**-*R* samples were prepared as in 7.2.3.1 ($\bar{w}$ = 25.0 σ 0.5 mg). To each sample, the

stock solution was added to achieve an equimolar ratio of *rac*-1-PE to **CC3**-*R* ($\bar{V}$ = 0.62 σ 0.01 mL) and stirred for the equilibration time of interest. After stirring, the resulting slurries were filtered through a 0.2 μm PTFE syringe filter. Filtrates and calibrations were analysed as in 7.2.1.1.2 to measure the *ee* and amount of 1-PE adsorbed.

It is assumed that any host-guest process is halted after filtration. Therefore, mixing time is equivalent to the host-guest equilibration time. Results are presented in main text, Figure 3-6 (p51).

7.2.3.8   The effect of guest equivalents on the equilibration between *rac*-1-PE and CC3-*R* was investigated in the following manner.

Seven *rac*-1-PE : **CC3**-*R* molar ratios were investigated in duplicate: 8, 4, 2, 1, 0.5, 0.25, and 0.125. Fourteen samples containing **CC3**-*R* were prepared as in 7.2.3.1 ($\bar{w}$ = 29.0 σ 0.5 mg).

A stock solution of bromomesitylene in 1-*tert*-butyl-3,5-dimethylbenzene was made. Seven solutions of *rac*-1-PE in the stock were made at different accurate concentrations: 216.19, 108.10, 54.05, 27.02, 13.51, 6.76, and 3.38 μmol L⁻¹. These solutions were used for both the host-guest exchange process and GC calibration. Calibration was performed as described in 7.2.1.1.2 (R^2 = 0.99). The stock solutions were added to the samples to achieve the molar ratios of interest. After addition, samples were mixed for 18 h and filtered through a 0.2 μm PTFE syringe filter. Filtrates and calibrations were analysed as in 7.2.1.1.2 to measure the *ee* and amount of 1-PE adsorbed.

Each stock concentration was used to produce a desired guest:host ratio in the addition step; for example, the 216.9 μmol mL⁻¹ solution was used to produce 8:1 guest:host ratio slurries. This means that, for all guest:host equivalents within the experiment, the overall volume of the slurry did not greatly differ ($\bar{V}$ = 0.960 σ 0.02 mL). This helped to remove any differences in mixing efficiency between samples and increase reproducibility of the data. A comparison with the values measured in 7.2.3.9 is available in the Appendix (p138-139). Results are presented in main text, Figure 3-6 (p51).

7.2.3.9 A comprehensive study into the selective adsorption of *rac*-1-PE into several forms of CC3 was performed in the following manner.

The results generated by this experiment were used directly in a Nature Materials publication. [66] Additional studies of the host-guest behaviour of **CC3**, which are not discussed in the main text of this thesis, can be found in the Electronic Supplementary Information (ESI) of that publication.

A schematic of this process is available in the main text (Figure 3-8, p55). This experiment investigated the selective adsorption of *rac*-1-PE enantiomers into **CC3**-*R*; **CC3**-*S*; *rac*-**CC3**; and **CC3**-*R+S*; a chiral conglomerate of **CC3**-*R* and **CC3**-*S*, at seven different *rac*-1-PE to **CC3** molar ratios. It can be seen as an expanded version of experiment 7.2.3.8; consequently, data-set comparisons are available in the Appendix (p138-139). The ratios investigated were 2, 1.75, 1.5, 1.25, 1, 0.75, 0.5. Each sample was prepared in triplicate for GC analysis with additional samples prepared in parallel for other analyses. GC analysis was used to quantify the uptake of 1-PE into **CC3**. There are three distinct stages of interest: pre-exchange, post-exchange (guest-adsorbed **CC3** and guest-depleted filtrate), and post-removal (guest-removed **CC3** and guest-washout filtrate). The phase, morphology, and chemical composition of **CC3** were measured by PXRD, scXRD, SEM, ^{1}H NMR, TGA, and FTIR at all stages.

A stock solution of bromomesitylene in 1-*tert*-butyl-3,5-dimethylbenzene was made. Seven solutions of *rac*-1-PE in the stock were made at different accurate concentrations: 56.67, 49.87, 42.50, 35.70, 28.34, 21.25, and 15.59 µmol mL^{-1}. These were used for both the host-guest exchange process and for GC calibration. In addition, four lower-concentration solutions were made by serial dilution for exclusive use in GC calibration: 7.79, 3.90, 1.95, and 0.97 µmol mL^{-1}. Calibration was performed as described in 7.2.1.1.2 ($R^2 = 0.99$).

CC3 was prepared as in 7.2.3.1 ($\bar{w} = 30.3$ σ 0.7 mg). The stock solutions were added to samples to achieve the molar ratios of interest. After addition, samples were mixed for 18 h and filtered through a glass-fiber disc. The filtrates were analysed as in 7.2.1.1.2 to measure the *ee* and amount of 1-PE adsorbed (Figure 3-9, p56, for representative chromatograms). Additionally, HPLC analysis was performed on the filtrates to measure the dissolution of **CC3** into the exchange mixture (results presented in Figure 3-13, p59). These filtrates are referred to as *guest-depleted* while the filtered solids are referred to as *guest-adsorbed* **CC3**.

As in 7.2.3.8, each concentration was chosen to produce the desired guest:host ratio in the later experimental steps; for example, the 56.67 µmol mL^{-1} solution was used to produce 2:1 guest:host ratio slurries. This means that, for all guest:host equivalents, the overall slurry volume did not greatly differ (V = 0.95 σ 0.03 mL).

1-PE was removed from guest-adsorbed **CC3** by displacement with acetonitrile. 1 mL of acetonitrile was added to guest-adsorbed **CC3** solids (a large excess) followed by the same mixing and filtration procedure to extract the adsorbed 1-PE into the solution phase. The resulting *guest-washout* filtrates were analysed by GC to calculate the *ee* of 1-PE desorbed from **CC3** (Figure 3-10, p56, for representative chromatograms). The *ee* values measured in this manner were in-line with predictions from atomistic simulations (GC: 29 %, simulated: 24–32 %; graphical representation in main text, Figure 3-18, p64) and aligned well with values calculated from the guest-depleted filtrates (comparison in main text, Figure 3-11, p57). Additionally, HPLC analysis was performed on the acetonitrile filtrates to measure the dissolution of **CC3**; however, no **CC3** was observed in the resulting chromatogram.

As an alternative to the above technique it was investigated if 1-PE could be removed in a vacuum oven. Guest-adsorbed **CC3** was placed in a vacuum oven at 90 °C overnight and the resulting guest-desorbed **CC3** solids were analysed and, compared to guest-washout **CC3** samples, no chemical change could be observed (see Appendix, p140).

7.2.3.10 The solubility of CC3-*R* in mesitylene; 1-*tert*-butyl-3,5-dimethyl benzene; and 3,5-di-*tert*-butyltoluene was investigated in the following manner.

Excess **CC3**-*R* ($\bar{w}$ = 20 σ 5 mg) was placed into vials containing (1.5 ± 0.02) mL of mesitylene; 1-*tert*-butyl-3,5-dimethyl benzene; or 3,5-di-*tert*-butyltoluene. Samples were prepared in duplicate. The resulting slurries were stirred for 18 h to reach saturation point and filtered through a 0.2 µm PTFE syringe filter. (90 ± 2) µL aliquots of the filtrates were added to (900 ± 10) µL of methanol to give the final samples for HPLC analysis. Each sample was analysed in duplicate to yield four data points per **CC3**-*R* : solvent combination.

Five calibration standards were prepared at varying concentrations: 1, 0.5, 0.25, 0.125, and 0.0625 mg mL^{-1}. These standards were analysed in duplicate by HPLC to produce

a linear calibration curve (R^2 = 0.97) which was used to calculate the saturation concentration of **CC3**-*R* in each analyte sample.

Mean saturation values were as follows (standard error in parenthesis): mesitylene = 3.31 (0.086); 1-*tert*-butyl-3,5-dimethylbenzene = 0.67 (0.009); 3,5-di-*tert*-butyltoluene = 0.04 (0.004) mg mL^{-1}.

7.3   Chromatographic Separations with Organic Cages

Xylene isomers, alkane isomers, dichloromethane, SP-2100, blank intermediate-polarity fused-silica columns (15 m × 0.25 mm, Supelco, Cat. 25760-U), and racemic mixtures were purchased from Sigma Aldrich and used as received. **CC3**-*R* was synthesised as described previously.[50] A suspension of *rac*-**CC3** nanoparticles in dichloromethane was synthesised as described previously.[50] As a brief summary, two 5 mg mL^{-1} solutions of **CC3**-*R* and **CC3**-*S* were rapidly combined, with stirring, at -78 °C. The resulting suspension of *rac*-**CC3** nanoparticles was warmed to room temperature and used in the preparation of a GC capillary column (7.3.4.3).

7.3.1   Characterization Methods

7.3.1.1   Gas Chromatography (GC)

GC is the primary technique presented in Chapter 4. The instrumentation and setup is described in Section 6.1.1 (p90). No specialised equipment was required to fit the custom-made **CC3** columns discussed in this Chapter. A variety of GC methods were used to produce the chromatograms presented in the main text, a summary of all methods can be found in the Appendix (p126).

7.3.1.2   Scanning Electron Microscopy (SEM)

SEM was used to image the GC column and control columns produced in experiment 7.3.4.3. Instrumentation and setup is described in Section 6.4 (p95). In each case, a specialised SEM stub containing a clamp was used to help mount GC capillaries vertically. GC columns were carefully cut with a ceramic column cutter to give a relatively clean break. Small pieces of double-sided graphite tape were placed on the inner edge of the clamp and the small (*c.a.* 1 cm) cuttings were mounted vertically and clamped.

7.3.2   Computational Methods

Computational simulations were carried out by Linjiang Chen. A full explanation of the methodology, **<u>written by Linjiang</u>**, is available in the Appendix (10.4.1).

7.3.3 Association thermodynamics from Van't Hoff relationships

Equation 7-3 was used to calculate association enthalpies from column elution. It is derived from the Van't Hoff equation (Equation 7-2) by substitution of the equilibrium constant with the retention factor/phase ratio relationship (Equation 7-4).[117]

$$-RT \ln K = \Delta H^0 - T\Delta S^0 \qquad \text{Equation 7-2}$$

Rearrange
$$\ln K = -\frac{\Delta H^0}{RT} + \frac{\Delta S^0}{R}$$

Substitute
Equation 7-4
$$\ln k\beta = -\frac{\Delta H^0}{RT} + \frac{\Delta S^0}{R}$$

Rearrange
$$\ln k = -\frac{\Delta H^0}{RT} + \frac{\Delta S^0}{R} - \ln \beta \qquad \text{Equation 7-3}$$

Relationships Used:

$$k = \frac{t - t_0}{t_0}$$

$$\beta = \frac{d_c}{4d_f}$$

$$K = k\beta \qquad \text{Equation 7-4}$$

Where R is the gas constant, T is the absolute temperature, K is the equilibrium constant for association, ΔH^0 is the standard enthalpy of association, ΔS^0 is the standard entropy change of association, k is the retention factor, t is the retention time of the analyte, t_0 is the retention time of an un-retained compound on the column, β is the phase ratio, d_c is the column's internal diameter (ID), and d_f is the film thickness of the stationary phase.

Based on these relationships, a plot of $\ln k$ against $1/T$ should be linear with a gradient of $\Delta H^0/R$ and an intercept of $(\Delta S^0/R) - \ln \beta$. Experimentally, a series of separations with controlled isothermal GC oven methods were performed. These yielded k values for each temperature of interest. From these measurements, ΔH^0 was calculated from the gradient. To calculate ΔS^0 from the intercept, the phase ratio must be known. It was calculated using Equation 7-5 from a literature source.[117]

$$d_\text{f} = 2.5 \times d_\text{c} \times (\% \text{ conc. of coating sol}^\text{n}) \qquad \text{Equation 7-5}$$

For the **CC3**-*R* coated column, based on a coating solution of 3 mg mL^{-1} and a 0.25 mm ID column, the phase ratio was calculated to be 1333.3. For the *rac*-**CC3** particle-coated column, based on a coating solution of 1 mg mL^{-1} and 0.25 mm ID column, the phase ratio was calculated to be 4000. In the latter case, the effect of SP-2100 on the phase ratio is assumed to be minimal because it has no effect on the separation and does not significantly decrease the columns ID. Thermodynamic values calculated using these relationships are presented in the main text (p70 & p82).

7.3.4   Experimental Methods

7.3.4.1   Producing a GC Column

Prototype GC columns produced in this Chapter were made with the static coating technique.[117] A blank intermediate-polarity fused-silica capillary column was cut open at both ends. One end of the column was immersed into the loading mixture while the other end was exposed to a vacuum to pull the solution through. Once droplets were observed at the vacuumed end, the vacuum was released and one end of the column was flame sealed closed. The column was immersed in a water bath set to 30 °C and its open end was exposed to a vacuum to begin the removal of volatile solvent. Finished columns were conditioned on the gas chromatograph by heating to 40 °C for 20 min, raising the temperature to 180 °C at 10 °C min^{-1}, and maintaining that temperature for a further 30 min under a 1 mL min^{-1} helium flow.

7.3.4.2   The Preparation of a GC Column Containing a Coating of CC3-*R*

Two columns containing a solid coating of **CC3**-*R* were produced as described in Section 7.3.4.1. The loading solutions for each column contained different amounts of **CC3**-*R* in dichloromethane (3 mg mL^{-1} or 6 mg mL^{-1}). Both were filtered through a 0.2 μm PTFE syringe filter before loading. A comparison between the two resulting columns can be found in the main text (Figure 4-1, p70). Chiral separations in the main text were performed on the column produced from the 3 mg mL^{-1} loading solution.

7.3.4.3 The Preparation of a GC Column Containing a Coating of *rac*-CC3 Nanoparticles

A 5 mg mL^{-1} suspension of *rac*-**CC3** nanoparticles was prepared as previously described.[50] The suspension was diluted to 1 mg mL^{-1} with dichloromethane. SP-2100 was added until its concentration was 2.5 mg mL^{-1}. The resulting loading mixture was used to produce a GC column as described in 7.3.4.1. This column was used to separate a variety of achiral mixtures described in the main text (*e.g.* linear alkanes, Figure 4-2, p71). Cuttings of this column were taken for SEM analysis as described in 7.3.1.2.

7.3.4.4 Investigating Separations with CC3 GC Columns

The **CC3** GC columns produced were a standard fused-silica capillary format. As a result of this, they required no special handling and were fitted as normal. Mixtures were placed into a GC headspace vial and static headspace samples were taken as described in 7.3.1.1. No solvent was used in these separations. Discussion around the resulting separations can be found in the main text. GC methods available in Appendix (p126).

7.3.4.5 Investigating CC3 GC Column Durability

Both the **CC3**-*R* column (3 mg mL^{-1}) and *rac*-**CC3** nanoparticle columns' durability were tested in the following manner. For the **CC3**-*R* column, *rac*-3-hydroxytetrahydrofuran was placed into a headspace vial and eluted through the column 36 times (results presented in main text, Figure 4-13, p83). For the *rac*-**CC3** column, a hexane isomer mixture was placed into a headspace vial and eluted through the column 50 times (results presented in main text, Figure 4-14, p84). As a general observation, no change in selectivity or retention was observed for either during their use (>400 injections).

7.3.4.6 The Preparation of a GC Column Containing a Coating of CCX-*S*

CCX-*S* was prepared as described in Section 7.1.3.6 (p102). A 2 mg mL^{-1} solution of **CCX**-*S* in dichloromethane was made and filtered through a 0.2 μm PTFE syringe filter. This loading mixture was used to produce a GC column as described in 7.3.4.1. The resulting column was found to retain racemic mixtures but was unable to perform chiral separations (see Appendix p143).

8 **References**

[1]   T. C. Drage, C. E. Snape, L. A. Stevens, J. Wood, J. Wang, A. I. Cooper, R. Dawson, X. Guo, C. Satterley, R. Irons, *J. Mater. Chem.* **2012**, *22*, 2815–2823.

[2]   J. Graetz, *Chem. Soc. Rev.* **2008**, *38*, 73–82.

[3]   Z. R. Herm, E. D. Bloch, J. R. Long, *Chem. Mater.* **2014**, *26*, 323–338.

[4]   R. S. Middleton, G. N. Keating, P. H. Stauffer, A. B. Jordan, H. S. Viswanathan, Q. J. Kang, J. W. Carey, M. L. Mulkey, E. J. Sullivan, S. P. Chu, et al., *Energy Environ. Sci.* **2012**, *5*, 7328–7345.

[5]   R. M. Davidson, *Post-Combustion Carbon Capture from Coal Fired Plants: Solvent Scrubbing*, IEA Clean Coal Centre, **2007**.

[6]   C. Wang, H. Luo, D. Jiang, H. Li, S. Dai, *Angew. Chem. Int. Ed.* **2010**, *49*, 5978–5981.

[7]   K. S. W. Sing, *Pure Appl. Chem.* **1985**, *57*, 603–619.

[8]   A. Taguchi, F. Schüth, *Microporous Mesoporous Mater.* **2005**, *77*, 1–45.

[9]   R. C. Schroden, M. Al-Daous, S. Sokolov, B. J. Melde, J. C. Lytle, A. Stein, M. C. Carbajo, J. T. Fernández, E. E. Rodríguez, *J. Mater. Chem.* **2002**, *12*, 3261–3267.

[10]   R. Krishna, *Chem. Soc. Rev.* **2012**, *41*, 3099–3118.

[11]   N. B. McKeown, P. M. Budd, D. Book, *Macromol. Rapid Commun.* **2007**, *28*, 995–1002.

[12]   D. M. D'Alessandro, B. Smit, J. R. Long, *Angew. Chem. Int. Ed.* **2010**, *49*, 6058–6082.

[13]   A. Corma, *Chem. Rev.* **1997**, *97*, 2373–2420.

[14]   M. D. Ward, *Chem. Commun.* **2009**, 4487–4499.

[15]   S. L. James, *Chem. Soc. Rev.* **2003**, *32*, 276–288.

[16]   A. Phan, C. J. Doonan, F. J. Uribe-Romo, C. B. Knobler, M. O'Keeffe, O. M. Yaghi, *Acc. Chem. Res.* **2010**, *43*, 58–67.

[17]   T. Kyotani, *Carbon* **2000**, *38*, 269–286.

[18]   S. Shinkai, *Tetrahedron* **1993**, *49*, 8933–8968.

[19]   A. I. Cooper, *Adv. Mater.* **2009**, *21*, 1291–1295.

[20]   X. Feng, X. Ding, D. Jiang, *Chem. Soc. Rev.* **2012**, *41*, 6010–6022.

[21]   K. Kim, N. Selvapalam, Y. H. Ko, K. M. Park, D. Kim, J. Kim, *Chem. Soc. Rev.* **2007**, *36*, 267–279.

[22]   S. Xu, Y. Luo, B. Tan, *Macromol. Rapid Commun.* **2013**, *34*, 471–484.

[23]   N. B. McKeown, P. M. Budd, *Chem. Soc. Rev.* **2006**, *35*, 675–683.

[24]   T. Ben, S. Qiu, *CrystEngComm* **2012**, *15*, 17–26.

[25]   G. Zhang, M. Mastalerz, *Chem. Soc. Rev.* **2014**, *43*, 1934–1947.

[26]   M. E. Davis, *Microporous Mesoporous Mater.* **1998**, *21*, 173–182.

[27]   S. Wang, Y. Peng, *Chem. Eng. J.* **2010**, *156*, 11–24.

[28]   J. V. Smith, *Chem. Rev.* **1988**, *88*, 149–182.

[29] R. J. Argauer, G. R. Landolt, *Crystalline Zeolite Zsm-5 and Method of Preparing the Same*, **1972**, US3702886 A.

[30] T. F. Degnan, G. K. Chitnis, P. H. Schipper, *Microporous Mesoporous Mater.* **2000**, *35–36*, 245–252.

[31] P. B. Venuto, *Microporous Mater.* **1994**, *2*, 297–411.

[32] Z. R. Herm, B. M. Wiers, J. A. Mason, J. M. van Baten, M. R. Hudson, P. Zajdel, C. M. Brown, N. Masciocchi, R. Krishna, J. R. Long, *Science* **2013**, *340*, 960–964.

[33] G. J. de A. A. Soler-Illia, C. Sanchez, B. Lebeau, J. Patarin, *Chem. Rev.* **2002**, *102*, 4093–4138.

[34] J. Caro, M. Noack, P. Kölsch, R. Schäfer, *Microporous Mesoporous Mater.* **2000**, *38*, 3–24.

[35] O. M. Yaghi, M. O'Keeffe, N. W. Ockwig, H. K. Chae, M. Eddaoudi, J. Kim, *Nature* **2003**, *423*, 705–714.

[36] B. F. Hoskins, R. Robson, *J. Am. Chem. Soc.* **1990**, *112*, 1546–1554.

[37] R. W. Gable, B. F. Hoskins, R. Robson, *J. Chem. Soc. Chem. Commun.* **1990**, 1677–1678.

[38] H. Li, M. Eddaoudi, M. O'Keeffe, O. M. Yaghi, *Nature* **1999**, *402*, 276–279.

[39] H. Furukawa, K. E. Cordova, M. O'Keeffe, O. M. Yaghi, *Science* **2013**, *341*, 1230444.

[40] J.-R. Li, J. Sculley, H.-C. Zhou, *Chem. Rev.* **2012**, *112*, 869–932.

[41] G. Férey, *Chem. Soc. Rev.* **2007**, *37*, 191–214.

[42] M. P. Suh, H. J. Park, T. K. Prasad, D.-W. Lim, *Chem. Rev.* **2012**, *112*, 782–835.

[43] P. Horcajada, C. Serre, M. Vallet-Regí, M. Sebban, F. Taulelle, G. Férey, *Angew. Chem. Int. Ed.* **2006**, *45*, 5974–5978.

[44] B. Chen, S. Xiang, G. Qian, *Acc. Chem. Res.* **2010**, *43*, 1115–1124.

[45] L. R. MacGillivray, C. M. Lukehart, *Metal-Organic Framework Materials*, John Wiley & Sons, **2014**.

[46] Y. Yu, Y. Ren, W. Shen, H. Deng, Z. Gao, *TrAC Trends Anal. Chem.* **2013**, *50*, 33–41.

[47] N. A. Rakow, M. S. Wendland, J. E. Trend, R. J. Poirier, D. M. Paolucci, S. P. Maki, C. S. Lyons, M. J. Swierczek, *Langmuir* **2010**, *26*, 3767–3770.

[48] T. Mitra, X. Wu, R. Clowes, J. T. A. Jones, K. E. Jelfs, D. J. Adams, A. Trewin, J. Bacsa, A. Steiner, A. I. Cooper, *Chem. – Eur. J.* **2011**, *17*, 10235–10240.

[49] T. Mitra, K. E. Jelfs, M. Schmidtmann, A. Ahmed, S. Y. Chong, D. J. Adams, A. I. Cooper, *Nat. Chem.* **2013**, *5*, 276–281.

[50] T. Hasell, S. Y. Chong, K. E. Jelfs, D. J. Adams, A. I. Cooper, *J. Am. Chem. Soc.* **2012**, *134*, 588–598.

[51] T. Hasell, S. Y. Chong, M. Schmidtmann, D. J. Adams, A. I. Cooper, *Angew. Chem. Int. Ed.* **2012**, *51*, 7154–7157.

[52]   J. T. A. Jones, D. Holden, T. Mitra, T. Hasell, D. J. Adams, K. E. Jelfs, A. Trewin, D. J. Willock, G. M. Day, J. Bacsa, et al., *Angew. Chem.-Int. Ed.* **2011**, *50*, 749–753.

[53]   P. M. Budd, E. S. Elabas, B. S. Ghanem, S. Makhseed, N. B. McKeown, K. J. Msayib, C. E. Tattershall, D. Wang, *Adv. Mater.* **2004**, *16*, 456–459.

[54]   T. Hasell, H. Zhang, A. I. Cooper, *Adv. Mater.* **2012**, *24*, 5732–5737.

[55]   B. S. Ghanem, N. B. McKeown, P. M. Budd, J. D. Selbie, D. Fritsch, *Adv. Mater.* **2008**, *20*, 2766–2771.

[56]   H. Hopf, *Classics in Hydrocarbon Chemistry: Syntheses, Concepts, Perspectives*, Wiley VCH, Weinheim ; New York, **2000**.

[57]   T. Tozawa, J. T. A. Jones, S. I. Swamy, S. Jiang, D. J. Adams, S. Shakespeare, R. Clowes, D. Bradshaw, T. Hasell, S. Y. Chong, et al., *Nat. Mater.* **2009**, *8*, 973–978.

[58]   G. Zhang, O. Presly, F. White, I. M. Oppel, M. Mastalerz, *Angew. Chem. Int. Ed.* **2014**, *53*, 1516–1520.

[59]   S. J. Rowan, S. J. Cantrill, G. R. L. Cousins, J. K. M. Sanders, J. F. Stoddart, *Angew. Chem. Int. Ed.* **2002**, *41*, 898–952.

[60]   N. M. Rue, J. Sun, R. Warmuth, *Isr. J. Chem.* **2011**, *51*, 743–768.

[61]   M. Mastalerz, *Angew. Chem.-Int. Ed.* **2010**, *49*, 5042–5053.

[62]   S.-Y. Ding, W. Wang, *Chem. Soc. Rev.* **2012**, *42*, 548–568.

[63]   B. Içli, N. Christinat, J. Tönnemann, C. Schüttler, R. Scopelliti, K. Severin, *J. Am. Chem. Soc.* **2009**, *131*, 3154–3155.

[64]   M. L. C. Quan, D. J. Cram, *J. Am. Chem. Soc.* **1991**, *113*, 2754–2755.

[65]   D. P. Lydon, N. L. Campbell, D. J. Adams, A. I. Cooper, *Synth. Commun.* **2011**, *41*, 2146–2151.

[66]   L. Chen, P. S. Reiss, S. Y. Chong, D. Holden, K. E. Jelfs, T. Hasell, M. A. Little, A. Kewley, M. E. Briggs, A. Stephenson, et al., *Nat. Mater.* **2014**, *13*, 954–960.

[67]   M. Mastalerz, *Chem. Commun.* **2008**, 4756–4758.

[68]   M. Mastalerz, M. W. Schneider, I. M. Oppel, O. Presly, *Angew. Chem. Int. Ed.* **2011**, *50*, 1046–1051.

[69]   M. Brutschy, M. W. Schneider, M. Mastalerz, S. R. Waldvogel, *Adv. Mater.* **2012**, *24*, 6049–6052.

[70]   J. L. Culshaw, G. Cheng, M. Schmidtmann, T. Hasell, M. Liu, D. J. Adams, A. I. Cooper, *J. Am. Chem. Soc.* **2013**, *135*, 10007–10010.

[71]   K. E. Jelfs, E. G. B. Eden, J. L. Culshaw, S. Shakespeare, E. O. Pyzer-Knapp, H. P. G. Thompson, J. Bacsa, G. M. Day, D. J. Adams, A. I. Cooper, *J. Am. Chem. Soc.* **2013**, *135*, 9307–9310.

[72]   Y. J. Colón, R. Q. Snurr, *Chem. Soc. Rev.* **2014**, *43*, 5735–5749.

[73]   A. B. Beeler, S. Su, C. A. Singleton, J. A. Porco, *J. Am. Chem. Soc.* **2007**, *129*, 1413–1419.

[74] P. Wollmann, M. Leistner, U. Stoeck, R. Grunker, K. Gedrich, N. Klein, O. Throl, W. Grahlert, I. Senkovska, F. Dreisbach, et al., *Chem. Commun.* **2011**, *47*, 5151–5153.

[75] J. R. Smith, A. Seyda, N. Weber, D. Knight, S. Abramson, J. Kohn, *Macromol. Rapid Commun.* **2004**, *25*, 127–140.

[76] P. Canepa, C. A. Arter, E. M. Conwill, D. H. Johnson, B. A. Shoemaker, K. Z. Soliman, T. Thonhauser, *J. Mater. Chem. A* **2013**, *1*, 13597–13604.

[77] D. W. Robbins, J. F. Hartwig, *Science* **2011**, *333*, 1423–1427.

[78] J. Greeley, T. F. Jaramillo, J. Bonde, I. Chorkendorff, J. K. Nørskov, *Nat. Mater.* **2006**, *5*, 909–913.

[79] J. F. McCabe, *CrystEngComm* **2010**, *12*, 1110–1119.

[80] C. E. Wilmer, M. Leaf, C. Y. Lee, O. K. Farha, B. G. Hauser, J. T. Hupp, R. Q. Snurr, *Nat. Chem.* **2012**, *4*, 83–89.

[81] H. Bienaymé, C. Hulme, G. Oddon, P. Schmitt, *Chem. - Eur. J.* **2000**, *6*, 3321–3329.

[82] F. M. Menger, A. V. Eliseev, V. A. Migulin, *J. Org. Chem.* **1995**, *60*, 6666–6667.

[83] J. Wang, Y. Yoo, C. Gao, I. Takeuchi, X. Sun, H. Chang, X.-D. Xiang, P. G. Schultz, *Science* **1998**, *279*, 1712–1714.

[84] H. Ma, K. Y. Horiuchi, *Drug Discov. Today* **2006**, *11*, 661–668.

[85] E. Fenster, T. R. Long, Q. Zang, D. Hill, B. Neuenswander, G. H. Lushington, A. H. Zhou, C. Santini, P. R. Hanson, *Acs Comb. Sci.* **2011**, *13*, 244–250.

[86] D. Chan-Seng, M. Zamfir, J.-F. Lutz, *Angew. Chem. Int. Ed.* **2012**, *51*, 12254–12257.

[87] Y.-S. Bae, R. Q. Snurr, *Angew. Chem. Int. Ed.* **2011**, *50*, 11586–11596.

[88] B. Liu, *J. Mater. Chem.* **2012**, *22*, 10094–10101.

[89] F. Schuth, K. S. W. Sing, J. Weitkamp, *Handbook of Porous Solids*, Wiley, **2002**.

[90] S. Kulprathipanja, Ed. , *Zeolites in Industrial Separation and Catalysis*, Wiley VCH, Weinheim, **2010**.

[91] D. G. Hannan, C. R. E. Merkle, *Am. Ind. Hyg. Assoc. J.* **1968**, *29*, 136–139.

[92] F. Vögtle, W. M. Müller, U. Werner, H.-W. Losensky, *Angew. Chem. Int. Ed. Engl.* **1987**, *26*, 901–903.

[93] S. Kubik, *Angew. Chem. Int. Ed.* **2009**, *48*, 1722–1725.

[94] R. Meyers, *Handbook of Petroleum Refining Processes*, McGraw-Hill Professional, New York, **2003**.

[95] K. Iwayama, M. Suzuki, in *Stud. Surf. Sci. Catal.* (Ed.: Tadashi Hattori and Tatsuaki Yashima), Elsevier, **1994**, pp. 243–250.

[96] M. Maes, F. Vermoortele, M. Boulhout, T. Boudewijns, C. Kirschhock, R. Ameloot, I. Beurroies, R. Denoyel, D. E. De Vos, *Microporous Mesoporous Mater.* **2012**, *157*, 82–88.

[97] V. Finsy, H. Verelst, L. Alaerts, D. De Vos, P. A. Jacobs, G. V. Baron, J. F. M. Denayer, *J. Am. Chem. Soc.* **2008**, *130*, 7110–7118.

[98]   V. Finsy, C. E. A. Kirschhock, G. Vedts, M. Maes, L. Alaerts, D. E. De Vos, G. V. Baron, J. F. M. Denayer, *Chem. – Eur. J.* **2009**, *15*, 7724–7731.

[99]   Z.-Y. Gu, D.-Q. Jiang, H.-F. Wang, X.-Y. Cui, X.-P. Yan, *J. Phys. Chem. C* **2010**, *114*, 311–316.

[100]   Y. Liu, W. Xuan, Y. Cui, *Adv. Mater.* **2010**, *22*, 4112–4135.

[101]   I. Ilisz, R. Berkecz, A. Péter, *J. Pharm. Biomed. Anal.* **2008**, *47*, 1–15.

[102]   T. H. Webb, C. S. Wilcox, *Chem. Soc. Rev.* **1993**, *22*, 383–395.

[103]   H. Lorenz, A. Seidel-Morgenstern, *Angew. Chem. Int. Ed.* **2014**, *53*, 1218–1250.

[104]   L. Tang, L. Shi, C. Bonneau, J. Sun, H. Yue, A. Ojuva, B.-L. Lee, M. Kritikos, R. G. Bell, Z. Bacsik, et al., *Nat. Mater.* **2008**, *7*, 381–385.

[105]   J. Sun, C. Bonneau, Á. Cantín, A. Corma, M. J. Díaz-Cabañas, M. Moliner, D. Zhang, M. Li, X. Zou, *Nature* **2009**, *458*, 1154–1157.

[106]   J. S. Seo, D. Whang, H. Lee, S. I. Jun, J. Oh, Y. J. Jeon, K. Kim, *Nature* **2000**, *404*, 982–986.

[107]   O. R. Evans, H. L. Ngo, W. Lin, *J. Am. Chem. Soc.* **2001**, *123*, 10395–10396.

[108]   R.-G. Xiong, X.-Z. You, B. F. Abrahams, Z. Xue, C.-M. Che, *Angew. Chem. Int. Ed.* **2001**, *40*, 4422–4425.

[109]   J. Yu, R. Xu, *J. Mater. Chem.* **2008**, *18*, 4021–4030.

[110]   D. A. Collins, E. P. Nesterenko, B. Paull, *Analyst* **2014**, *139*, 1292–1302.

[111]   K. A. Cychosz, R. Ahmad, A. J. Matzger, *Chem. Sci.* **2010**, *1*, 293–302.

[112]   V. Schurig, *J. Chromatogr. A* **2001**, *906*, 275–299.

[113]   E. M. M. Del Valle, *Process Biochem.* **2004**, *39*, 1033–1046.

[114]   E. Smolková-Keulemansová, *J. Chromatogr. A* **1982**, *251*, 17–34.

[115]   L. Szente, J. Szejtli, *Adv. Drug Deliv. Rev.* **1999**, *36*, 17–28.

[116]   V. Schurig, H.-P. Nowotny, *J. Chromatogr. A* **1988**, *441*, 155–163.

[117]   C. F. Poole, Ed. , *Gas Chromatography*, Elsevier, S.l., **2012**.

[118]   E. Smolková-Keulemansová, L. Feltl, S. Krýsl, *J. Incl. Phenom.* **1985**, *3*, 183–196.

[119]   A. Smolková-Keulemansová, E. Neumannová, L. Feltl, *J. Chromatogr. A* **1986**, *365*, 279–288.

[120]   N. A. Ramsahye, P. Trens, C. Shepherd, P. Gonzalez, T. K. Trung, F. Ragon, C. Serre, *Microporous Mesoporous Mater.* **2014**, *189*, 222–231.

[121]   S. Xie, X. Zhang, B. Wang, M. Zhang, J. Zhang, L. Yuan, *Chromatographia* **2014**, *77*, 1359–1365.

[122]   A. L. Nuzhdin, D. N. Dybtsev, K. P. Bryliakov, E. P. Talsi, V. P. Fedin, *J. Am. Chem. Soc.* **2007**, *129*, 12958–12959.

[123]   S.-M. Xie, Z.-J. Zhang, Z.-Y. Wang, L.-M. Yuan, *J. Am. Chem. Soc.* **2011**, *133*, 11892–11895.

[124]   Z.-Y. Gu, X.-P. Yan, *Angew. Chem. Int. Ed.* **2010**, *49*, 1477–1480.

[125]   L. Fan, X.-P. Yan, *Talanta* **2012**, *99*, 944–950.

[126]   N. Chang, X.-P. Yan, *J. Chromatogr. A* **2012**, *1257*, 116–124.

[127]   B. Chen, C. Liang, J. Yang, D. S. Contreras, Y. L. Clancy, E. B. Lobkovsky, O. M. Yaghi, S. Dai, *Angew. Chem. Int. Ed.* **2006**, *45*, 1390–1393.

[128] M. E. Briggs, K. E. Jelfs, S. Y. Chong, C. Lester, M. Schmidtmann, D. J. Adams, A. I. Cooper, *Cryst. Growth Des.* **2013**, *13*, 4993–5000.

[129] M. W. Schneider, I. M. Oppel, H. Ott, L. G. Lechner, H.-J. S. Hauswald, R. Stoll, M. Mastalerz, *Chem. – Eur. J.* **2012**, *18*, 836–847.

[130] M. W. Schneider, I. M. Oppel, A. Griffin, M. Mastalerz, *Angew. Chem. Int. Ed.* **2013**, *52*, 3611–3615.

[131] M. E. Belowich, J. F. Stoddart, *Chem. Soc. Rev.* **2012**, *41*, 2003–2024.

[132] M. Mastalerz, *Chem. – Eur. J.* **2012**, *18*, 10082–10091.

[133] T. Hasell, X. F. Wu, J. T. A. Jones, J. Bacsa, A. Steiner, T. Mitra, A. Trewin, D. J. Adams, A. I. Cooper, *Nat. Chem.* **2010**, *2*, 750–755.

[134] J. Skarżewski, A. Gupta, *Tetrahedron Asymmetry* **1997**, *8*, 1861–1867.

[135] K. E. Jelfs, E. G. B. Eden, J. L. Culshaw, S. Shakespeare, E. O. Pyzer-Knapp, H. P. G. Thompson, J. Bacsa, G. M. Day, D. J. Adams, A. I. Cooper, *J. Am. Chem. Soc.* **2013**, *135*, 9307–9310.

[136] E. L. First, C. E. Gounaris, C. A. Floudas, *Langmuir* **2013**, *29*, 5599–5608.

[137] C. Schouwey, R. Scopelliti, K. Severin, *Chem. – Eur. J.* **2013**, *19*, 6274–6281.

[138] B. Kolb, *J. Chromatogr. A* **1999**, *842*, 163–205.

[139] J. Zhang, S.-H. Chai, Z.-A. Qiao, S. M. Mahurin, J. Chen, Y. Fang, S. Wan, K. Nelson, P. Zhang, S. Dai, *Angew. Chem. Int. Ed.* **2015**, *54*, 932–936.

[140] A. Kewley, A. Stephenson, L. Chen, M. E. Briggs, T. Hasell, A. I. Cooper, *Chem. Mater.* **2015**, DOI 10.1021/acs.chemmater.5b01112.

[141] L. Alaerts, C. E. A. Kirschhock, M. Maes, M. A. van der Veen, V. Finsy, A. Depla, J. A. Martens, G. V. Baron, P. A. Jacobs, J. F. M. Denayer, et al., *Angew. Chem.* **2007**, *119*, 4371–4375.

[142] A. S. Münch, J. Seidel, A. Obst, E. Weber, F. O. R. L. Mertens, *Chem. – Eur. J.* **2011**, *17*, 10958–10964.

[143] Z. Ji, R. E. Majors, E. J. Guthrie, *J. Chromatogr. A* **1999**, *842*, 115–142.

[144] N. Chang, Z.-Y. Gu, X.-P. Yan, *J. Am. Chem. Soc.* **2010**, *132*, 13645–13647.

[145] S. Krýsl, E. Smolková-Keulemansová, *J. Chromatogr. A* **1985**, *349*, 167–172.

[146] R. Wawrzyniak, W. Wasiak, *J. Sep. Sci.* **2003**, *26*, 1219–1224.

[147] P. S. Bárcia, D. Guimarães, P. A. P. Mendes, J. A. C. Silva, V. Guillerm, H. Chevreau, C. Serre, A. E. Rodrigues, *Microporous Mesoporous Mater.* **2011**, *139*, 67–73.

[148] T. Hasell, M. Schmidtmann, A. I. Cooper, *J. Am. Chem. Soc.* **2011**, *133*, 14920–14923.

[149] T. Hasell, M. Schmidtmann, C. A. Stone, M. W. Smith, A. I. Cooper, *Chem. Commun.* **2012**, *48*, 4689–4691.

[150] S. Jiang, J. Bacsa, X. Wu, J. T. A. Jones, R. Dawson, A. Trewin, D. J. Adams, A. I. Cooper, *Chem. Commun.* **2011**, *47*, 8919–8921.

[151] K. E. Jelfs, X. Wu, M. Schmidtmann, J. T. A. Jones, J. E. Warren, D. J. Adams, A. I. Cooper, *Angew. Chem. Int. Ed.* **2011**, *50*, 10653–10656.

[152] H. Poppe, *J. Chromatogr. A* **1997**, *778*, 3–21.

[153] T. Holm, *J. Chromatogr. A* **1999**, *842*, 221–227.

[154] G. M. Sheldrick, *Acta Crystallogr. A* **2008**, *64*, 112–122.

[155] K. D. M. Harris, M. Tremayne, B. M. Kariuki, *Angew. Chem. Int. Ed.* **2001**, *40*, 1626–1651.

[156] R. Balamurugan, A. K. Mohanakrishnan, *Tetrahedron* **2007**, *63*, 11078–11085.

[157] B. Raju, G. S. Krishna Rao, *Synthesis* **1985**, *1985*, 779–781.

[158] D. Breuer, C. Friedrich, in *MAK-Collect. Occup. Health Saf.*, Wiley-VCH Verlag GmbH & Co. KGaA, **2002**.

[159] D. Frenkel, B. Smit, *Understanding Molecular Simulation: From Algorithms to Applications*, Academic Press Inc, San Diego, **2001**.

[160] J. I. Siepmann, D. Frenkel, *Mol. Phys.* **1992**, *75*, 59–70.

[161] D. Dubbeldam, A. Torres-Knoop, K. S. Walton, *Mol. Simul.* **2013**, *39*, 1253–1292.

[162] W. L. Jorgensen, D. S. Maxwell, J. Tirado-Rives, *J. Am. Chem. Soc.* **1996**, *118*, 11225–11236.

[163] M. G. Martin, J. I. Siepmann, *J. Phys. Chem. B* **1998**, *102*, 2569–2577.

[164] M. G. Martin, J. I. Siepmann, *J. Phys. Chem. B* **1999**, *103*, 4508–4517.

[165] D. Dubbeldam, R. Krishna, S. Calero, A. Ö. Yazaydın, *Angew. Chem. Int. Ed.* **2012**, *51*, 11867–11871.

9 **Curriculum Vitae**

Online Profile: uk.linkedin.com/in/adamk117

Right now, I'm drinking coffee, eating discounted pastries, and wondering why I signed up to write this thesis. Writing can be quite challenging at times; however, after this is finished, I will face an even bigger challenge: applying the skills I have learnt. If you're looking to hire someone with experience in chemistry, software, and a little bit of design—hopefully, if you've read this far, I've convinced you that I can do an *okay* job at chemistry—then please feel free to contact me. Even if I'm already taken (those burgers won't flip themselves), I might be able to help you out.

Personal Profile

- I tend to take an analytical approach to solving problems, using statistical models, logic, and experimental measurements to understand systems, as evidenced by this thesis
- I'm trustworthy, with extensive experience in working with sensitive (and valuable) chemicals, equipment, and data in academic, public-sector, and private institutions
- An able communicator. As part of completing this thesis and my previous placements, I presented my work to a variety of audiences in the form of reports, articles, presentations, and meetings
- Team player. I have worked with a variety of teams ranging from large multidisciplinary research teams to small startups

Experience

- Academically qualified in chemistry. I received numerous awards and grants while achieving my official qualifications. During my bachelor's degree, I primarily chosen mathematics, and analytical/physical chemistry modules. I won academic excellence awards in each year of my bachelor's degree for being a top achiever. My master's degree, which I was lucky enough to have been awarded grant sponsorship for, is in nanoscience. Nanoscience is a multidisciplinary field which spans chemistry, physics, and materials science. My PhD, presented by this thesis, included extensive use of automated synthesis robots, the design of elabo-

rate analytical experiments, and the preparation of capillary columns for gas chromatography. During my degrees courses, I have been lucky enough to conduct research under three supervisors who were each world-leaders in their respective research fields

- Participated in a broad range of teaching and outreach programs over the last decade. This includes demonstrating practical techniques to undergraduates as part of my PhD placement, visiting local secondary schools to demonstrate spectroscopic techniques, and attempting (sometimes successfully!) to inspire visiting sixth-form students to get excited about chemistry

- Experienced with computers. Ever since I managed to create a minigun rocket launcher in DOOM 2, I have maintained a sustained interest in software development and design. This includes PHP, Haskell, python, C++, and java but I spend most of my time developing websites with ruby on rails, HTML5, javascript, and CSS at the moment. Additionally, I have spent an extensive amount of time (>2000 h) mastering client-side C# and F# (WPF UI with MVVM architecture). I am comfortable with procedural, object oriented, and functional programming styles

- Experience in design. Specifically, I have used Blender and the Adobe creative suite (mainly Photoshop and Illustrator) to create a variety of designs, see the start of this thesis and my LinkedIn profile for examples

Achievements

- Designed and developed several elaborate analytical experiments which involved the careful analysis of hundreds of samples. This work contributed directly to a Nature Materials publication[66] (see <u>LinkedIn profile</u>)

- I figured out how to coat gas chromatography capillary columns, which can be quite a secretive process, with a new stationary phase. This work contributed directly to a Chemistry of Materials publication (see <u>LinkedIn profile</u>)

- I have been lucky enough to design software with two small companies. In the first case, this involved developing a complex excel spreadsheet in VBA to analyze industrial processes. In the second case, this involved designing an interactive web frontend for a clinical audit product

- I hiked up mount Fujii. I ascended it through the night, paying ~£20 for canned air, and, as dawn gently illuminated a layer of cloud that stretched to the horizon, I witnessed a truly unique sight: there's vending machines at the top

Career History

- Feb/2015 to Present – Part-Time Web Frontend Developer – Crown Informatics Ltd
- Mar/2011 to Feb/2015 – Student, PhD (this thesis) – University of Liverpool
- Dec/2010 to Feb 2011 – VBA Software Development – Henkan Ltd.
- Sep/2009 to Sep/2010 – Student, MSc in Nanoscience – University of Nottingham – Dissertation focused on the synthesis of inorganic microporous materials
- Summer of 2008 – Research Placement, Air-Sensitive Synthetic Organic Chemistry – University of Nottingham
- Sep/2007 to Jul/2009 – Student, BSc in Chemistry – University of Nottingham
- Summer of 2007 – Pharmacy Order Picker – Wirral NHS Trust
- Summer of 2006 – Civil Engineering Assistant – Mouchel PLC, Ellesmere Port

Education and Qualifications

- PhD in Materials Chemistry, University of Liverpool
- Merit-class MSc. (hons.) in Nanoscience, University of Nottingham
- First-class BSc. (hons.) in Chemistry, University of Nottingham
- A-levels in chemistry (A), physics (A), and computing (A)

Personal Details

- adamk117@gmail.com
- 162 Frankby Road, West Kirby, CH48 9XA
- 07849589843
- References are available on request

10 **Appendix**

10.1 Gas Chromatography (GC) Methods

All injections were performed with an injector and detector temperature of 300 °C. The carrier gas was helium in all cases and injections were performed as constant-temperature split-mode injections. The flame ionization detector had hydrogen, air, and make-up flow-rates of 35, 350, and 35 mL min^{-1} respectively.

Table 10-1 | GC methods used to perform separations presented in the thesis. Instrumentation used is presented in the characterization Section (p90).

Mixture Separated	GC Method
Separations performed on a Beta DEX 325 column[†]	
Xylene Isomers	Temperature program: 40 °C for 1 min, raise to 180 °C at 4 °C min^{-1}. Isomer mixture agitated at 40 °C for 20 min followed by injecting 1 mL of the headspace. Injector split: 20:1 with a column flow of 1 mL min^{-1}.
rac-1-Phenylethanol *rac*-3-Hydroxytetrahydrofuran	Temperature program: 95 °C for 35 min, raise to 150 °C at 10 °C min^{-1}. Samples agitated at 40 °C for 10 min followed by injecting 5 μL of the headspace. Injector split: 5:1 with a column flow of 1 mL min^{-1}.
Nine-Component Aromatic Mixture (p136)	Temperature program: 40 °C for 1 min, raise to 100 °C at 2 °C min^{-1}. Mixture agitated at 100 °C for 5 min before injecting 1 mL of the headspace. Injector split: 20:1 with a column flow of 1 mL min^{-1}.
Separations performed on the CC3-*R* column	
rac-1-Pentyn-3-ol *rac*-1-Penten-3-ol *rac*-1-Phenyl-2-propanol *rac*-3-Hydroxytetrahydrofuran *rac*-2-Aminobutane *rac*-2-Aminopentane *rac*-5-Methyl-1-hexyn-3-ol	Temperature program: 60 to 180 °C at 10 °C min^{-1}. Samples were agitated at 40 °C for 5 min before injecting 10 μL of the headspace. Injector split: 100:1 with a column flow of 2 mL min^{-1}.

[†]Supelco Beta DEX 325 (30 m × 0.25 mm × 0.25 μm). A commercial 2,3-di-O-methyl-6-O-TBDMS-β-cyclodextrin capillary column.

rac-3-Methyl-2-butanol *rac*-3-Buten-2-ol *rac*-2-Ethyl-1,3-hexanediol	Temperature program: 50 to 180 °C at 10 °C min^{-1}. Samples were agitated at 40 °C for 5 min before injecting a 1 mL sample of the headspace. Injector split: 100:1 with a column flow of 1.2 mL min^{-1}.
rac-4-Phenyl-2-butanol *rac*-1,3-Butanediol	Temperature program: 60 to 180 °C at 10 °C min^{-1}. Samples were agitated at 110 °C for 5 min before injecting 250 µL of the headspace. Injector split: 50:1 with a column flow of 2 mL min^{-1}.
rac-1-Phenylethanol	Temperature program: 60 to 180 °C at 10 °C min^{-1}. Samples were agitated at 40 °C for 5 min before injecting 10 µL of the headspace. Injector split: 50:1 with a column flow of 1.2 mL min^{-1}.
rac-α-Methylbenzylamine	Temperature program: 60 to 180 °C at 10 °C min^{-1}. Samples were agitated at 110 °C for 5 min before injecting 10 µL of the headspace. Injector split: 100:1 with a column flow of 2 mL min^{-1}.
C6-C12 Linear Alkanes 2-Substituted Chiral Alcohols	Temperature program: 50 to 180 °C at 10 °C min^{-1}. Components dissolved in diethyl ether at a concentration of *c.a.* 0.2 mg mL^{-1} per component before injecting 10 µL of this solution. Injector split: 50:1 with a column flow of 2 mL min^{-1}.
C5-C12 Linear Alkanes (Headspace)	Temperature program: 50 to 180 °C at 10 °C min^{-1}. A pure C5-C12 alkane mixture was agitated at 40 °C for 5 min before injecting 10 µL of the headspace. Injector split: 200:1 with a column flow of 1.2 mL min^{-1}.
2-Substituted Chiral Alcohols (Headspace)	Temperature program: 40 °C for 3.5 min, raise to 180 °C at 10 °C min^{-1}. A pure chiral alcohol mixture was agitated at 40 °C for 2 min before injecting 10 µL of the headspace. Injector split: 200:1 with a column flow of 1.2 mL min^{-1}.
rac-2- and 3-Heptanol	Temperature program: 60 to 180 °C at 10 °C min^{-1}. Mixture agitated at 75 °C for 5 min before injecting 250 µL of the headspace. Injector split: 100:1 with a column flow of 2 mL min^{-1}.

Separations performed on the *rac*-CC3 column	
Xylene Isomers	Temperature program: 50 to 140 °C at 10 °C min^{-1}. The isomer mixture was agitated at 40 °C for 10 min before injecting 1 µL of the headspace. Injector split: 100:1 with a column flow of 1.2 mL min^{-1}.
Mesitylene & Benzene	Temperature program: 40 °C for 4 min. Samples were agitated at 40 °C for 2 min before injecting 5 µL of the headspace. Injector split: 250:1 with a column flow of 1.2 mL min^{-1}.
Hexane Isomers	Temperature program: 40 °C for 3.5 min, raise to 100 °C at 10 °C min^{-1}. The isomer mixture was agitated at 40 °C for 2 min before injecting 5 µL of the headspace. Injector split: 250:1 with a column flow of 1.2 mL min^{-1}. The split ratio is high because hexane has a high headspace concentration at 40 °C.
Separations performed on a BP1‡ column	
Hexane Isomers	*Same as above*
Separations performed on the CCX-*S* column	
rac-1-Phenylethanol	Temperature program: 60 to 180 °C at 10 °C min^{-1}. The mixture was agitated at 40 °C for 5 min followed by injecting 10 µL of the headspace. Injector split: 50:1 with a column flow of 1.2 mL min^{-1}.

---

‡ SGE-BP1 (30 m × 0.32 mm × 0.25 µm). A commercial 100 % PDMS column.

10.2 Discovering Novel Organic Cages
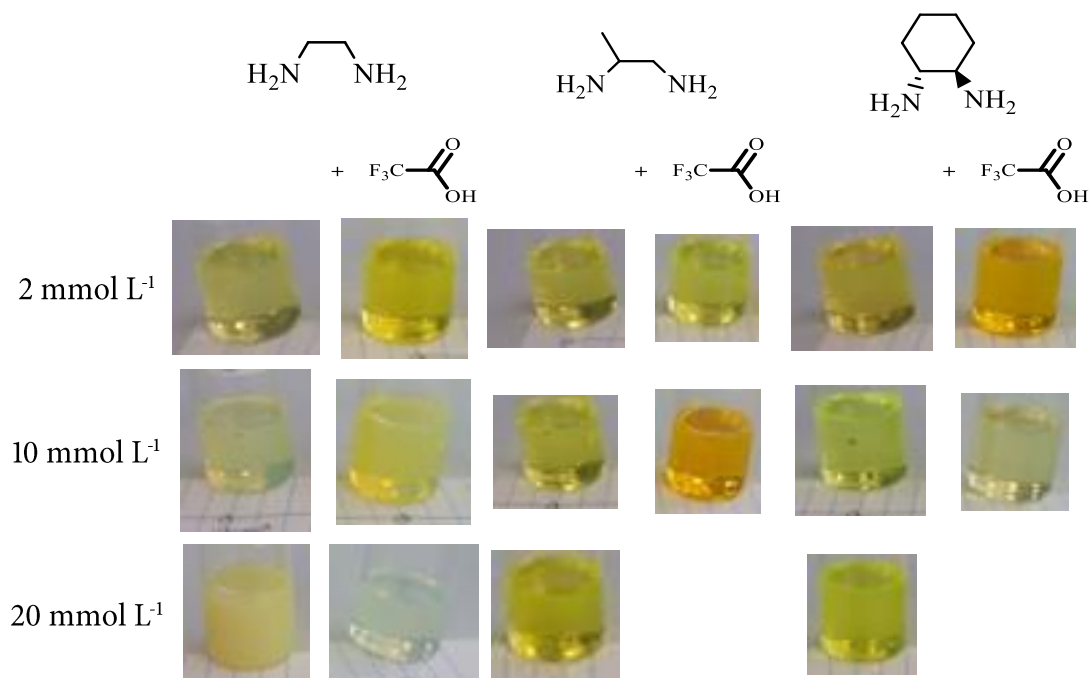
Figure 10-1 Sample images from combichem screen presented in main text (p33) | Combinations with ethylene diamine (columns 1-2) produced a precipitate at all but the lowest concentration (2 mmol L⁻¹). The same is true with 1,2-cyclohexanediamine solutions at 20 mmol L⁻¹. Other combinations did not contain solids; however, the presence of TFA appeared to affect the appearance of the solutions in some cases. As shown, the solution can change to an orange colour when TFA is present. This is likely to be due to protonation of the tertiary aniline in the trialdehyde.
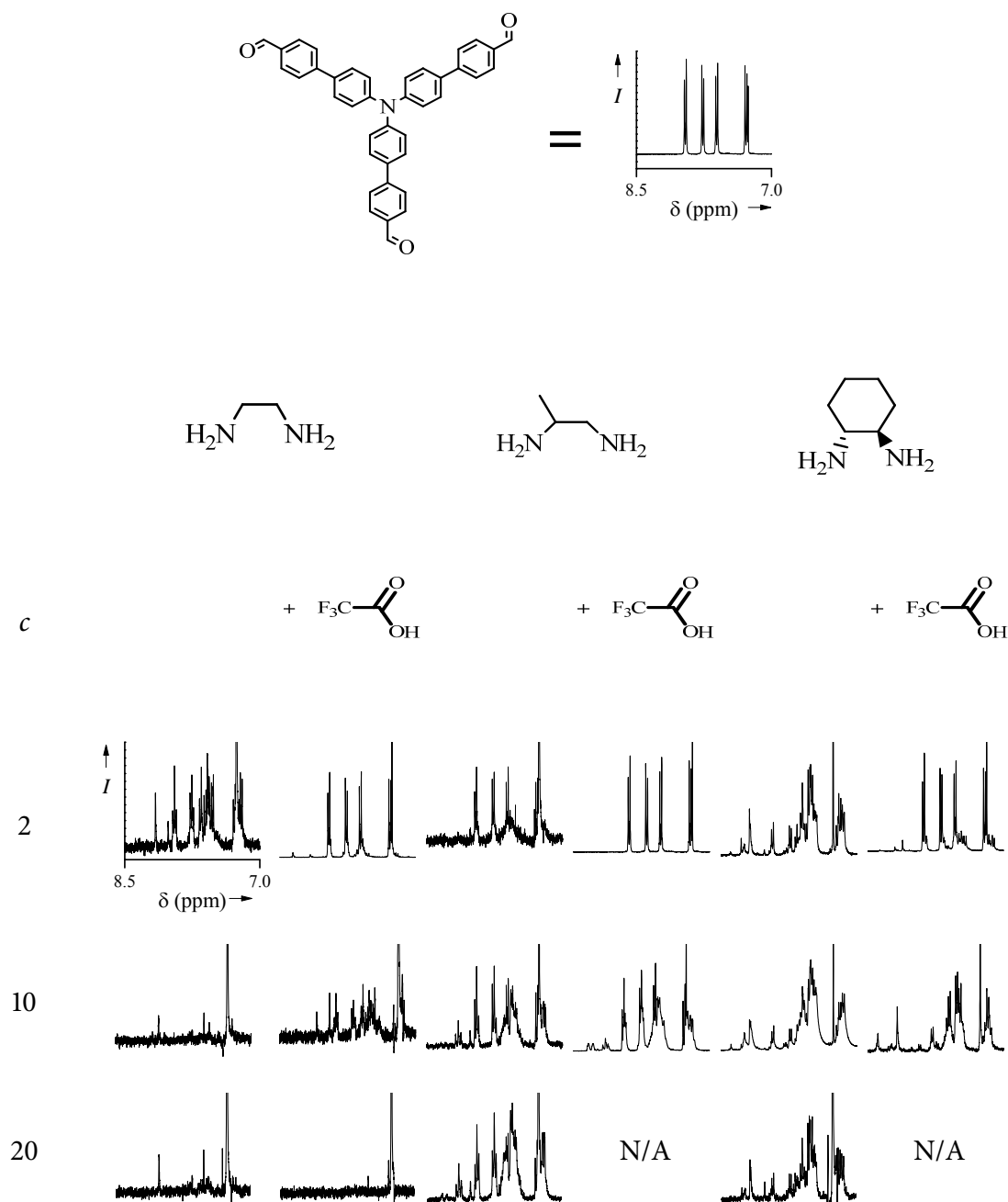
Figure 10-2 Product NMR spectra from combichem screen presented in main text (p33) | ¹H NMR (CDCl₃) spectra of product samples after drying steps. The 8.5-7.0 ppm regions of the resulting spectra are presented since aromatic and imine environments tend to reside there. ¹H NMR of the starting trialdehyde is shown at the top. The diamines have no resonances in this region. TFA catalyst appears to hinder the reaction, most combinations involving TFA look closer to the starting material than a product. Protonation of the central tertiary nitrogen would hinder resonance effects, which is likely why acid catalysts do not have the desired effect. The cleanest conversion to the imine moiety is seen for 1,2-cyclohexane diamine combinations, the other diamines appear to have a measurable amount of starting material, which is reinforced by comparison of GPC measurements.
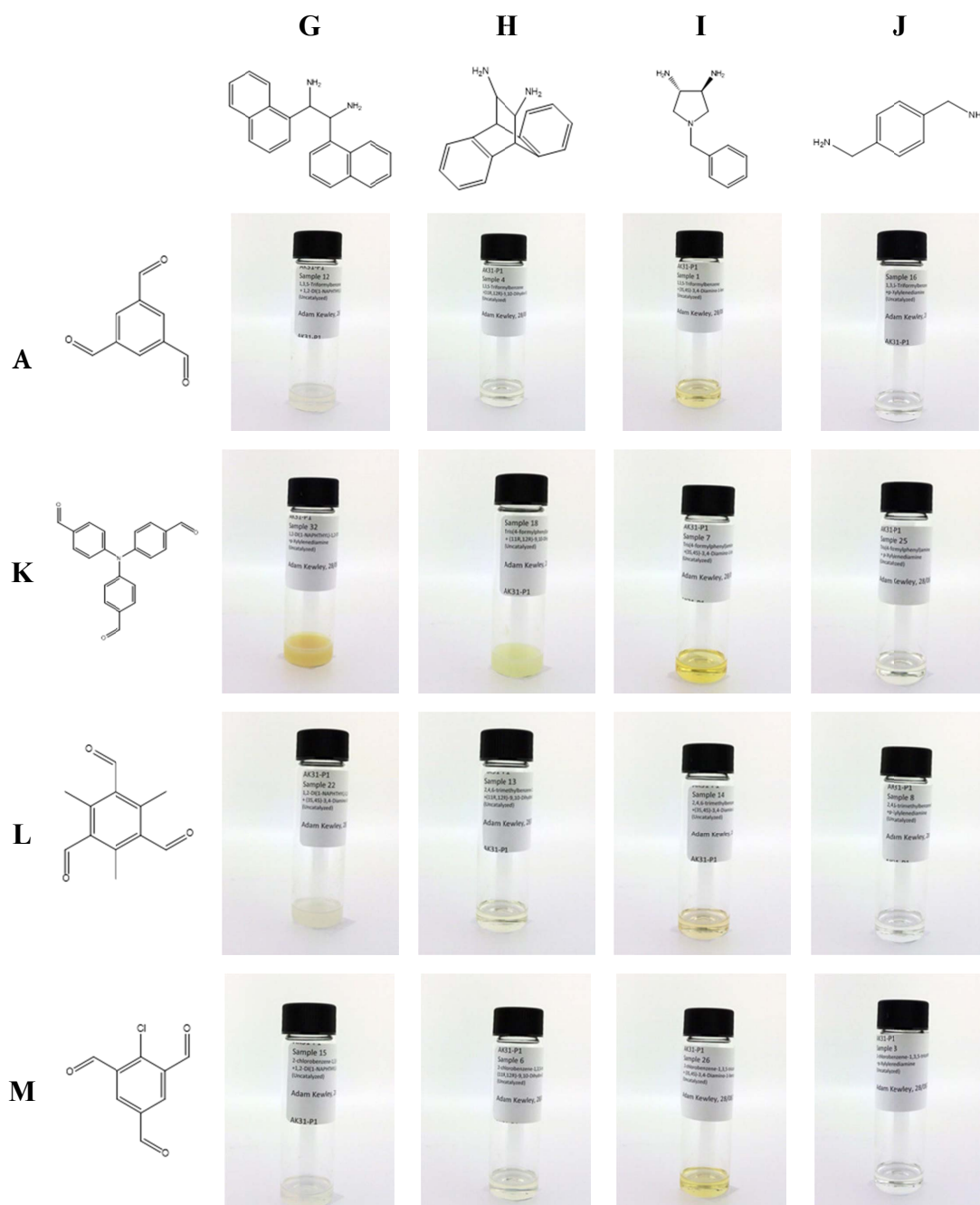
Figure 10-3 | Sample images from combichem screen discussed in main text (p34) | Solutions of (3*S*, 4*S*)-3,4-diamino-1-benzopyrollidine (**I**) and *tris*(4-formylphenyl)amine (**K**) were yellow while other solutions were colourless. Precipitates were observed in combinations involving 1,2-di(1-napthyl)-1,2-ethanediamine (**G**) with any trialdehyde or (11*R*, 12*R*)-9,10-ethanoanthracene-11,12-diamine (**H**) combined with *tris*(4-formylphenyl)amine (**K**). It is likely that **G** formed polymers due to steric considerations. The di-napthyl groups freely rotate with respect to the C2 backbone of the diamine and, because they are quite large, there is scope for inter-napthyl collisions. Consequently, this restricts the range of accessible conformations which, because the formation of cage compounds requires the diamine moieties to rotate into a specific conformation, prevented cage formation. Other combinations produced clear solutions; however, other analyses indicate that mixtures or unreacted starting materials account for this in most cases.
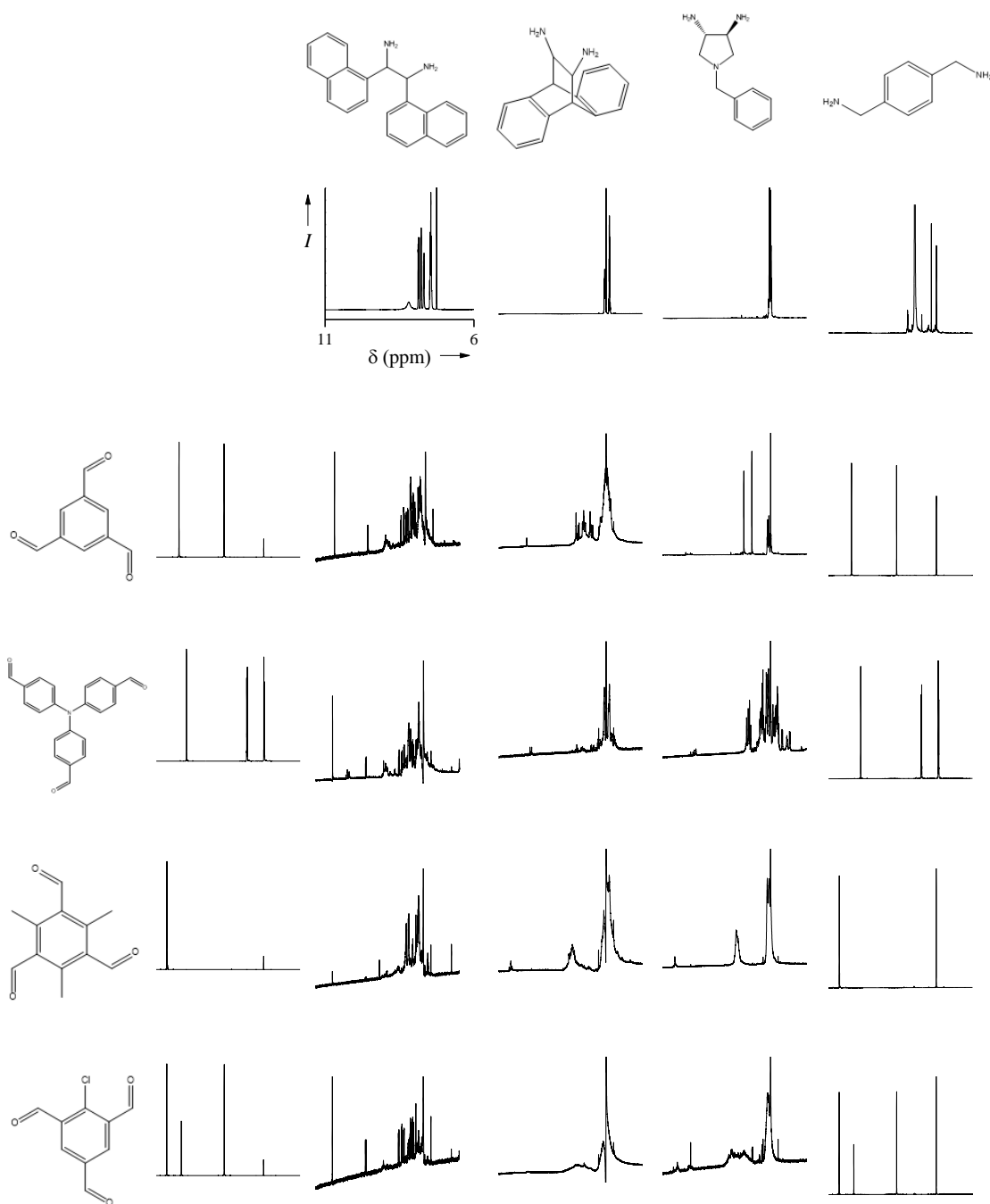
Figure 10-4 | ¹H NMR spectra from combichem screen discussed in main text (p34). ¹H NMR (CDCl₃) spectra of product samples after drying steps. The 11-6 ppm regions of the resulting spectra are presented since aromatic, imine, and aldehyde environments tend to reside there. No reaction was observed for combinations involving *p*-xylylenediamine, likely due to decomposition. The formation of imine environments was observed in many combinations but highly symmetric imine products were observed for benzene-1,3,5-trialdehyde with (3*S*, 4*S*)-3,4-diamino-1-benzylpyrollidine, prompting further scale-ups (see main text, p35).
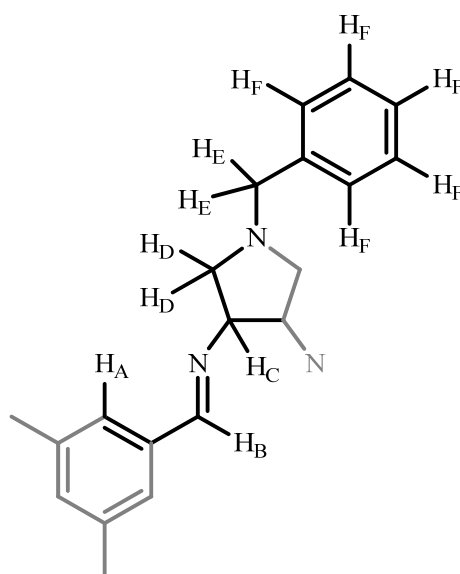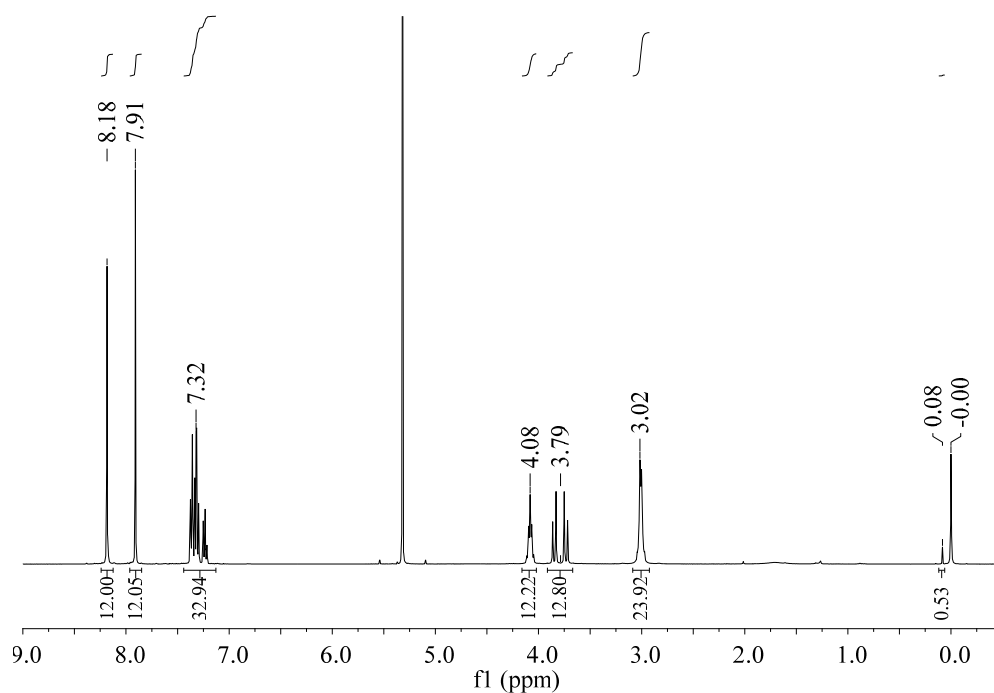
δ (ppm)	Multiplicity	*J* (Hz)	Integration	Assignment
8.18	s		12.00 (12)	-C*H*N (H$_B$)
7.91	s		12.05 (12)	-Ar*H* (H$_A$)
7.4-7.19	m		32.94 (30)	-Ar*H* (H$_F$)
4.14-4.02	m		12.22 (12)	-C*H* (H$_C$)
3.79	dd	44.9, 13.1	12.80 (12)	-C*H$_2$* (H$_E$)
3.07-2.93	m		23.92 (24)	-C*H$_2$* (H$_D$)

Figure 10-5 | ^{1}H NMR (CD$_2$Cl$_2$) of CCX-*S*. ^{1}H NMR (CD$_2$Cl$_2$, 400 MHz) δ 8.18 (s, 12H, -C*H*=N), 7.91 (s, 12H, -ArH), 7.44-7.18 (m, 30H, -ArH), 4.17-4.00 (m, 12H, -CH$_2$), 3.85 (d, *J*=13.1 Hz, 6H, -CH), 3.73 (d, *J*=13.1 Hz, 6H –CH), 3.11-2.91 (m, 24H, -CH$_2$) ppm;
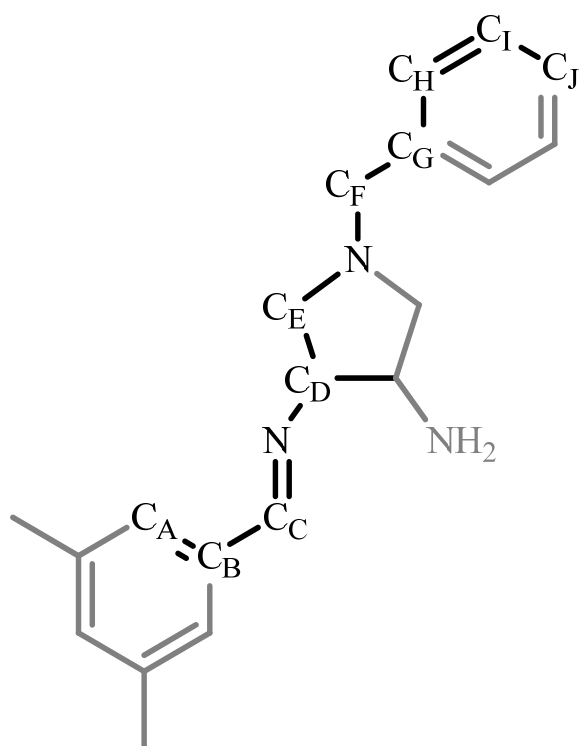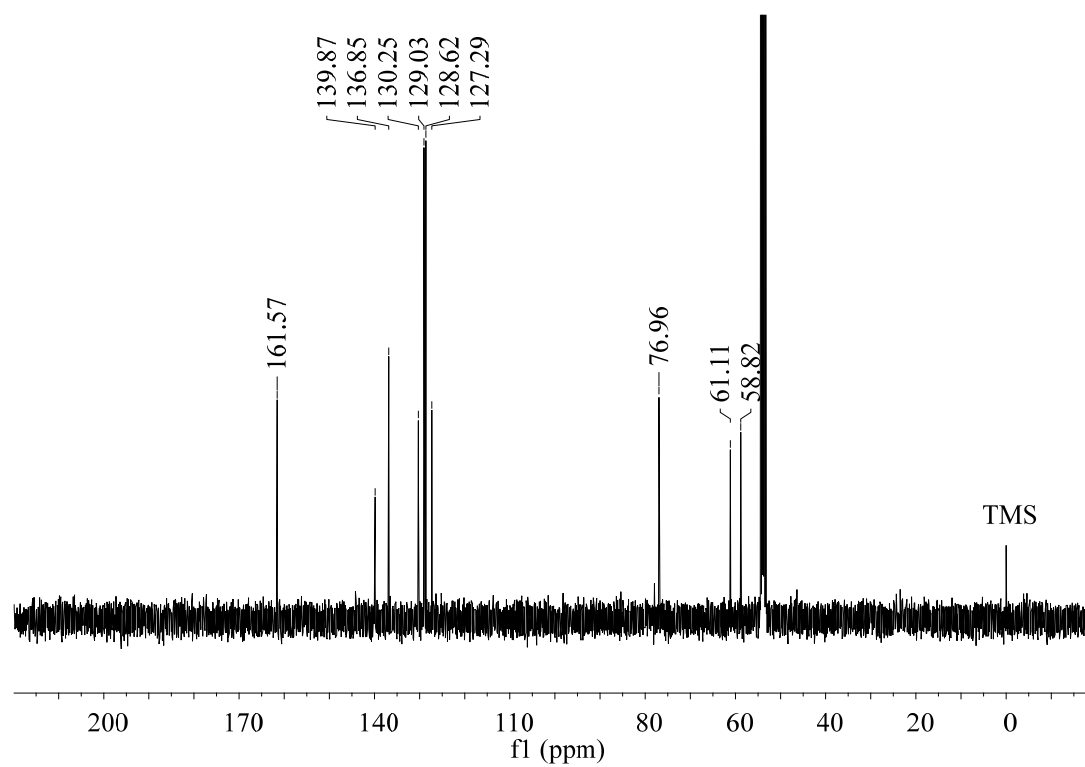
Figure 10-6 | ¹³C-NMR (CD₂Cl₂) of CCX-*S*. ¹³C NMR (CD₂Cl₂, 100 MHz) δ 161.57, 139.87, 136.85, 130.25, 129.03, 128.62, 127.29, 76.96, 61.11, 58.82 ppm;
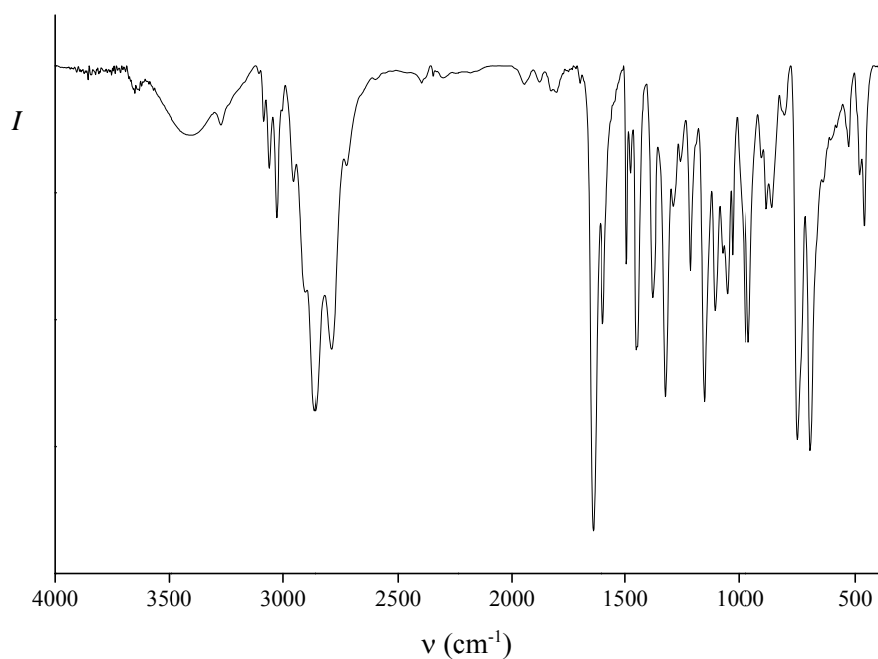
Figure 10-7 | FTIR (KBr pellet) spectrum of CCX-*S*. FTIR (KBr pellet, ν) 3405 (br), 3271 (w), 3083 (w), 3059 (w), 3025 (w), 3059 (w), 3026 (w), 2953 (w), 2882 (s), 2792 (m), 1643 (v.s.), 1598 (m), 1494 (m), 1476 (w), 1450 (m), 1378 (m), 1322 (m), 1288 (w), 1257 (w), 1213 (m), 1151 (m), 1105 (m), 1071 (m), 1050 (m), 1027 (m), 969 (w), 969 (m), 911 (w), 890 (w), 866 (w), 811 (w), 754 (s), 698 (s), 529 (w), 481 (w), 460 (w) cm^{-1};
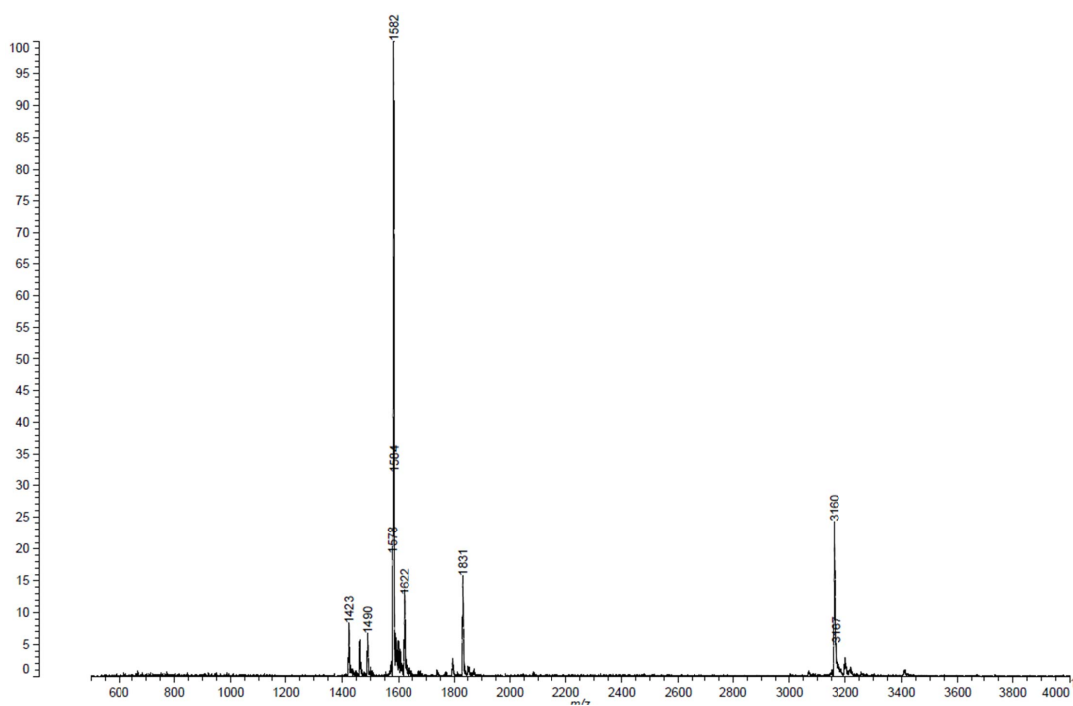
Figure 10-8 | MALDI-TOF mass spectrum of CCX-*S*. Dithranol matrix, *m/z* 1582 Da for $C_{102}H_{102}N_{18}$ [M+H]$^+$, 3160 Da for $C_{204}H_{204}N_{36}$ [2M]$^+$;

10.3 Organic Cages as Selective Sorbents
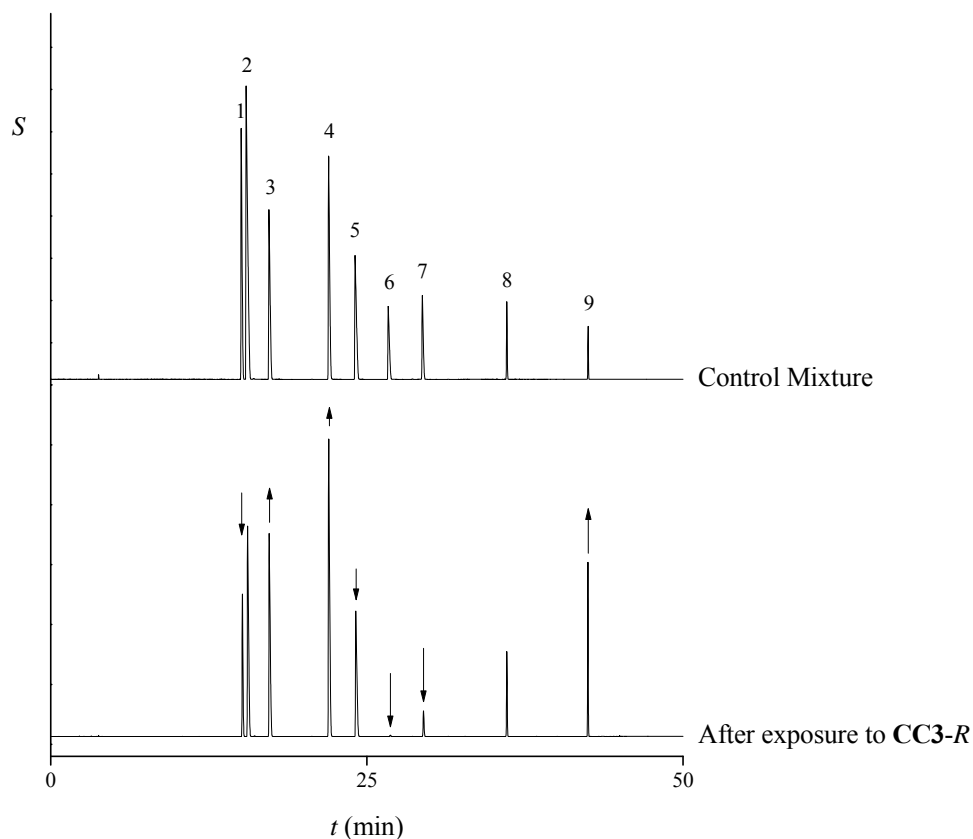
Figure 10-9 | Screening for selectivity with multi-component mixtures. GC-FID chromatograms of a mixture of nine aromatic compounds: *p*-xylene (1), *m*-xylene (2), *o*-xylene (3), mesitylene (4), 2-ethyl-toluene (5), 1,4-dichlorobenzene (6), 1,4-diethylbenzene (7), 3,5-dimethyl-1-*tert*-butylbenzene (8), and 3,5-di-*tert*-butyltoluene (9) before and after exposure to **CC3**-*R*. In the main text, binary mixtures are presented exclusively as, while general trends of adsorption could be measured from multicomponent mixtures, it was difficult to tell the order of preference; however, as indicated by arrows, preferential adsorption could be observed. In this example, the 1,4-dichlorobenzene was barely detectable after exposure to **CC3**-*R*.

Guest Mixtures Acquired (67)

DL-Glyceraldehyde; DL-α-hydroxy-β,β-dimethyl-γ-butyrolactone; 1,2-dibromopropane; 1,2-dichloropropane; 1,2,3-trichloropropane; 2-bromo-3-methylbutyric acid; 2-*sec*-butylphenol; 2-ethyl-1-hexanol; 4-*sec*-butylphenol; 3-chloro-1,2-propanediol; 1,2,3-tribromopropane; 2-pentanol; 3-butyn-2-ol; 1-pentyn-3-ol; 3-methyl-1-pentyn-3-ol; 5-methyl-1-hexyn-3-ol; 2-phenyl-1-propanol; *tert*-butyl glycidyl ether; 2-cyclohexen-1-ol; (1-chloroethyl)benzene; 2-hexanol; 1-penten-3-ol; 2,3-dichloro-1-propanol; 3-methyl-2-butanol; 3-buten-2-ol; 3-methylcyclohexanone; 3,3,5-trimethylcyclohexanone; 4-carvomenthenol; 3-hydroxytetrahydrofuran; *sec*-butylbenzene; α-(trifluoromethyl)benzyl alcohol; 1-phenyl-2-propanol; ethyl 2-bromopropionate; 4-fluoro-α-methylbenzyl alcohol; 4-phenyl-2-butanol; 1-chloro-2-propanol; 1,2-epoxy-3-phenoxypropane; menthyl acetate; 2-pentanol; 1-(4-methylphenyl)-3-buten-1-ol; methyl DL-lactate; 1,3-butanediol; 1,2-propanediol; glyceraldehyde; 2-ethyl-1,3-hexanediol; hexylene glycol; atropine; 3,7-dimethyl-1,6-octadien-3-yl acetate; 2-heptanol; isophorone diisocyanate; 3,5,5-trimethyl-1-hexanol; 2-methylglutaronitrile; 3-carene; 2-methylglutaronitrile; camphor; 3,5-dimethyl-2-cyclohexen-1-one; 2-iodobutane; 2-bromopentane; 2-methylbutyronitrile; 3-heptanol; α-Pinene; terpineol; 3,3-dimethyl-2-butanol; linalool oxide; whiskey lactone; 1-phenylethanol; and 2-butanol

Guest Mixtures Separated (16)

1,2-Propanediol; 1-phenylethanol; 2,3-dimethylheptane; α-methylbenzylamine; α-pinene; β-citronellol; citronellal; 1,2-isopropylineglycerol; linalool; terpinol; whiskey lactone; 3-hydroxytetrahydrofuran; 4-fluoro-α-methylbenzyl alcohol; 1-phenyl-2-propanol; α-(Trifluoromethyl)benzyl alcohol; and 3-phenyl-1-propanol

Guest Mixtures Which Selectively Adsorbed into CC3 (6)

3-Hydroxytetrahydrofuran, 4-fluoro-α-methylbenzyl alcohol, 1-phenyl-2-propanol, α-(Trifluoromethyl)benzyl alcohol, and 3-phenyl-1-propanol

Figure 10-10 | Racemic guests screened for enantioselective adsorption in CC3-*R*. A general screening approach was used to identify suitable guest mixtures (see main text, p44). Sixty-seven guest mixtures were acquired (top) but, because chiral separations are particularly difficult, only sixteen separated to baseline (middle), a requirement for selective adsorption measurements. Of these mixtures, six were found to selectively adsorb into **CC3**-*R* (bottom).
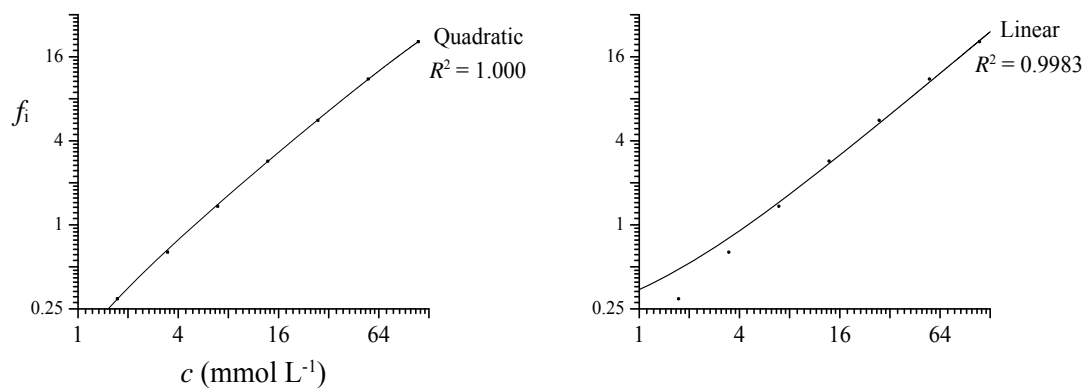
Figure 10-11 | Quadratic *vs* linear fitting of GC calibration data. GC-FID Calibration plots of response factor (f_i) vs stock concentration (c). In most cases, there should be a linear relationship between f_i and c with an FID. However, because **CC3**-*R* may adsorb a large amount of the guest, the concentration ranges explored in selective adsorption experiments may be vast enough for detector non-linearity to become an issue. Consequently, linear fits may be invalidated (right plot, points vs curve). Quadratic fits are a common method of correcting for detector non-linearity; consequently, GC calibration fits for the presented selective adsorption experiments used this approach.
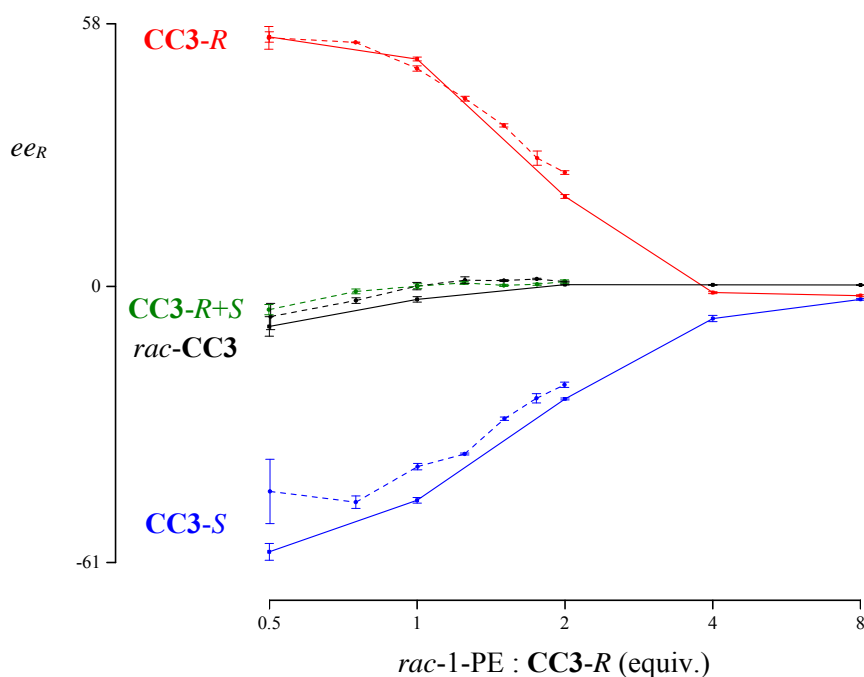
Figure 10-12 | Inter-experimental comparison of measured enantiomeric excesses. Excesses measured after **CC3** samples were exposed to differing concentrations of *rac*-1-PE solutions. An earlier experiment (solid lines) and later experiment (dotted lines) performed two months apart are compared. Good agreement between experiments was observed, indicating that the approach used is quite reproducible. A larger *rac*-1-PE : **CC3**-*R* range was used in the earlier experiment; however, it was difficult to measure the effect of **CC3**-*R* on the (in excess) guest above 2 equivalents. Consequently, a smaller (0.5 – 2) range was used in the later experiment.
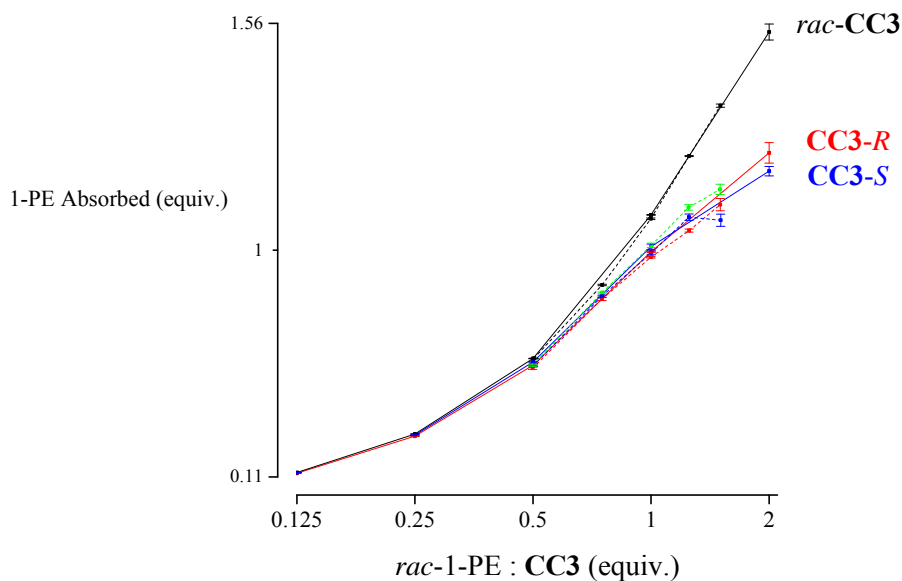
Figure 10-13 | Inter-experimental comparison of measured 1-PE adsorbed. Calculated equivalents of 1-PE adsorbed into different **CC3** samples. An earlier experiment (solid lines) and later experiment (dotted lines) performed two months apart are compared. Unlike in Figure 10-12, calculated data points for higher (>2) are omitted because it was difficult to calculate the effect of **CC3** when the guest is in great excess.
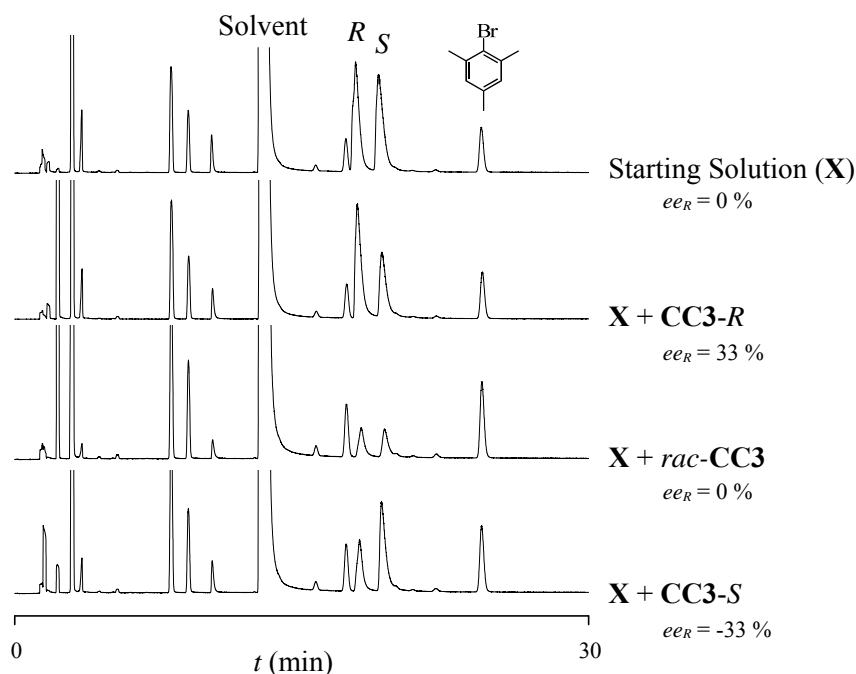
Figure 10-14 | Representative full GC-FID chromatograms of guest-depleted filtrates. Guest-depleted filtrates collected after mixing a 1-PE solution with **CC3** samples. While impurities are present, it is likely they were large, preventing their adsorption into **CC3**, or volatile, raising their headspace concentration and FID signal. This is reinforced by analysis of guest-extracted filtrates where only small amounts of the impurities were measured (Figure 10-15).
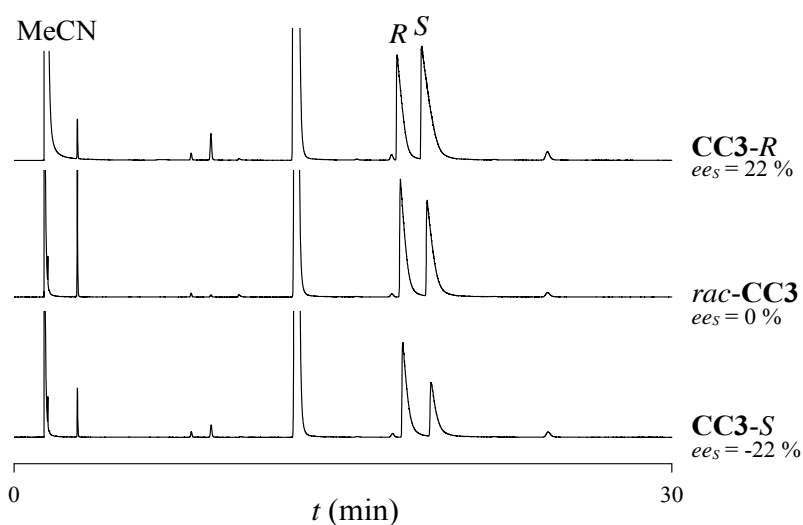
Figure 10-15 | Representative full GC-FID chromatograms of guest-extracted filtrates. Samples were gently dried in the filter funnel to prevent guest-desorption resulting in the presence of some residual 1-*tert*-butyl-3,5-dimethylbenzene (*ca.* 14 min) and bromomesitylene (*ca.* 22 min) adsorbed on the surface of the crystals.
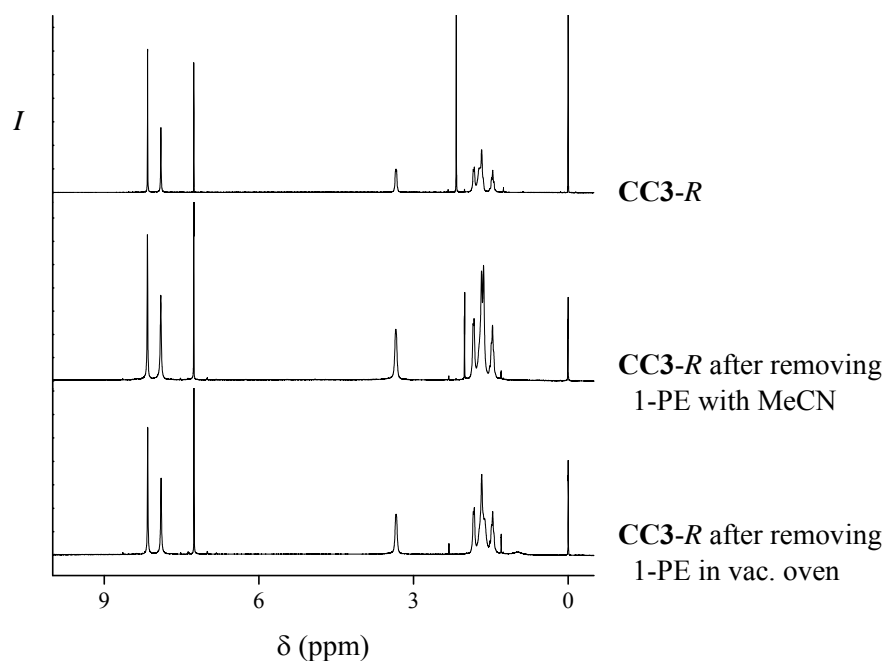
Figure 10-16 | Comparing wash-out to vacuum-removal of 1-PE. ^{1}H NMR (CDCl$_3$) spectra of **CC3**-*R* before the addition of 1-PE (top), after removal of 1-PE by washing with acetonitrile (MeCN, middle), and after removal of 1-PE in a vacuum oven (bottom). Experiments in the main text focused on the wash-out approach because the guest-extracted washings could be analysed; however, the addition and removal by either technique reproduced the **CC3**-*R*.
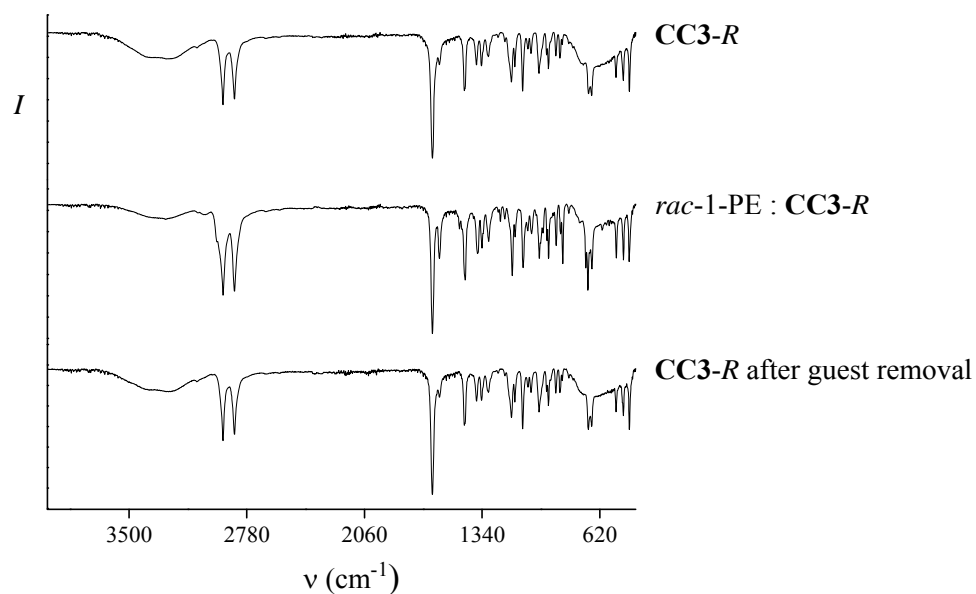
Figure 10-17 | Representative FTIR (ATR) spectra of CC3-*R* at various stages of host-guest exchange. Spectra of **CC3** before (top) and after (bottom) 1-PE removal appear to be the same, indicating that host-guest exchange did not irreversibly chemically alter **CC3**. *rac*-1-PE : **CC3** adducts (middle) contain additional peaks which may be attributed to 1-PE, and residual 1-*tert*-butyl-3,5-dimethylbenzene solvent.
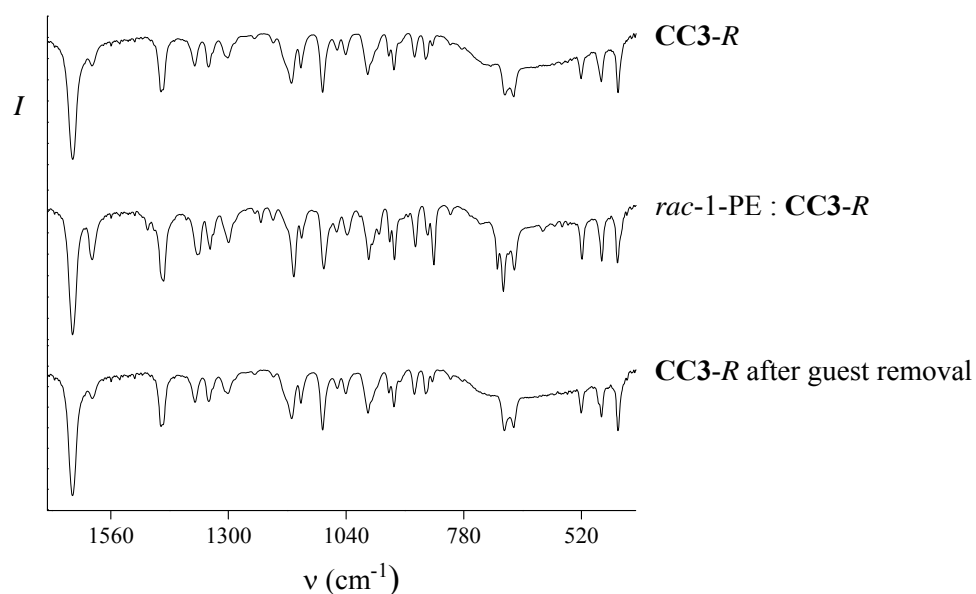
Figure 10-18 | Representative FTIR (ATR) spectra of CC3-*R* at various stages of host-guest exchange in 1600-500 cm^{-1} range of Figure 10-17.
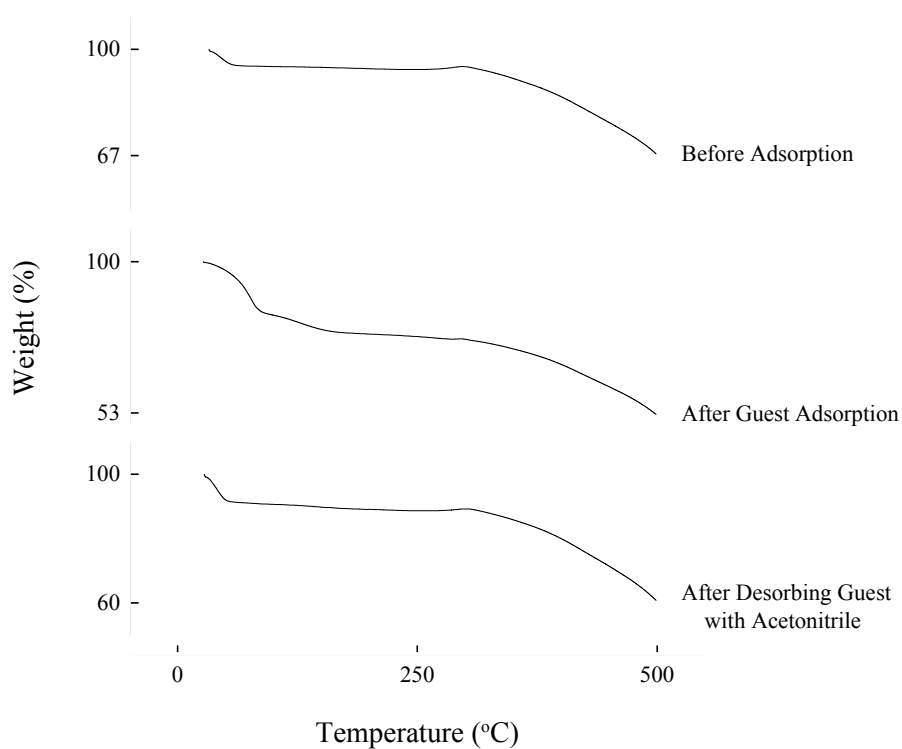
Figure 10-19 | TGA of CC3-*R* at various stages of host-guest exchange. Measurements on **CC3**-*R* pre-adsorption (top), post-adsorption (middle), and post-desorption (bottom). **CC3**-*R* remained largely the same pre-adsorption and post-desorption. Slightly larger weight loss was measured after guest desorption and is likely due to residual acetonitrile within **CC3**-*R*'s structure because samples were not vacuum dried prior to measurement. In guest-adsorbed samples (middle) there was a broad drop in sample weight between 20-85 °C which was likely to be the slow evaporation of 1-PE and residual 1-*tert*-butyl-3,5-dimethylbenzene solvent.

10.4 Chromatographic Separations with Organic Cages
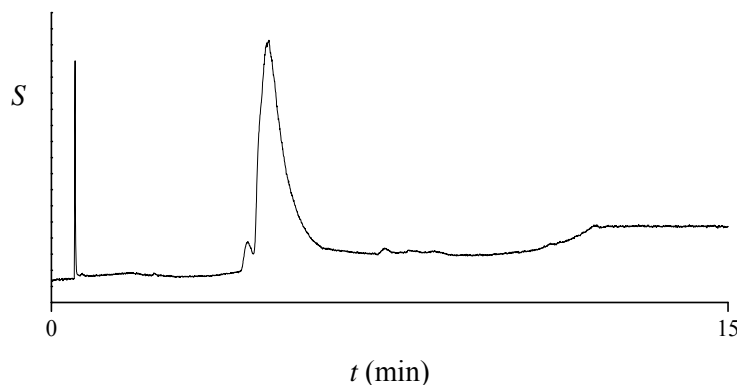
Figure 10-20 | GC-FID chromatogram of *rac*-1-PE separated on a CCX-*S* column. CCX-*S* was a novel cage discovered in Chapter 2. The column was produced as described in experimental Section 7.3.4.6 (p115). Poor separation performance observed for **CCX**-*S* was likely due to two reasons: it contains a tertiary amine, which is likely to strongly bind with analytes, causing peak tailing; and it does not spontaneously pack into an ordered structure upon solvent removal, which is likely to diminish its shape-sorting abilities when compared with **CC3**. However, while it does not perform chiral separation of 1-PE, it was retained. Further development of **CCX**-*S* as a stationary phase may improve on the discussed issues.
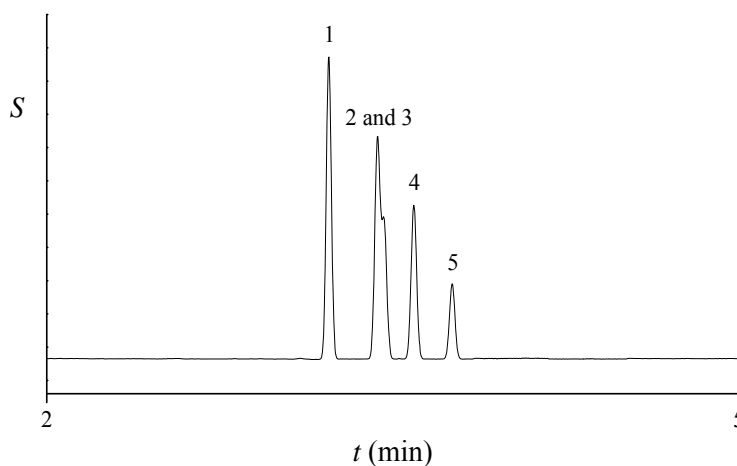
Figure 10-21 | GC-FID chromatogram of a hexane isomer mixture separated on a commercial column. Separations on a SGE-BP1 (30 m × 0.32 mm × 0.25 μm) are presented. Hexane isomers may be separated using commercially-available stationary phases; however, few stationary phases are capable of separating all five isomers of hexane, necessitating the use of a dual-column setup in standard preparations.[158] One advantage that commercial stationary phases have over **CC3** is that they are heavily developed and produce much sharper peaks. Consequently, lower selectivities are required in commercial stationary phases to achieve separation.
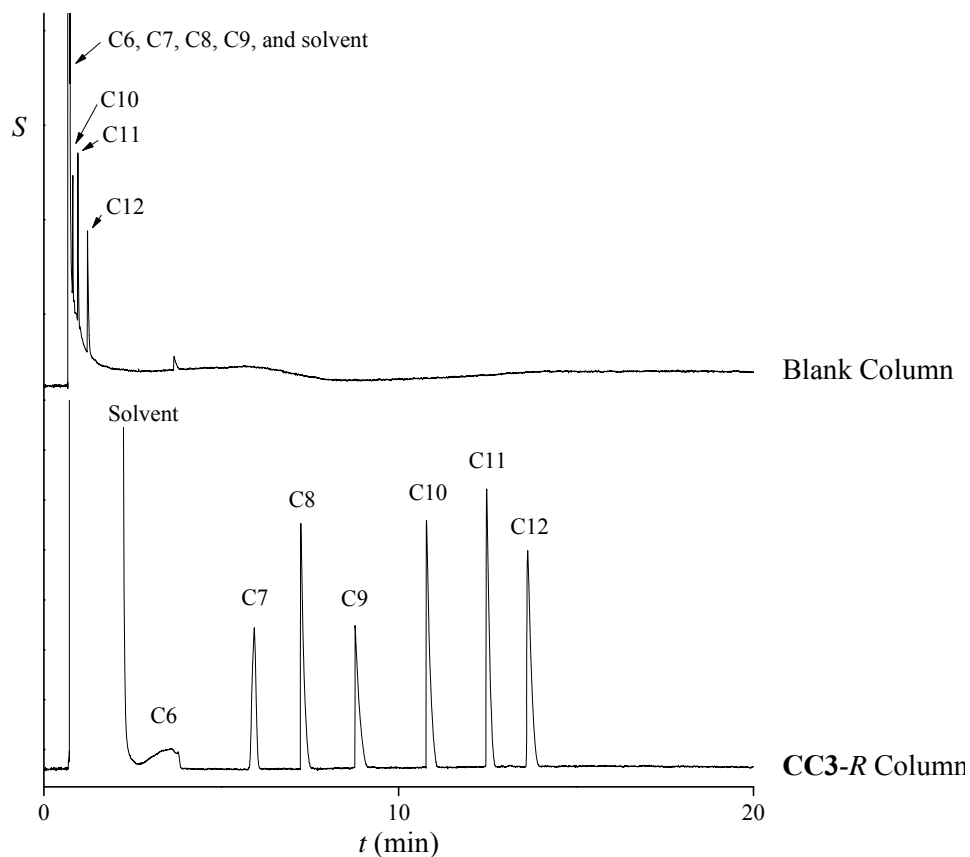
Figure 10-22 | GC-FID chromatograms of a C6-C12 linear alkane mixture separated on a blank (top) and CC3-*R* coated (bottom) column. A mixture of seven linear alkanes dissolved in diethyl ether were injected: *n*-hexane (C6), *n*-heptane (C7), *n*-octane (C8), *n*-nonane (C9), *n*-decane (C10), *n*-undecane (C11), and *n*-dodecane (C12). Longer-chain alkanes partially separated on the blank column due to their relatively high boiling points (215 °C for dodecane) while the shorter-chain components co-eluted with the solvent.
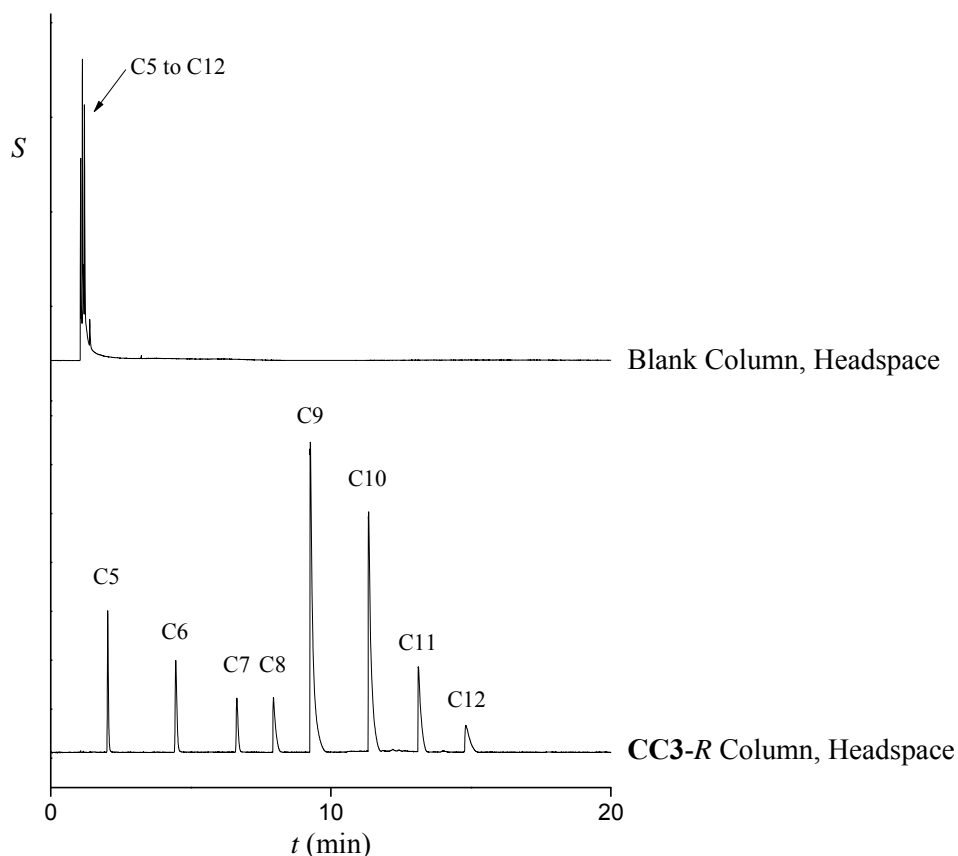
Figure 10-23 | GC-FID chromatograms of a C5–C12 linear alkane mixture separated on a blank (top) and CC3-*R* coated (bottom) column introduced as headspace injections. While headspace injections allowed solvent to be omitted, peak areas were directly related to a components boiling point. Because of this, additional C9–C12 was added into this sample so that the corresponding peaks may be visible in the chromatogram. A mixture of eight linear alkanes was introduced into the system: *n*-pentane (C5), *n*-hexane (C6), *n*-heptane (C7), *n*-octane (C8), *n*-nonane (C9), *n*-decane (C10), *n*-undecane (C11), and *n*-dodecane (C12).
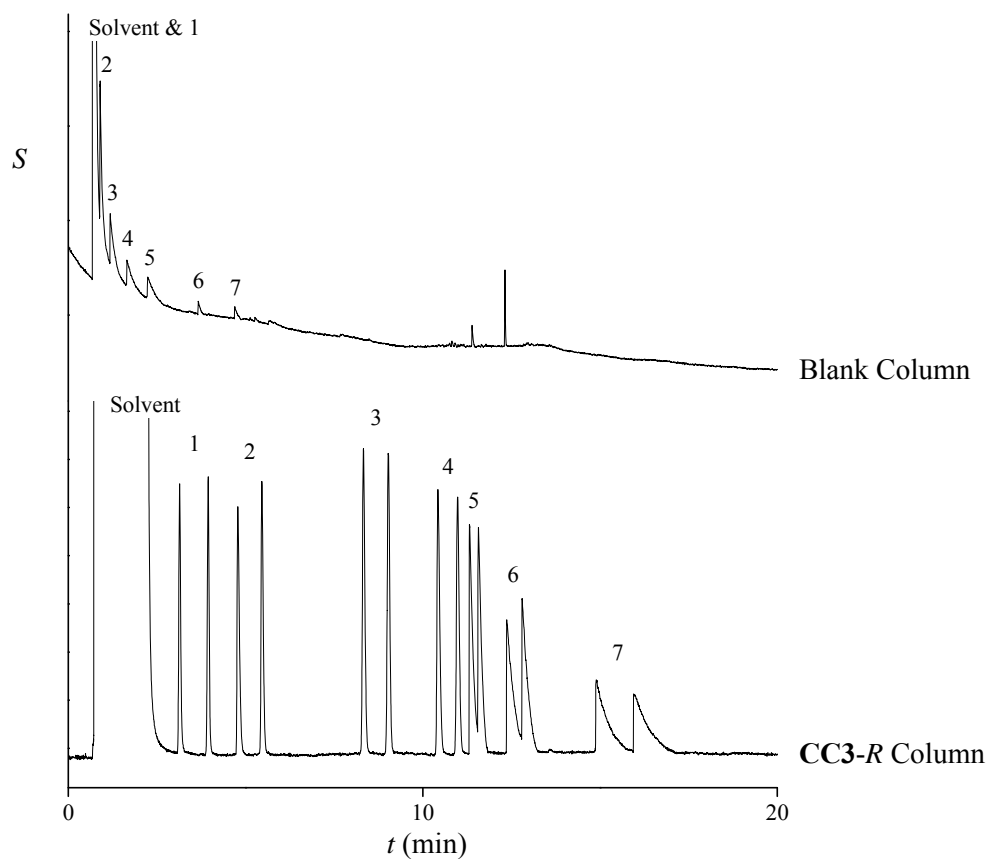
Figure 10-24 | GC-FID chromatograms of a mixture of seven linear 2-substituted alcohols separated on a blank (top) and CC3-*R* coated (bottom) column. Due to the large boiling point range of the alcohols (90 °C to 211 °C) the blank column was able to separate the different chain length racemates. However, no chiral separation was observed. By contrast, the **CC3**-*R* column chirally separated each racemate. A mixture of the seven racemic alcohols in diethyl ether was injected onto the GC: *rac*-2-butanol (1), *rac*-2-pentanol (2), *rac*-2-hexanol (3), *rac*-2-heptanol (4), *rac*-2-octanol (5), *rac*-2-nonanol (6), and *rac*-2-decanol (7).
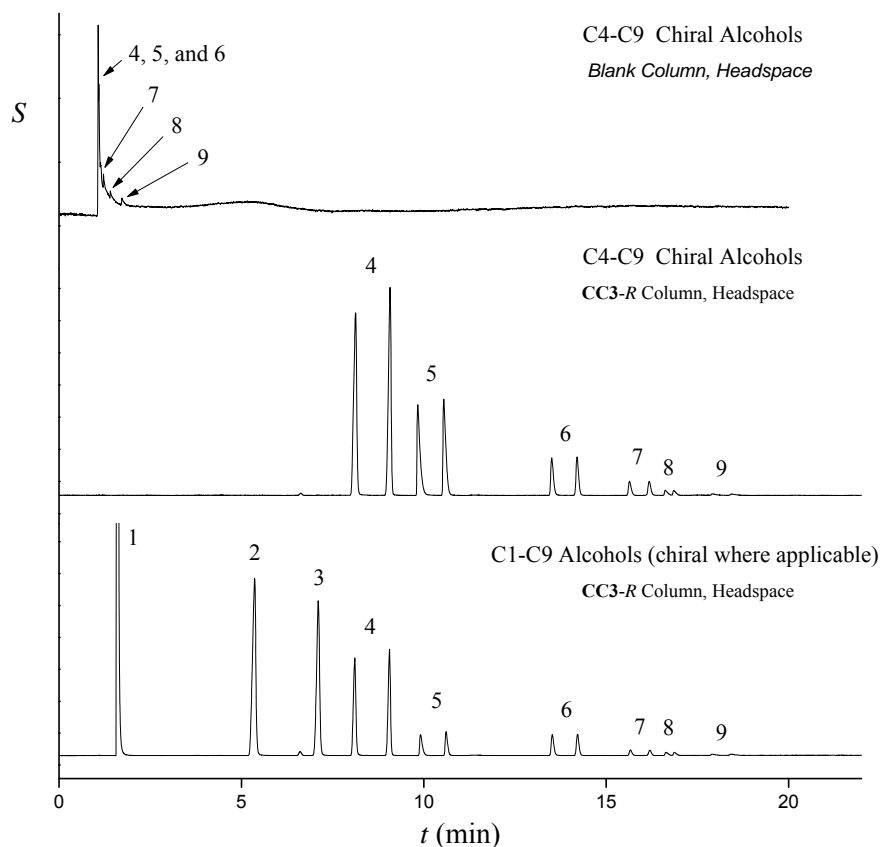
Figure 10-25 │ Separation of linear, 2-substituted (where applicable), C1–C9, alcohols on the CC3-*R* column introduced as headspace injections. Headspace injections may be performed without solvent; however, peak areas are directly related to a components boiling point. Only 2-butanol (4) and longer-chain alcohols are chiral, therefore only single peaks were seen for shorter-chain components. A mixture of nine alcohols was introduced into the system: methanol (1), ethanol (2), 2-propanol (3), *rac*-2-butanol (4), *rac*-2-pentanol (5), *rac*-2-hexanol (6), *rac*-2-heptanol (7), *rac*-2-octanol (8), and *rac*-2-nonanol (9).
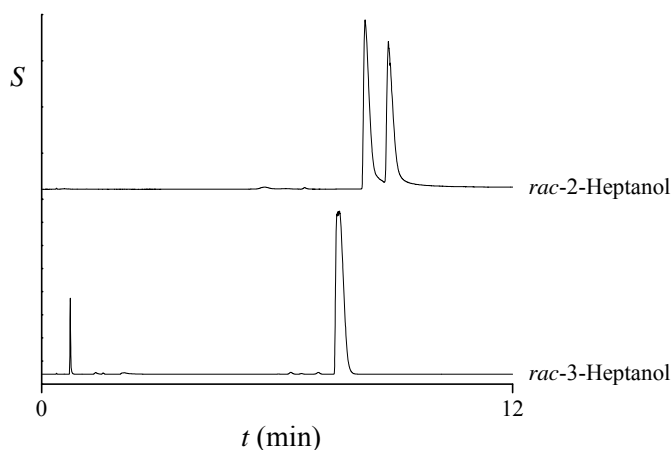
Figure 10-26 | Comparison between 2- and 3-substituted heptanol separations on the CC3-*R* column. While both are chiral, enantiomeric separation was only observed for the 2-substituted species. This is likely to be a consequence of steric environment of the hydroxy group. Chiral separation occurred because of favourable intramolecular interactions, including the formation of a hydrogen bond between guest's –OH group and **CC3**-*R*.[66] In 2-substituted, cyclic, and alkene/alkyne-substituted systems, the –OH group is well-exposed for hydrogen bonding. Whereas in 3-substituted linear saturated alcohols, both side chains may sterically crowd the –OH group, therefore interrupting the hydrogen bonding and consequently chiral separation was not seen.
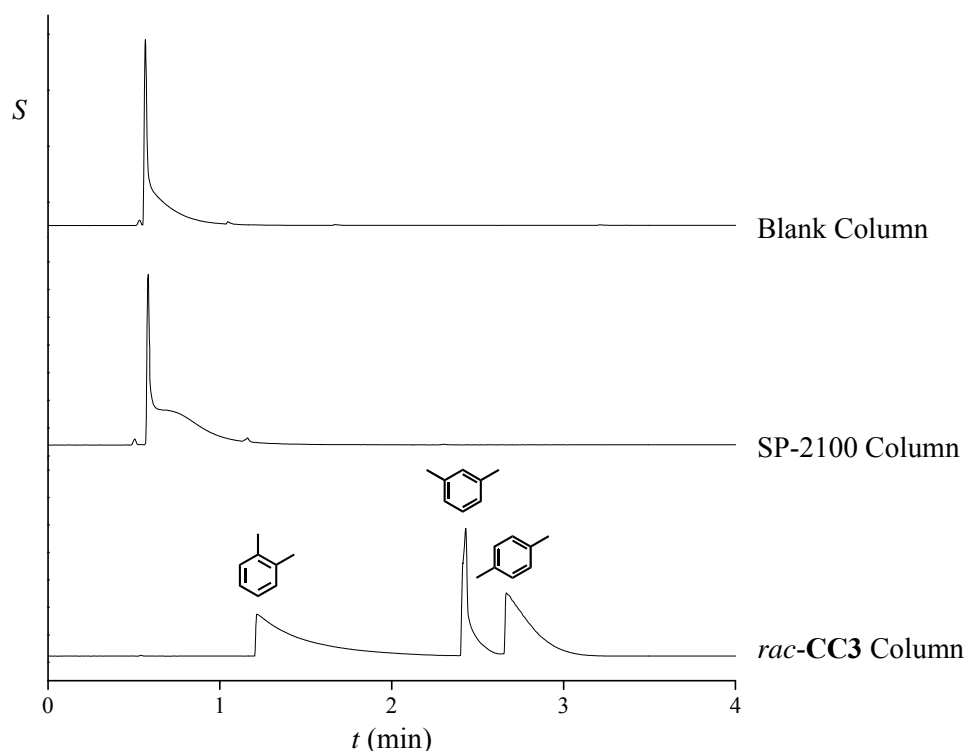

Figure 10-27 | GC-FID chromatograms of a xylene mixture separated on a blank (top), SP-2100 coated (middle) and *rac*-CC3 nanoparticle (bottom) coated colum. The order of elution (*o*-, *m*-, then *p*-xylene) is discussed in the main text and follows the expected order based on a previous study.[49]
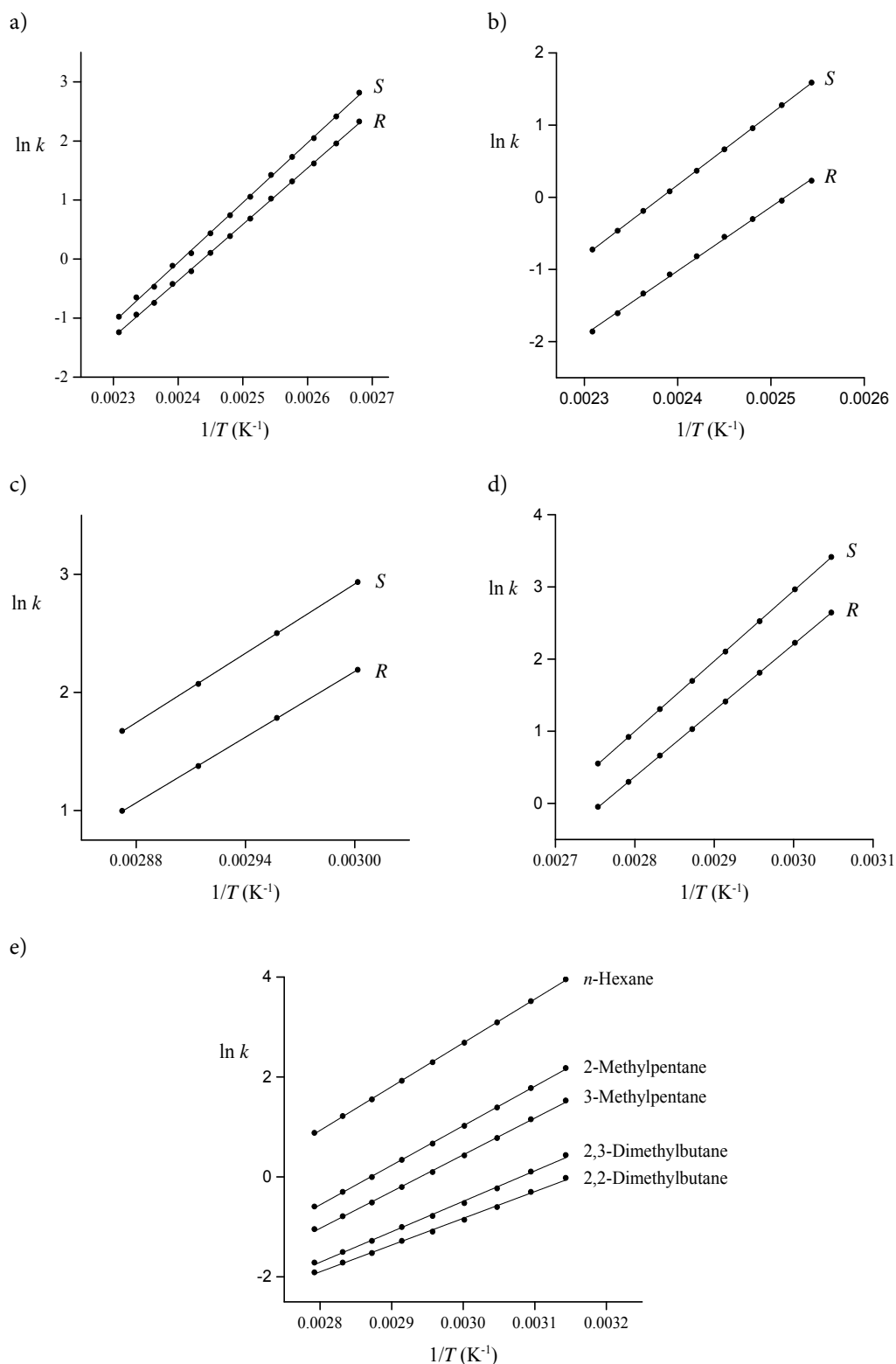
Figure 10-28 | Van't Hoff plots for a variety of systems separated on either the CC3-*R* column (a-d) or the *rac*-CC3 column (e). Retention factors (*k*) obtained from isothermal separations performed in 5 °C steps across various temperature ranges (in parentheses). Five mixtures are presented: *rac*-1-phenylethanol (**a**, *T* = 100-160 °C); *rac*-α-methylbenzylamine (**b**, 60-75); *rac*-2-butanol (**c**, 55-90); *rac-sec*-butylamine (**d**, 120-160); and a mixture of the five isomers of hexane (**e**, 45-85). R^2 values for linear fits > 0.99 in all cases.
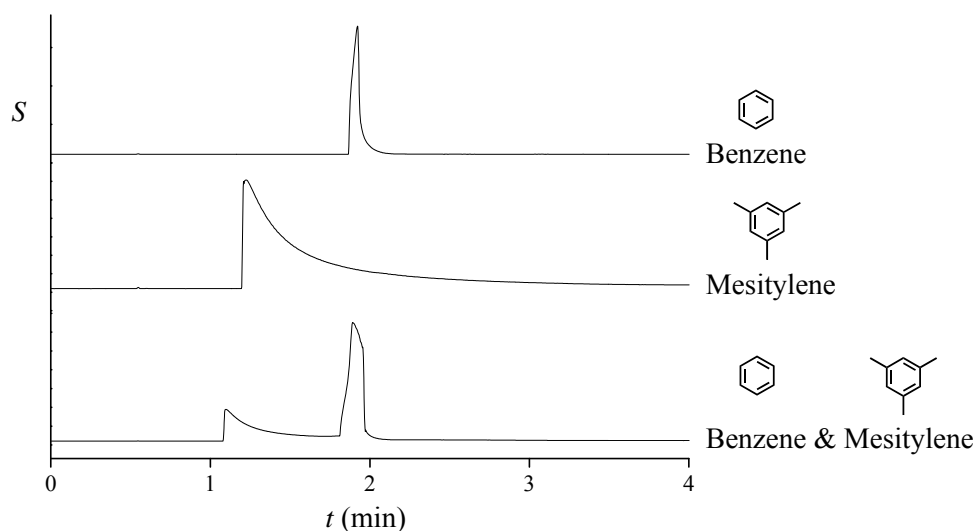
Figure 10-29 | GC-FID chromatograms of benzene separated from mesitylene on the *rac*-CC3 nanoparticle column. Usually, GC peak elution order matches the order of boiling points for each component in a mixture. However, the reverse was true for this system (b.p. = 80 °C for benzene 160 °C for mesitylene at 1 bar). Differences in peak area between mesitylene and benzene were due to their headspace concentration, which is a direct consequence of their boiling points.
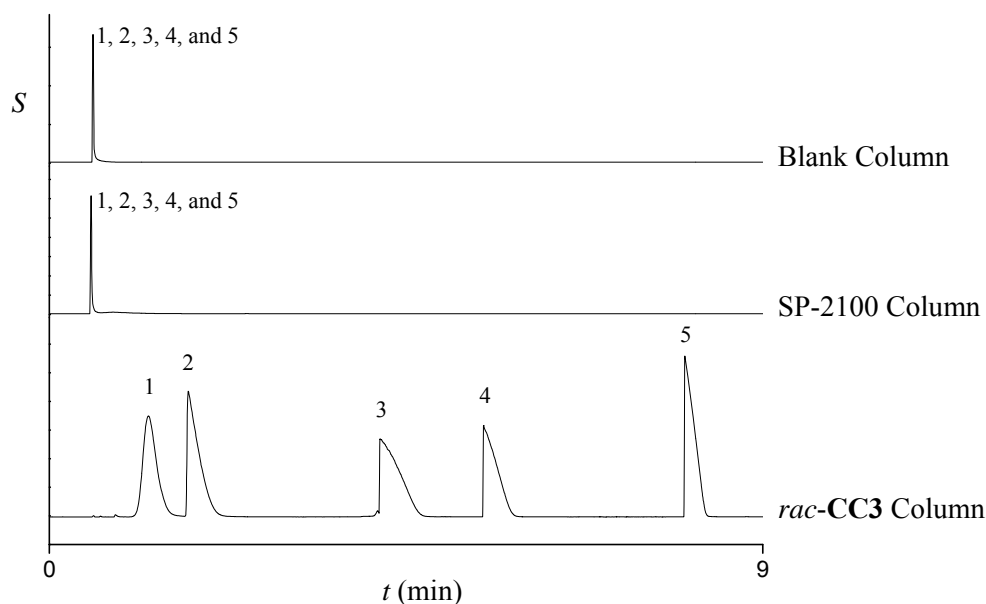

Figure 10-30 | GC-FID chromatograms of the five isomers of hexane separated on the *rac*-CC3 nanoparticle column. 2,2-Dimethylbutane (1), 2,3-dimethylbutane (2), 3-methylpentane (3), 2-methylpentane (4), *n*-hexane (5). The sample could not be introduced as a dilute solution injection because the solvent peak would likely overlap with the peaks for highly branched hexanes.

10.4.1 Computational Methods

*Computational methods were used to rationalise the separation behaviour of the rac-**CC3** column that is presented in Chapter 4.* <u>**These simulations were carried out by Dr. Linjiang Chen, who has written a detailed explanation of the process, copied into this Section.**</u>

10.4.1.1 Configurational-Bias Monte Carlo Simulations of the Adsorption of Hexane Isomers in *rac*-CC3

Configurational-bias Monte Carlo (CBMC) simulations of adsorption were used to help reveal the underlying principles which give rise to the impressive performance of *rac*-**CC3** in the separation of hexane isomers. Instead of attempting to insert an adsorbate molecule as a whole, which conventional MC does, CBMC grows the molecule segment-by-segment so that energetically unfavourable configurations—for example, where the molecule overlaps with the host and/or other guests—are largely avoided. The input of a CBMC simulation includes the temperature and chemical potential of the gas molecules in the reservoir (the grand-canonical ensemble), and the output of the simulation include the average number of adsorbed molecules and various sorts of information on adsorption (*e.g.,* adsorption enthalpies, adsorbate locations, *etc.*). A CBMC simulation is analogous to an adsorption experiment, in which the temperature and bulk pressure of a gas are specified and the corresponding uptake is measured. The chemical potential, as used in simulations, can be related to the gas-phase pressure, as specified in experiments, by an equation of state. The Peng–Robinson equation was used here. The CBMC simulations performed in this work included a 500,000-cycle equilibration period and a 500,000-cycle production run. One cycle consisted of n MC steps, with n being equal to the number of adsorbate molecules (*i.e.,* n fluctuated during the simulation). The trial MC moves included configurational-biased insertion, deletion, translation, rotation, and full/partial reinsertion; these moves were randomly attempted with equal probabilities. The isosteric heats of adsorption at zero coverage (infinite dilution) were obtained from MC simulations in the NVT (constant number of particles, volume, and temperature) ensemble using the Widom test particle method. Details on the simulation methodologies can be found in the literature.[159–161]

The atomistic representation of the *rac*-**CC3** crystal structure was constructed from the experimental crystallographic data, with all the cage atoms kept fixed at their

<u>**This Section was written entirely by Dr. Linjiang Chen. It is presented for completeness: the methodology used has not (yet) been published.**</u>

positions during the simulation. A $1 \times 1 \times 1$ unit-cell representation of the *rac*-**CC3** crystal structure was used in the CBMC simulations with periodic boundary conditions exerted in three dimensions. Lennard–Jones (LJ) parameters for *rac*-**CC3** were taken from the OPLS-AA force field.[162] The hexane isomers were described by the so-called united atom model, in which CH_3, CH_2, and CH are considered single entities; *i.e.,* a carbon atom and all of its bonded hydrogen atoms are lumped together to form one interaction site (a bead). Two neighbouring beads were connected by a harmonic bonding potential. A harmonic bending potential described the bond bending between three neighbouring beads, and changes in the torsional angle were controlled by a three-cosine potential. The beads in a chain separated by more than three bonds interacted with each other through a LJ potential. The force-field parameters used for hexane were taken from TraPPE,[163,164] while a detailed description of its application to adsorption simulations of nanoporous materials can be found in Dubbeldam *et al.*[163] The Lorentz–Berthelot combining rules were used to calculate both host–guest and guest–guest LJ cross-parameters, and a real-space cutoff of 12.0 Å was applied to all LJ interactions.

10.4.1.2   4.2 Molecular Dynamics Simulations of the Diffusion of Hexane Isomers in *rac*-CC3

A molecular dynamics (MD) simulation mimics the natural pathway of molecular motion to sample successive configurations, following the classical Newtonian mechanics, which thereby yields a trajectory that describes the positions, velocities, and accelerations of the particles as they evolve in time. Here, an initial configuration of the system was created by randomly placing one molecule of the desired hexane isomer into the simulation box consisting of one unit cell of the *rac*-**CC3** crystal structure. The adsorbate position was then equilibrated using 100,000 MC cycles with translation, rotation, and reinsertion moves. Next, velocities were assigned according to the Maxwell–Boltzmann distribution and an MD equilibration was run for 5 ns, with a time step of 0.5 fs, in the isothermal–isobaric (*NPT*) ensemble. The *NPT* MD simulation was continued for *ca.* 15 ns for production of results. In all the MD simulations, both the hexane isomers and the *rac*-**CC3** host were modelled as flexible. Again, the hexane isomers were described by the TraPPE force field and *rac*-**CC3** by the OPLS-AA force field. A cut-off radius of 12.0 Å was used for all LJ interactions, while all Coulomb interactions were computed using the Ewald summation technique with a relative precision of 10^{-6}. The Lorentz–Berthelot combining rules were

This Section was written entirely by Dr. Linjiang Chen. It is presented for completeness: the methodology used has not (yet) been published.

used to calculate the host–guest and intra-guest LJ cross-parameters, while the cross-parameters within and between **CC3** cages were determined via geometric means (as adopted by OPLS-AA). All MD and MC simulations were performed with the RASPA code developed by D. Dubbeldam, S. Calero, D. E. Ellis, and R. Q. Snurr.

10.4.1.3 Hexane Interactions with a CC3 'Surface'

When considering the perfect, static *rac*-**CC3** crystal structure, CBMC simulations predicted that 2,2-dimethylbutane (2,2-DMB) binds more strongly in the host than 2,3-dimethylbutane (2,3-DMB) does, hence suggesting that the latter would elute first in a GC experiment. This contradicts the experimental elution order of a hexane mixture from the *rac*-**CC3** column (Figure 2, main text). On the other hand, MD simulations, taking into account internal flexibility of the **CC3** cages, indicated that 2,2-DMB and 2,3-DMB have almost equivalent diffusivities within the *rac*-**CC3** structure. Since both di-branched isomers were suggested to be the slowest diffusing species, it would therefore seem reasonable to expect them to diffuse least-extensively within the particles of *rac*-**CC3** before exiting. It therefore follows that the relative interaction strengths of 2,3-DMB and 2,3-DMB with the *surface* of *rac*-**CC3** particles might contribute more significantly to their elution sequence compared to the less-branched isomers, which diffuse more extensively.

To explore this hypothesis, we created *in-silico* a 'surface' of **CC3**, as shown in Figure 10-31a. In this **CC3** surface, the cages maintain the same window-to-window packing and *R–S* chirality pairing as they do in the *rac*-**CC3** crystal structure, with the uppermost layer of **CC3** cages having a window facing upward. The surface was replicated infinitely in the *x–y* plane by periodic boundary conditions. In order to examine the extreme situation when hexane isomers only interact with the outermost region of *rac*-**CC3** particles, any void space below the surface defined by the centres of mass of the uppermost cages was blocked to adsorption. We calculated zero-coverage heats of adsorption for all five hexane isomers on this artificial surface model and compared the results with those obtained for the bulk *rac*-**CC3** crystal structure and with those obtained by experiment (Figure 10-31b).

Although 2,2-DMB was again predicted to have a stronger binding affinity with the *rac*-**CC3** crystal structure than 2,3-DMB does at infinite dilution, the **CC3** surface was predicted to interact more strongly with 2,3-DMB than with 2,2-DMB. In other

This Section was written entirely by Dr. Linjiang Chen. It is presented for completeness: the methodology used has not (yet) been published.

words, the *rac*-**CC3** particle surface might have a better retention ability for 2,3-DMB than for 2,2-DMB. Together with the simulated slow diffusion of both isomers within *rac*-**CC3**, this appears to suggest that the experimentally observed elution order might arise from a combination of kinetic and thermodynamic effects, and in specifically stronger adsorption of the 2,3-DMB species on the *rac*-**CC3** particle surface.
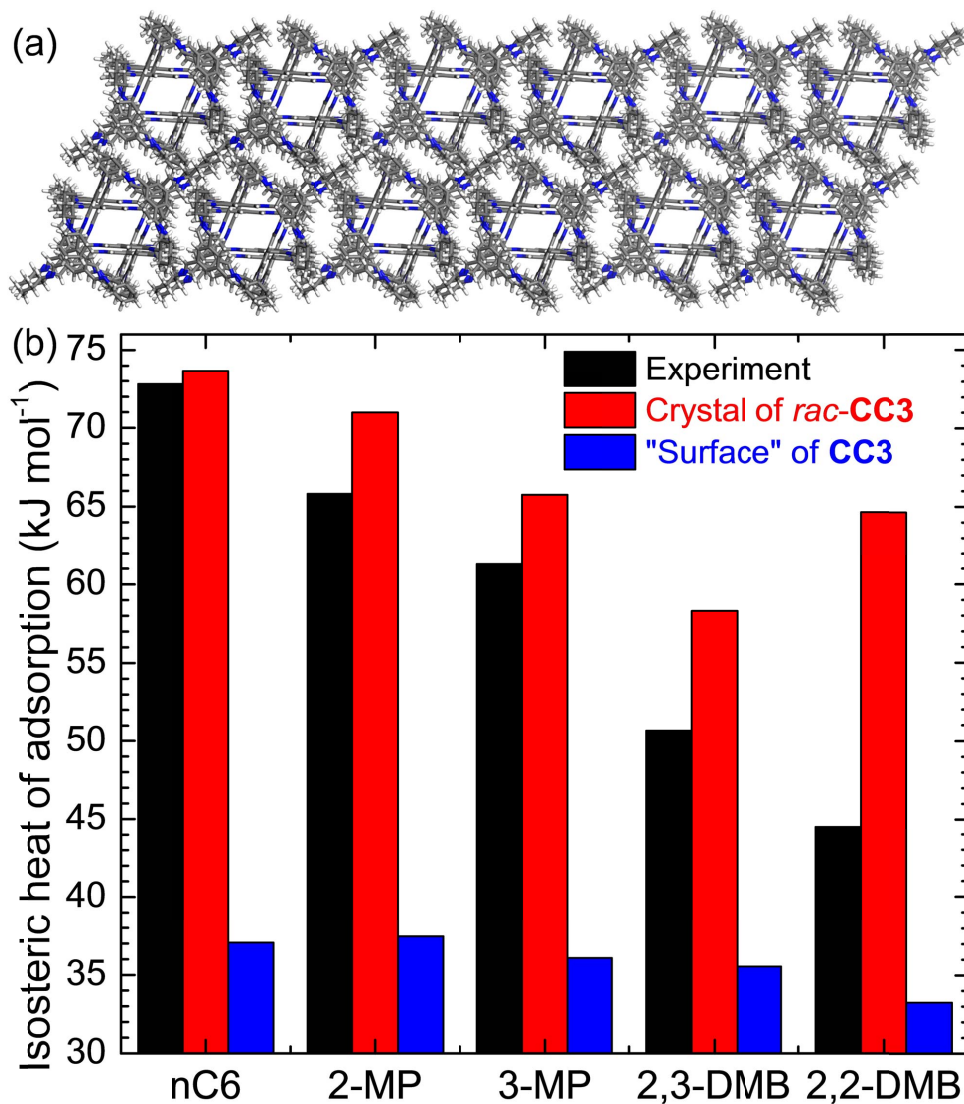

Figure 10-31 | (a) A surface model for **CC3** as described in the text. (b) Simulated zero-loading isosteric heats of adsorption for *n*-hexane (nC6), 2-methylpetane (2-MP), 3-methylpentane (3-MP), 2,3-dimethylbutane (2,3-DMB), and 2,2-dimethylbutane (2,2-DMB) in the *rac*-**CC3** crystal structure and on the **CC3** surface (all at 298 K), compared with the experimental values taken from Table 4-2 in the main text (p82). *Figure prepared by Dr. Linjiang Chen for his write up of the procedure.*

This Section was written entirely by Dr. Linjiang Chen. It is presented for completeness: the methodology used has not (yet) been published.